Observational Constraints on Supernova Progenitors

By

YIZE DONG
DISSERTATION

Submitted in partial satisfaction of the requirements for the degree of

DOCTOR OF PHILOSOPHY

in

Physics

in the

OFFICE OF GRADUATE STUDIES

of the

UNIVERSITY OF CALIFORNIA

DAVIS

Approved:

Stefano Valenti, Chair

Christopher Fassnacht

David Wittman

Committee in Charge

2024

I dedicate this thesis to my grandfather, who passed away in 2023.
I would not have reached this step without his encouragement and wisdom.

This page is intentionally left blank.

Contents

Abstract

In the last decade, time-domain surveys have dramatically enhanced our understanding of stellar evolutionary pathways by providing accurate measurements of the physical parameters of many stars. Despite these advancements, significant gaps remain in our understanding of how massive stars conclude their life cycles and the details of their final evolutionary stages. For instance, what experiences do red supergiants undergo in the months to years before their explosions? What are the origins of the pre-explosion outbursts in interaction-powered supernovae, and how can these inform our understanding of their progenitors? Can Type Ia supernovae result from helium-shell detonations? Is there a continuum among stripped-envelope supernovae?

In this dissertation, I will present progress on these topics through studies of five supernovae, including SN 2018cuf, SN 2023ixf, SN 2016dsg, SN 2022crv, and SN 2023fyq. Utilizing well-sampled photometric and spectroscopic data, alongside detailed hydrodynamic modeling, I have placed strong constraints on the progenitors of these supernovae. Remarkably, my findings suggest multiple mechanisms may be responsible for the dense circumstellar materials around Type II supernovae; some peculiar thermonuclear supernovae likely originate from thick helium-shell detonations; there is indeed a continuum between Type IIb and Type Ib supernovae; and a promising progenitor channel for Type Ibn supernovae involves a binary system with a compact object companion, capable of producing long-standing, bright pre-explosion emissions.

Acknowledegments

It was a truly wonderful journey.

When I first walked into Prof. Stefano Valenti's office, he showed me his research, and I suddenly realized this is what I should do: discover and explore the unknown. I decided to work with Stefano, and now I can say that it was one of the smartest decisions of my life. I thank Stefano for his support over the past six years, both professionally and emotionally. I also thank Prof. David Sand for supervising me throughout my PhD. His insights have been invaluable. I am grateful to Azalee Bostroem for guiding me through coding and transient research. I also thank my fellow graduate students Yutan Zhang, Zihao Shen, Fei Ge, Wei Wei, Yunshu Shi, Junying Huang, Wei Du, Tianqi Zhang, Keerthi Vasan, Pratik Gandhi, Emily Hoang, Nicolas Retamal, Darshana Mehta, Aravind Ravi, and many others for all the mutual support along the way. I thank the six hens in my backyard, who all sadly passed away earlier this year due to a yellow weasel/raccoon attack. I greatly appreciate the numerous eggs they laid.

I thank the UC Davis Symphony Orchestra for allowing me to play in the first violin section. It was one of the most wonderful and sweet moments I spent in Davis. I particularly thank Catherine Heusner for encouraging me to join the orchestra and helping me prepare for the audition. I also thank the Davis Chinese Orchestra, where I played the Erhu for many performances. I will never forget all the rehearsals we had together and all the lovely people in both orchestras.

I enjoyed every moment walking in the arboretum. Those trees, flowers, birds, squirrels, benches, the river, and the people I walked with–those memories will always be a treasure of my life. Jiahe, I will never forget the time we spent there together, where it all began.

Finally, I would like to thank my mom, dad, sister, grandma, and grandpa for giving me the opportunity to pursue research in astronomy. I barely spent time with them during my PhD, but it is their encouragement that helped me reach this far.

CHAPTER 1

Introduction

Supernovae (SNe) are the end points of massive stars and represent some of the most energetic events in the Universe. Observations of SNe can be confidently traced back to ∼1000 years ago (e.g., Stephenson, 2017). For example, in AD 1054, a bright SN was recorded by astronomers in China and Japan and was referred to as a "guest star". The remnant of this SN, known as the Crab Nebula, is still observable today. During the explosion, the heavy elements formed by nuclear reactions within stars, such as oxygen, carbon and iron, are ejected into space. This process is responsible for producing most of the elements in the Universe. SNe are powerful enough to expel gas from galaxies, inhibiting the formation of new stars and thus influencing the evolution of galaxies. On the small scale, SNe give us opportunities to study the mechanisms of stellar explosions and the conditions stars endure in the final stages of their lives. Therefore, understanding the physics of stellar explosions is a fundamental quest of astrophysics, linking transient research to stellar evolution, galaxy evolution, and cosmology.

Observationally, the two main types of data we collect for SNe are photometry and spectroscopy. These data are crucial for linking the explosions to their progenitors, thereby enhancing our understanding of the final stages of massive star evolution.

By taking time-series images of SNe using different bandpasses, we can obtain multiband light curves and construct the time evolution of the spectral energy distributions of SNe, which can provide valuable insights into the progenitor star. Light curves can be powered by various energy sources, such as shock cooling, hydrogen recombination, ^{56}Ni decay, and circumstellar material (CSM) interaction (e.g., Bersten & Mazzali, 2017; Zampieri, 2017;

Branch & Wheeler, 2017). Following the SN explosion, a radiation-dominated shock is emitted, breaking out from the stellar surface. The shock breakout is typically associated with bright X-ray/UV emission, and the subsequent cooling process of the shock-heated material can significantly influence the early phases of the SN light curves (Waxman & Katz, 2017). After that, if a sufficient amount of ^{56}Ni is generated during the explosion, the light curve can be powered by ^{56}Ni decay, potentially creating a second peak. In cases where the progenitor envelope contains a large hydrogen mass, hydrogen can be ionized by the initial shock, and the light curve can be dominated by the energy emitted by the hydrogen recombination front. This process often results in a plateau phase lasting approximately 100 days, a characteristic commonly observed in Type II supernovae. Additionally, if there is CSM around the progenitor, the interaction between the SN ejecta and the CSM can contribute to the SN light curve and produce some peculiar behaviours. By analyzing the light curve evolution, we can constrain the kinetic energy of the explosion, the mass and radius of the progenitor, and the mass loss history of the progenitor system.

Spectra, on the other hand, can provide constraints on the ejecta geometry, explosion energy, and the nucleosynthesis of the progenitor. The SN classification system is also based on the spectroscopic features of SNe (Minkowski, 1941; Harkness et al., 1987; Wheeler & Harkness, 1990; Filippenko, 1988, 1997) (see Figure 1.1). SNe showing strong hydrogen features are classified as Type II; those without significant hydrogen are categorized as Type I. Type I SNe are further divided into Type Ia, Type Ib, and Type Ic SNe. Type Ia SNe exhibit strong silicon lines. Type Ib SNe show strong He lines, which are absent in Type Ic SNe. A peculiar Type "IIb" is designated for objects that display clear hydrogen lines at early phases but become similar to Type Ib SNe at late phases. In addition, three new types-Type IIn, Type Ibn, and Type Icn-have been introduced to characterize objects that show narrow lines in their spectra (e.g., Matheson et al., 2000; Smith, 2017; Modjaz et al., 2019).

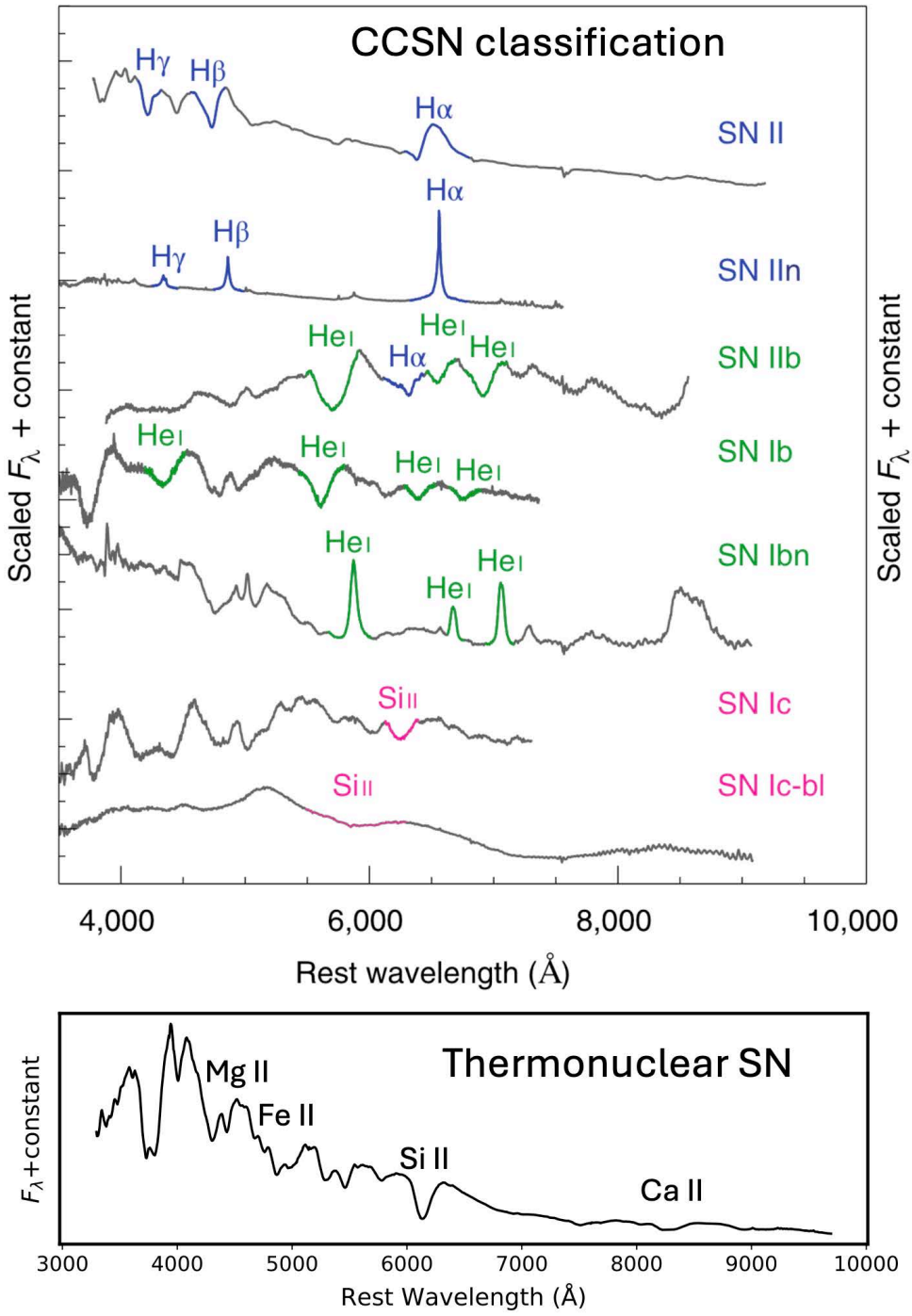

Figure 1.1 The classification system of SNe. The upper panel shows the comparison of different types of core-collapse SNe. The lower panel shows the spectrum of a typical Type Ia SN. The upper panel is reproduced from Modjaz et al. (2019). The spectrum in the lower panel is taken from Pereira et al. (2013).

Through either direct or indirect evidence, we are able to map many types of SNe to their progenitors. Type Ia SNe are believed to be from the explosions involving white dwarfs, and are usually called thermonuclear SNe. Type II SNe are thought to be originated from the explosions of red supergiants (RSGs), and are often called hydrogen-rich core-collapse SNe. Type IIb, Ib, and Ic SNe, known as stripped-envelope SNe, are massive stars that maintain varying amounts of hydrogen and helium in their envelopes right before exploding. Type IIn, Ibn, and Icn SNe experience strong interactions due to the presence of dense CSM around the progenitors, which produces narrow lines observed in their spectra. However, the progenitor systems of these interaction-powered SNe are still poorly understood.

Although we have a rough framework of SNe explosions, many questions remain open. For example, what are the physical mechanisms that enhance the mass loss of RSGs just before the explosions of core-collapse SNe? What are the progenitors of peculiar Type I SNe and how do they connect to Type Ia SNe. Is there an intrinsic continuum among stripped-envelope SNe? What are the progenitors of interaction-powered SNe? Progress in addressing these questions can significantly advance our understanding of transient phenomena and the final-stage evolution of massive stars.

In order to answer some of these open questions, we will need to investigate the still poorly explored phases of SNe, including the very early, very late, and pre-explosion phases. Fortunately, the search for transient phenomena in the Universe has entered a new era. The development of wide-field optical telescopes, equipped with large fields of view and operated in dedicated survey modes, now enables the daily scanning of the entire visible sky. This technological advancement opens a new window for transient research. In this thesis, I will present studies on various types of SNe, including hydrogen-rich core-collapse SNe (Type II), thermonuclear SNe (Type Ia), stripped-envelope SNe (Type Ib/c and IIb), and interaction-powered SNe (Type Ibn). The main topics covered are outlined below.

1.1. Hydrogen-Rich Core-Collapse SNe (Type II)

Hydrogen-Rich Core-Collapse SNe (Type II) are the most common types of SNe in the Universe (Li et al., 2011). Studies of hydrogen-rich SNe using pre-explosion imaging from the Hubble Space Telescope have directly pointed to RSG stars as their progenitors (Van Dyk et al., 2003a; Smartt, 2009). In recent years, very early spectroscopic observations of hydrogen-rich core-collapse SNe have revealed "flash" recombination lines, which quickly disappear a few days after the explosion (e.g., Förster et al., 2018; Bruch et al., 2023). A common interpretation of this feature is that these lines are due to the presence of dense and confined CSM around the progenitors. After the SN explosion, the CSM around the RSGs can be ionized by the photons from the SN shock breakout, resulting in a spectrum that shows a blue continuum with high ionization narrow emission lines from the CSM. This feature only lasts for a few days before it is swept up by the SN ejecta. In addition, hydrodynamical light curve modelling also suggests that most progenitors of SNe II are surrounded by dense CSM (e.g., Morozova et al., 2018), which requires intense mass loss in the months to years leading up to explosion. The dense CSM around Type II SNe implies that RSGs can experience enhanced mass loss right before their cores collapse, a situation not expected by classical stellar evolutionary theories.

In Chapter 2, I will present studies on SN 2018cuf (Type II), a hydrogen-rich SN exploded in the galaxy IC 5092. By using a set of light curve model generated by the Supernova Explosion Code (SNEC, Morozova et al. 2015), I constrained the initial progenitor mass of SN 2018cuf to 14.5 $M_{\odot}$. In addition, the very early light curve was best fitted by a model with 0.07 $M_{\odot}$ of CSM. This confirms that normal RSG stars can be surrounded by dense CSM right before their explosions, which requires enhanced mass loss at the final stages of their evolution.

In addition to modeling light curve and analyzing flash features in early spectra, searching for signs of pre-explosion activity or precursor emission of SNe can provide a more direct

probe of final-stage stellar activities and thus, the mass loss history (Ofek et al., 2014; Strotjohann et al., 2021a). However, such precursor activities are often faint and can typically only be detected for very nearby SNe or with large-aperture survey telescopes like the upcoming Legacy Survey of Space and Time (LSST).

In 2023, SN 2023ixf (Type II), a hydrogen-rich SN, exploded in the nearby galaxy M101, providing a perfect laboratory for transient studies. I conducted a comprehensive search for optical precursor emission from the progenitor of SN 2023ixf. Strikingly, no significant outbursts were detected within five years before the SN explosion. This is very different from the pre-explosion stellar activities that were observed in a previous case (SN 2020tlf, Jacobson-Galán et al. 2022), which showed precursor emission around -11.5 absolute magnitude in r, i, and z filters over $\sim$100 days before the explosion. This implies that there are very likely more than one physical mechanism behind the dense CSM around normal Type II SNe. The details are presented in Chapter 3.

1.2. Thermonuclear SNe (Type Ia)

Type Ia SNe are known to be the explosion of carbon-oxygen (CO) white dwarfs that gain mass from their companion star in binary systems and have been successfully used for cosmology studies for years. However, identifying the explosion mechanism and the secondary star are still open questions (see Howell (2011) for a review). While the prototypical progenitor system of a SN Ia is a white dwarf exploding when it reaches the Chandrasekhar mass, it was proposed decades ago that the explosion can also be trigger for a sub-Chandrasekhar mass white dwarf in a binary system (Nomoto, 1982a; Livne, 1990; Livne & Glasner, 1991; Woosley & Weaver, 1986, 1994; Livne & Arnett, 1995; Hoeflich & Khokhlov, 1996; Nugent et al., 1997). In this scenario, a thick helium shell can accumulate on an accreting carbon-oxygen (C/O) white dwarf, leading to a detonation at the base of the helium layer. This event triggers a core detonation, causing the white dwarf to explode at a sub-Chandrasekhar mass in a process known as double detonation (Woosley & Weaver, 1994; Livne & Arnett,

1995). However, these early thick helium shell models failed to reproduce Type Ia SNe spectra or colors since too much iron-group elements were produced during the He-shell burning (Nugent et al., 1997). Recently, several events have been found to be consistent with the theoretical predictions of double detonations with thick He shells (Inserra et al., 2015; De et al., 2019), but we are still missing the smoking gun proof that those events are actually connected with double detonations.

In Chapter 4, I will present studies on a peculiar event SN 2016dsg. SN 2016dsg showed strongly suppressed UV flux in the spectra at early times due to the iron-group elements produced during He-shell burning. In addition, the signature of unburnt helium was identified in the near-infrared spectra of SN 2016dsg, marking the first such detection. These observations provide compelling evidence that double detonations do exist in nature and contribute to a subset of thermonuclear SNe.

1.3. Stripped-envelope SNe (Type IIb, Ib, and Ic)

Stripped-envelope SNe are a subclass of core-collapse SNe that have partially or completely lost their progenitor envelope prior to their explosions. Stripped envelope SNe are spectroscopically classified as Type IIb, Type Ib and Type Ic SNe depending on the presence or absence of hydrogen and helium lines in the optical spectra. The loss of the progenitor envelope of a stripped-envelope supernova can be due to strong stellar winds of a single massive star or the mass transfer in a close binary system (Smith et al., 2011). However, how many stripped-envelope SNe are produced in binary systems is still an open question. If most stripped-envelope SNe are produced in binary systems, there might be some transitional objects with residual hydrogen or helium in their progenitors (Yoon et al., 2010). Quantifying how much residual hydrogen there is in a Type Ib supernova will provide unique information about the evolutionary state of the progenitor and the associated mass loss mechanism. However, this kind of transitional object is rarely unambiguously identified (Liu et al., 2016a).

In Chapter 5, I will present analyses of SN 2022crv, a transitional object on the continuum of Type Ib and Type IIb. SN 2022crv was discovered and classified by the Distance Less Than 40 Mpc (DLT40; Tartaglia et al., 2018) survey. When it was just discovered, the classification of this object was debatable. The early spectrum of SN 2022crv featured a very broad absorption line at ∼6200 Å, which could be interpreted as a silicon line or a hydrogen line. As the object evolves, we found that SN 2022crv should be classified as a Type IIb SN. However, detailed spectral analysis revealed that SN 2022crv is a not normal Type IIb. Specifically, the hydrogen features in SN 2022crv disappeared much faster than those in other Type IIb SNe, likely due to the low hydrogen envelope mass in SN 2022crv. Based on hydrodynamical modeling, we were able to put a strong constraint on the amount of hydrogen left in the envelope of SN 2022crv. Through nebular spectral modeling, we found that the progenitor is consistent with an explosion of a ∼5 $M_\odot$ He star that evolved from a ∼16–22 $M_\odot$ zero-age main sequence star in a binary system. The relatively low progenitor mass derived for SN 2022crv suggests that SN 2022crv was likely in a binary system and most of hydrogen envelope was stripped through binary interaction.

1.4. Interaction-powered SNe (Type IIn, Ibn)

Interaction-powered SNe are characterized by narrow emission lines in their spectra. The progenitors of these SNe are surrounded by dense CSM. Typically, the interaction between the SN ejecta and the CSM serves as the primary energy source for these SNe. Due to the presence of optically thick CSM, it is not easy to probe the progenitor systems and the explosion mechanisms of these SNe.

One method to constrain their progenitors is searching for the flares/precursor emission from the progenitors of these SNe months to years before explosion. The precursor emission is commonly observed in Type IIn SNe (e.g., Ofek et al., 2014; Strotjohann et al., 2021a), which show narrow hydrogen lines in their spectra and are powered by the interaction between the SNe ejecta and the surrounding circumstellar material (CSM). The precursors from Type IIn

SNe can last for months and are usually brighter than around -13 magnitude (Strotjohann et al., 2021a). The bright precursors directly link these SNe to luminous blue variables (e.g., Mauerhan et al., 2013). For Type Ibn SNe, precursors have only been observed in two objects with unsatisfactory data coverage (Pastorello et al., 2007; Strotjohann et al., 2021a). In Chapter 6, I will discuss the long-standing precursor emission observed in SN 2023fyq, one of the closest Type Ibn SNe. The precursors observed in SN 2023fyq provide valuable insights into the final days of progenitors of Type Ibn SNe. My findings suggest that a binary system is likely involved in order to explain the pre-explosion activities. In addition, an equatorial disk was likely formed during the pre-explosion binary interactions. This configuration of the progenitor system is consistent with both the photometric and spectroscopic evolution observed in SN 2023fyq.

CHAPTER 2

Supernova 2018cuf: A Type IIP Supernova with a Slow Fall from Plateau

Published as Dong et al 2021. in The Astrophysical Journal, Volume 906, Issue 1, id.56, 15 pp.

2.1. Abstract

In this chapter, we present multi-band photometry and spectroscopy of SN 2018cuf, a Type IIP ("P" for plateau) supernova (SN) discovered by the Distance Less Than 40 Mpc survey (DLT40) within 24 hours of explosion. SN 2018cuf appears to be a typical Type IIP SN, with an absolute V-band magnitude of -16.73 ± 0.32 at maximum and a decline rate of 0.21 ± 0.05 mag/50d during the plateau phase. The distance of the object is constrained to be 41.8 ± 5.7 Mpc by using the expanding photosphere method. We use spectroscopic and photometric observations from the first year after the explosion to constrain the progenitor of SN 2018cuf using both hydrodynamic light curve modelling and late-time spectroscopic modelling. The progenitor of SN 2018cuf was most likely a red supergiant of about 14.5 $M_\odot$ that produced 0.04 ± 0.01 $M_\odot$ ^{56}Ni during the explosion. We also found ~ 0.07 $M_\odot$ of circumstellar material (CSM) around the progenitor is needed to fit the early light curves, where the CSM may originate from pre-supernova outbursts. During the plateau phase, high velocity features at ~ 11000 km s^{-1} are detected both in the optical and near-infrared spectra, supporting the possibility that the ejecta were interacting with some CSM. A very shallow slope during the post-plateau phase is also observed and it is likely due to a low degree of nickel mixing or the relatively high nickel mass in the SN.

2.2. Introduction

Type II supernovae (SNe), the most common type of core-collapse supernova (CCSN), originate from the collapse of stars more massive than $\sim$8 $M_{\odot}$. In the Type IIP subclass, the SN experiences a period of nearly constant luminosity for $\sim$ 2–3 months after maximum as the hydrogen envelope recombines. This is then followed by a rapid drop from the plateau where the light curve becomes dominated by radioactive decay and the SN enters the nebular phase.

From pre-explosion imaging at the location of the explosions, the progenitors of Type IIP SNe have been mostly attributed to red supergiants (RSGs) with initial masses of $\sim$ 8–17 $M_{\odot}$ (Van Dyk et al., 2003b; Smartt et al., 2009; Smartt, 2015). However, evolutionary codes predict that the progenitors of Type IIP SNe can have masses up to 30 $M_{\odot}$ (e.g. Heger et al., 2003; Ekström et al., 2012). This discrepancy between observations and theory has been dubbed the "red supergiant (RSG) problem." This problem has been discussed by many authors (e.g. Walmswell & Eldridge, 2012; Kochanek et al., 2012; Horiuchi et al., 2014; Davies & Beasor, 2018, 2020), and remains an open question. An alternative method that is widely used to estimate the progenitor masses of Type II SNe is hydrodynamic modelling of SN light curves (e.g. Utrobin & Chugai, 2015, 2017; Morozova et al., 2017, 2018; Paxton et al., 2018; Goldberg et al., 2019; Martinez & Bersten, 2019). Through comparing observed light curves with model light curves, many progenitor properties, such as mass, radius and explosion energy, could be determined. Another approach to estimate the progenitor mass is nebular spectral modelling (Jerkstrand et al., 2012, 2014). Here the structure and composition of the ejecta can be constrained, and the intensity of the O I $\lambda\lambda$6300,6363 doublet can be used to derive the progenitor mass.

These various methods sometimes do not predict a consistent progenitor mass for a given SN, so continued observational and theoretical work is necessary for these different techniques to converge (Jerkstrand et al., 2014; Morozova et al., 2018; Davies & Beasor,

2018). The progenitor mass distribution inferred from hydrodynamic modelling is generally higher than the observed mass range from direct imaging, mitigating the RSG problem (Morozova et al., 2018). On the other hand, Jerkstrand et al. (2014) found that, from nebular spectral modelling, there is no evidence yet that the progenitor of an observed Type II SN is more massive than 20 $M_{\odot}$, supporting the presence of the RSG problem. However, some recent SN studies have found more massive progenitors based on nebular spectral modelling (Anderson et al., 2018; Bose et al., 2020). It is important to note that the sample of SNe that have been studied by these two modelling techniques is small. Increasing the sample size is necessary to fully examine the existence of the RSG problem.

For this purpose, observations both in the first few days after explosion and during the nebular phase (∼300-500 days after explosion) are required. Unfortunately rapid discovery and follow-up of SNe is still rare, and often Type IIP SNe are not followed out to the nebular phase when larger telescopes are needed. Thankfully, modern SN surveys such as the All Sky Automated Survey for SNe (ASAS-SN, Shappee et al. 2014a; Kochanek et al. 2017a), the Zwicky Transient Facility (ZTF, Bellm et al. 2019), the Asteroid Terrestrial-Impact Last Alert System (ATLAS, Tonry 2011; Smith et al. 2020a), and the Distance Less Than 40 Mpc survey (DLT40, Tartaglia et al. 2018) are now able to discover SNe within hours of explosion and use dedicated facilities for follow-up, such as the Las Cumbres Observatory (LCOGT, Brown et al., 2013a). The very early light curves of core-collapse SNe provided by these surveys can be used to constrain the progenitor radius (and potentially the envelope structure), ejected mass, and kinetic energy of the explosion (e.g. Rabinak & Waxman, 2011; Sapir & Waxman, 2017; Bersten et al., 2018; Arcavi et al., 2017; Piro et al., 2017, for selected theoretical and observational results).

In this paper, we present optical and infrared photometry and spectroscopy of SN 2018cuf, a Type II SN discovered within 30 hours of explosion by the DLT40 survey and densely monitored within the Global SN Project (GSP)[1] for over 340 days. This paper is organized

[1]GSP is a Key Project at Las Cumbres Observatory

as follows: the observations of SN 2018cuf are presented in Section 2.3, while the reddening and host galaxy properties are presented in Section 2.4. Further observational properties, such as the distance and explosion epoch, are constrained in Section 2.5. In Section 2.6 we analyze the light curves and in Section 2.7 the spectroscopic evolution is described. We constrain the nickel mass and progenitor mass using our extensive observational data set in Section 2.8, and finally we present our conclusions in Section 2.9.

2.3. Observations

SN 2018cuf was discovered at RA(2000) = $21^h16^m11^s.58$, Dec(2000) = $-64°28'57''.30$ in the nearby SBc galaxy IC 5092 (see Figure 2.1) on 2018 June 23 (Valenti et al. 2018, JD 2458292.86093, $r = 17.4$), during the course of the DLT40 SN search (Tartaglia et al., 2018), utilizing the 0.4-m PROMPT5 telescope (Reichart et al., 2005) at the Cerro Tololo Inter-American Observatory (CTIO). A non-detection ∼24 hours earlier (JD 2458291.74456; $r \lesssim 19.4$) strongly constrains the explosion epoch (see Figure 2.2). The 1-day cadence of the DLT40 SN search is designed to discover ∼ 10 nearby SNe (< 40 Mpc) per year within 24 hours of explosion. The mechanics of the survey have been described elsewhere (Yang et al., 2017; Tartaglia et al., 2018; Yang et al., 2019a), along with the recent addition of a second telescope in Australia (for an effective ∼12 hour cadence), and improvements to our machine learning search algorithm, and fast telescope triggering infrastructure (Bostroem et al., 2020).

Shortly after discovery, we triggered high cadence observations with the world-wide network of robotic telescopes associated with Las Cumbres Observatory and also the Neil Gehrels *Swift* Observatory (Gehrels et al., 2004). The photometric data from the Las Cumbres Observatory were reduced using the PyRAF-based photometric reduction pipeline LCOGTSNPIPE (Valenti et al., 2016). This pipeline uses a low-order polynomial fit to remove the background and calculates instrumental magnitudes using a standard point-spread function fitting technique. Apparent magnitudes were calibrated using APASS (B, V, g, r, i)

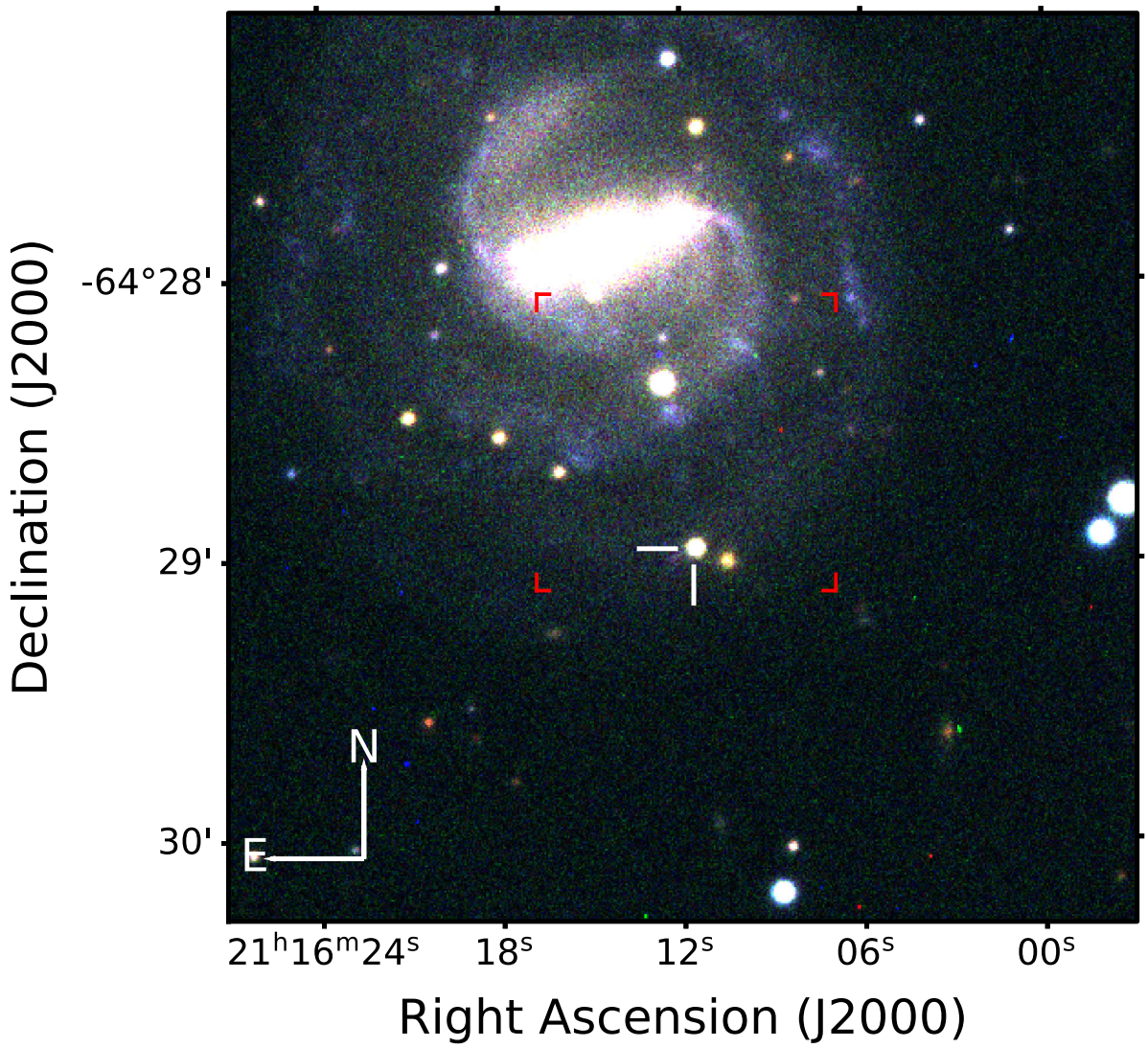

Figure 2.1 RGB image of SN 2018cuf (indicated by white tick marks) in IC 5092 obtained with the Las Cumbres Observatory on 2018 September 17. The red markers delineate the MUSE field of view, as described in Section 3.2.

and Landolt (U) catalogs. The clear presence of background contamination was identified in the r-band images of SN 2018cuf beginning around ∼280 days after explosion. This contamination was removed by subtracting a reference image and the photometry was extracted

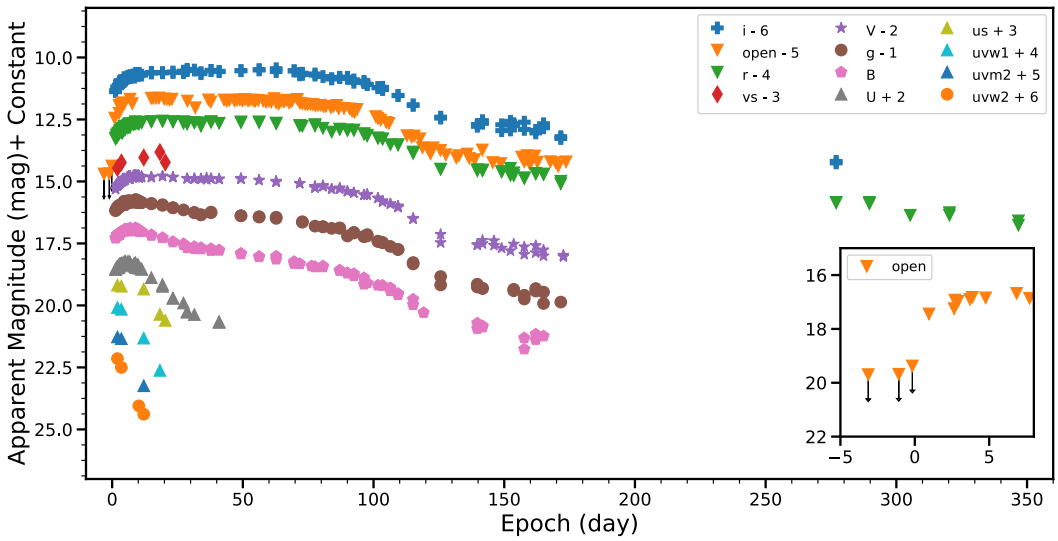

Figure 2.2 Multi-band light curves for SN 2018cuf with respect to the epoch of explosion. An *Open* filter is used by the PROMPT5 0.4 m telescope and is calibrated to the r-band. The insert is a zoom on the *Open* filter illustrating the DLT40 detection limit ∼1 day before discovery.

from the subtracted image. At earlier epochs the photometry from difference imaging was consistent with the PSF photometry from the original (unsubtracted) image but with larger scatter. We therefore use difference imaging for all bands only for observations taken after 200 days, when contamination was significant. The *Swift* UVOT images are reduced using the method described in Brown et al. (2009) using the updated zeropoints of Breeveld et al. (2011). The multi-band light curves are shown in Figure 2.2. The *Swift* photometry is available in the Swift Optical Ultraviolet Supernova Archive (SOUSA; Brown et al. 2014).

The spectroscopic observations of SN 2018cuf started on 2018 June 24 (∼1 day after discovery) and continued through 2019 October 19. A number of optical spectra were collected by the Southern African Large Telescope (SALT), including the first classification spectrum, which classified SN 2018cuf as a young SN Type II (Jha, 2018). In addition, many low dispersion optical spectra were obtained by the FLOYDS spectrograph (Brown et al., 2013a) on the 2m Faulkes Telescope South (FTS) in Australia. One optical spectrum was taken

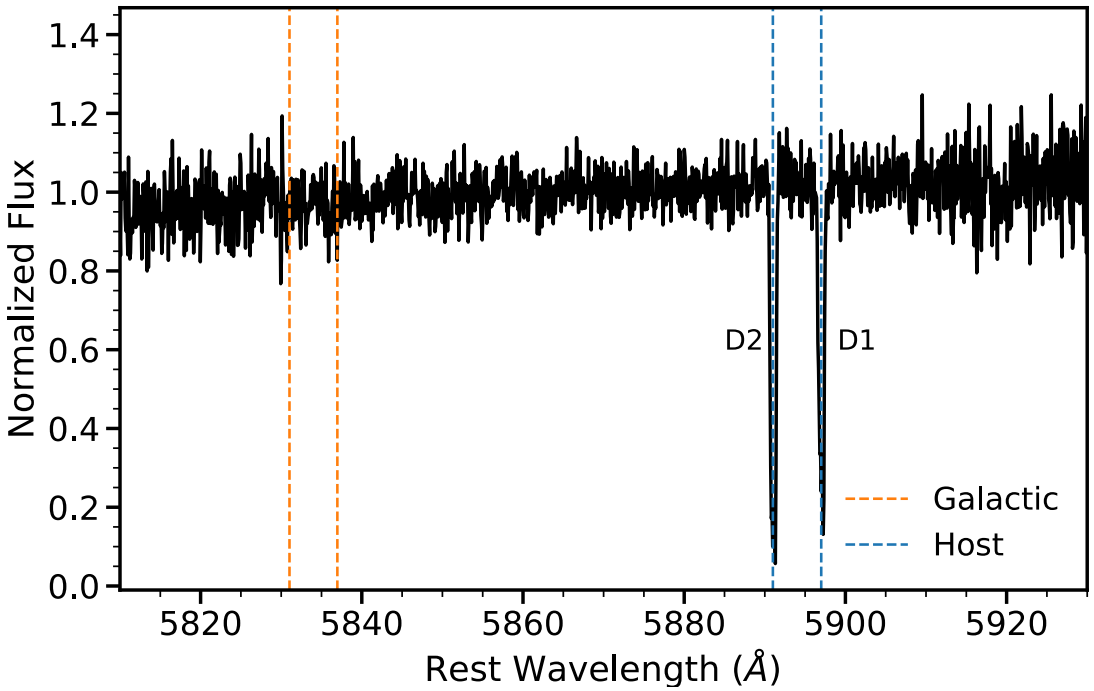

Figure 2.3 An echelle spectrum with a resolution of R $\simeq$ 40000 from Magellan/MIKE taken on +19.6 d showing the region around the galactic (dashed orange lines) and host (dashed blue lines) NaID lines.

with the GMOS instrument (Hook et al., 2004; Gimeno et al., 2016) at the Gemini South telescope on 2018-06-24 05:33:32 UT, under program GS-2018A-Q-116. GMOS was used in longslit spectroscopy mode with the B600 grating, with a total exposure time of 750 s. However, this spectrum has a very low S/N, so we did not use it for analysis. We also used FORS2 (Appenzeller et al., 1998) at the Very Large Telescope (VLT) with the GRIS_150I grism and GG435 blocking filter to observe SN 2018cuf on 2018-12-14 00:48:30 UT, as part of the FOSSIL program (Kuncarayakti et al., in prep.). The total exposure time was 2700 s. The data were reduced using EsoReflex software (Freudling et al., 2013). The low dispersion optical spectra are shown in Figure 2.4. There is also one high resolution optical spectrum taken by the Magellan Inamori Kyocera Echelle instrument (MIKE) (Bernstein et al., 2003) on the Magellan Clay Telescope (Figure 2.3). Near-infrared (NIR) spectra were taken with

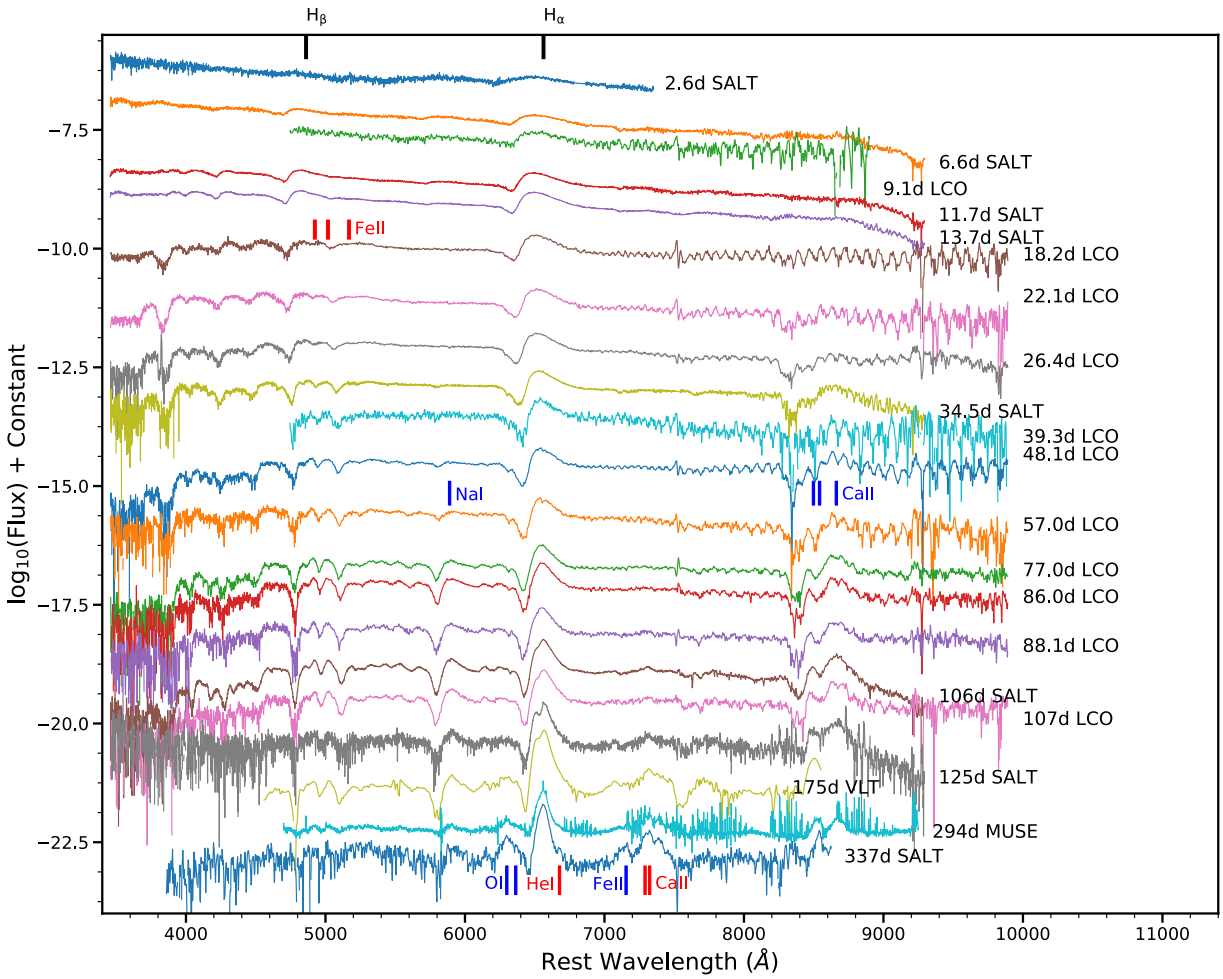

Figure 2.4 The optical spectroscopic evolution of SN 2018cuf from 2 to 337 days after explosion.

the FLAMINGOS-2 instrument (F2, Eikenberry et al. 2006) at Gemini South Observatory and the Folded-port InfraRed Echellette instrument (FIRE, Simcoe et al. 2013) on the Magellan Baade telescope. The Magellan FIRE spectra were obtained in high throughput prism mode with a 0.6 arcsec slit, giving continuous wavelength coverage from 0.8 to 2.5 μm. For the Gemini South F2 spectra, we observed with the JH grism and 0.72 arcsec slit in place, yielding a wavelength range of 1.0–1.8 μm. For both the FIRE and F2 data, observations were taken with a standard ABBA pattern for sky subtraction, and an A0V star was observed adjacent to the science exposures for both telluric corrections and flux calibration. Data for

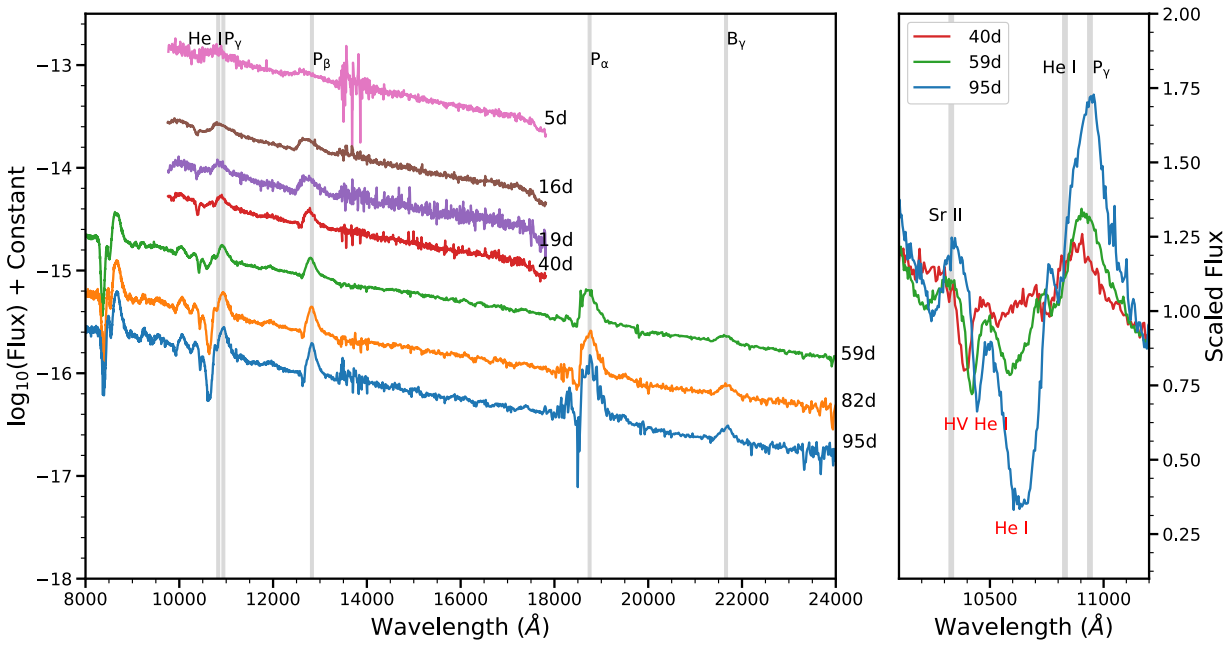

Figure 2.5 Left: Near-infrared spectra of SN 2018cuf from Gemini+FLAMINGOS-2 and Magellan+FIRE. Right: A zoom-in version for spectra at day 40, day 59 and day 95. The high velocity (HV) He I feature and He I absorption are labelled.

both instruments was reduced in a standard way as described in Hsiao et al. (2019a), and we refer the reader there for the details. The NIR spectra are presented in Figure 2.5. All the spectroscopic observations will be available on WISeREP (Yaron & Gal-Yam, 2012)[2].

2.4. Reddening and host properties

2.4.1. Reddening. The Milky Way line-of-sight reddening towards SN 2018cuf is $E(B-V)_{MW} = 0.0273 \pm 0.0003$ mag (Schlafly & Finkbeiner, 2011a). This low extinction value is also supported by the lack of NaID lines from the Milky Way in the Magellan/MIKE Echelle spectrum taken on 2018 July 12 and shown in Figure 2.3. The equivalent width (EW) of the NaID line is often used to estimate the SN reddening with the assumption that it is a good tracer of gas and dust (Munari & Zwitter, 1997; Poznanski et al., 2012). The measured EW of the host galaxy NaID λ5890 (D_2) and NaID λ5896 (D_1) are 0.677Å and

[2] http://www.weizmann.ac.il

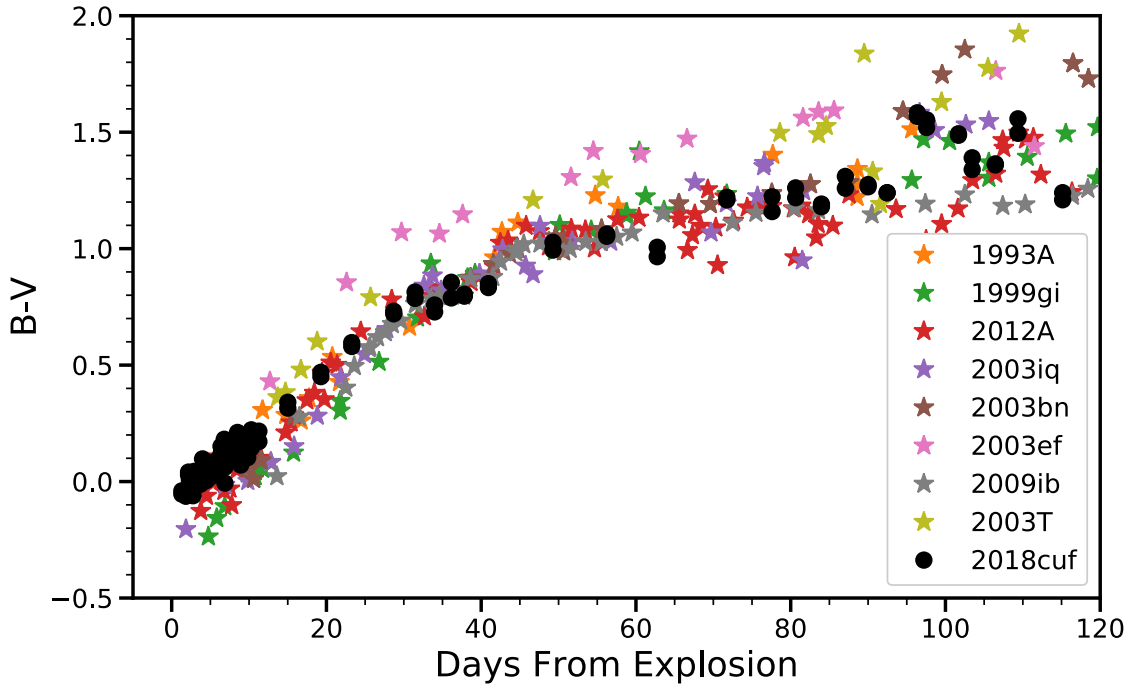

Figure 2.6 Color evolution of SN 2018cuf, after correcting for a MW color excess of $E(B-V)_{MW} = 0.0273$ mag. We also plot a sample of Type II SNe with published reddening estimates (see Section 2.4 for details). With only this MW reddening correction, SN 2018cuf shows a similar color evolution as the other objects, suggesting there is not a significant amount of host reddening.

0.649Å respectively. The intensity ratio of D_2 to D_1 (D_2 / D_1 ~1) is far from the typical value of 2 we usually observe (Munari & Zwitter, 1997), suggesting that at least D_2 may be saturated (see Figure 2.3). Using only D_1, we find a host galaxy extinction of $E(B-V)_{host}$ = 0.699 ± 0.17 mag.

Phillips et al. (2013) suggests that the most accurate predictor of extinction is the diffuse interstellar band (DIB) absorption feature at 5780 Å. However, this feature does not appear to be present in our high resolution spectrum of SN 2018cuf, suggesting the host galaxy extinction is negligible, which is inconsistent with the high host reddening derived from NaID lines. For this reason, we estimate the extinction by comparing the $B-V$ color evolution of SN 2018cuf to a sample of other similar Type II SNe with published reddening estimates.

This includes SN 1993A (Anderson et al., 2014; Galbany et al., 2016a), SN 1999gi (Leonard et al., 2002a), SN 2003iq (Faran et al., 2014), SN 2003bn (Anderson et al., 2014; Galbany et al., 2016a), SN 2003ef (Anderson et al., 2014; Galbany et al., 2016a), SN 2003T (Anderson et al., 2014; Galbany et al., 2016a), SN 2009ib (Takáts et al., 2015) and SN 2012A (Tomasella et al., 2013), as is shown in Figure 2.6. SN 2018cuf has a similar V-band light curve slope after maximum with these selected SNe. de Jaeger et al. (2018) found that the color evolution of SNe are related to the slope of the V-band light curve, so these selected SNe should have consistent colors with SN 2018cuf after dereddening. We find that an $E(B-V)_{host} \approx 0$ mag gives us a consistent color evolution with the other objects, suggesting a low extinction at the location of SN 2018cuf. Therefore throughout this paper we will only consider the Milky Way reddening as the total value, and adopt an $E(B-V)_{tot} = 0.0273 \pm 0.0003$ mag, as well as an $R_V = 3.1$ (Cardelli et al., 1989).

The disagreement between host reddening values obtained from the NaID lines versus direct color comparisons to other similar objects is not a unique problem. Leonard et al. (2002b) found a similar situation for SN 1999em, i.e., the equivalent width of the sodium lines suggested a high reddening for SN 1999em, but a low value was assumed based on color comparisons.

2.4.2. Host Properties. Multi Unit Spectroscopic Explorer (MUSE) (Bacon et al., 2010) integral field unit (IFU) observations of IC 5092 were taken on 2019 April 12, as a part of the All-weather MUse Supernova Integral-field Nearby Galaxies (AMUSING; Galbany et al. 2016b) survey. MUSE is mounted to the 8.2m Yepun UT4 Very Large Telescope, with a field-of-view of $1' \times 1'$and $0.2'' \times 0.2''$spatial elements, small enough to sample the PSF. See Figure 2.1 for an outline of the MUSE footprint. The spectral coverage is from 4750 to 9300Å, with a spectral resolution that ranges from R$\simeq$3500 in the blue end, $\simeq$1700 in the red end. Four 580s exposures (2320s total exposure time), rotating 90 deg between frames,

were taken centered on the South-West side of the galaxy, which covered the SN position and its environment.

We extracted a 3.6″ aperture spectrum centered at the SN position (corresponding to a ∼800 pc diameter) to study the properties of the environment. The resulting spectrum is shown in Figure 2.4. MUSE observations were performed 293 days after SN 2018cuf's explosion, and some SN features were still visible in the spectrum, with the most pronounced being a broad Balmer Hα emission, in addition to a HII region spectrum with narrow emission lines. To measure the flux of the strongest ionized gas emission lines in that region (N II λ6548, Hα and N II λ6583), we excluded the SN broad component by fitting 4 Gaussians, 3 narrow and 1 broad, simultaneously. The bluer region of the spectrum was not strongly contaminated by SN features, and we fit single Gaussians to measure the narrow Hβ and O III λ5007 emission line fluxes from the ionized gas.

An estimate of the reddening can be obtained from the line-of-sight gas column by the ratio of the Balmer lines, assuming a case B recombination (Osterbrock & Ferland, 2006) and a theoretical ratio of Hα/Hβ = 2.86. Our lines present a ratio of 4.54, which corresponds to $E(B-V) = 0.399 \pm 0.021$ mag. This value is not consistent with the reddening estimated from our color comparison (Figure 2.6), and would make the light curves of SN 2018cuf significantly bluer and brighter than other similar Type II SNe. A possible explanation for this disagreement is that the SN is in front of the HII region and not influenced by the dust but the MUSE measurement gets the full column of gas.

With the host galaxy reddening-corrected fluxes we estimate the SN environmental oxygen abundance (O/H) by using the N2 and O3N2 calibrators from Pettini & Pagel (2004a). We obtain a consistent oxygen abundance of 12+log(O/H) = 8.71 ± 0.07 dex and 12+log(O/H) = 8.72 ± 0.08 dex with the N2 and O3N2 calibrators, respectively, both being consistent with solar abundance (Asplund et al., 2009a). We used the Hα luminosity to estimate the star formation rate (SFR) at the SN location using the expression provided

by Kennicutt (1998). We obtain a SFR of 0.0014 ± 0.0001 $M_\odot$ yr^{-1}, and a SFR intensity of 0.0027 ± 0.0001 $M_\odot$ yr^{-1} kpc^{-2}. To understand where SN 2018cuf stands in the Type II SNe group, we compare the values we derived above with the host properties of all Type II SNe in the PMAS/PPak Integral-field Supernova hosts COmpilation (PISCO) sample (Galbany et al., 2018a)[3]. The average host oxygen abundance and SFR intensity for all PISCO Type II hosts are $12+\log(O/H) = 8.53 \pm 0.062$ dex and 0.013 ± 0.0014 $M_\odot$ yr^{-1} kpc^{-2}, respectively, suggesting that the region around SN 2018cuf has a higher oxygen abundance but a lower SFR intensity than the average of Type II SNe.

2.5. Observational Properties

2.5.1. Distance. The distance to IC 5092 is not well constrained since it has only been measured using the Tully-Fisher relation (Mathewson et al., 1992; Willick et al., 1997) to be 32.0±5.8 Mpc. While the Tully-Fisher relation can be used to measure distances to most spiral galaxies, the intrinsic scatter hinders the accuracy of the measurement for a single galaxy (Czerny et al., 2018). One commonly used approach to independently measure the distances to Type II SNe is the expanding photosphere method (EPM), although it requires the object to have well-sampled light curves and spectra. The EPM was first developed by Kirshner & Kwan (1974) to calculate the distance to Type IIP SNe based on the Baade (1926) method. Assuming that the photosphere is expanding freely and spherically, we can obtain the distance from the linear relation between the angular radius and the expanding velocity of the photosphere using the function:

$$t = D\,(\frac{\theta}{v_{phot}}) + t_0 \tag{2.1}$$

where D is the distance, t_0 is the explosion epoch, θ is the radius of the photosphere (in angular units) and v_{phot} is the velocity of the photosphere. Assuming that the photosphere radiates as a dilute blackbody, we combine the multi-band photometry to simultaneously

[3]observations are updated to June 2020

Table 2.1. The velocities of Fe II λ5169 used in EPM

Date	Fe II λ5169 velocity (km/s)
2018-07-10	7641.3 ± 141.8
2018-07-14	6664.1 ± 68.3
2018-07-18	6328.8 ± 79.8
2018-07-31	4311.7 ± 210.1

derive the angular size (θ) and color temperature (T_c) by minimizing the equation:

$$\epsilon = \sum_{\nu \in S} \{m_\nu + 5log[\theta\xi(T_c)] - A_\nu - b_\nu(T_c)\}^2 \tag{2.2}$$

where ξ and b_ν are a dilution factor and synthetic magnitude respectively, and both of them can be treated as a function of T_c (Hamuy et al., 2001; Dessart & Hillier, 2005a), A_ν is the reddening, m_ν is the observed magnitude and S is the filter subsets, i.e., {BV}, {BVI} and {VI}. We estimate the photospheric velocity by measuring the minimum of the Fe II λ5169 P Cygni profile. To accurately estimate the error on this measurement and avoid noise induced local minima, we smooth the spectra with Savitzky-Golay filters (Savitzky & Golay, 1964; Poznanski et al., 2010) with different widths, deriving the photospheric velocity for each width. For our distance measurement we use the mean and standard deviation of these velocity measurements. After $\sim$ 40 days, the relation between θ/v and t is clearly nonlinear (Jones et al., 2009) and for this reason we only use four early spectra with clear Fe II λ5169 detection, and interpolate the photometry data to the corresponding epoch. The measured velocities are listed in Table 2.1. In order to use the dilution factor derived by Dessart & Hillier (2005a), we convert rp and ip magnitude to I magnitude by using the equations given by Lupton et al. (2005). The results for three filter subsets {BV}, {BVI} and {VI} are presented in Figure 2.7. From these measurements, we obtain distances of 47.1 $\pm$ 6.2 Mpc, 41.1 $\pm$ 5.1 Mpc and 39.8 $\pm$ 6.1 Mpc, respectively, and the weighted average is calculated to be 42.4 $\pm$ 4.9 Mpc by using the method described in Schmelling (1995). In the rest of the paper, we will adopt this value for the analysis.

2.5.2. Explosion Epoch. We derive the explosion epoch from the EPM analysis, obtaining similar values from each of the three filter subsets used: JD 2458292.21 ± 2.97 days in {BV}, JD 2458292.03 ± 2.79 days in {BVI}, and JD 2458291.21 ± 3.71 days in {VI}). The weighted average of these measurements is JD 2458291.91 ± 3.04 , which we adopt as the explosion epoch throughout this paper. We note that this is consistent with the tight constraints of the DLT40 survey which place the explosion epoch between JD 2458291.74456 (the last non-detection) and JD 2458292.8609 (the first detection, which is just 0.95 d after the estimated explosion epoch).

As an independent check, we also estimate the explosion epoch by matching the spectra of SN 2018cuf with the spectral templates in SN Identification (SNID) code (Blondin & Tonry, 2007a). This method has been used by Anderson et al. (2014) and Gutiérrez et al. (2017) to constrain the explosion epochs of a sample of Type II SNe. Gutiérrez et al. (2017) found that with the addition of new spectral templates to the SNID database, the explosion epoch derived from spectral matching may constrain the explosion to within 3.9 days. Following the work of Gutiérrez et al. (2017), we fixed the fitting range in SNID to 3500-6000 Å since the blue end of the spectrum contains more information about the SN and evolves more consistently with time for Type II SNe. Fixing the explosion epoch to be JD 2458291.91 (from the EPM method), we compare the spectra at 11.20, 18.16, 22.09 and 26.39 days with the SNID templates, where the explosion epochs are given by the EPM. The top five matches are then averaged to compute the epoch of the spectra and the error is given by the standard deviation. The epochs of spectra derived from this method are 10.84 ± 1.87, 17.82 ± 4.74, 25.02 ± 4.65 and 31.74 ± 6.79 days, respectively, consistent with the spectral epochs inferred from the EPM.

2.6. Photometric evolution

The full multi-band light curves of SN 2018cuf are shown in Figure 2.2. The V-band light curve shows an initial rise to reach a maximum brightness of $M_V = -16.44 \pm 0.22$ mag on

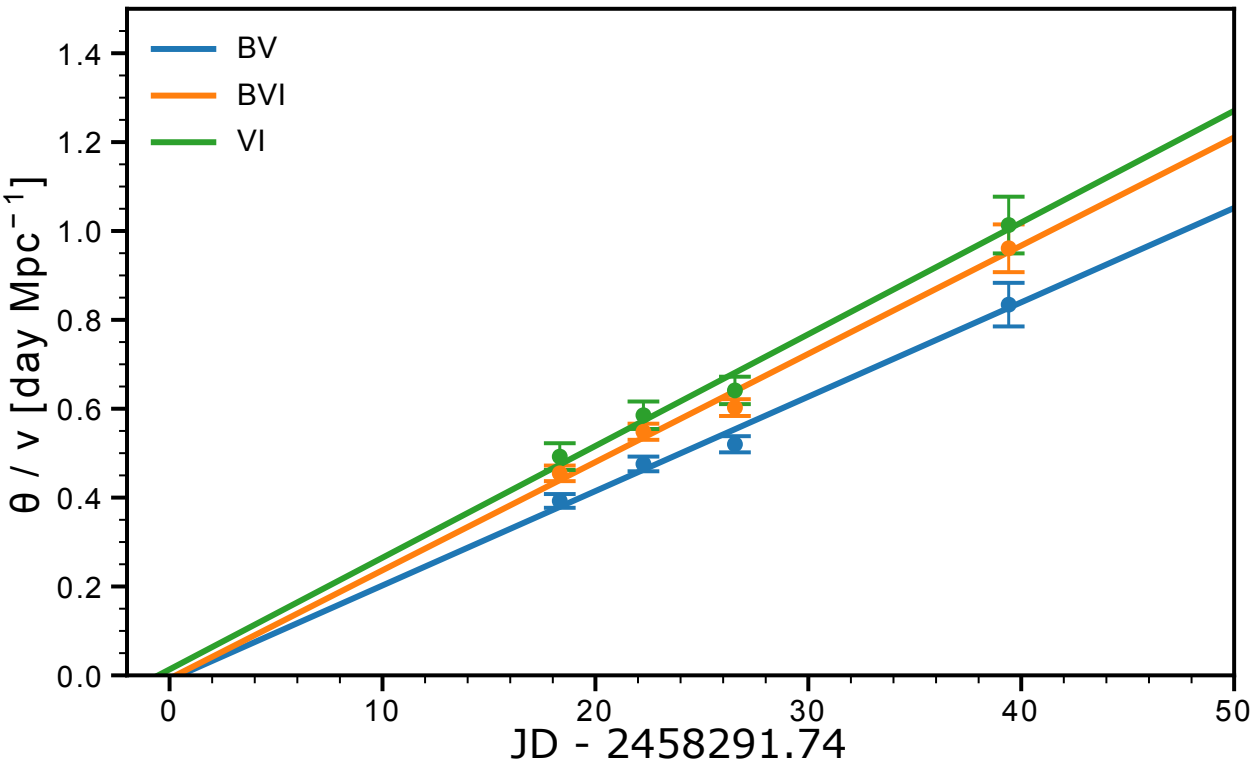

Figure 2.7 EPM fitting for SN 2018cuf using three filter subsets: {BV}, {BVI} and {VI}. The derived distances are 47.08 ± 6.24 Mpc, 41.06 ± 5.07 Mpc and 39.78 ± 6.11 Mpc for the three filter subsets, respectively, and the weighted average is 42.4 ± 4.9 Mpc.

JD 2458300.537, ∼9 days after the date of explosion. A plateau of approximately constant brightness follows due to the hydrogen envelope recombination that extends up to roughly day 114. The other filters show similar trends with bluer bands peaking slightly earlier, and redder bands later. Following the plateau phase, the light curves show an unusually slow drop and finally settles onto a linear decline phase.

After maximum brightness, Type II SNe light curves exhibit a wide range of properties. In order to understand where SN 2018cuf lies in the family of Type II SNe, we measure several light curve parameters and compare them with other Type II SNe. One of the most studied parameters is the rate of decline after maximum light, which is used to classify sub-types of Type II SNe into SNe IIP and SNe IIL ("L" for linear). Statistical analyses of Type II SNe also point out that there is a correlation between the decline rate and the maximum

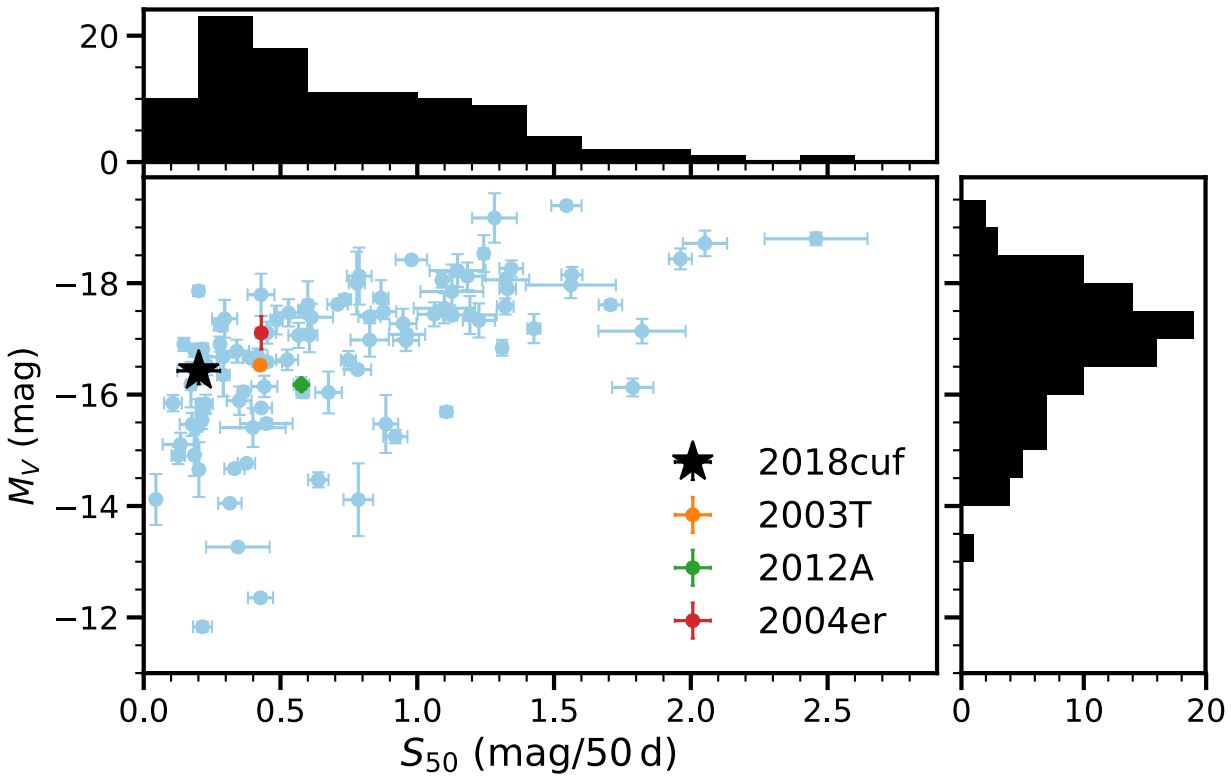

Figure 2.8 The M_V compared to S_{50V} for SN 2018cuf and a sample of Type II SNe. The SNe in this sample are from Anderson et al. (2014) and Valenti et al. (2016), and are available in SNDAVIS. In this plot, IIP-like SNe are usually towards the left, and IIL-like SNe are towards the right. SN 2018cuf, SN 2003T, SN 2004er, and SN 2012A are highlighted with different colors, and the detailed discussion for there four objects can be found in Section 2.6.

absolute magnitude (Li et al., 2011; Anderson et al., 2014; Valenti et al., 2016; Galbany et al., 2016a). Following Valenti et al. (2016) we measure the slope of the light curve per 50 d in V band (S_{50V}) of SN 2018cuf. We find S_{50V}=0.20 ± 0.07 mag $(50d)^{-1}$, which combined with M_V (see Figure 2.8) places SN 2018cuf nicely within the region of Type IIP SNe.

After ∼100 days, the light curves of Type II SNe transition from being powered primarily by the recombination in the photosphere, to being powered by the radioactive decay of ^{56}Ni → ^{56}Co → ^{56}Fe. This period, known as the fall from plateau, can be characterized as a

Fermi-Dirac function (Olivares E. et al., 2010; Valenti et al., 2016):

$$y(t) = \frac{-a0}{1 + e^{(t-t_{\rm PT})/\omega 0}} + (p0 \times t) + m0, \tag{2.3}$$

where $t_{\rm PT}$ refers to the length of the plateau, $\omega 0$ indicates the slope of the light curve during the post-plateau phase (a large $\omega 0$ implies a small slope), and $a0$ is the depth of the drop. We fit the V-band light curve using the package emcee (Foreman-Mackey et al., 2013) and the best-fitting values are found to be $t_{PT} = 114.25^{+0.63}_{-0.62}$ d, $\omega 0 = 7.95^{+0.67}_{-0.62}$ d and $a0 = 1.96^{+0.041}_{-0.039}$ mag. We find that SN 2018cuf has one of the highest $\omega 0$ values in our sample of Type II SNe from the SNDAVIS database[4] (see Figure 2.9), indicating that the slope of the fall from plateau is shallower than most type II SNe. Another SN with a slow fall from plateau is SN 2004er (Anderson et al., 2014) (see Figure 2.10), but sparse data on the tail and a lack of multi-color observations make further comparisons difficult.

The effect of ^{56}Ni mixing on the SN light curve, in particular in its relation to the fall from plateau, has been studied by many authors (e.g. Kasen & Woosley, 2009; Bersten et al., 2011; Goldberg et al., 2019). It is possible that the slow fall from plateau is related to a low mixing of the ^{56}Ni distribution in the ejecta at the moment of explosion. For instance, Goldberg et al. (2019) produced several model light curves with different ^{56}Ni distributions (see their Figure 10), showing that insufficient mixing of ^{56}Ni results in a shallow slope in the post-plateau phase. Alternatively, increasing the total mass of ^{56}Ni can also lead to a shallower fall from plateau (e.g., see Figure 2 in Kasen & Woosley 2009 and Figure 13 in Goldberg et al. 2019).

Which of these two effects, ^{56}Ni mixing or total ^{56}Ni mass, is more important to explain the shallow slope of SN 2018cuf is unclear. To try to disentangle these effects, we identify two other type IIP SNe, SN 2012A and SN 2003T, in the literature that have either a similar progenitor (the progenitor of SN 2018cuf is discussed in Section 2.8) or similar light-curve

[4] http://dark.physics.ucdavis.edu/sndavis/transient

parameters to SN 2018cuf. The V-band light curve of SN 2018cuf is compared with those of other SNe in Figure 2.10. All three objects are spectroscopically similar with roughly the same maximum absolute magnitude (see Figure 2.8) and plateau length. The progenitor of SN 2012A has been well studied (Tomasella et al., 2013; Utrobin & Chugai, 2015; Morozova et al., 2018), and it has similar progenitor mass, radius and explosion energy to the progenitor of SN 2018cuf but a lower nickel mass. Additionally, SN 2012A has a similar maximum magnitude to SN 2018cuf but a steeper fall from plateau (see Figure 2.10). By comparing SN 2018cuf with SN 2012A, we may then conclude that the shallow slope of the fall from plateau of SN 2018cuf is due to the larger nickel produced by SN 2018cuf. On the other hand, a different conclusion is supported by comparing SN 2018cuf with SN 2003T. The nickel mass of SN 2003T is very similar to SN 2018cuf according to its tail magnitude, while the fall from plateau of SN 2003T is much faster than that of SN 2018cuf, suggesting that a low degree of nickel mixing in SN 2018cuf could also contribute to the shallow fall from plateau. In addition, the ^{56}Ni mass of SN 2018cuf is measured to be 0.03 (0.01) $M_{\odot}$ (see Section 2.8). This is consistent with the amount of nickel typically produced in SNe II (Anderson et al., 2014; Müller et al., 2017; Anderson, 2019). Since the ^{56}Ni mass of SN 2018cuf is typical for the Type II family, it is more likely that the shallow slope is due to mixing; however, both scenarios are possible and we are unable to conclusively disentangle the effects.

2.7. Spectroscopic Evolution

2.7.1. Optical spectra. The optical spectroscopic evolution of SN 2018cuf is shown in Figure 2.4. The early spectrum shows a blue continuum with a broad Hα line clearly detected. Over time, the spectra become redder and develop hydrogen Balmer lines with P Cygni features. The Fe II $\lambda\lambda\lambda$ 4924, 5018 and 5169 lines, good tracers for the photospheric velocity, can be seen after day 18. Other typical features such as Ca II $\lambda\lambda$ 3934, 3968, the Ca II infrared triplet $\lambda\lambda\lambda$ 8498, 8542, 8662, and Na I $\lambda\lambda$ 5890, 5896 also appear in emission

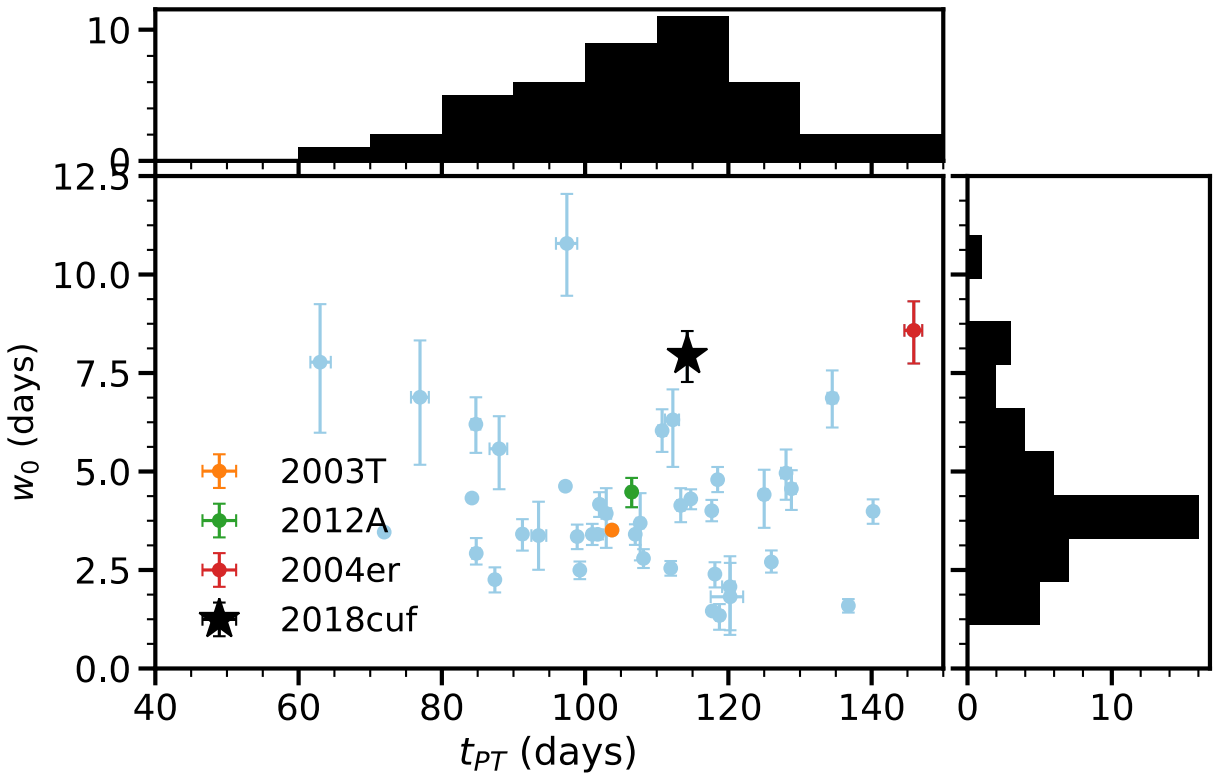

Figure 2.9 Comparison of $t_{\rm PT}$ and $w0$ for V band as described in the text. A large $\omega 0$ implies a shallow post-plateau slope. SN 2018cuf, SN 2003T, SN 2004er, and SN 2012A are highlighted with different colors.

as the SN evolves. During the nebular phase, strong Ca II $\lambda\lambda$ 7291, 7324 emission lines emerge along with Fe II λ7155, He I λ6678 and O I $\lambda\lambda$ 6300, 6364.

Interestingly, from day 106 to day 175, a small notch appears on the Hα profile with a velocity of $\sim$ 1000km/s, and its origin is unclear. One possibility is that this feature is from dust formation either in the ejecta or in CSM interaction. The signatures of dust formation have been detected in many Type IIn SNe. Type IIn SN2010jl shows notches or double peaked profiles at an earlier stage and later shows more dominant blue-wings (see Extended Data Figure 3 of Gall et al., 2014). Type IIn SN1998S also show a notch feature in their broad emission lines (Mauerhan & Smith, 2012). However, for SN 2018cuf, this notch feature emerges starting at day 106, and the temperature of the ejecta may still be too hot for dust

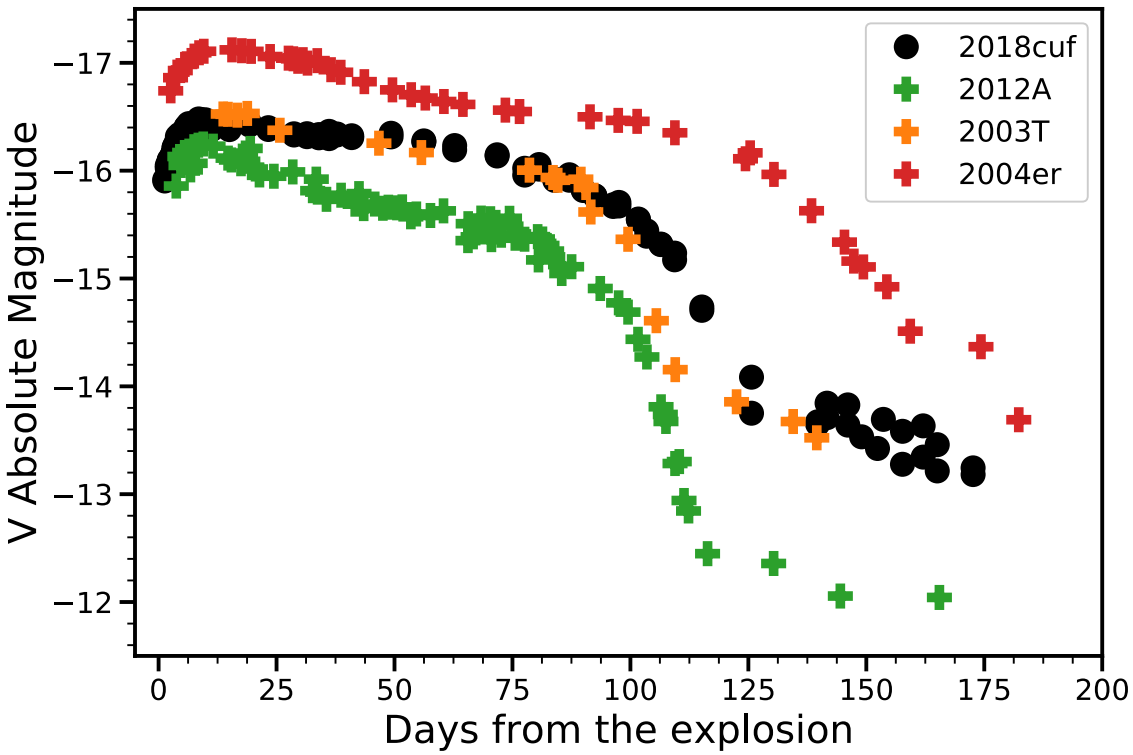

Figure 2.10 V-band light curves of SN 2018cuf, SN 2003T, SN 2012A, and SN 2004er compared in absolute magnitude. As can be seen in Figure 2.8, SN 2012A and SN 2003T peak at roughly the same magnitude as SN 2018cuf but have a slightly steeper post-plateau slope. SN 2004er has a shallow post-plateau slope, similar to SN 2018cuf, but with a much brighter absolute magnitude and a much longer plateau phase. .

formation. On the other hand, the feature is not detected in spectra after day 294, which is hard to reconcile with dust formation. By comparing Hα with other hydrogen line profiles, we do not find any evidence of red-side attenuation for lines that occur at bluer wavelengths, as is expected for dust creation. For these reasons, we can not unambiguously attribute this feature to dust formation and equally rule out the possibility of dust formation.

The evolution of Hα and Hβ lines during the photospheric phase is shown in Figure 2.11. Starting at day 22, an extra absorption line can be seen on the blue side of the Hα and Hβ P Cygni absorption lines, becoming more obvious by day 34. These lines have been studied

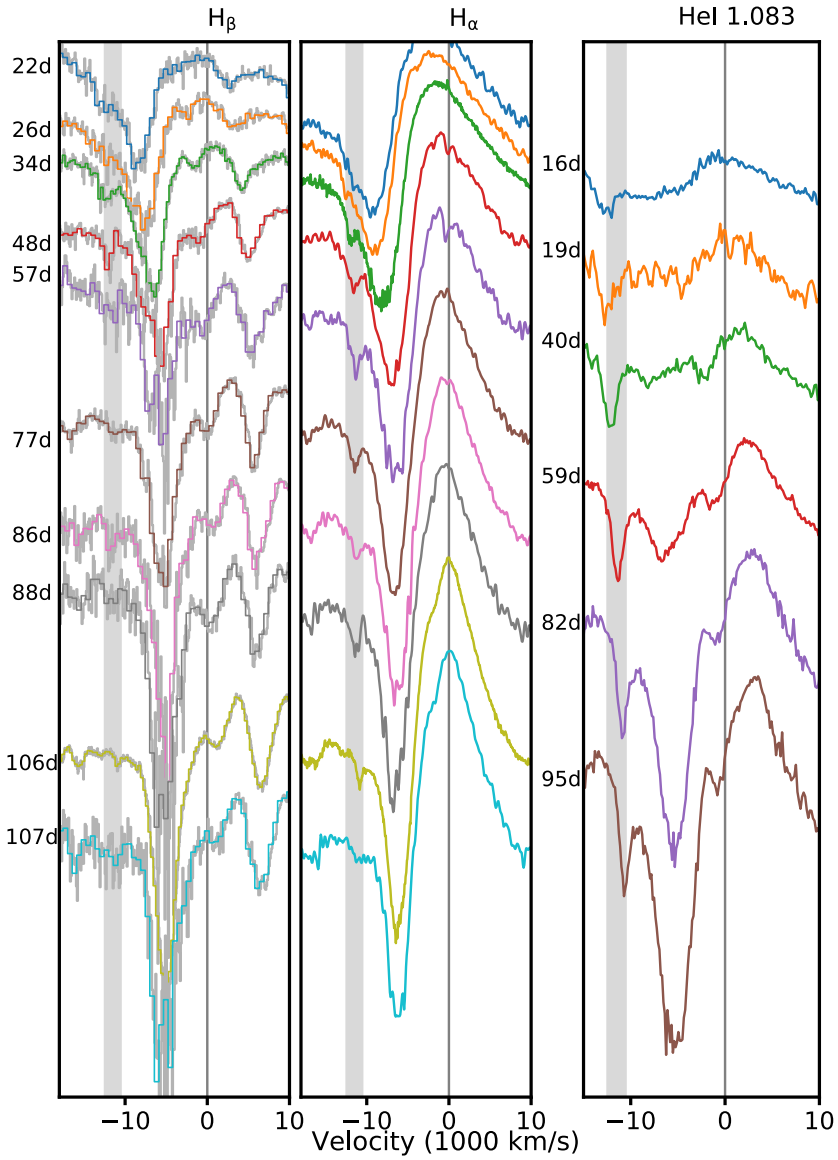

Figure 2.11 The evolution of Cachito features in Hα, Hβ and He I λ1.083 μm during the photospheric phase. In the left panel, the spectra from FLOYDS and SALT are binned to 9 Å pixel^{-1} and 5 Å pixel^{-1}, respectively, and the grey background lines are the original spectra. The shaded area marks -12500km/s to -10500km/s. The Cachito features in all three lines show consistent velocities, supporting their presence as HV features.

in many SNe II and have been most often associated with Si II λ6355 when seen at early phases (< 30 d) and to HV hydrogen if seen at a later phase (50-100 d) (e.g., Chugai et al. 2007; SN 2005cs, Pastorello et al. 2006; SN 2009bw, Inserra et al. 2012; SN 2013ej, Valenti et al. 2014a). This ambiguous absorption feature is often referred to as the "Cachito" feature (Gutiérrez et al., 2017). In the case of SN 2018cuf, because this feature appears at roughly 30 days it is likely associated with HV hydrogen, an interpretation that is confirmed by the additional presence of the HV feature in Hβ at similar velocities.

2.7.2. NIR Spectra. The NIR spectra from day 5 to day 95 are plotted in Figure 2.5 and show an evolution typical of Type II SN. The first spectrum at day 5 is nearly featureless with weak Paschen lines but by day 16 these features have strengthened and He I λ10830 has also appeared. Both Pa α and Br γ lines can be seen in our spectra after day 59.

In general, the line evolution in NIR spectra is consistent across Type II SNe. However, Davis et al. (2019a) points out that Type II SNe can be classified as spectroscopically strong or weak based on the pseudo-equivalent width (pEW) of the He I λ10830 absorption line and the features seen in the spectra. They find that SNe with weak He I (pEW $<$ 50Å) are slow-declining Type IIP SNe and that SNe with strong He I (pEW $>$ 50Å) correspond to the faster-declining Type IIL SNe class. Interestingly, SN 2018cuf seems to be an exception to this rule. The pEWs of He I absorption for days 40, 59, 82, and 95 are 4.9 Å, 25.2 Å, 82.5 Å and 105 Å, respectively, which makes it hard to classify it as either a strong or weak SN based on the pEW alone. In addition to smaller pEW, weak SNe usually show the Pγ/Sr II absorption feature at earlier epochs ($\sim$ 20 days after explosion), and are accompanied by a HV He I feature. For SN 2018cuf, the Pγ/Sr II absorption feature shows up at day 19, consistent with a weak SN. Additionally, there is clearly an extra absorption feature on the blue side of He I (see the right panel of Figure 2.5 or Figure 2.11). Other than HV He I, this feature could also be explained as C I λ10693. However, the lack of other C I lines in the NIR spectra makes it unlikely that this feature is originating from C I λ10693. We also

note that the velocity of HV He I matches the velocity of HV Hα and HV Hβ in optical spectra, which further strengthens our conclusion that this feature can be interpreted as HV He I. Although the pEW of SN 2018cuf is higher than the 50 Å limit used in Davis et al. (2019a), the presence of Pγ/Sr II at early phase and HV He I suggests that our object still falls into the weak SN II category. This implies that the 50 Å limit from Davis et al. (2019a) is probably too low.

Chugai et al. (2007) proposed that HV absorption features, like those seen in SN 2018cuf, come from the interaction between the circumstellar (CS) wind and the SN ejecta. They argue that there are two physical origins of HV absorption: enhanced excitation of the outer layers of unshocked ejecta, which contributes to the shallow HV absorption in the blue side of Hα and He I λ10830, and the cold dense shell (CDS), which is responsible for the HV notch in the blue wing of Hα and Hβ. For the former case, the Hβ HV is not expected to be seen due to the low optical depth in Hβ line-forming region, whereas in the latter case the HV Cachito can form in both Hα and Hβ. For SN 2018cuf, the presence of Cachito features in Hα, Hβ, and He I λ10830 supports the CDS interpretation, but does not completely rule out the first scenario.

Paβ and Paγ were also investigated to look for the presence of HV features. However, the existence of other strong lines around Paγ makes it difficult to identify a HV feature if present, and there is no HV feature in the blue side of Paβ. Chevalier & Fransson (1994) suggested that the temperature of the CDS should be low enough that this region is dominated by low-ionization lines, which causes Paβ absorption to form in a low optical depth region and may explain the absence of HV feature in Paβ.

2.8. Progenitor Properties

2.8.1. Nickel Mass. The nebular phase of Type II SNe is driven by radioactive decay ^{56}Ni $\rightarrow$ ^{56}Co $\rightarrow$ ^{56}Fe. If the γ-rays produced by this process are completely trapped by the ejecta, the bolometric luminosity at late times can be used to estimate the amount of ^{56}Ni.

Since our photometry after ∼100 days does not cover the full SED, we use two different methods to derive the ^{56}Ni mass. The first method is to calculate the pseudo-bolometric luminosity of SN 2018cuf and compare it with the pseudo-bolometric light curve of SN 1987A. Assuming SN 2018cuf and SN 1987A have the same normalized SED, the nickel mass is given by Spiro et al. (2014):

$$M_{\rm Ni} = 0.075 \times \frac{L_{SN}}{L_{87A}} {\rm M}_{\odot} \tag{2.4}$$

where L_{SN} and L_{87A} are the pseudo-bolometric luminosity of SN 2018cuf and SN 1987A, respectively. For the pseudo-bolometric luminosity, we follow the method described by Valenti et al. (2008). The observed magnitudes are converted to flux at each band and integrated by using Simpson's rule, which uses a quadratic polynomial to approximate the integral. Photometric data from day 135 to day 170 is used to calculate the pseudo-bolometric luminosities of SN 2018cuf and SN 1987A by using passbands {BVgri} and {BVRI}, respectively, resulting in a ^{56}Ni mass of $0.030^{+0.002}_{-0.002}$ M$_{\odot}$.

An alternative approach to estimate the nickel mass is to compute a full-band bolometric light curve by performing a black body fit to all available filters at each photometric epoch and integrating the black body. The advantage of this method is that it does not require the assumption that SN 2018cuf and SN 1987A have the same normalized SED, although the approximation to a black body may not be completely valid due to the line blanketing in the UV bands. The ^{56}Ni mass derived from this approach is $0.041^{+0.025}_{-0.007}$ M$_{\odot}$. Given the limitations of each method, we choose to use the pseudo-bolometric luminosity method to compute the ^{56}Ni mass, but take the difference between the results from the two methods as an indicator of the uncertainty of the measurement. The final nickel mass is found to be $M_{\rm Ni} = 0.030$ (0.01) M$_{\odot}$. By comparing the pseudo-bolometric light curve of SN 2018cuf with that of SN 1987A, we found that the decline rate of SN 2018cuf in the radioactive tail is either consistent with or slightly faster than ^{56}Co decay. It is hard to be sure which one is

the case here due to the lack of data in the radioactive tail. If the decline rate of SN 2018cuf is slightly faster than ^{56}Co decay, the ^{56}Ni mass we derived here could be treated as a lower limit.

2.8.2. Progenitor Mass. Progenitor mass is a fundamental parameter of a SN, and can be constrained by using multiple techniques. In this section, we derive the progenitor mass of SN 2018cuf from nebular spectra and hydrodynamic light curve modelling.

2.8.2.1. *From Nebular Spectroscopy.* During the nebular phase, spectra can provide useful information about the inner structure of a SN. At this stage, the ejecta has become optically thin, revealing the core nucleosynthesis products. The strength of the O I $\lambda\lambda6300, 6364$ doublet in the nebular spectra has been found to be a good indicator of progenitor mass (Jerkstrand et al., 2014). By comparing the intensities of O I $\lambda\lambda6300, 6364$ with theoretical models during this phase, the progenitor mass can be well constrained. Jerkstrand et al. (2014) modelled the nebular spectra for 12, 15, 19, and 25 $M_\odot$ progenitors at different phases. They start with the SN ejecta evolved and exploded with KEPLER (Woosley & Heger, 2007) and use the spectral synthesis code described in Jerkstrand et al. (2011) to generate the model spectra.

Although we have six nebular spectra for SN 2018cuf taken from day 175 to day 484, four of them are contaminated by the host galaxy. Therefore, we only compare the nebular spectra of SN 2018cuf at day 175 and day 337 with the models computed by Jerkstrand et al. (2014) in Figure 2.12. We scale the nebular spectra taken at day 175 and day 337 to r-band photometry, and the models have been scaled to the observed spectrum so that they have the same integrated flux. We find that the strength of O I in our spectrum is between the 12 $M_\odot$ and the 15 $M_\odot$ models, which implies the progenitor mass of SN 2018cuf is likely in this range.

Synthetic nebular spectra can also be used to give an independent estimate of the nickel mass (Jerkstrand et al., 2018; Bostroem et al., 2019). By using the scale factors we used

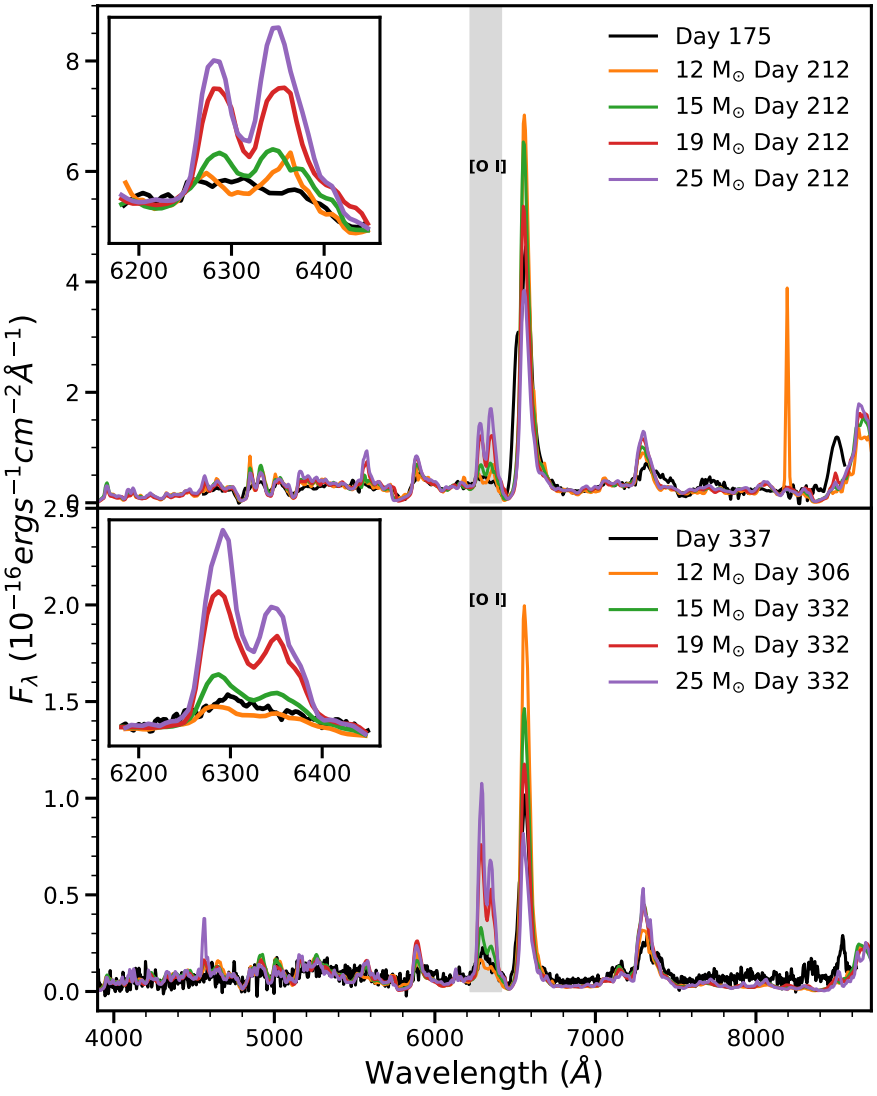

Figure 2.12 Comparison of the nebular spectra of SN 2018cuf from day 175 and day 337 with four models at similar epochs. The insets show the [O I] doublet, which is a good indicator of progenitor mass. From this line, we estimate the progenitor mass to be between 12 and 15 $M_\odot$ as discussed in the text.

to scale the model spectra, the nickel mass can be derived using the following relation from Bostroem et al. (2019):

$$\frac{F_{obs}}{F_{mod}} = \frac{d_{mod}^2}{d_{obs}^2} \frac{M_{^{56}Ni_{obs}}}{M_{^{56}Ni_{mod}}} exp\left(\frac{t_{mod} - t_{obs}}{111.4}\right) \tag{2.5}$$

where F_{obs} is the total observed flux and F_{mod} is the total flux from the model spectrum. d_{obs} is the distance of the SN and $d_{mod} = 5.5$ Mpc is the distance used to compute the model; $M_{^{56}Ni}$ indicates nickel mass for the SN ($M_{^{56}Ni_{obs}}$) and the model ($M_{^{56}Ni_{mod}} = 0.062 M_\odot$), and t_{obs} and t_{mod} is the phase of the spectra for the observation and model, respectively. We then derive nickel masses of 0.031 $M_\odot$ and 0.034 $M_\odot$ for day 175 and day 337, respectively. These values are consistent with what we get in the previous subsection, where we measure the nickel mass from the radioactive decay tail photometry when the SN just falls from the plateau (day 135 – 170).

2.8.2.2. *From Hydrodynamic Modelling.* An alternative way of constraining the mass of the progenitor is to compare the light curves to hydrodynamic models (e.g. Utrobin & Chugai, 2015, 2017; Morozova et al., 2017, 2018; Paxton et al., 2018; Goldberg et al., 2019; Martinez & Bersten, 2019). We have used the SN Explosion Code (SNEC; Morozova et al., 2015), an open-source hydrodynamic code for core-collapse SNe, to constrain the progenitor parameters of SN 2018cuf. SNEC assumes diffusive radiation transport and local thermodynamic equilibrium (LTE), which are valid assumptions from shock breakout through the end of the plateau. However, as the SN becomes nebular this assumption breaks down. For this reason, we compare our light curve only out to $t_{\rm PT} = 114.25$ days with the SNEC models. Our inputs of evolved progenitor stars for the SNEC code are the non-rotating solar metallicity RSG models generated from the KEPLER code and described in Sukhbold et al. (2016a). A steady-state wind with a density profile

$$\rho(r) = \frac{\dot{M}}{4\pi r^2 \nu_{wind}} = \frac{K}{r^2} \tag{2.6}$$

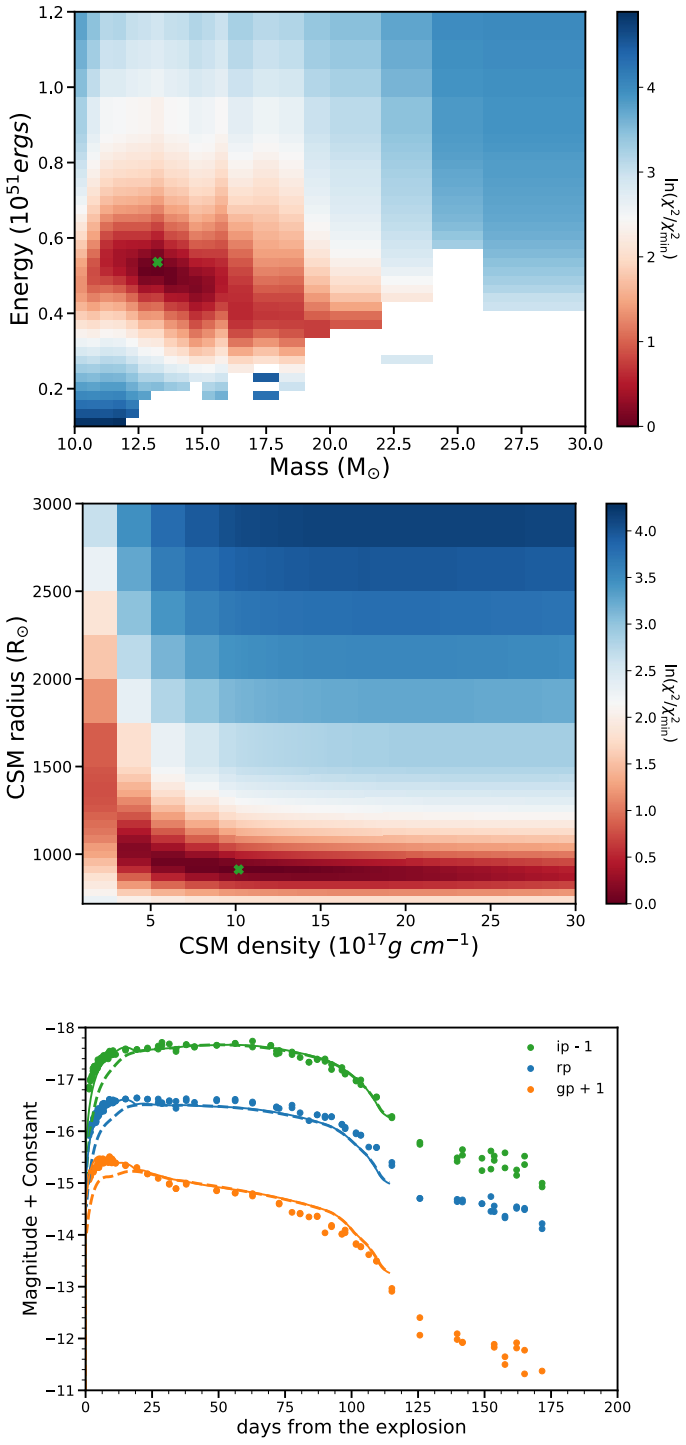

Figure 2.13 Top and middle: The color indicates the χ^2 value, and green cross represents the best-fitting SNEC model. Bottom: Dots are the observational data, while different colors represent different bands. Solid lines and dashed lines are the best-fitting SNEC model with and without CSM respectively.

is also added above these models to explore the effect of CSM on light curves, where $\dot{M}$ is the wind mass-loss rate and ν_{wind} is the wind velocity. We will use parameter K to describe the constant wind density, which extends up to radius R_{ext}. For each explosion, SNEC takes a variety of progenitor and explosion parameters as input and then generates a bolometric light curve and, assuming blackbody radiation, the optical light curves. We followed the approach of Morozova et al. (2017), exploring variations in progenitor mass (M), nickel mass, explosion energy (E), K and R_{ext}, fixing the Nickel mass to $M_{\rm Ni} = 0.03$ M$_\odot$, which we obtained from the tail photometry. We note that the degree of ^{56}Ni mixing can also be a free parameter in SNEC models. However, the SNEC model can not reproduce the light curves well during the fall from plateau since the radiation diffusion approach used in SNEC is no longer valid during and after this period, so we are not able use SNEC to explore the effect of ^{56}Ni mixing on the post-plateau light curves. Morozova et al. (2015) also found that the light curves generated by SNEC are not sensitive to the degree of ^{56}Ni mixing, so we fixed the initial ^{56}Ni mixing, and mixed ^{56}Ni up to 5 M$_\odot$ in the mass coordinates.

Morozova et al. (2018) points out that only the early phase of the light curve is dominated by CSM, so it is possible to adopt a two-step approach to fit the light curves. In the first step, we evaluate the fit for the part of the light curve that is mostly dominated by the hydrogen-rich envelope and vary only M and E. The fitting range is chosen to be between the end of $s1$ (38.09 days from explosion for SN 2018cuf) and $t_{\rm PT}$, where $s1$ is the initial steeper slope of the light curve. This allows us to determine the best fit progenitor mass and explosion energy. In the next step, we fix the progenitor mass and explosion energy found in step one and we explore the influence of CSM, varying K and R_{ext} and fitting the whole light curve through $t_{\rm PT}$. This substantially reduces the number of models needed to explore the parameter space, allowing us to search over a finer grid in each parameter.

At each stage, the best fit model was determined by interpolating the models to the observed epochs in g, r, i filters and minimizing the χ^2 over these filters. For the first stage,

the range of parameters considered is 10 $M_\odot$ < M < 30 $M_\odot$ and 0.1 < E < 1.2 (in unit of 10^{51} ergs). We obtain the best fit of $M = 13$ $M_\odot$, which corresponds to a 704 $R_\odot$ progenitor star from Table 2 of Sukhbold et al. (2016a), and $E = 5.24 \times 10^{50}$ ergs as shown in the upper panel of Figure 2.13. In the next step, the CSM parameter range is set to be $1 < K < 20$ (in unit of 10^{17} $g\ cm^{-1}$) and 717 $R_\odot$ < R_{ext} < 3000 $R_\odot$, and the fitting range also includes the early part of the light curve, i.e., we fit the light curves from the explosion to $t_{\rm PT}$. The result is presented in the middle panel of Figure 2.13, and the best-fitting model is $K = 10 \times 10^{17}$ $g\ cm^{-1}$ and $R_{ext} = 891$ $R_\odot$. In the bottom panel of Figure 2.13, we show the light curves of the best-fitting models with and without dense CSM. The progenitor mass (13 $M_\odot$) we get from SNEC model is in good agreement with what we get from the synthetic nebular spectra analysis (12 - 15 $M_\odot$), and this is a moderate mass for a Type II SN. It should be noted that we did not fit the model photospheric velocity with the ejecta velocity derived from the Fe II λ 5169 line. Both Goldberg et al. (2019); Goldberg & Bildsten (2020) pointed out that fitting the ejecta velocities inferred from the Fe II λ 5169 line can barely break the degeneracy between the explosion properties, so we choose not to fit the ejecta velocity in our SNEC modelling.

Previous workers (Morozova et al., 2017, 2018; Bostroem et al., 2019) found that there is a strong degeneracy between the density profile and the external radius of CSM, and the total mass of CSM derived from the fits is more robust. If we adopt the progenitor radius of 704 $R_\odot$ as the inner CSM radius, the total CSM mass of our best fit model is found to be 0.08 $M_\odot$ by integrating Equation 2.6 over r. If we interpret this wind as that of a typical RSG, adopting a wind speed of 10 km s^{-1}, the mass-loss rate would be 0.20 $M_\odot$ yr^{-1} within a timescale of 4.9 months, much higher than the steady winds observed in RSGs (Smith, 2014a). The possible explanation is that such dense CSM may originate from pre-SN outbursts due to the late-stage nuclear burning in the stellar interior (Quataert & Shiode, 2012; Smith & Arnett, 2014a; Fuller, 2017; Morozova et al., 2020). Due to the presence of

dense CSM around the SN, it is also expected to see flash signatures in the early spectrum (Yaron et al., 2017; Nakaoka et al., 2018; Rui et al., 2019). However, such a signature is not found for SN 2018cuf, which may imply that the dense CSM is very close to the progenitor, consistent with the small CSM radial extent derived from the SNEC model.

2.8.3. Shock Cooling Model. After the shock breakout, the SN emission is dominated by shock cooling, and carries useful information about the radius and pre-explosion evolution of the progenitor star system. Sapir & Waxman (2017) updated the model presented by Rabinak & Waxman (2011) and found that the photospheric temperature and bolometric luminosity during the early phase for a SN with a RSG progenitor (convective envelope with n = 3/2) can be written as:

$$T(t) = T_1 * t_d^{-0.45} \tag{2.7}$$

$$L(t) = L_1 \; exp\left[-\left(\frac{1.67 * t_d}{t_{tr}}\right)^{0.8}\right] * t_d^{-0.17}, \tag{2.8}$$

where T_1 and L_1 are the temperature and the luminosity $\sim$ 1 day after the explosion respectively, t_d is the time from explosion, t_{tr} is the time when the envelope is starting to become transparent. We apply this model to SN 2018cuf, which was discovered well before t_{tr}, using the code developed by Hosseinzadeh et al. (2018); Hosseinzadeh (2020). This Markov Chain Monte Carlo (MCMC) routine is adopted to give the posterior probability distributions of T_1, L_1, t_{tr} and t_0 simultaneously, where t_0 is the explosion epoch. This analytical model is only valid for T $<$ 0.7 eV, and we have checked that the final fitting results satisfy this condition. The MCMC converge to an explosion epoch MJD 58290.06 $\pm$ 0.04 (or JD 2458290.56 $\pm$ 0.04), which is about one day earlier than our last non-detection (JD 2458291.74). An explosion epoch earlier than our first non-detection is possible as the SN may be below our detection limits shortly after explosion. However, in order to fit the U- and V-band light curves, we require t_{tr} = 38000 days, which is unphysically late. For this reason we do not attempt to derive progenitor or explosion parameters using this method. The inability

of this method to fit the blue part of the light curve has been noted by several authors (Arcavi et al., 2017; Hosseinzadeh et al., 2018). One possible reason for the fitting failure could be that there is a CSM-ejecta interaction around the progenitor, which is supported by the light curve modelling as we discussed in the last subsection. In addition, the effect of UV-band line blanketing is underestimated in the model spectrum, so that assuming black body radiation can not well reproduce the light curves in UV bands.

2.9. conclusions

In this paper, we have presented the spectroscopic and photometric observations of SN 2018cuf in the galaxy IC 5092. The object was discovered by the DLT40 survey within $\sim$1 day of explosion, and the well-sampled light curves and spectra from GSP were used to constrain the progenitor properties. In general, SN 2018cuf is consistent with other Type II SNe, while it has a relatively slow fall from the plateau, which could be a result of insufficient mixing of ^{56}Ni or high ^{56}Ni mass. During the plateau phase, we identified HV features in Hα, Hβ and He I λ10830, suggesting interaction between ejecta and CSM.

We use the EPM method to derive a distance of 42.4 $\pm$ 4.9 Mpc to SN 2018cuf and an explosion epoch of JD 2458291.91 $\pm$ 3.04, which is confirmed by SNID and consistent with the last nondetection from DLT40. From the pseudo-bolometric luminosity of the radioactive decay tail, the nickel mass is found to be 0.03 (0.01) $M_\odot$, which is further confirmed by the nickel mass derived from nebular spectra. SNEC modelling is used to determine the progenitor parameters finding a progenitor mass of 13 $M_\odot$ with an explosion energy of $E \approx 5.24 \times 10^{50}$ erg, and a CSM mass of $M_{CSM} \approx 0.08$ $M_\odot$. The progenitor mass from SNEC is in good agreement with what we get from nebular spectral modelling ($12-15$ $M_\odot$). The dense CSM inferred from SNEC modelling may imply that the progenitor experienced some outbursts due to the late-stage nuclear burning before explosion. We also tried to apply the shock cooling model to the early light curve, but find it yields unphysical results. From the SNEC model, we infer significant CSM around SN 2018cuf, which could be a main

reason for the fitting failure, since the shock cooling model is no longer valid in the presence of dense CSM. In addition, the underestimate of the effect of UV-band line blanketing for the model spectra may also contribute to the failure of model fitting.

We found that, at least for this single object, hydrodynamical modelling and nebular spectral modelling give consistent progenitor mass. In the future, with more and more young SNe detected, we will be able to investigate the systematic bias for these techniques and finally have the ability to better understand the progenitors of Type IIP SNe.

Acknowledgements

We would like to thank Daniel Kasen and Nir Sapir for beneficial discussions. Research by Y.D., and S.V., and K.A.B is supported by NSF grants AST-1813176. Research by DJS is supported by NSF grants AST-1821967, 1821987, 1813708, 1813466, 1908972, and by the Heising-Simons Foundation under grant #2020-1864. This work makes use of observations from the Las Cumbres Observatory network. DAH, JB, and DH are supported by NSF grant AST-1911225 and NASA Swift grant 80NSSC19k1639. L.G. was funded by the European Union's Horizon 2020 research and innovation programme under the Marie Skłodowska-Curie grant agreement No. 839090. This work has been partially supported by the Spanish grant PGC2018-095317-B-C21 within the European Funds for Regional Development (FEDER). The SALT observations presented here were made through Rutgers University programs 2018-1-MLT-006 and 2019-1-MLT-004 (PI: Jha); supernova research at Rutgers is supported by NSF award AST-1615455. E.Y.H. and S.D. acknowledge the support provided by the National Science Foundation under Grant No. AST-1613472. IA is a CIFAR Azrieli Global Scholar in the Gravity and the Extreme Universe Program and acknowledges support from that program, from the European Research Council (ERC) under the European Union's Horizon 2020 research and innovation program (grant agreement number 852097), from the Israel Science Foundation (grant numbers 2108/18 and 2752/19), from the United States -

Israel Binational Science Foundation (BSF), and from the Israeli Council for Higher Education Alon Fellowship. H.K. was funded by the Academy of Finland projects 324504 and 328898. Based on observations collected at the European Southern Observatory under ESO programme 0102.D-0356. X.W. is supported by National Natural Science Foundation of China (NSFC grants 11633002 and 11761141001), and the National Program on Key Research and Development Project (grant no. 2016YFA0400803). L.W. is sponsored (in part) by the Chinese Academy of Sciences (CAS), through a grant to the CAS South America Center for Astronomy (CASSACA) in Santiago, Chile.

This research has made use of the NASA/IPAC Extragalactic Database (NED), which is operated by the Jet Propulsion Laboratory, California Institute of Technology, under contract with the National Aeronautics and Space Administration.

CHAPTER 3

A Comprehensive Optical Search for Pre-explosion Outbursts from the Quiescent Progenitor of SN 2023ixf

Published as Dong et al 2023. in The Astrophysical Journal, Volume 957, Issue 1, id.28, 8 pp.

3.1. Abstract

In this chapter, we will present a comprehensive search for optical precursor emission at the position of SN 2023ixf using data from the DLT40, ZTF and ATLAS surveys. By comparing the current data set with precursor outburst hydrodynamical model light curves, we find that the probability of a significant outburst within five years of explosion is low, and the circumstellar material (CSM) ejected during any possible precursor outburst is likely smaller than $\sim 0.015 M_{\odot}$. By comparing to a set of toy models, we find that, if there was a precursor outburst, the duration must have been shorter than $\sim$100 days for a typical brightness of $M_r \simeq -9$ mag or shorter than 200 days for $M_r \simeq -8$ mag; brighter, longer outbursts would have been discovered. Precursor activity like that observed in the normal type II SN 2020tlf ($M_r \simeq -11.5$) can be excluded in SN 2023ixf. If the dense CSM inferred by early flash spectroscopy and other studies is related to one or more precursor outbursts, then our observations indicate that any such outburst would have to be faint and only last for days to months, or it occurred more than five years prior to the explosion. Alternatively, any dense, confined CSM may not be due to eruptive mass loss from a single red supergiant (RSG) progenitor. Taken together, the results of SN 2023ixf and SN 2020tlf indicate that

there may be more than one physical mechanism behind the dense CSM inferred around some normal type II SNe.

3.2. Introduction

Red supergiant (RSG) stars with zero-age main sequence masses in the range $\sim 8 - 17$ $M_\odot$ can explode as Type II supernovae (SNe) (Van Dyk et al., 2003a; Smartt, 2009, 2015; Van Dyk, 2017; Van Dyk et al., 2023). Early SN observations provide hints about the circumstellar environment around the progenitor star just prior to explosion. For instance, spectroscopic observations within days of explosion show narrow 'flash' recombination lines in a significant fraction of normal SNe II, which quickly disappear after several days (e.g.. Khazov et al., 2016; Bruch et al., 2021, 2023). A standard interpretation is that these lines signal dense, confined CSM that has been ionized by the shock breakout (e.g. Yaron et al., 2017) or ejecta interaction (e.g. Leonard et al., 2000; Smith et al., 2015a; Terreran et al., 2022). Meanwhile, the fast rise of type II SN light curves has also been interpreted as a sign of dense CSM around the progenitor star, as indicated by hydrodynamic modeling (Morozova et al., 2017, 2018). Between 40–70% of standard type IIP SNe show evidence of dense CSM around their progenitor stars (e.g. Förster et al., 2018; Morozova et al., 2018; Bruch et al., 2023).

The dense CSM around the progenitor requires intense mass loss, equivalent to $\sim 10^{-4}$–10^{-2} $M_\odot$ yr^{-1}, in the months to years leading up to explosion, much higher than the mass loss due to the normal stellar winds of RSGs. However, how and when this enhanced mass loss occurs is still a mystery. Some of the possible mass-loss mechanisms are mass ejection driven by wave transport (Quataert & Shiode, 2012; Shiode & Quataert, 2014; Fuller, 2017; Morozova et al., 2020), common envelope interaction with a compact object (Chevalier, 2012a; Soker, 2013), and dynamical instability associated with turbulent convection in the core (Smith & Arnett, 2014a).

One direct method to constrain very late-stage mass-loss mechanisms of SN progenitors is searching for signs of pre-explosion activity or precursor emission. Precursor emission has been observed in many SNe IIn (e.g., Mauerhan et al., 2013; Ofek et al., 2013; Tartaglia et al., 2016; Pastorello et al., 2013, 2018) and statistical studies on a sample of SNe IIn also support the idea that most experienced outbursts prior to exploding (Ofek et al., 2014; Strotjohann et al., 2021b). In contrast, pre-explosion activity in normal Type IIP/L has only been seen in SN 2020tlf, where excess emission is observed ∼130 days prior to and all the way up until the ultimate SN explosion (Jacobson-Galán et al., 2022). Based on the pre-explosion images of four Type IIP/L SN progenitors, Johnson et al. (2018) found that the probability that their progenitors had extended outbursts after oxygen ignition is low. However, they could not exclude short outbursts on the time-scale of months from their data.

Recently, there has been theoretical research on the morphology of precursor light curves of Type IIP/L SNe. Davies et al. (2022) constructed model spectra of the precursor emission for different mass-loss scenarios. They suggested that the precursor outburst likely occurs within one year of the explosion and would be optically bright for a few days with $M_R \simeq -8.5$, accompanied by intense mass loss. In addition, RSGs can be very faint in the optical right before explosion due to the cooling of their surfaces and an increase of the molecular opacity (Davies et al., 2022). Tsuna et al. (2023) modeled precursor outbursts by injecting energy into the base of the RSGs' hydrogen envelopes, and explored the corresponding observational light curves. They found that these outbursts can last for hundreds of days, with a peak brightness of ~ -8.5 to -10 mag in the R band, depending on the amount of energy injected. These kinds of precursors are usually too faint to be detected by most ongoing wide-field surveys. However, if a Type IIP/L SN explodes in a very nearby galaxy, its precursor activity can be used as an early warning of the explosion.

In this paper, we present optical pre-explosion monitoring data at the position of SN 2023ixf, a type II SN that exploded in the very nearby galaxy M101 (also known as the Pinwheel

Galaxy). The SN displayed strong flash features indicative of dense, confined CSM around the progenitor star (Yamanaka et al., 2023; Jacobson-Galan et al., 2023; Smith et al., 2023; Bostroem et al., 2023; Singh Teja et al., 2023). Given the proximity of SN 2023ixf and the wealth of available pre-explosion data, it provides an excellent opportunity to link the signatures of CSM in the SN data to one or more pre-explosion events. Pre-explosion photometry was gathered from several time domain programs: the Distance Less Than 40 Mpc (DLT40, Tartaglia et al., 2018) survey, the Zwicky Transient Facility (ZTF, Bellm et al., 2019; Graham et al., 2019), and the Asteroid Terrestrial-Impact Last Alert System (ATLAS, Tonry 2011; Tonry et al. 2018; Smith et al. 2020b). The pre-explosion observations span about 3, 5 and 6 years prior to the explosion of SN 2023ixf for DLT40, ZTF and ATLAS, respectively. The high-cadence observations enable us to put strong constraints on any precursor outbursts or other activities.

The pre-explosion observations at the position of SN 2023ixf, and associated photometric limits, are described in Section 3.3. We use these photometric limits from multiple surveys to constrain the duration and brightness of any pre-explosion outbursts in Section 3.4, using both toy-model outbursts and those derived from hydrodynamic models. We also discuss our outburst constraints in the context of other evidence for dense, confined CSM in SN 2023ixf and other normal core collapse SNe. Finally, we present our conclusions in Section 3.5.

3.3. Data set

SN 2023ixf was discovered on 2023 May 19 in the Pinwheel Galaxy (Itagaki, 2023) and was classified as a Type II SN (Perley & Gal-Yam, 2023). The distance to SN 2023ixf is only 6.85 Mpc ($\mu = 29.18$ mag) (Riess et al., 2022), providing an unique opportunity to study a Type II SN in great detail. Following Bostroem et al. (2023), we adopted a Milky Way extinction of $E(B-V) = 0.0077$ mag (Schlafly & Finkbeiner, 2011a) and a host extinction of $E(B-V) = 0.031$ mag (Smith et al., 2023), as well as $R_V = 3.1$. In this section, we present the pre-explosion data of SN 2023ixf taken by DLT40, ZTF and ATLAS. We also

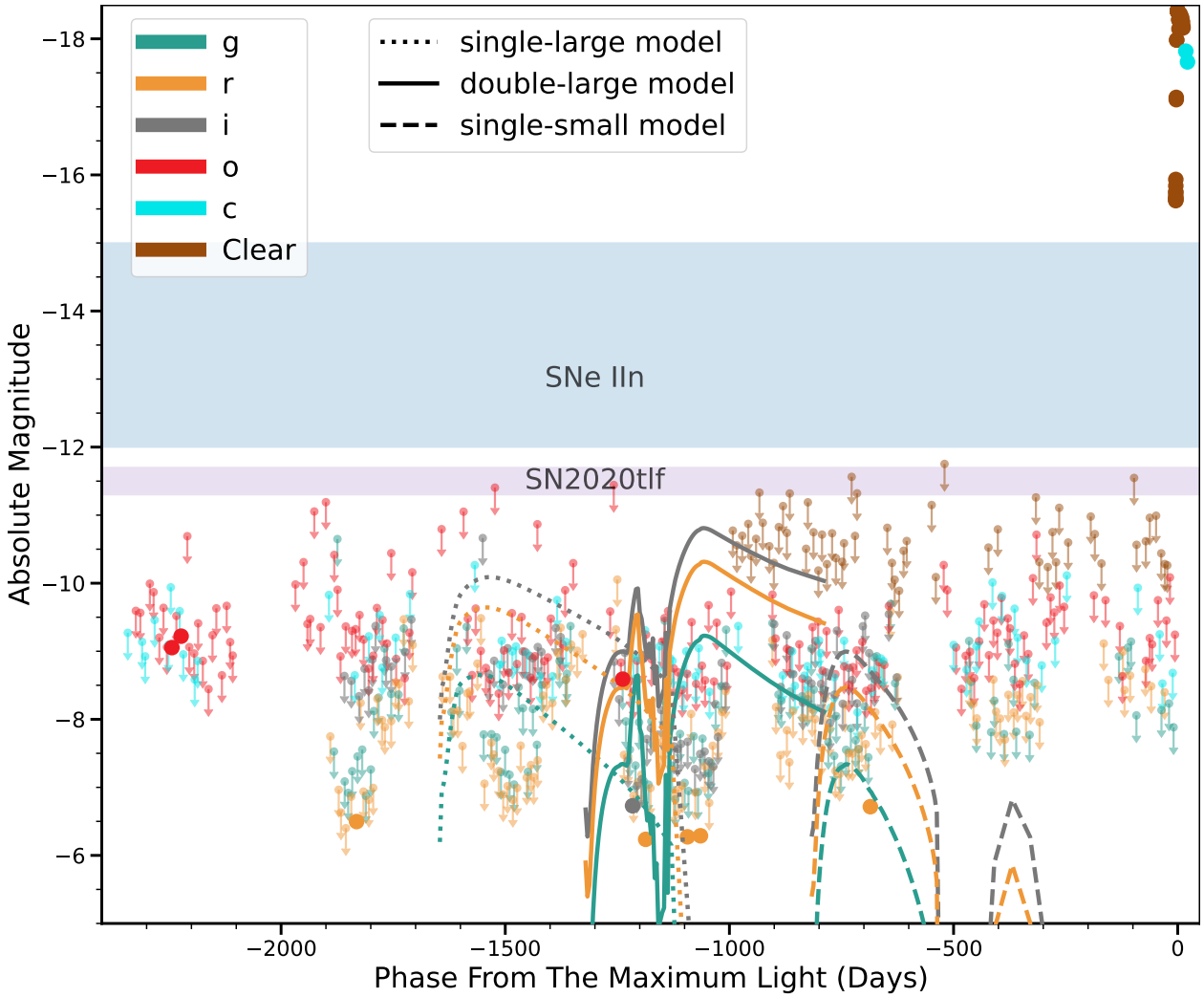

Figure 3.1 Limits on the pre-explosion activity of SN 2023ixf. The Clear filter is calibrated to the r band. A few precursor models from Tsuna et al. (2023) are plotted here for reference. The phases of the models are arbitrarily chosen. The typical brightness of precursor emission in SNe IIn is shown in the blue area. The brightness of precursor emission seen prior to SN 2020tlf is indicated by the purple area. The limits of our data set are generally deeper than the precursor ourbursts observed in Type IIn SNe and in the normal Type IIP SN 2020tlf.

examined the pre-explosion data taken by the All-Sky Automated Survey for Supernovae (ASAS-SN, Shappee et al. 2014b; Kochanek et al. 2017b). However, since the survey is ∼2 mag shallower than the other surveys considered, we did not include the ASAS-SN data in our analysis.

3.3.1. DLT40 observations. The DLT40 survey is a sub-day-cadence SN search (Tartaglia et al., 2018; Yang et al., 2019b), targeting prominent galaxies within 40 Mpc with the aim of finding about 10 very young and nearby SNe per year. DLT40 has been monitoring M101 since 2020 using the PROMPT-USask 0.4m telescope at Sleaford Observatory, Canada. These observations resulted in 264 frames taken in the Clear band, with an average time between two adjacent images of ∼3.7 days. Each image has an exposure time of 45s and a field of view of $10' \times 10'$.

Before doing any analysis, all the available images were visually inspected, and those of bad quality were removed from the sample. A deep template was made using SWarp (Bertin et al., 2002) with images taken between 2020-05-12 and 2020-08-31. The rest of the images are stacked in windows of 10 days, and image subtraction against the template was done using HOTPANTS (Becker, 2015). Aperture photometry was done on difference images to search for any precursor emission at the position of SN 2023ixf. For aperture photometry, we adopt an aperture 2 times the FWHM of the image, a signal-to-noise threshold of 3 for source detections and a signal-to-noise threshold of 5 for computing upper limits, following Masci (2011). The final Clear-band aperture photometry was performed in a Python-based pipeline and was calibrated to the r-band using the APASS catalog. This process resulted in a median limiting magnitude of $r \sim -10.6$ mag.

3.3.2. ZTF observations. ZTF is a time-domain survey using the Palomar 48-inch Oschin telescope at Palomar Observatory (Bellm et al., 2019; Graham et al., 2019). ZTF observes the whole visible sky from Palomar in the g and r filters every two to three nights, and although there is both a public and private portion of the survey, both components are released at regular intervals. The position of SN 2023ixf had been observed by ZTF for over 5 years before the SN explosion. There are 1092, 1152, and 345 frames taken in the g, r, and i filters, respectively. The average time between two adjacent images is ∼1.7 days for the g band, ∼1.6 days for the r band, and ∼3.6 days for the i band. We obtained forced

photometry from the template-subtracted images using the ZTF Forced Photometry Service (ZFPS; Masci et al., 2023a). Following Masci (2011), we adopted a signal-to-noise threshold of 3 for the source detection and a signal-to-noise of 5 for computing the upper limit. Bad-quality data were removed following the description in Masci et al. (2023a). We also removed epochs that have status code 56 to avoid the impact of bad or blank pixels. The single-epoch flux measurements were combined in 10-day time bins following the method described by Masci et al. (2023a). The median limiting magnitudes are $\sim$−7.9 mag in g band, $\sim$−7.8 mag in r band, $\sim$−8.5 mag in i band.

3.3.3. ATLAS observations. ATLAS is an all-sky daily-cadence survey, using two filters, orange (o) and cyan (c), similar to Pan-STARRS filters $r + i$ and $g + r$, respectively. For over six years prior to the SN explosion, ATLAS had collected 1787 images in the o band and 475 images in the c band. The average time between two adjacent images is $\sim$1.3 days for the o band and $\sim$5.0 days for the c band. We obtained forced photometry at the supernova position from the ATLAS forced photometry server (Shingles et al., 2021). The single-epoch flux measurements have been stacked in 10-day bins following Young (2022) to reach a deeper limit. The median depths we can reach are ~ -9.2 mag in o band and ~ -8.9 mag in c band.

3.3.4. Spurious detections. All the stacked measurements and limits are shown in Figure 3.1, with a zoom-in around the time of SN 2023ixf's explosion in Figure 3.2. There are a handful of epochs, both in ZTF and ATLAS, which have reported fluxes larger than 3σ and thus are marked as detections (Figure 3.1). In all cases, the signal-to-noise ratio of these observations are slightly higher than 3 but smaller than 4. In addition, none of these pre-explosion detections are consecutive in time; they are bracketed by non-detections of similar depth. For this reason, they are likely not true detections of precursor variability. Given the hundreds of epochs examined, it is expected that some detections at this level would occur, even if they do not indicate true pre-explosion variability. Assuming the noise

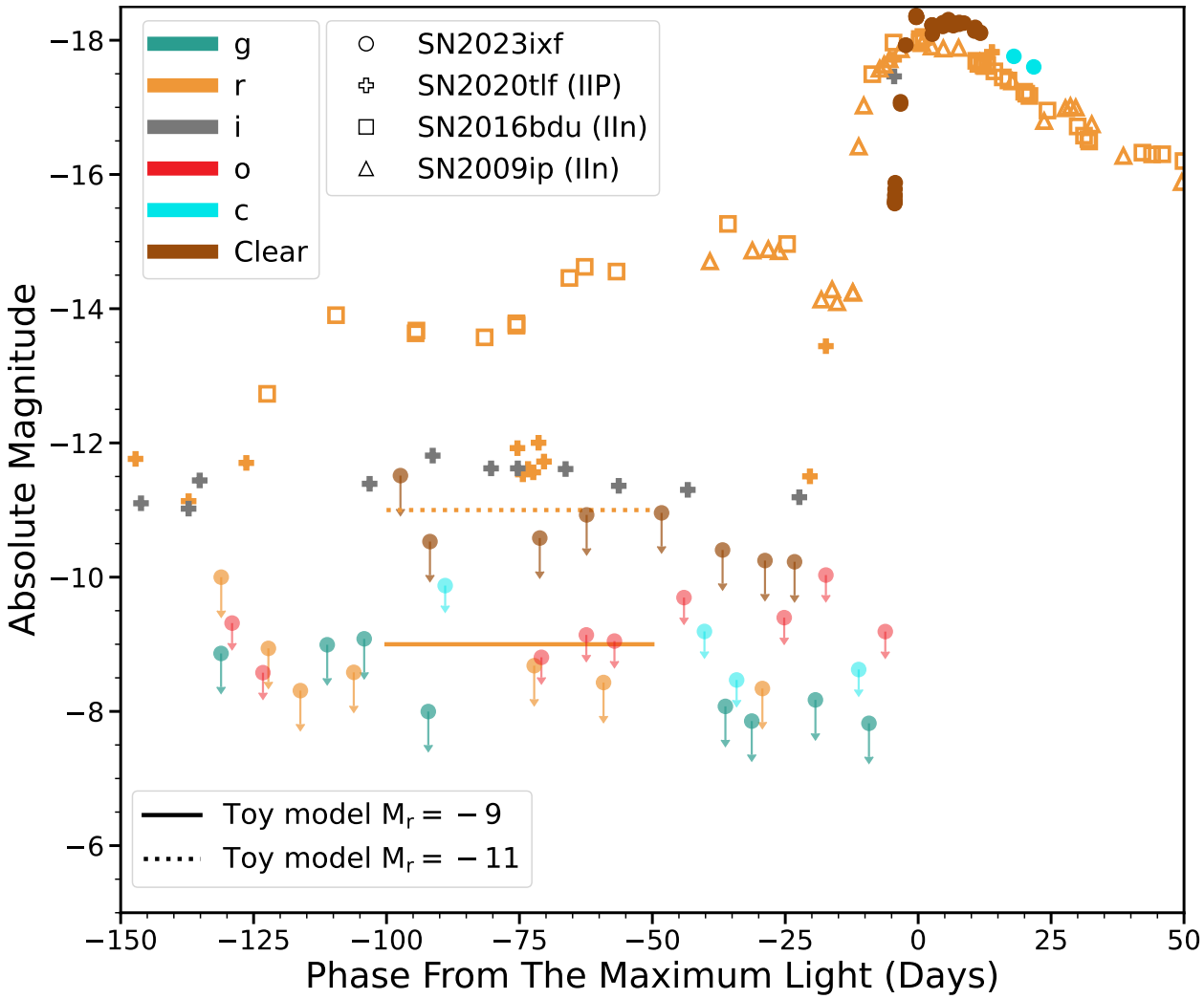

Figure 3.2 A zoomed-in section of Figure 3.1 close to the explosion. The precursor light curves of SN 2020tlf (Type IIP, Jacobson-Galán et al., 2022), SN 2009ip (Type IIn; Mauerhan et al., 2013), and SN 2016bdu (Type IIn; Pastorello et al., 2018) are overplotted for comparison. Toy models with a duration of 50 days and luminosities of $M_r = -9$ mag and -11 mag are also shown.

is Gaussian, the number of such data points would be 1 for ZTF and ATLAS, respectively. Additionally, the spurious detections could be potentially due to image reduction issues and unsatisfactory weather conditions.

To further examine the reliability of the detections, we chose 12 positions around the SN position, separated by ∼4 to 10 pixels, corresponding to ∼4 to 10 arcsecs (illustrated in Figure 3.3). We then performed forced photometry on these sample positions in an identical

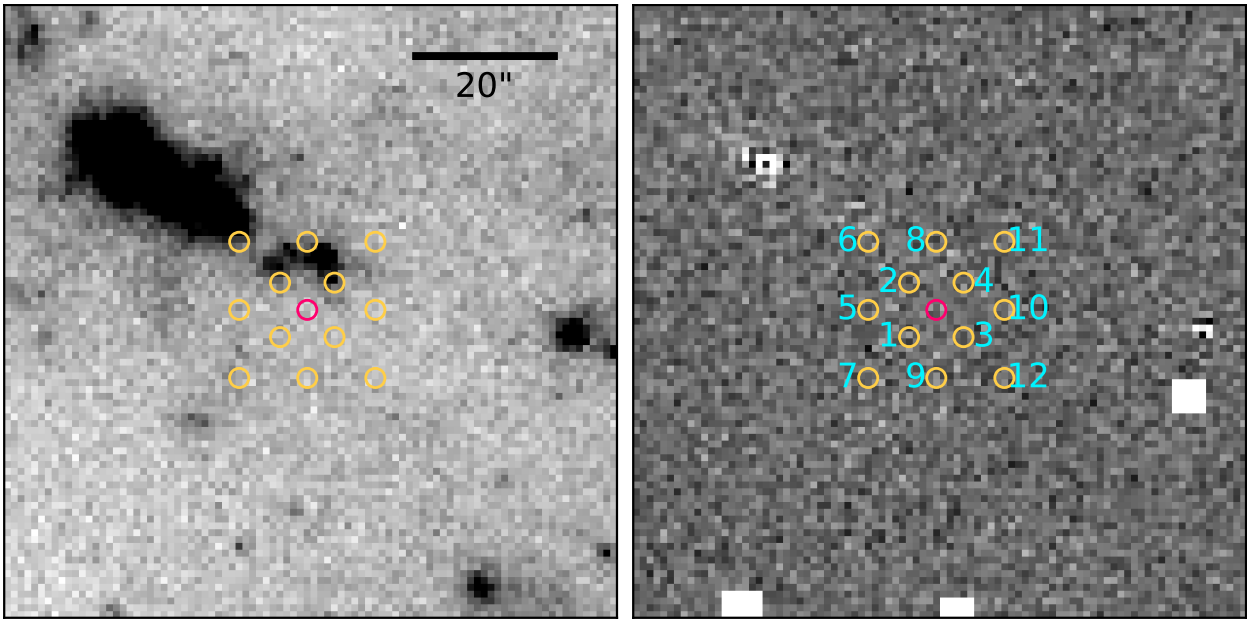

Figure 3.3 ZTF science and difference images at the position of SN 2023ixf before the explosion. The images are downloaded from the ZTF Science Data System (Masci et al., 2019; IRSA, 2022) for illustrative purposes. The magenta circle marks the position of the SN. The 12 orange circles show a grid of sample positions around the SN. We performed forced photometry on these sample positions in addition to the SN location to check the reliability of the detections.

manner as we did at the SN position. By itself, this grid of positions around the SN is unrelated to any transient, but with their close proximity to SN 2023ixf, we can use the sample positions to gauge the rate of random and low signal-to-noise detections in the data. If there are detections at multiple sample positions, this would be a indication of a large scale image artifacts or large random noise fluctuation in data from that time period, so the detections at the SN position at similar phases would be not reliable.

For the ZTF data, we found that there are several low significance 'detections' in the r and i bands, in sample position 3 and 5 in particular, at similar phases to our nominal detections at the SN position. Since position 3 and 5 are not related to any transients, the 'detections' in these two positions suggest that there were likely a large scale artifacts or large random noise fluctuation at the time period that the images were taken. Therefore, the detections at the SN position are treated as spurious. Likewise for the ATLAS data, we

found that there are detections in the o and c bands at similar phases for most of the grid sample positions. Given all of the above, we treat the low-significance detections at the SN position as spurious and do not include them in our analysis.

3.4. Discussion

3.4.1. Constraints on the Precursor Activity. The combined DLT40, ZTF and ATLAS data provide an opportunity to put a strong limit on the brightness and duration of any possible precursor activity in SN 2023ixf. In this section, we discuss the constraint we put on a toy outburst model and the hydrodynamic precursor models of Tsuna et al. (2023).

3.4.1.1. *Toy precursor model.* We consider a toy burst model with constant brightness and finite duration. Examples of the toy model are shown in Figure 3.2. For each brightness and duration, we randomly distributed 5,000 outburst light curves during the 5-year period prior to the SN explosion. If at one epoch the toy model light curve is brighter than the limit, the data point at that epoch would be marked as a detection. If there are at least two such epochs within 30 days, we will consider the event to be a detected precursor outburst. We note that since we use a signal-to-noise ratio of 5 for calculating the non-detection limit, the 'detections' in the experiment presented here would be much more significant than the spurious detections we discussed in Section 3.3.4. We calculate the detection rate f for each outburst, where f is defined as the number of light curves marked as detections divided by the total number of light curves we considered here (5000). If f is high, then the probability that we missed a precursor outburst before the explosion of SN 2023ixf is low. Only the r-band light curve is used in this analysis. The upper panel of Figure 3.4 shows f as a function of the r-band absolute magnitude (M_r) for various outburst durations (solid lines). Another set of simulations is done by fixing the brightness of the outburst and varying its duration. The result is also shown in solid lines in the bottom panel of Figure 3.4.

In order to take advantage of the high-cadence multiband light curves, we assume the precursor has a perfect blackbody spectrum with a constant temperature. We then calculate

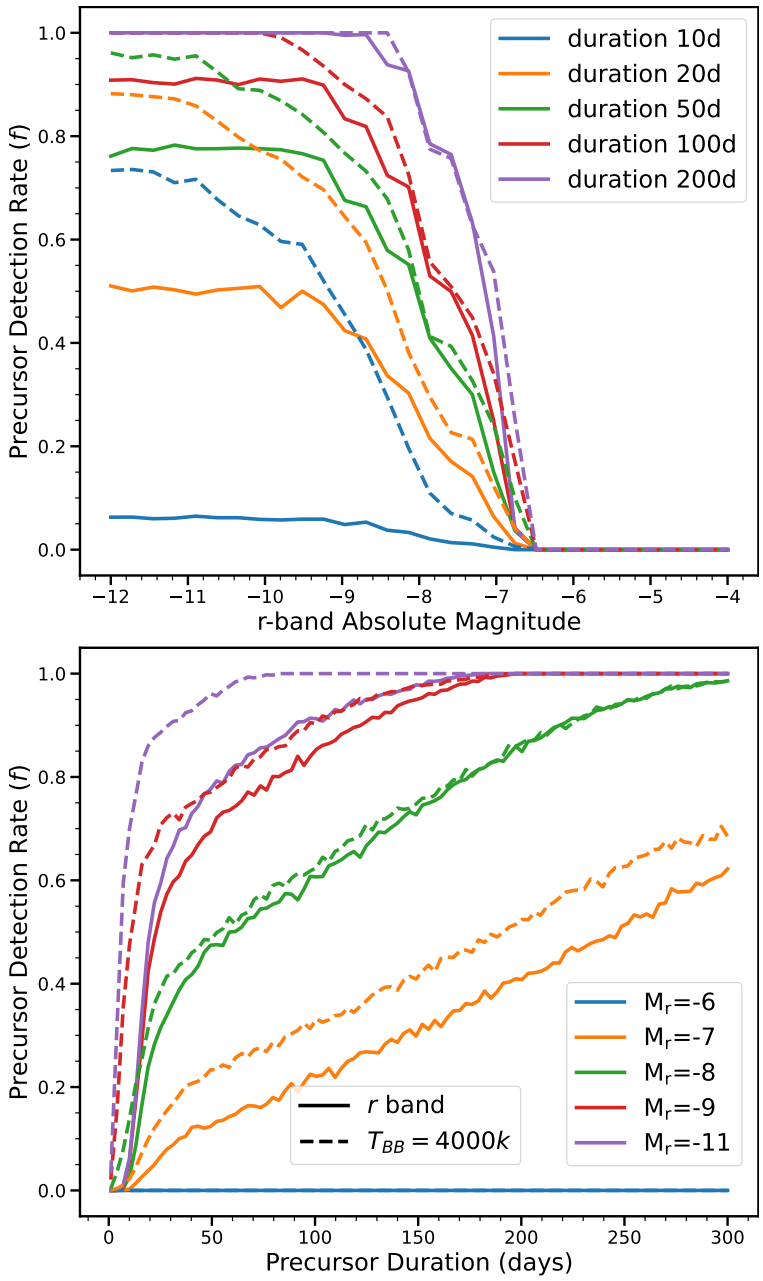

Figure 3.4 Upper: The detection rate of toy-model precursor outbursts given our data set as a function of the r-band absolute magnitude for various outburst durations. The solid line only uses the r-band data. The dashed line assumes that the precursor outburst has a blackbody spectrum with a temperature of 4000 K and uses the data from all the filters. Bottom: The detection rate of a precursor outburst as a function of duration for various outburst absolute magnitudes.

the magnitude for each filter based on the M_r. In the outburst precursor model presented by Davies et al. (2022), the temperature at the progenitor surface can increase by about 1200 K during the outburst. The stellar temperature of the progenitor of SN 2023ixf was estimated to be 3500^{+800}_{-1400} K (Jencson et al., 2023). Therefore, we tentatively adopt a blackbody temperature of 4000 K here. In the whole data set, if the simulated light curve is brighter than the limit at more than two data points within 30 days, we consider the outburst to be detected by the survey. We calculate f using the same method as described above. The results are shown in Figure 3.4 as dashed lines. We note that the blackbody temperature of the precursor in SN 2020tlf is around 5000 K (Jacobson-Galán et al., 2022). As an additional test, we run the same simulation with a temperature of 5000 K and find that this only marginally changes the result.

As presented in Figure 3.4, for an outburst brighter than $M_r = -9$ mag and longer than 100 days, the detection rate of a precursor (f) is larger than ∼0.9. Such a precursor is very likely to have been detected. In addition, for an outburst brighter than $M_r = -8$ mag, f is larger than 0.9 for a precursor that lasts longer than 200 days. Therefore, we conclude that if there was a precursor for SN 2023ixf, the outburst must have been shorter than 100 days if it was brighter than about $M_r = -9$ mag, or shorter than 200 days if it was brighter than about $M_r = -8$ mag.

3.4.1.2. *Hydrodynamical precursor models.* Tsuna et al. (2023) modeled precursor outbursts by injecting energy into the hydrogen-rich envelope of a 15 $M_\odot$ RSG progenitor. Two situations were considered in their models, where energy injection occurs once and twice. The models are differentiated by both the number of energy injections and their amounts. To match the passbands of our data set, we produce blackbody spectra based on the temperature and radius from their model results and applied appropriate filter transmission functions. Examples of a few models are shown in Figure 3.1.

The progenitor mass of SN 2023ixf is estimated to be 11 ± 2 $M_\odot$ by Kilpatrick et al. (2023), 9 to 14 $M_\odot$ by Neustadt et al. (2023), 17 ± 4 $M_\odot$ by Jencson et al. (2023), and 20 ± 4 $M_\odot$ by Soraisam et al. (2023). To take the uncertainty of the progenitor mass into account, we added an uncertainty to the brightness of each model. Tsuna et al. (2023) showed that, for different progenitor masses, the brightness of the precursor light curve varies by less than a factor of 2. Therefore, we varied the precursor brightness taken from Tsuna et al. (2023) using a Gaussian distribution centered on the model light curve with a standard deviation of 0.4 mag, which is roughly equivalent to a factor of 2 of luminosity change.

For each model, we generated 10,000 light curves by varying the luminosity as described above. These light curves are then randomly distributed in the 5 years of the pre-explosion observations. The energy injection time is at least 200 days prior to the SN explosion, so that all the models can reach the (first) light curve peak before the time of explosion. We calculated f using the same method as described in Section 3.4.1.1 and listed the results in Table 3.4.1.2. For all the models, the probability that there was a precursor that was not detected is low. The model with the lowest detection rate (f) is the single-small model. This is because this model has the smallest total injected energy, and thus the light curve is faster and dimmer than other models. The CSM mass that is ejected in the single-small model is 0.015 $M_\odot$, which is the lowest ejected mass among all the models. Given that this model has the lowest detection probability, we can use it to put an upper limit for the mass ejected during the possible pre-explosion outburst. We conclude that the probability that we would not detect the single-small model precursor is 23 % within $\sim$5 years prior to the explosion of SN 2023ixf, while this probability is below about 10 % for all other models. Therefore, the upper limit of mass ejection during the precursor outburst (if there was one) is around 0.015 $M_\odot$. However, it should be noted that the existence of dust around the progenitor would weaken the constraints we derived above.

.

Table 3.1. Detection rate of several outburst models

Model	f	Unbound CSM ($M_\odot$)
Single-large	1.0	1.2
Single-fid	0.97	0.35
Single-small	0.77	0.015
Double-large	1.0	3.6
Double-fid	0.96	1.3
Double-long	0.91	1.2

Note. — The detection rate of a precursor in our data set for different models from Tsuna et al. (2023). These models are differentiated by both the number of energy injections and their amounts.

3.4.2. Comparison with other precursor studies. Precursor emission has been observed in many Type IIn SNe. These objects likely have extended, dense CSM around their progenitors, which is driving their long-duration narrow-line emission, and which may have been produced by pre-explosion activity in the progenitor (Mauerhan et al., 2013; Pastorello et al., 2013; Ofek et al., 2014; Strotjohann et al., 2021b). This pre-explosion emission could be powered by the interaction with the surrounding CSM or the continuum-driven wind, while the underlying triggering mechanism is still uncertain. The precursor outbursts in SNe IIn usually have an absolute magnitude between −15 mag and −12 mag, which is much brighter than the limits in our observations (see Figures 3.1 and 3.2).

From SN observations, a significant fraction of RSGs are believed to have dense and confined CSM prior to the explosion, which may be because they have experienced intense mass loss before they explode as Type II SNe (e.g., Morozova et al., 2018; Förster et al., 2018; Morozova et al., 2020; Bruch et al., 2023). However, after analyzing the pre-explosion progenitors of four Type IIP/L SNe using data from the Large Binocular Telescope, Johnson et al. (2018) found that these progenitors were quiescent and the probability that they had

extended outbursts after oxygen ignition (around 5.4−2.6 years before the SN explosion) is low. To date, precursor emission in a normal Type IIP SN has only been observed in SN 2020tlf (Jacobson-Galán et al., 2022). Both spectroscopic and photometric observations suggest that the progenitor of SN 2020tlf had experienced enhanced mass loss prior to the explosion, and its precursor emission is likely due to the ejection of the outer layer of its progenitor star during final-stage nuclear burning (Jacobson-Galán et al., 2022). The precursor emission in SN 2020tlf is around -11.5 mag in the r, i, and z bands over about 100 days before explosion, which is about 1 mag brighter than our current limit in the DLT40 Clear band and about 3 mag brighter than our limit in the ZTF g and r bands (see Figures 3.1 and 3.2). Therefore, the type of precursor observed in SN 2020tlf can be excluded in SN 2023ixf.

Multiple flash-spectroscopy studies have found evidence of dense CSM around the progenitor of SN 2023ixf, which requires a mass loss rate of $10^{-3} - 10^{-2} M_{\odot} yr^{-1}$ (Jacobson-Galan et al., 2023; Bostroem et al., 2023), comparable to or slightly lower than the mass loss rate estimated for SN 2020tlf (10^{-2} $M_{\odot} yr^{-1}$) (Jacobson-Galán et al., 2022). The lack of similar precursor activity in SN 2023ixf may suggest that there are various physical mechanisms for the formation of dense CSM around the progenitors of normal Type II SNe. For instance, Matsuoka & Sawada (2023) proposed that the binary interaction in the final evolutionary stage of RSG stars could contribute to the dense CSM around the SN progenitor. Recently, Smith et al. (2023) found that the CSM around the progenitor of SN 2023ixf is likely asymmetric, which could be a consequence of binary interaction triggered by pre-SN inflation of the RSG during Ne or O burning. In such a binary scenario, eruptive mass loss from a single RSG may not be the driving force behind the dense CSM that we observe. In addition, Soker (2021, 2023) suggested that the long-lived effervescent zone formed around RSGs could be an alternative scenario for the dense CSM around the progenitors of Type II SNe.

3.4.3. Quiescent progenitor of SN 2023ixf versus enhanced pre-SN mass loss. After the discovery of SN 2023ixf, many independent studies have suggested that there is

dense and confined CSM around the progenitor, implying an enhanced mass loss prior to the explosion. Recently, by analyzing the early flash spectroscopy of SN 2023ixf, Bostroem et al. (2023) and Jacobson-Galan et al. (2023) suggest that, to produce the dense CSM around the progenitor, the mass-loss rate of the progenitor of SN 2023ixf should be around $10^{-3} - 10^{-2}$ $M_{\odot}yr^{-1}$. Based on the hard X-ray observations, Grefenstette et al. (2023) also found evidence of dense pre-existing CSM, which requires a mass loss rate of $3 \times 10^{-4} M_{\odot}yr^{-1}$ before the explosion. In addition, Jencson et al. (2023) analyzed the near- and mid-infrared pre-SN imaging of SN 2023ixf and found a lower mass-loss rate of $10^{-5} - 10^{-3}$ $M_{\odot}yr^{-1}$, but it is still higher than the mass-loss rate of typical RSGs in the same luminosity range. They also found that there was no evidence of infrared precursor outbursts up to $\sim$10 days before the explosion. Furthermore, Hosseinzadeh et al. (2023) found that the very early light curve evolution of SN 2023ixf is inconsistent with shock cooling models, which could be explained by the interaction of dense pre-existing CSM with the SN ejecta, and thus implies an enhanced mass loss before the SN explosion. However, they also suggested that the unusual light curve behaviour could be due to a pre-explosion eruption around one day before the explosion or even extended duration emission from the shock breakout.

Neustadt et al. (2023) examined imaging from the Large Binocular Telescope ranging from 5600 days to 400 days before the explosion of SN 2023ixf, and they found no progenitor variability in the R band at the level of $10^3 L_{\odot}$ up to 400 days before the explosion. Due to the sparse coverage of their data, they could not directly exclude short-lived outbursts. However, they argue that short outbursts would still have had a long-lived effect on the dust optical depth, leading to an increase of progenitor luminosity for decades, which they would have observed. Our data set has a higher cadence up to about 10 days before the SN explosion, but we still found no signs of strong pre-SN activity from the progenitor. The enhanced pre-SN mass-loss rate of SN 2023ixf derived from the flash spectroscopy and other studies seems in tension with the lack of any precursor emission in SN 2023ixf.

It is possible that the progenitor star had a relatively faint outburst on a time-scale of days to months. The probability that we would have detected this kind of outburst is low. Davies et al. (2022) suggested that the precursor in SNe II-P is likely in the form of abrupt outbursts, in which the progenitor would only be optically bright for a few days before becoming fainter and redder than normal RSGs and ejecting a significant amount of mass into the surrounding space. The detection of such an outburst would require higher-cadence observations prior to the time of explosion. In addition, the flash spectroscopy may not necessarily imply enhanced mass loss. Kochanek (2019) suggested that, in a binary system, the shocked boundary layer produced by the collision of winds from two stars generates a high-density CSM around the progenitor, which produces the flash spectroscopy observed in SNe II. If the progenitor of SN 2023ixf was in such binary configurations, then enhanced mass loss or an outburst prior to explosion would not be required.

3.5. Conclusions

We used 5 years of pre-explosion data from DLT40, ZTF, and ATLAS to constrain pre-explosion activity in the progenitor of SN 2023ixf. By comparing the data with a toy precursor model, we found that if there was any precursor activity, an outburst with a typical brightness of $M_r \simeq -9$ must have had a duration shorter than 100 days, and an outburst with $M_r \simeq -8$ must have had a duration shorter than 200 days. We also found that the probability that there was a precursor outburst similar to the models of Tsuna et al. (2023) is low, and therefore that the ejected mass prior to the explosion is likely less than 0.015 $M_\odot$. The precursor activity like the outburst observed in SN 2020tlf can be excluded in SN 2023ixf. The enhanced mass loss inferred from the early flash spectroscopy and other studies of SN 2023ixf is in some tension with the non-detection of any precursor outbursts. It is possible that there was a faint precursor within five years of the SN explosion that occurred on a time-scale of days to months. Such an outburst would likely not be detected by our current data set. Alternatively, the dense, confined CSM may not be due to the

enhanced mass loss from a single RSG progenitor. The dense CSM could have, for instance, originated from the interaction of stellar winds of two stars in a binary system. In summary, it is likely there are various physical mechanisms for the formation of the dense CSM around the progenitors of normal Type II SNe. In the near future, with the help of the Legacy Survey of Space and Time (LSST) survey, we will be able to put strong constraints on the precursor activities for a sample of Type IIP/L SNe, which will help us better understand the origin of the dense, confined CSM and the very last stages of RSG stellar evolution.

Acknowledgements

We would like to thank Daichi Tsuna for providing the precursor light curve models.

Research by Y.D., and S.V., N.M.R, and E.H. is supported by NSF grant AST-2008108. Time domain research by D.J.S. is also supported by NSF grants AST-1821987, 1813466, 1908972, & 2108032, and by the Heising-Simons Foundation under grant #2020-1864.

This publication was made possible through the support of an LSSTC Catalyst Fellowship to K.A.B., funded through Grant 62192 from the John Templeton Foundation to LSST Corporation. The opinions expressed in this publication are those of the authors and do not necessarily reflect the views of LSSTC or the John Templeton Foundation.

Based on observations obtained with the Samuel Oschin Telescope 48-inch and the 60-inch Telescope at the Palomar Observatory as part of the Zwicky Transient Facility project. ZTF is supported by the National Science Foundation under Grant No. AST-2034437 and a collaboration including Caltech, IPAC, the Weizmann Institute for Science, the Oskar Klein Center at Stockholm University, the University of Maryland, Deutsches Elektronen-Synchrotron and Humboldt University, the TANGO Consortium of Taiwan, the University of Wisconsin at Milwaukee, Trinity College Dublin, Lawrence Livermore National Laboratories,

and IN2P3, France. Operations are conducted by COO, IPAC, and UW. The ZTF forced-photometry service was funded under the Heising-Simons Foundation grant #12540303 (PI: Graham).

This research made use of Photutils, an Astropy package for detection and photometry of astronomical sources (Bradley et al., 2022).

CHAPTER 4

SN 2016dsg: A Thermonuclear Explosion Involving A Thick Helium Shell

Published as Dong et al 2022. in The Astrophysical Journal, Volume 934, Issue 2, id.102, 13 pp.

4.1. Abstract

A thermonuclear explosion triggered by a helium-shell detonation on a carbon-oxygen white dwarf core has been predicted to have strong UV line blanketing at early times due to the iron-group elements produced during helium-shell burning. We present the photometric and spectroscopic observations of SN 2016dsg, a sub-luminous peculiar Type I SN consistent with a thermonuclear explosion involving a thick He shell. With a redshift of 0.04, the *i*-band peak absolute magnitude is derived to be around -17.5. The object is located far away from its host, an early-type galaxy, suggesting it originated from an old stellar population. The spectra collected after the peak are unusually red, show strong UV line blanketing and weak O I λ7773 absorption lines, and do not evolve significantly over 30 days. An absorption line around 9700-10500 Å is detected in the near-infrared spectrum and is likely from the unburnt helium in the ejecta. The spectroscopic evolution is consistent with the thermonuclear explosion models for a sub-Chandrasekhar mass white dwarf with a thick helium shell, while the photometric evolution is not well described by existing models.

4.2. Introduction

Thermonuclear explosions involving white dwarfs (WDs) have often been associated with Type Ia supernovae (SNe Ia) (Whelan & Iben, 1973; Iben & Tutukov, 1984; Webbink, 1984;

Nomoto et al., 1984; Branch et al., 1995). One of the promising channels to trigger such an explosion is through the detonation of a helium layer atop a sub-Chandrasekhar/near-Chandrasekhar mass WD. In some cases, the initial helium-shell (He-shell) detonation triggers the detonation of the carbon-oxygen (CO) WD core, dubbed double detonation (Nomoto, 1982b; Livne, 1990; Livne & Glasner, 1991; Woosley & Weaver, 1986, 1994; Livne & Arnett, 1995; Hoeflich & Khokhlov, 1996; Nugent et al., 1997). Historically, the observational features produced by a double detonation with a thick He shell are thought to be quite different from what we see in normal Type Ia SNe (Woosley & Weaver, 1994; Hoeflich & Khokhlov, 1996; Nugent et al., 1997). However, recent theoretical work suggests that a double detonation could lead to a normal SN Ia if the He shell is thin enough and, in some studies, polluted by carbon from the underlying CO WD core (Fink et al., 2010; Kromer et al., 2010; Woosley & Kasen, 2011; Shen & Bildsten, 2014; Townsley et al., 2019; Polin et al., 2019; Gronow et al., 2020; Boos et al., 2021; Magee et al., 2021; Shen et al., 2021). By varying the mass of the He shell and the WD, double detonations can lead to a variety of observational properties and have been used to explain different peculiar sub-types of SNe Ia, including OGLE-2013-SN-079 (Inserra et al., 2015), SN 2016jhr (Jiang et al., 2017), SN 2018byg (De et al., 2019), SN 2016hnk (Jacobson-Galán et al., 2020, although see Galbany et al. 2019) and SN 2019yvq (Siebert et al., 2020, although see Miller et al. 2020 and Burke et al. 2021).

A detonation may only happen in the He shell and fail to trigger a subsequent WD core detonation; this scenario has been dubbed a single detonation or a He-shell detonation (Nomoto, 1982b; Woosley & Weaver, 1986; Bildsten et al., 2007; Shen et al., 2010; Waldman et al., 2011; Sim et al., 2012; Dessart & Hillier, 2015). While it has been shown that the secondary CO WD core detonation is likely to be robustly triggered by even a thin He shell (Fink et al., 2010; Shen & Moore, 2014), a pure He-shell detonation still could happen for a low-mass CO WD or a O/Ne WD (Shen & Moore, 2014). A pure He-shell detonation produces a faint and fast SN and has been invoked to explain calcium-strong transients (Perets

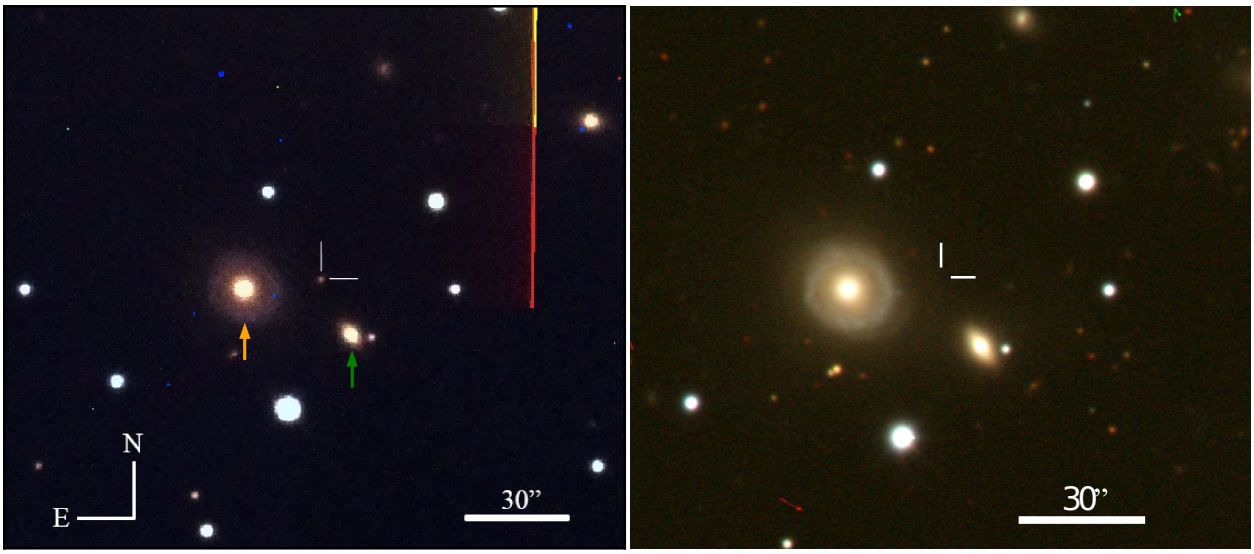

Figure 4.1 Left: Composite BVr image of SN 2016dsg obtained with the Las Cumbres Observatory on 2016 February 27. The two possible host galaxies, ESO 254- G 019 (orange arrow) and WISEA J060707.31-451108.4 (green arrow), are indicated. Right: Archival image of the field of SN 2016dsg from the DESI Legacy Imaging Surveys. The position of SN 2016dsg is indicated by white tick marks in both images.

et al., 2010; Waldman et al., 2011) and a handful of other peculiar transients (Poznanski et al., 2010; Kasliwal et al., 2010; Inserra et al., 2015). To avoid confusion, we will use 'single detonation' to refer to a pure He-shell detonation, in which the initial detonation of the He shell does not trigger the secondary detonation of the CO core.

In this paper, we present the light curves and spectra of SN 2016dsg, a sub-luminous peculiar Type I SN consistent with a thermonuclear explosion involving a thick He shell. The paper is organized as follows: the observations of SN 2016dsg are presented in Section 4.3. We compare SN 2016dsg with single/double detonation models in Section 4.4. In Section 4.5, we discuss the implications of the observational data, and finally we present our conclusions in Section 4.6.

4.3. Observations

SN 2016dsg was discovered by the *Gaia* Photometric Alert System (Hodgkin et al., 2021) on 2016 February 21 (JD 2 457 440.02) at RA(2000) = $06^h07^m08^s.18$, DEC(2000) =

Table 4.1. Spectroscopic observations of SN 2016dsg

UT Date	Julian Date (Days)	Phase (Days)	Telescope	Instrument	Resolution ($\lambda/\Delta\lambda$)	wavelength range (Å)
2016-02-26	2457444.66	4.7	NTT	EFOSC2	355	3639-9232
2016-02-27	2457445.97	6.0	FTS	FLOYDS	400-700	5000-9000
2016-03-02	2457450.38	10.4	SALT	RSS	360	3695-9196
2016-03-07	2457454.66	14.7	NTT	EFOSC2	355	3637-9231
2016-03-09	2457456.60	16.6	NTT	SofI	550	9377-16468
2016-03-14	2457462.33	22.3	SALT	RSS	360	3696-9197
2016-03-19	2457467.33	27.3	SALT	RSS	360	3697-9197
2016-04-10	2457489.27	49.3	SALT	RSS	360	3798-8196
2016-04-15	2457494.25	54.2	SALT	RSS	360	3798-8196

Note. — Phase with respect to the discovery date

$-45°10'52\overset{''}{.}23$ as Gaia16afe and was given the IAU name SN 2016dsg (Delgado et al., 2016). SN 2016dsg will be used to refer to the source hereafter. Two nearby galaxies, ESO 254-G 019 (z = 0.040, Jones et al. 2004, 2009) and WISEA J060707.31-451108.4 (z = 0.039, Jones et al. 2004, 2009), are identified within 1 arcmin radius of the SN 2016dsg. SN 2016dsg is at a projected offset of $22\overset{''}{.}49$ (18.5 kpc) and $18\overset{''}{.}75$ (15.4 kpc) from these two galaxies, respectively (see Figure 4.1). The Milky Way line-of-sight reddening toward SN 2016dsg is $E(B-V) = 0.099$ mag (Schlafly & Finkbeiner, 2011a). Given that the object is far from both plausible host galaxies and there are no obvious narrow Na I D absorption lines from the optical spectra (Poznanski et al., 2012), we assume there is no host galaxy extinction. Throughout the paper, we will adopt a redshift of z = 0.04, corresponding to a luminosity distance of 169 Mpc with $H_0 = 73$ km s^{-1} Mpc^{-1}, $\Omega_M = 0.27$ and $\Omega_\Lambda = 0.73$ (Spergel et al., 2007).

The follow-up observations started from 2016 February 26. Photometric data were obtained through Global Supernova Project with the Las Cumbres Observatory (Brown et al., 2013b) and were reduced with the PyRAF-based photometric reduction pipeline LCOGT-SNPIPE (Valenti et al., 2016). The final PSF magnitudes were calibrated using the APASS

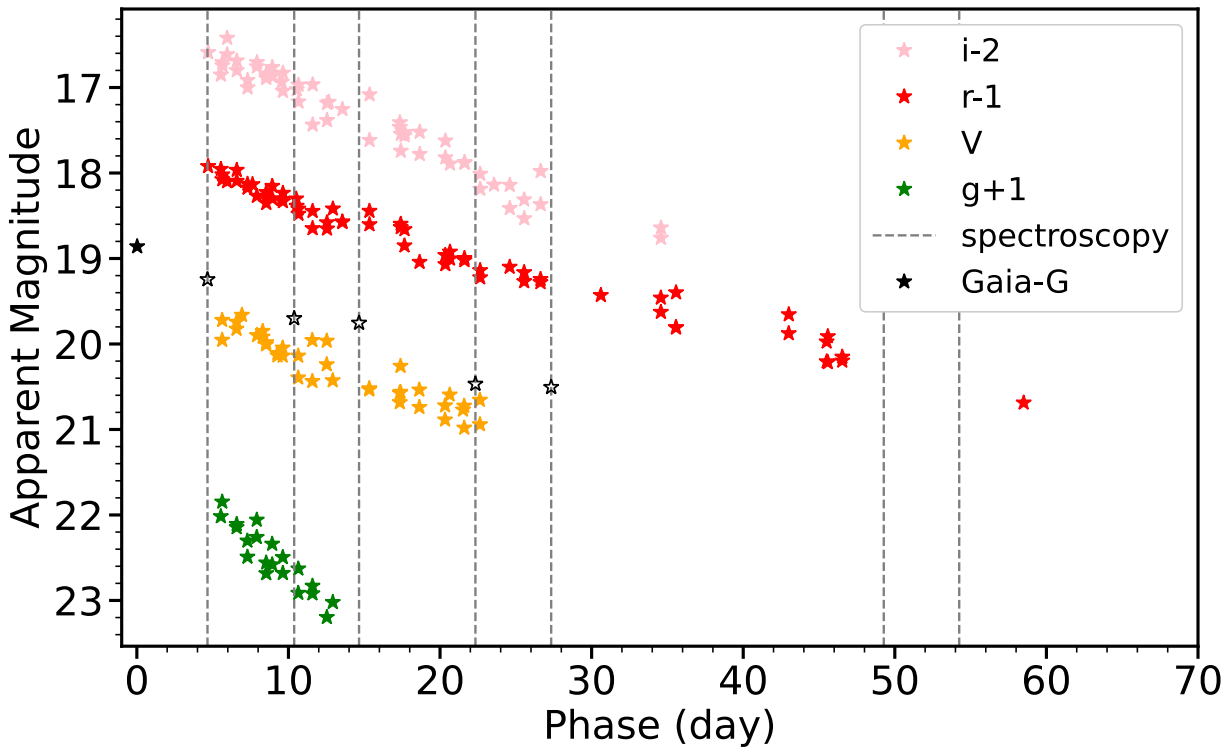

Figure 4.2 Photometric evolution of SN 2016dsg with respect to the epoch of discovery. The phase is measured from the discovery. The vertical lines indicate the epochs when the spectroscopy was taken. For the Gaia *G*-band light curve, the first data point is from direct Gaia observation and the rest of them (hollow stars) are calculated by performing synthetic photometry on spectra.

(Henden et al., 2012) catalog stars in the SN field. The background contamination was removed with HOTPANTS (Becker, 2015) by subtracting reference images obtained on 2020 August 23, over four years after the explosion.

Two optical spectra and one near-infrared (NIR) spectrum were obtained by the PESSTO collaboration (Smartt et al., 2015). The optical spectra were taken with the ESO Faint Object Spectrograph and Camera (v.2) (EFOSC2; Buzzoni et al., 1984) on the 3.6-m New Technology Telescope (NTT). The NIR spectrum was taken with the Son of ISAAC infrared spectrograph and imaging camera (SofI; Moorwood et al., 1998) on the NTT. All these spectra were reduced using the PESSTO pipeline as described in Smartt et al. (2015). In addition, five optical spectra were collected with the Southern African Large Telescope

(SALT) using the Robert Stobie Spectrograph (RSS; Smith et al., 2006) with a 1.″5 longslit. We used the PG0300 grating in two tilt angles to cover the optical wavelength range and a custom data reduction pipeline based on the PySALT package (Crawford et al., 2010a). One low-dispersion optical spectrum was obtained on 2016-02-27 by the FLOYDS spectrograph (Brown et al., 2013b). The FLOYDS spectrum was reduced following standard procedures using the FLOYDS pipeline (Valenti et al., 2014b). However, this spectrum had a low signal-to-noise ratio, so we did not use it for analysis. The optical spectra were calibrated to interpolated r-band photometry, and the resulting flux uncertainty is about 10 percent. All the spectroscopic observations are listed in Table 4.1 and will be available on WISeREP (Yaron & Gal-Yam, 2012)[1].

4.3.1. Photometric Evolution. The light curves of SN 2016dsg are shown in Figure 4.2. The photometry we collected does not show the rise phase, and the decline is almost linear. In the top panel of Figure 4.3, we compare the i-band light curve of SN 2016dsg with i/I-band light curves of other thermonuclear SNe with various subtypes: normal Type Ia SN 2011fe (Nugent et al., 2011); 1991bg-like SN Ia: SN 1991bg (Filippenko et al., 1992); Ca-strong 1991bg-like SN Ia: SN 2016hnk (Galbany et al., 2019); Ca-strong transients: SN 2012hn (Valenti et al., 2014c) and SN 2010et (Kasliwal et al., 2012); single/double detonation candidate: OGLE-2013-SN-079 (Inserra et al., 2015) and double detonation candidates: SN 2018byg (De et al., 2019) and SN 2016jhr (Jiang et al., 2017). The phase is measured from the discovery for SN 2016dsg and from the i/I-band maximum for other objects. The g/V-band light curve comparison and $g-r/V-R$ color comparison are shown in the middle and bottom panel of Figure 4.3, respectively. In order to compare photometric data in AB and Vega system, the V- and I-band magnitudes have been shifted to the AB magnitude system by applying a zero point correction. In i/I band, SN 2016dsg is less luminous than normal SNe Ia and SN 2016jhr, brighter than some Ca-strong transients and comparable to

[1] http://www.weizmann.ac.il

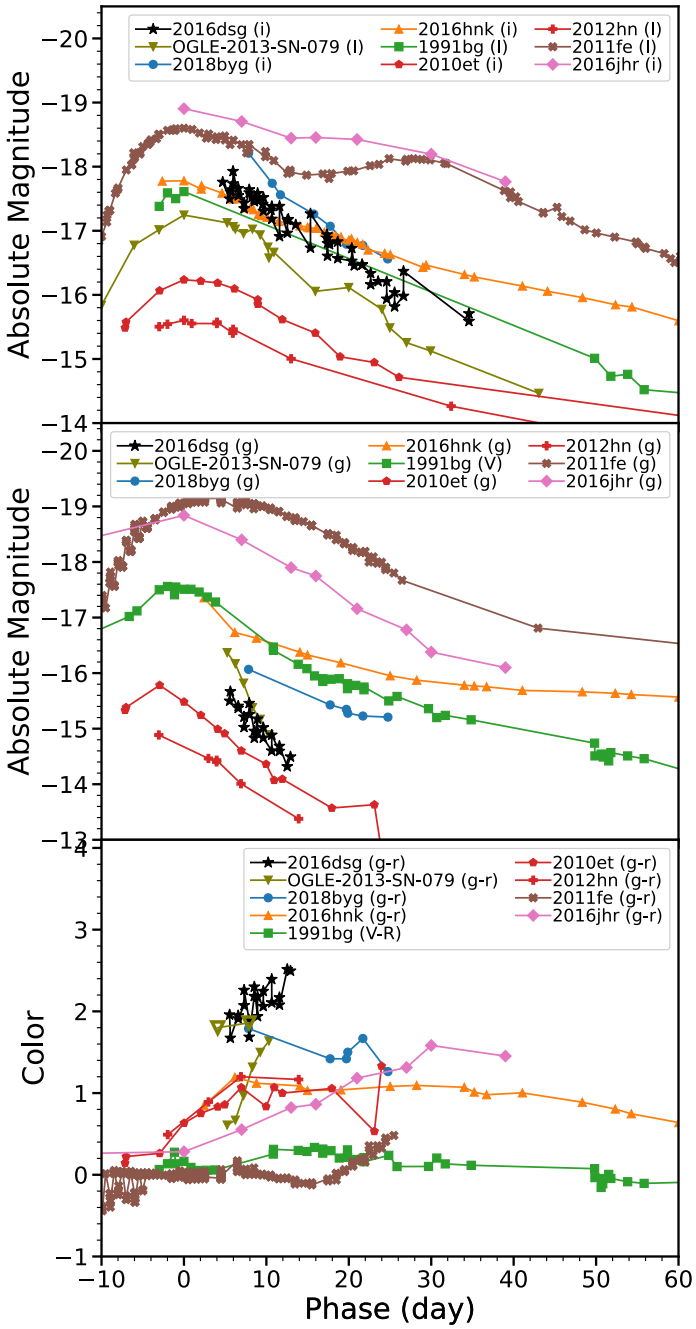

Figure 4.3 Top: i/I-band comparison of SN 2016dsg and various subtypes of thermonuclear SNe. SN 2016dsg is fainter than normal SNe Ia but brighter than Ca-strong transients. Middle: g/V-band comparison of SN 2016dsg and various subtypes of thermonuclear SNe. Bottom: Color comparison of SN 2016dsg and various subtypes of thermonuclear SNe. The hollow triangles are derived from synthetic photometry of OGLE-2013-SN-079. Around the peak light, SN 2016dsg, OGLE-2013-SN-079 and SN 2018byg are redder than all other objects in our sample. All the objects are extinction corrected. The Vega magnitudes have been converted to AB magnitude system.

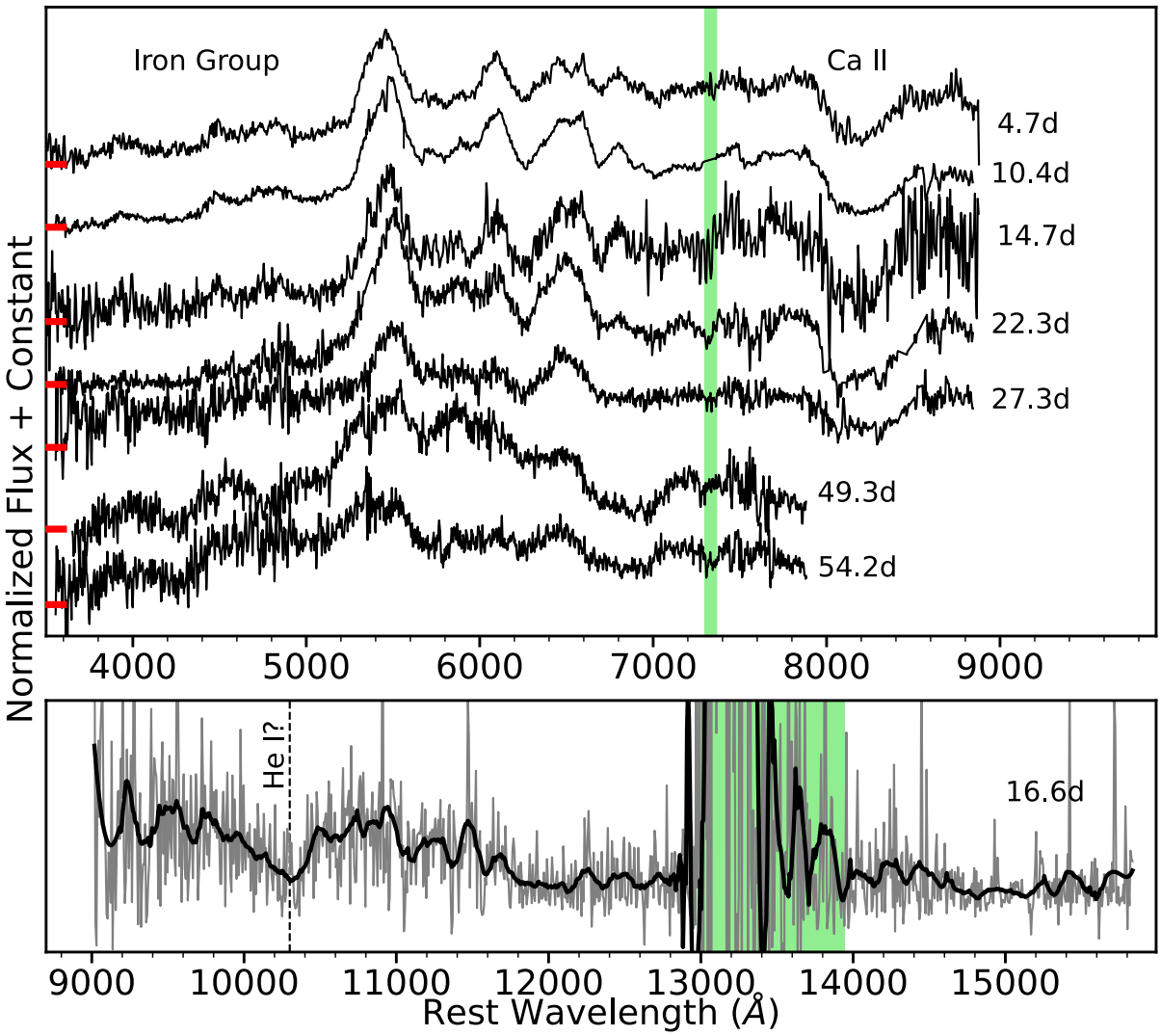

Figure 4.4 Top: spectroscopic evolution of SN 2016dsg. The zero flux levels of each spectrum are indicated by the red ticks. All the spectra have been normalized in the range 4000-7000Å. Bottom: The NIR spectrum taken at day 16.6. The spectrum has been smoothed with a second order Savitzky-Golay filter, and the gray background line is the original spectrum. The green band marks the strongest telluric absorptions.

1991bg-like transients (SN 1991bg and SN 2016hnk), OGLE-2013-SN-079 and SN 2018byg. The i-band decline rate of SN 2016dsg is around 0.077(0.003) mag/day, similar to those of single/double detonation candidates and slightly faster than other objects. In g/V-band,

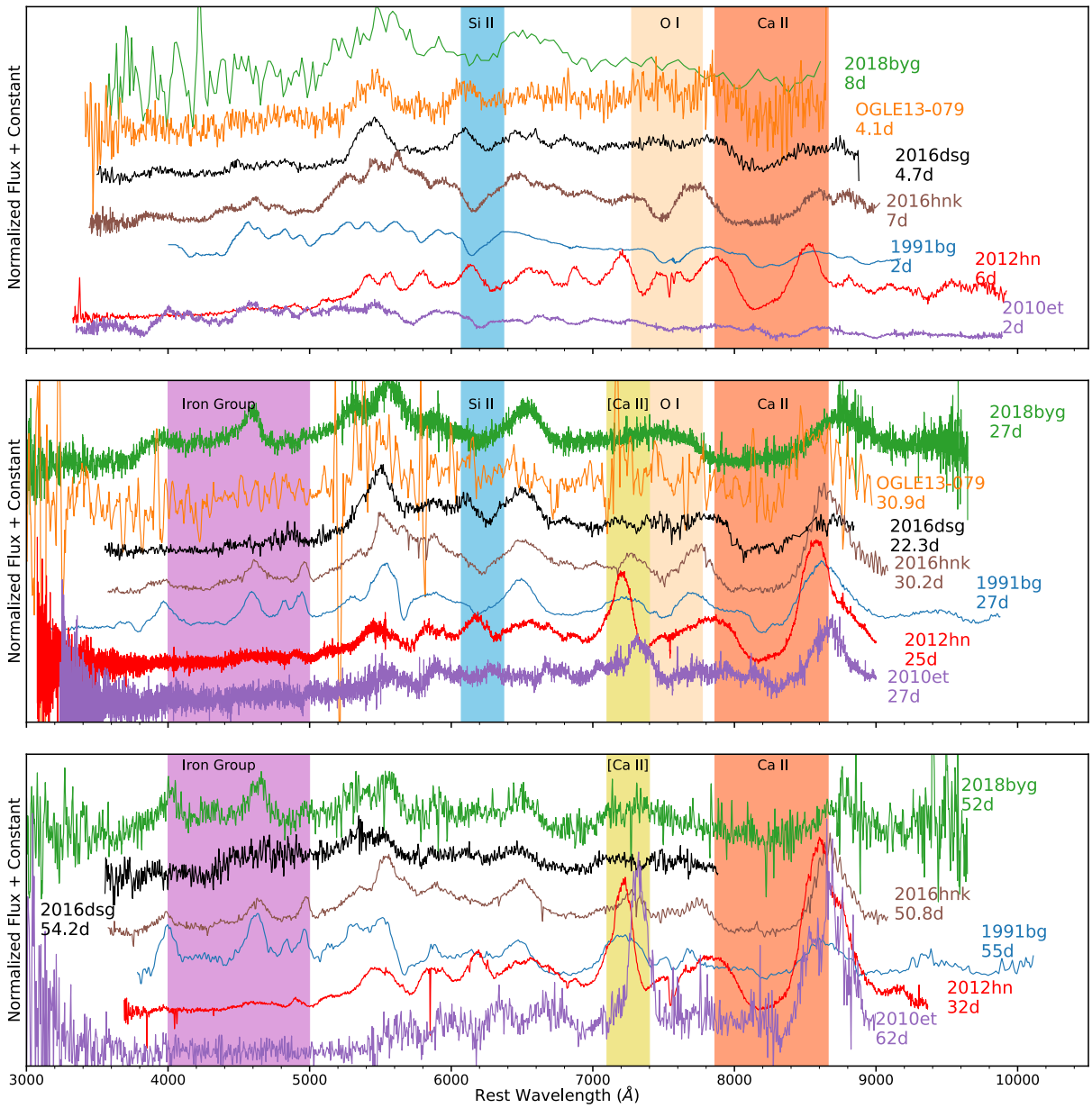

Figure 4.5 Optical spectral comparison of SN 2016dsg to other thermonuclear SNe, including 1991bg-like SNe Ia: SN 1991bg and SN 2016hnk; Ca-strong transients: SN 2012hn and SN 2010et; single/double detonation candidate: OGLE-2013-SN-079 and double detonation candidate: SN 2018byg.

SN 2016dsg shows a faster decline rate than other objects except for OGLE-2013-SN-079. At $\sim$ day 4.7, the $g-r$ color of SN 2016dsg is $\sim$1.8, redder than normal SNe Ia, 1991bg-like

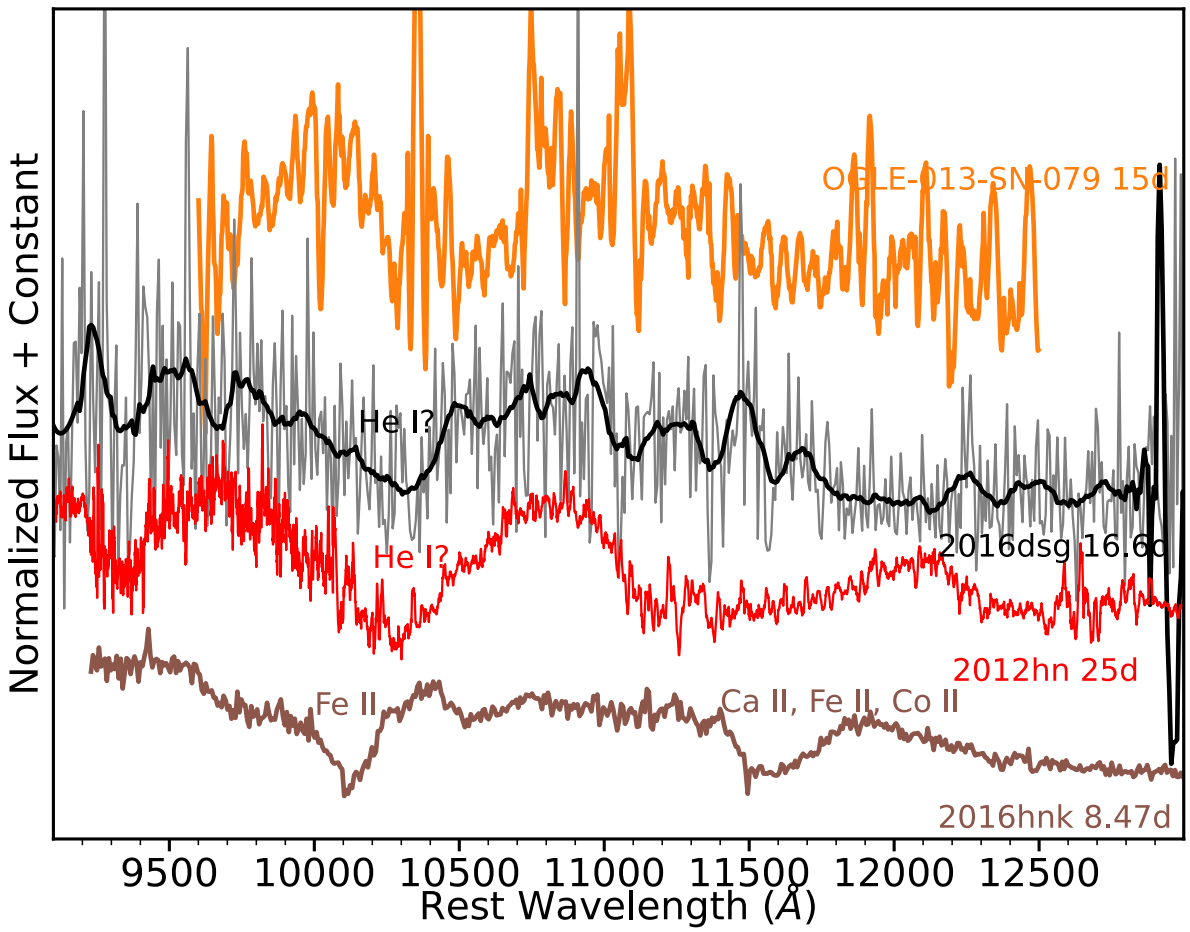

Figure 4.6 The NIR spectrum of SN 2016dsg compared to other transients. A He I absorption feature is likely present in SN 2016dsg.

transients and Ca-strong transients. It is likely that the g-band photometry of OGLE-2013-SN-079 at first a few epochs was affected by a zero point issue, leading to a bluer color. Therefore, we derived the synthetic photometry from spectroscopy, and the resulting $g - r$ colors are similar to those of SN 2016dsg and SN 2018byg at similar epochs.

As shown in Figure 4.2, SN 2016dsg declined continuously in the Gaia unfiltered white light G bandpass (G-band, Jordi et al. 2010) based on synthetic photometry derived from our spectra after initial detection, implying that maximum light occurred before discovery. However, as will be discussed in Section 4.5.2, the epoch of discovery of SN 2016dsg, i.e.,

JD 2 457 440.0, is likely close to the epoch of maximum light, which we adopt as the reference epoch throughout the paper. In this case, the maximum i-band absolute magnitude of SN 2016dsg is about -17.5 mag, fainter than normal SNe Ia.

4.3.2. Spectroscopic Evolution. The optical spectra are shown in the upper panel of Figure 4.4. These spectra are all collected after the peak brightness, and the spectral features do not evolve too much. The most prominent feature is the strong line blanketing on the blue side of the spectra. Such a feature has been observed in the spectra of OGLE-2013-SN-079 and SN 2018byg, and has been attributed to iron-group elements (Inserra et al., 2015; De et al., 2019). In the bottom panel of Figure 4.4, we show the NIR spectrum taken at day 16.6, where the spectrum is smoothed with a Savitzky-Golay filter (Savitzky & Golay, 1964).

In Figure 4.5, we compare the optical spectra of SN 2016dsg at day 4.7, day 22.3 and day 54.2 with those of other thermonuclear SNe at similar epochs. OGLE-2013-SN-079 and SN 2016dsg have almost identical spectroscopic features, implying that these two objects may have very similar progenitors. SN 2018byg also has strong UV line blanketing and shows slightly higher velocities than SN 2016dsg. Starting from at least day 27, strong emission lines of Fe-group elements appear on the blue side of the spectra of SN 2018byg (De et al., 2019). For SN 2016dsg and OGLE-2013-SN-079, such features are not observed. This is consistent with what we see in Figure 4.3, where SN 2018byg shows a shallower decline in the g band than SN 2016dsg and OGLE-2013-SN-079. Compared to 1991bg-like transients, SN 2016dsg shows rather weak O I λ7773 absorption. This could be due to the low abundance of oxygen in the ejecta and will be discussed in detail in Section 4.5. Ca-strong transients quickly develop strong [Ca II] $\lambda\lambda$7291, 7323 emission lines, which are either very weak or do not exist in SN 2016dsg.

In Figure 4.6, we show a NIR spectroscopic comparison between SN 2016dsg, SN 2012hn, OGLE-2013-SN-079 and SN 2016hnk. SN 2016dsg has a broad absorption line at 9700-10500 Å, which is likely to be He I λ10830. SN 2012hn and SN 2016hnk have similar features in

Table 4.2. A brief summary of the models which were compared to SN 2016dsg.

Model	Original Model Name	Detonation Type	WD Mass ($M_\odot$)	He Shell Mass ($M_\odot$)	Total Mass ($M_\odot$)	Nickel Mass ($M_\odot$)	Reference*
Polin0.8+0.08-D		Double	0.8	0.08	0.88	0.074	a
Polin0.9+0.08-D		Double	0.9	0.08	0.98	0.31	a
Polin0.76+0.15-D		Double	0.76	0.15	0.91	0.18	a
Polin0.76+0.15-0.2-D†		Double	0.76	0.15	0.91	0.18	a
Kromer0.81+0.126-D	Kromer model 1	Double	0.81	0.126	0.936	0.17	b
Kromer1.08+0.055-D	Kromer model 3	Double	1.08	0.055	1.135	0.55	b
Sim0.45+0.21-D	Sim CSDD-L	Double	0.45	0.21	0.66	0.0218	c
Sim0.58+0.21-D	Sim CSDD-S	Double	0.58	0.21	0.79	0.215	c
Sim0.58+0.21-S	Sim HeD-S	Single	0.58	0.21	0.79	0.065	c
Shen0.6+0.2-S	Shen 0.6+0.2	Single	0.6	0.2	0.8	0.026	d
Shen1.0+0.10-S	Shen 1.0+0.10	Single	1.0	0.1	1.1	0.0504	d

*(a) Polin et al. (2019); (b) Kromer et al. (2010); (c) Sim et al. (2012); (d) Shen et al. (2010).

† Polin0.76+0.15-0.2-D is similar to Polin0.76+0.15-D but includes 0.2 $M_\odot$ mixing in the outer ejecta.

this region, but this line has been identified as Fe II for SN 2016hnk (Galbany et al., 2019). This possible He I λ10830 absorption feature in SN 2016dsg will be discussed in Section 4.5.1.

4.4. Model Comparison

Since SN 2016dsg is fainter than normal Type Ia SNe, the possibility that its progenitor is a sub-Chandrasekhar mass WD can not be directly excluded (Sim et al., 2010; Blondin et al., 2017; Shen et al., 2018). However, a quick comparison with the models from Blondin et al. (2017) shows that the sub-Chandrasekhar mass models fail to match the level of absorption or line-blanketing below ∼5000Å of the observations. The models also predict significant O I λ7773 absorption lines that are not visible or rather weak in SN 2016dsg. The strong line-blanketing in the UV around the peak light is usually an indication of a large amount of iron-group elements in the outer ejecta and likely points to a single/double detonation. In the following section, we will compare the object with single detonation models from Shen et al. (2010) and Sim et al. (2012), and double detonation models from Kromer et al. (2010), Sim et al. (2012), and Polin et al. (2019).

In Shen et al. (2010), the observables of single detonations for various CO WD core masses (0.6, 1.0 and 1.2 $M_\odot$) and He envelope masses (0.05, 0.1, 0.2, 0.3 $M_\odot$) were explored. Kromer et al. (2010) explored the observable properties of double detonation models with minimum mass helium shells (from 0.0035 to 0.0126 $M_\odot$) studied in Fink et al. (2010). Sim et al. (2012) modeled a low mass system (0.45 $M_\odot$ WD + 0.21 $M_\odot$ He) and a high mass system (0.58 $M_\odot$ WD + 0.21 $M_\odot$ He) for both single detonation and double detonation scenarios. Polin et al. (2019) exploded double detonation models for a set of CO WD masses (from 0.6 to 1.2 $M_\odot$) with helium shells of 0.01, 0.05 and 0.08 $M_\odot$. In order to roughly match the brightness and the UV line-blanketing of SN 2016dsg, the models we chose to compare with SN 2016dsg are Polin0.8+0.08-D, Polin0.9+0.08-D, Polin0.76+0.15-D, Polin0.76+0.15-0.2-D, Kromer0.81+0.126-D, Kromer1.08+0.055-D, Sim0.45+0.21-D, Sim0.58+0.21-S, Sim0.58+0.21-D, Shen0.6+0.2-S and Shen1.0+0.10-S. In the literature, Sim0.45+0.21-D, Sim0.58+0.21-S and Shen0.6+0.2-S have been found to provide a reasonable match to the spectra of OGLE-013-SN-079 (Inserra et al., 2015). Polin0.76+0.15-0.2-D was compared to SN 2018byg (De et al., 2019) and well-reproduced the observations. We urge the reader to refer to the original references for further details. The original names and parameters of these models are listed in Table 4.2.

4.4.1. Light Curves. Since the detonation of a He shell is usually not symmetric, the viewing angle of the observer could have a significant influence on the observed light curves (Kromer et al., 2010; Sim et al., 2012; Gronow et al., 2020; Shen et al., 2021). The effect of viewing angle gets stronger for bluer bands and lower-mass progenitors (Shen et al., 2021); for this reason we focus on comparisons in the i/I band, which is less affected. In the top left panel of Figure 4.7, we compare the i-band light curve of SN 2016dsg with i/I-band light curves of models and other transients. We also show the r/R-band and g-band comparison in the top right panel of Figure 4.7 for the reference.

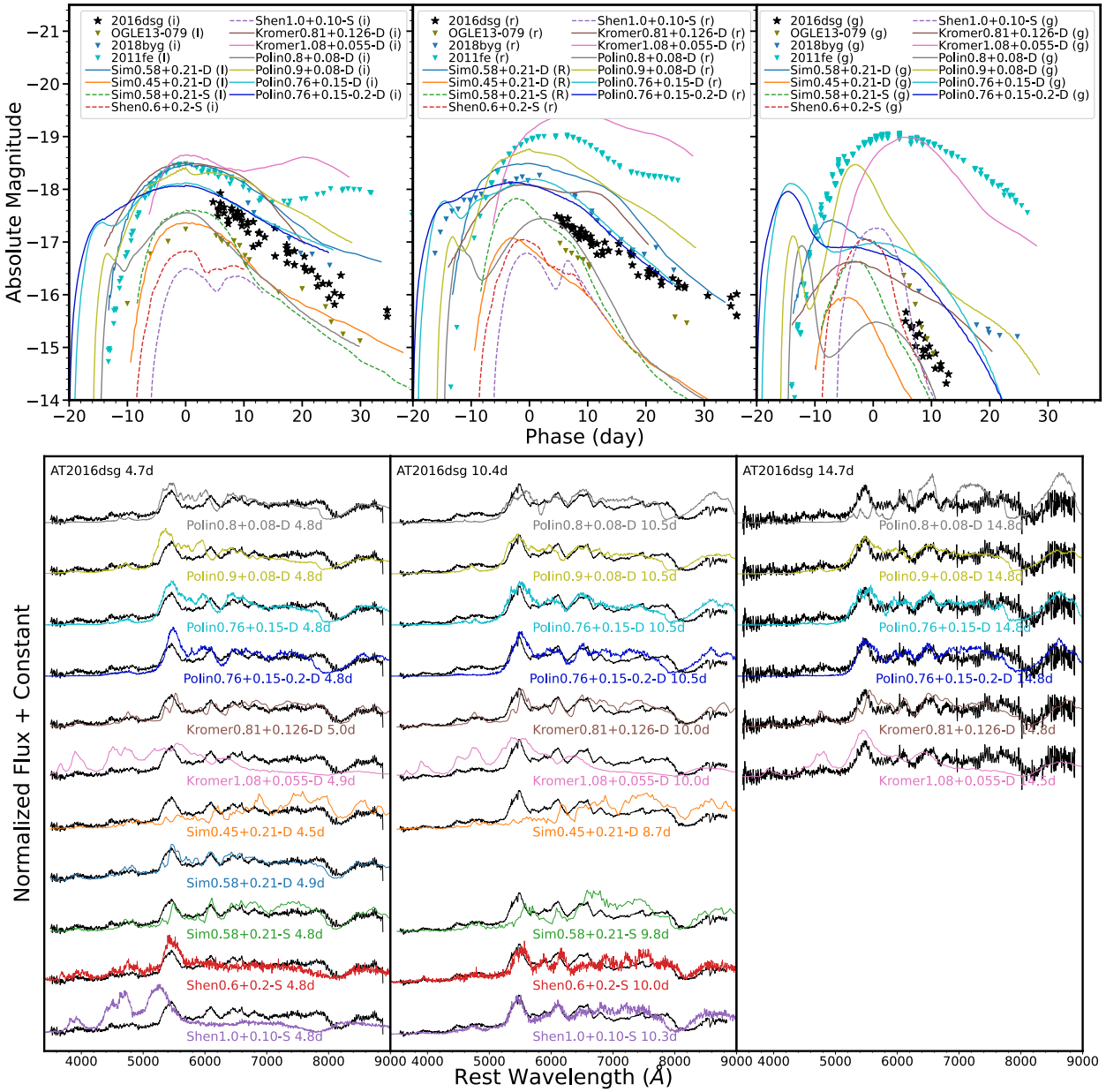

Figure 4.7 Top: light curve comparison between SN 2016dsg, other transients and models. The single detonation models and double detonation models are plotted with dashed lines and solid lines, respectively. The phase is measured from the i/I-band maximum. Bottom: Spectroscopic comparison between SN 2016dsg and single/double detonation models. All the spectra have been normalized in the range 4000-8500Å.

All the single detonation model light curves in the plot (Sim0.58+0.21-S, Shen0.6+0.2-S and Shen1.0+0.10-S) are slightly fainter than the observed light curves of SN 2016dsg. For

the i/I band, Polin0.76+0.15-D and Polin0.76+0.15-0.2-D roughly reproduce the brightness and the slope of the light curve. Sim0.45+0.21-D and Polin0.8+0.08-D underestimate the brightness of the light curve, while Polin0.9+0.08-D, Kromer0.81+0.126-D, Kromer1.08+0.055-D and Sim0.58+0.21-D overestimate the brightness. For the r/R band, Kromer0.81+0.126-D, Kromer1.08+0.055-D, Sim0.58+0.21-D, Polin0.9+0.08-D, Polin0.76+0.15-D and Polin0.76+0.15-0.2-D overestimate the brightness but reproduce the slope of SN 2016dsg. The rest of the models fail to reproduce both the brightness and the slope of the observed light curve.

In general, none of these models match the observed light curves well. However, the shape of the light curves is influenced by many factors, such as the mass of WD core and He shell (Shen et al., 2010; Kromer et al., 2010; Sim et al., 2012; Polin et al., 2019), the mixing degree of the outer layers (Polin et al., 2019; Gronow et al., 2020) and the viewing angle (Kromer et al., 2010; Sim et al., 2012; Gronow et al., 2020; Shen et al., 2021). In addition, the models we are comparing to are all from Local-Thermodynamic-Equilibrium (LTE) simulations or simplified non-LTE simulations, an assumption that is not suitable at very late time when the ejecta are optically thin. In order to nicely reproduce the whole light curves, a non-LTE simulation and a fine tuning to the WD and He-shell masses and other parameters would be needed.

4.4.2. Spectra. We compare the spectra of SN 2016dsg with angle-averaged model spectra in the bottom panel of Figure 4.7. As we described in Section 4.3.2, the spectra of SN 2016dsg show very strong line-blanketing on the blue side, which is reproduced by most of the models except for Kromer1.08+0.055-D. The Polin0.9+0.08-D, Polin0.76+0.15-D and Polin0.76+0.15-0.2-D models roughly fit the spectra of SN 2016dsg, while the Polin0.8+0.08-D model does not reproduce the spectral feature at day 14.7. All of Polin's models show higher calcium velocities than SN 2016dsg. Kromer0.81+0.126-D well reproduces the line strengths and velocities of SN 2016dsg. Kromer1.08+0.055-D shows low level absorption in the UV, which is likely because this model has a rather thin He shell (0.055 $M_\odot$) and the initial

detonation of the He shell does not produce enough iron-group elements to absorb photons in the UV. Sim0.45+0.21-D does not reproduce features around 5000-7000 Å. Sim0.58+0.21-D and Sim0.58+0.21-S are consistent with the observations at day 4.7, but Sim0.58+0.21-S slightly overpredicts the flux at around 6500-7500 Å. Shen0.6+0.2-S is able to reproduce most of the line features at day 4.7 and day 10.4, but is overall too blue relative to SN 2016dsg at day 4.7. Shen1.0+0.10-S shows low level absorption below ∼5000 Å at ∼day 4.8, while it well reproduces the observational spectra at day 10.3. Despite some small discrepancies, most of the models generally reproduce the main features of SN 2016dsg. This supports the idea that a He shell is likely to be involved for the progenitor of SN 2016dsg.

4.4.3. Progenitor Implications. The brightness of the object is roughly proportional to the total mass of the progenitor for double detonations or the He-shell mass of the progenitor for single detonations. However, there are some differences among the different models that we should take into account. For example, for a similar total mass, Sim's models are always brighter than others. This is likely due to the more complete burning in their models (Sim et al., 2012). In addition, Sim et al. (2012) assumed that the He shell is composed of pure He in their models. In reality, the He layer can be polluted by the WD core material (Piro, 2015), which would reduce the amount of radioactive material produced by He burning (Kromer et al., 2010; Waldman et al., 2011; Townsley et al., 2019; Gronow et al., 2020; Magee et al., 2021) and thus lead to a fainter transient at early times. Therefore, for a double detonation, Sim's models give the brightest event for a certain total progenitor mass. This can be used to constrain the lower limit of the progenitor's total mass in the double detonation scenario. The Sim0.45+0.21-D model is slightly fainter than SN 2016dsg in i/I band, so any double detonation models that have a total mass less than Sim0.45+0.21-D would be fainter than SN 2016dsg. As a result, we obtain a total mass lower limit of

$\sim$0.7$M_\odot$ for SN 2016dsg. On the other hand, SN 2016dsg is fainter than Polin0.9+0.08-D, Polin0.76+0.15-D, Polin0.76+0.15-0.2-D, Kromer0.81+0.126-D and Kromer1.08+0.055-D, implying that the total mass of the progenitor is no more than $\sim$0.9$M_\odot$. Similarly, for a single detonation, Sim's model will also be the brightest for a given He-shell mass. The Sim0.58+0.21-S model roughly matches the brightness of SN 2016dsg, so the He-shell mass of SN 2016dsg should be no less than $\sim$0.2$M_\odot$ for a single detonation.

The early time light curves of single/double detonations are powered by the radioactive material produced by the He-shell, so the early time photometric and spectroscopic data can be used to estimate the He-shell mass. In addition, the He-shell mass of the progenitor could also be roughly constrained by a spectral comparison with models. We found that when the He-shell mass is less than $\sim$0.1$M_\odot$ (Polin0.8+0.08-D , Kromer1.08+0.055-D and Shen1.0+0.10-S), the model cannot match the observed spectra well, suggesting that the He-shell mass of the progenitor should be larger than $\sim$0.1$M_\odot$ for either a double or a single detonation. However, we note that, without the early time photometric and spectroscopic data, the He-shell mass derived here is just a rough estimation.

It has been suggested that even a very low-mass He shell can detonate and then trigger the following WD detonation (Bildsten et al., 2007; Fink et al., 2010), inevitably leading to a double detonation, while Waldman et al. (2011) argued that the robustness of the second detonation in a double detonation scenario may need further investigations. Shen & Moore (2014) showed that a system with a low-mass CO WD or a O/Ne WD core is harder to be ignited by the initial He-shell detonation, so theoretically a single detonation can exist in nature. For SN 2016dsg, we are not able to distinguish between the single detonation scenario and the double detonation scenario, so both of them could be used to explain this object.

Due to the radioactive decay of elements synthesized in the He shell, the double detonation light curve may show an early red excess during the first few days (Noebauer et al., 2017;

Maeda et al., 2018; Polin et al., 2019). This phenomenon has been observed in SN 2016jhr (Jiang et al., 2017) and could be a unique signature for the double detonation scenario. Nevertheless, the lack of early photometric data prevents us from extracting more information from the photometry.

In conclusion, the comparison between models and observational data suggests that the progenitor of SN 2016dsg should have a total mass of 0.7-0.9 $M_\odot$ with a He-shell mass larger than 0.1 $M_\odot$ for a double detonation and a He-shell mass larger than 0.2 $M_\odot$ for a single detonation.

4.5. Discussion

4.5.1. Unburnt Helium? Recent simulations have revealed that unburnt helium exists in the outer ejecta of single detonations as well as double detonations (Fink et al., 2010; Shen et al., 2010; Kromer et al., 2010; Sim et al., 2012; Shen & Moore, 2014; Polin et al., 2019). By performing non-LTE simulations, Dessart & Hillier (2015) found that the spectral lines from unburnt He can be seen in the single detonation, with the most prominent one being the He I λ10830 line. In their model, He I λ10830 has a P-Cygni profile and is visible beyond 5 days after the explosion. However, the light curves produced by their model do not fit those of SN 2016dsg. Their I-band model light curve peaks at -16.1 mag, almost 2 mag fainter than our object. The observational signature of unburnt helium for double detonations has been explored by Boyle et al. (2017) using the Monte Carlo radiative transfer code TARDIS (Kerzendorf & Sim, 2014). They predict that a high velocity He I λ10830 line can be detected around maximum light in double detonations. In their work, they used Kromer et al. (2010)'s model 3 (referred to as Kromer1.08+0.055-D in this paper) as their high mass model and Sim et al. (2012)'s CSDD-S (referred to as Sim0.58+0.21-D in this paper) as their low mass model, and the high velocity He I λ10830 line appears much stronger in Sim0.58+0.21-D than in Kromer1.08+0.055-D.

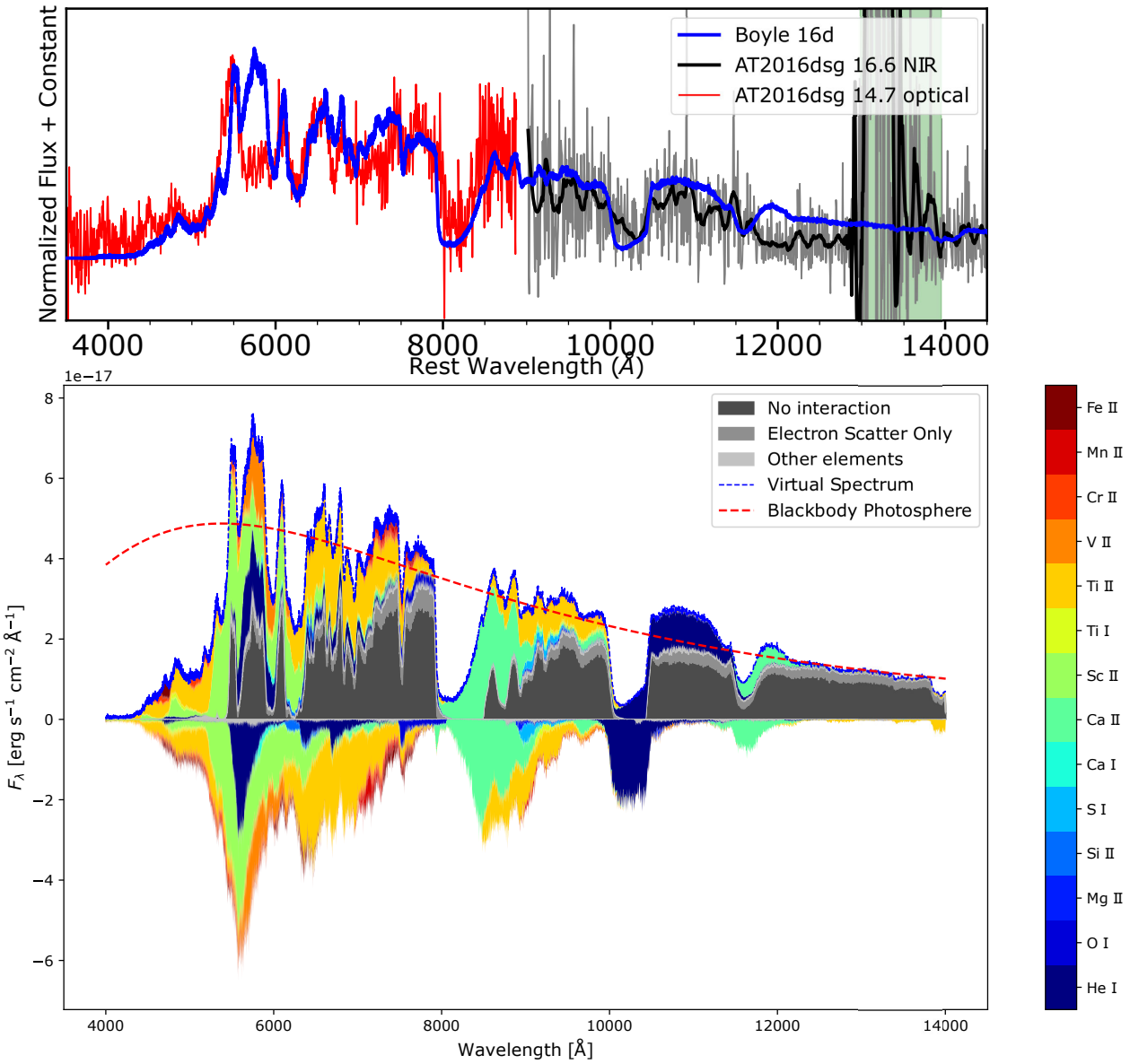

Figure 4.8 Top: Comparison of the optical-NIR spectrum of SN 2016dsg to the low mass double detonation model from Boyle et al. (2017). The green band marks the strongest telluric absorptions. Bottom: The SDEC plot produced by TARDIS. Different colors are used to illustrate the contributions from different elements. Absorption is represented by negative values. "Interaction" in this context refers to radiation-matter interaction above the blackbody photosphere; "no interaction" means that photons escape freely.

As discussed in Section 4.4, Sim0.58+0.21-D at day 4.7 can reproduce the optical spectra of SN 2016dsg well. In order to examine whether a strong high velocity He I feature is present

in SN 2016dsg, we generated a new model spectrum at 16 days after the i-band peak based on the model setup described in Boyle et al. (2017) with their low mass model (Sim0.58+0.21-D). Following Boyle et al. (2017), the inner velocity boundary in TARDIS is set to be 6250 km s^{-1}. A comparison between this model spectrum and the observed spectrum is shown in the top panel of Figure 4.8. As a sanity check, we also overplotted the optical spectrum at day 14.7. In the bottom panel of Figure 4.8, we show a Spectral element DEComposition (SDEC) plot of the TARDIS model. In the SDEC plot, the contributions of different elements in the synthetic model spectrum are illustrated by different colors. Negative values correspond to absorption contributions to the spectrum, while positive values indicate emission. The absorption line we see at around 9700-10500 Å in SN 2016dsg resembles the strong He I line in the model, implying that there is likely unburnt He present in the ejecta. This is consistent with our previous conclusion that SN 2016dsg could originate from a double detonation.

Boyle et al. (2017) pointed out that the He I λ10830 line can be used to distinguish between double detonations and single detonations. In double detonations, the unburnt He all resides in the outer ejecta and is only at high velocities, while in single detonations, the unburnt He is distributed at all velocities. Therefore, the emission part of the He I λ10830 line is shallower and broader in double detonations than in single detonations. However, due to the lack of a comparable single detonation model and the low signal-to-noise ratio of the observed spectrum, we are not able to use the NIR spectrum to distinguish between the single detonation scenario and the double detonation scenario.

4.5.2. Connections to Other Single/Double Detonation Candidates? OGLE-2013-SN-079 and SN 2018byg are thought to originate from single/double detonations with thick He shells (Inserra et al., 2015; De et al., 2019), and there are indeed many similarities between these two objects and SN 2016dsg. The spectrum of OGLE-2013-SN-079 is remarkably similar to the spectrum of SN 2016dsg (see Figure 4.9), implying that these two objects have very similar progenitors. SN 2018byg developed strong emission lines below

5000 Å after at least day 27, which is not observed in the spectra of SN 2016dsg or OGLE-2013-SN-079. This discrepancy could be solved by taking the viewing angle and the He-shell mass of the progenitor into account. Many authors have shown that the viewing angle has a significant impact on the spectra of double detonations (Kromer et al., 2010; Sim et al., 2012; Gronow et al., 2020; Shen et al., 2021). Specifically, the spectrum will be redder if one observes from the direction of the He-shell ignition point, where the He-shell burning is more efficient and thus produces more iron-group elements. It is possible that SN 2016dsg and OGLE-2013-SN-079 were observed closer to the ignition point than SN 2018byg, resulting in the higher level absorption below 5000 Å. In addition, a larger mass He shell is able to produce more iron-group elements, blocking the emission in the UV. Therefore, it is also possible that SN 2016dsg and OGLE-2013-SN-079 have more surface He than SN 2018byg does. On the other hand, SN 2018byg had higher expansion velocities than SN 2016dsg. If SN 2018byg were a double detonation, the He-shell ashes would likely become optically thin earlier than SN 2016dsg, and could develop emissions at relatively earlier phases.

Due to the similarities between SN 2016dsg and OGLE-2013-SN-079, it is natural to expect that these two objects also have similar photometric evolution. In Figure 4.3, SN 2016dsg's phase is shown with respect to the epoch of discovery, and it approximately matches the evolution of OGLE-2013-SN-079. If the maximum epoch is much earlier than the discovery date, SN 2016dsg would be much brighter than OGLE-2013-SN-079. Therefore, the epoch of discovery of SN 2016dsg is likely close to the true epoch of maximum light.

The origin of SN 2016hnk is still debated. Jacobson-Galán et al. (2020) proposed that SN 2016hnk is from a double detonation with a relatively thin He shell (0.02 $M_\odot$), while Galbany et al. (2019) found that this object is consistent with a near Chandrasekhar-mass CO WD explosion. Comparing the spectra, SN 2016hnk has a much stronger O I λ7773 absorption line than SN 2016dsg, OGLE-2013-SN-079 and SN 2018byg. The weak O I line is

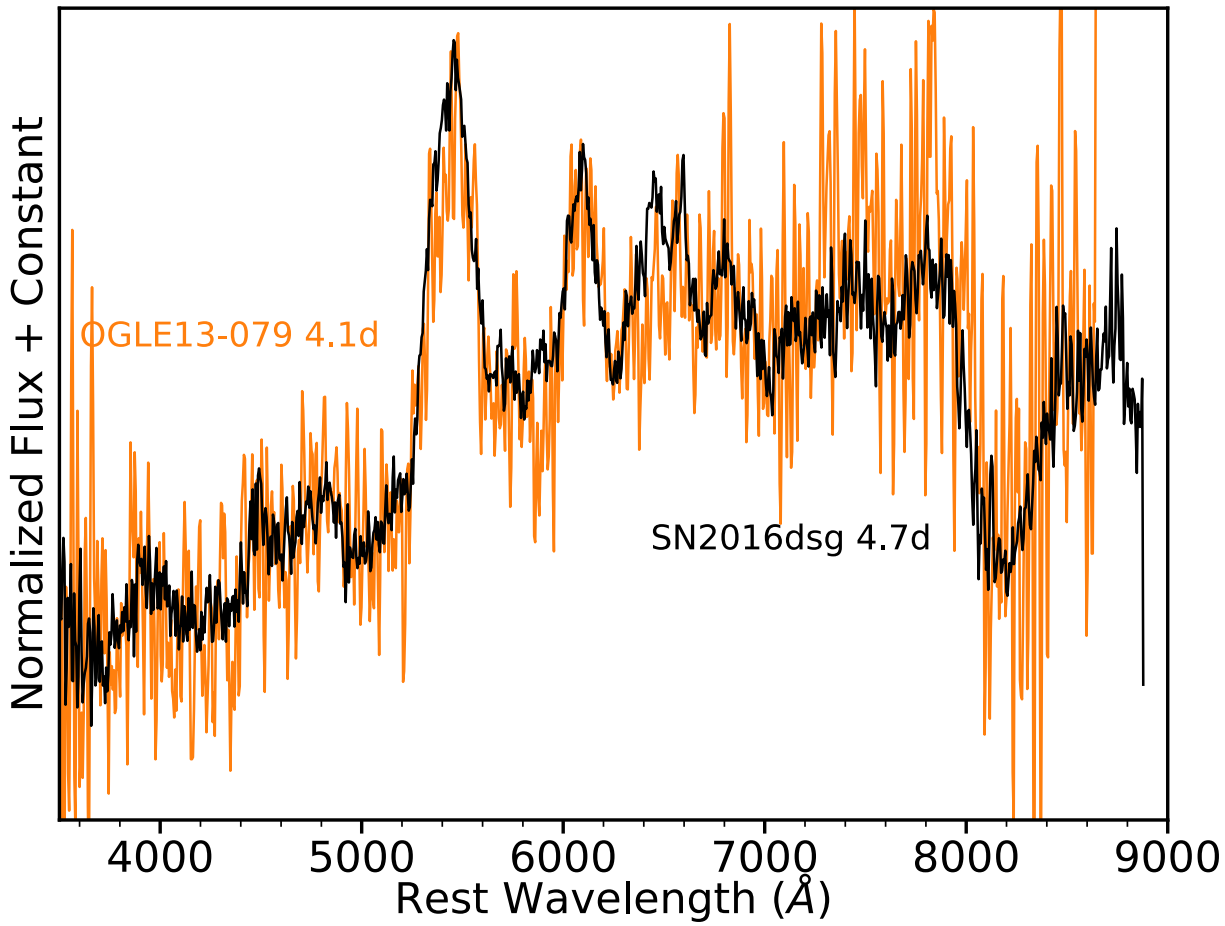

Figure 4.9 The spectrum of SN 2016dsg compared to OGLE-2013-SN-079. These two objects have similar spectroscopic features, suggesting that they have similar progenitors.

an indication of a lack of oxygen in the outer ejecta and could be a natural result of a single or double detonation with a thick He shell. For a single detonation, only a negligible amount of oxygen is produced (Shen et al., 2010; Waldman et al., 2011; Sim et al., 2012; Dessart & Hillier, 2015), so the ejecta have little oxygen. For a double detonation, the outermost ejecta are the ash of He-shell burning products and the unburnt oxygen from the core is confined underneath with a narrow velocity range (Kromer et al., 2010; Sim et al., 2012; Hoeflich, 2017; Polin et al., 2019). If the He shell is massive enough, the unburnt oxygen would reside in a deep layer of the ejecta and thus may not produce an obvious spectroscopic

Table 4.3. Summary of host galaxy properties

Object	Host	Host type	projection distance from the host
SN 2016dsg	ESO254-G019/WISEA J060707.31-451108.4	S0(r)	15.4/18.5kpc
SN 2018byg	-	elliptical	21.9kpc
OGLE-013-SN-079	2MASXJ00350521-6741147	elliptical	40-50kpc

Note. — Host galaxy properties of SN 2016dsg and other two spectroscopically similar transients.

feature at early phases. Therefore, the strong O I line in SN 2016hnk may imply that either SN 2016hnk is not from a double detonation, or that it is from a double detonation with a very low-mass He shell. If SN 2016hnk is from a double detonation, the diversity observed between SN 2016hnk and the other three objects could be achieved by varying the thickness of the He shell.

Compared to other sub-luminous SNe Ia, Ca-strong transients develop strong [Ca II] lines shortly after the peak. One promising model for Ca-strong transients is the single detonation (Perets et al., 2010; Waldman et al., 2011; Dessart & Hillier, 2015; Shen et al., 2019). In addition, Polin et al. (2021) found that double detonations, analogous to Ca-strong transients, are also expected to show strong [Ca II] emission at the nebular phase. A large proportion of Ca-strong transients have large offsets from their host galaxies (Perets et al., 2010; Kasliwal et al., 2012; Valenti et al., 2014c; De et al., 2020), which is similar to the other three promising single/double detonation candidates (see Table 4.3). This may suggest that there is a connection between the progenitors of Ca-strong transients and SN 2016dsg.

4.5.3. Remote Location. SN 2016dsg shares many similarities with OGLE-2013-SN-079 and SN 2018byg. Interestingly, they are all in the outskirts of their host galaxies, suggesting an origin in old stellar populations. Large host galaxy offsets have also been observed in many Ca-strong transients, and have been treated as evidence that the progenitors of Ca-strong transients could have travelled a long distance before exploding (Lyman et al., 2014, 2016). Although a sample of three SNe precludes any robust statistical analysis, the

offsets of these objects are very typical of Ca-strong transients' offsets (∼10-100kpc) (De et al., 2020). Foley (2015) proposed that the progenitors of Ca-strong transients are double WD systems that are ejected from the hosts through the interactions with supermassive black holes. Shen et al. (2019) found that the projected galactocentric radial distribution of Ca-strong transients is consistent with that of globular clusters. Therefore, they suggested that the progenitors of Ca-strong transients are formed inside globular clusters and ejected prior to mass transfer contact. The remote location of SN 2016dsg may also be explained by the mechanisms mentioned above.

Two hot subdwarf B binaries with white dwarf companions have been suggested as possible progenitors of double/single detonations (Geier et al., 2013; Kupfer et al., 2022). These systems are found in young populations, which is inconsistent with the fact that the three thick He-shell double/single detonation candidates are found in old populations. If sdB+WD binaries are the progenitors of these double/single detonations, they must have traveled a long way before detonating. However, the sample of double/single detonations and their possible sdB binary progenitors is still small, preventing further investigations at this point.

4.6. Conclusions

We have presented spectroscopic and photometric observations of SN 2016dsg, a sub-luminous peculiar SN I consistent with many of the hallmarks of the single/double detonation explosion mechanism, particularly those models with a thick He shell. Spectroscopic observations below ∼5000 Å show significant line blanketing, indicative of a large amount of iron-group elements in the outer ejecta. Compared to other sub-luminous SNe Ia, SN 2016dsg shows a rather weak O I λ7773 absorption, likely due to a low oxygen abundance in the ejecta. In addition, a absorption line around 9700-10500 Å is detected in the NIR spectrum. We argue this absorption line is from the unburnt He present in the outer ejecta. All of these unique observational features suggest that SN 2016dsg came from a single/double detonation.

We have compared SN 2016dsg with many single/double detonation models and found that the spectroscopic properties of SN 2016dsg can be reproduced well by these models. In order to fit the strong line blanketing below ∼5000 Å, a thick He shell has to be involved. For a double detonation scenario, the progenitor should have a total mass of around 0.7-0.9 $M_\odot$ with a He-shell mass of $\gtrsim$ 0.1 $M_\odot$. For a single detonation scenario, the mass of the He shell should be no less than 0.1 $M_\odot$, and the WD core is very likely to be a low-mass CO WD or an O/Ne WD.

To date, only a handful of candidate single/double detonation of WDs with thick He shells have been discovered, implying that they may be intrinsically rare in nature. The preference of these objects for remote locations is still a mystery and may give us a clue about the origin of their progenitors. The diversity of these transients in the existing sample could be explained by the variety of He-shell masses, WD-core masses, viewing angles, and the degree of mixing in the outer layers, which, however, is to be confirmed by more observational evidence. With the help of upcoming large sky surveys, we can expect that a statistical study of large samples of these types of transients will soon be in reach, which will help us further understand the nature of these peculiar transients.

Acknowledgements

Based on observations collected at the European Organisation for Astronomical Research in the Southern Hemisphere under ESO programme 1103.D-0328. This research made use of TARDIS, a community-developed software package for spectral synthesis in supernovae (Kerzendorf & Sim, 2014; Kerzendorf et al., 2022). The development of TARDIS received support from GitHub, the Google Summer of Code initiative, and from ESA's Summer of Code in Space program. TARDIS is a fiscally sponsored project of NumFOCUS. TARDIS makes extensive use of Astropy and Pyne. This work made use of the Heidelberg Supernova Model Archive (HESMA), https://hesma.h-its.org. This research has made use of the

NASA/IPAC Extragalactic Database (NED), which is operated by the Jet Propulsion Laboratory, California Institute of Technology, under contract with the National Aeronautics and Space Administration.

Research by Y.D., and S.V., and N.M.R is supported by NSF grants AST–1813176 and AST-2008108. Time domain research by D.J.S. is also supported by NSF grants AST-1821987, 1813466, 1908972, & 2108032, and by the Heising-Simons Foundation under grant #2020-1864. The SALT observations presented here were taken as part of Rutgers University program 2015-1-MLT-002 (PI: Jha). This work makes use of observations from the Las Cumbres Observatory network. The Las Cumbres Observatory team is supported by NSF grants AST-1911225 and AST-1911151, and NASA Swift grant 80NSSC19K1639. L.W. and M.G. acknowledge the Polish National Science Centre (NCN) grants Harmonia No. 2018/30/M/ST9/00311 and Daina No. 2017/27/L/ST9/03221 as well as the European Union's Horizon 2020 research and innovation programme under grant agreement No 101004719 (OPTICON-RadioNet Pilot, ORP) and MNiSW grant DIR/WK/2018/12. MG is supported by the EU Horizon 2020 research and innovation programme under grant agreement No 101004719. L.G. acknowledges financial support from the Spanish Ministerio de Ciencia e Innovación (MCIN), the Agencia Estatal de Investigación (AEI) 10.13039/501100011033, and the European Social Fund (ESF) "Investing in your future" under the 2019 Ramón y Cajal program RYC2019-027683-I and the PID2020-115253GA-I00 HOSTFLOWS project, from Centro Superior de Investigaciones Científicas (CSIC) under the PIE project 20215AT016, and the program Unidad de Excelencia María de Maeztu CEX2020-001058-M. JDL acknowledges support from a UK Research and Innovation Fellowship (MR/T020784/1). This work was supported by the 'Programme National de Physique Stellaire' (PNPS) of CNRS/INSU co-funded by CEA and CNES. This research was supported by the Excellence Cluster ORIGINS which is funded by the Deutsche Forschungsgemeinschaft (DFG, German Research Foundation) under Germany's Excellence Strategy EXC-2094-390783311. S.B. acknowledges

support from the ESO Scientific Visitor Programme in Garching. KM is funded by the EU H2020 ERC grant no. 758638.

CHAPTER 5

SN 2022crv: IIb, Or Not IIb: That is the Question

Dong et al. 2024 (resubmitted following the first round of revisions), submitted to ApJ. arXiv, arXiv:2309.09433.

5.1. Abstract

We present optical and near-infrared observations of SN 2022crv, a stripped-envelope supernova in NGC 3054, discovered within 12 hr of explosion by the Distance Less Than 40 Mpc Survey. We suggest that SN 2022crv is a transitional object on the continuum between SNe Ib and SNe IIb. A high-velocity hydrogen feature ($\sim -20,000$ to $-16,000$ km s^{-1}) was conspicuous in SN 2022crv at early phases, and then quickly disappeared. We find that a hydrogen envelope of $\sim 10^{-3}$ M$_\odot$ can reproduce the observed behavior of the hydrogen feature. The lack of early envelope cooling emission implies that SN 2022crv had a compact progenitor with an extremely low amount of hydrogen. A nebular spectral analysis shows that SN 2022crv is consistent with the explosion of a He star with a final mass of $\sim$ 4.5–5.6 M$_\odot$ that evolved from a $\sim$ 16–22 M$_\odot$ zero-age main-sequence star in a binary system with $\sim$ 1.0–1.7 M$_\odot$ of oxygen finally synthesized in the core. In order to retain such a small amount of hydrogen, the initial orbital separation of the binary system is likely larger than $\sim$ 1000 R$_\odot$. The near-infrared spectra of SN 2022crv show a unique absorption feature on the blue side of the He I line at $\sim$ 1.005 μm. This is the first time such a feature has been observed in an SN Ib/IIb, and it could be due to Sr II. Further detailed modeling of SN 2022crv can shed light on the progenitor and the origin of the mysterious absorption feature in the near-infrared.

5.2. Introduction

Stripped-envelope supernovae (SESNe) are a subclass of core-collapse supernovae (CC-SNe) that have partly or completely lost their progenitor envelope prior to their explosions (see Modjaz et al. 2019 for a recent review). SESNe are spectroscopically classified as SNe IIb, SNe Ib, and SNe Ic (Harkness et al., 1987; Wheeler & Harkness, 1990; Filippenko, 1997; Clocchiatti & Wheeler, 1997) depending on the presence or absence of H and He lines in the optical spectra. SNe Ib show strong He lines but not H lines, while SNe Ic exhibit neither H nor He lines. SNe IIb, first identified by Filippenko (1988), show clear H lines at early phases which become weaker over time, and the spectra are similar to those of SNe Ib at late phases. The sequence of SESNe (IIb→Ib→Ic) is commonly believed to result from progenitors experiencing varying extents of envelope stripping (e.g., Filippenko, 1997; Yoon, 2015; Gal-Yam, 2017; Hiramatsu et al., 2021).

These hydrogen-deficient SN progenitors have been suggested to either arise from massive and metal-rich stars undergoing mass loss via stellar winds (Woosley et al., 1993, 1995, 2002; Eldridge & Tout, 2004; Meynet & Maeder, 2005; Yoon, 2017) or from binary interactions (Podsiadlowski et al., 1992; Woosley et al., 1995; Wellstein & Langer, 1999; Eldridge & Tout, 2004; Fryer et al., 2007; Yoon et al., 2010; Eldridge et al., 2013; Yoon et al., 2010, 2017; Götberg et al., 2018). Owing to the high observed fraction of SESNe (Smith et al., 2011; Shivvers et al., 2019), relatively weak stellar winds derived from the X-ray and radio observations (e.g., Drout et al., 2016), and the small population of very massive stars assuming a Salpeter initial mass function (Salpeter, 1955), most SESN progenitors likely result from lower-mass stars in binary systems. This has been supported by direct imaging of progenitors (Aldering et al., 1994; Maund et al., 2004, 2011; Van Dyk et al., 2011; Eldridge et al., 2013; Fremling et al., 2014; Van Dyk et al., 2014; Eldridge et al., 2015; Folatelli et al., 2016;

Kilpatrick et al., 2017; Tartaglia et al., 2017; Kilpatrick et al., 2021), X-ray/radio observations (e.g., Wellons et al., 2012; Drout et al., 2016; Brethauer et al., 2022), and relatively low ejecta mass found from SESN light curves (Drout et al., 2011; Lyman et al., 2016).

With increasing numbers of well-observed SESNe for each subclass, many objects are becoming difficult to classify unambiguously because they are being discovered with overlapping properties. For instance, an absorption feature at around 6200 Å has been found in some SNe Ib and could be attributed to high-velocity Hα (Deng et al., 2000; Branch et al., 2002; Elmhamdi et al., 2006; Parrent et al., 2007; Stritzinger et al., 2009; James & Baron, 2010; Liu et al., 2016a; Holmbo et al., 2023), indicating that these objects may still contain a small amount of hydrogen. However, the 6200 Å features detected in these objects could also be due to Si II λ6355, C II λ6580, or Ne I λ6402 (Deng et al., 2000; Branch et al., 2002; Hamuy et al., 2002; Tanaka et al., 2009; Stritzinger et al., 2009; Dessart et al., 2011; Hachinger et al., 2012). Folatelli et al. (2014) identified a small sample of transitional Type Ib/c SNe that seem to shift from Type Ic to Type Ib over time (although see Liu et al. 2016a). These objects show initially weak helium features with nearly constant velocities during the photospheric phase, suggesting a dense shell in the ejecta. However, the weak hydrogen features seen in these objects technically result in a peculiar Type IIb classification (although see Liu et al. 2016a, where these objects are reclassified as Type Ib SNe). Milisavljevic et al. (2013) found that SESN 2011ei showed unambiguous hydrogen features at early times but these features quickly disappeared on a timescale of one week, suggesting the progenitor retained a thin hydrogen envelope at the time of explosion. Such a transformation is much faster than that observed in typical SNe IIb, which usually occurs on a timescale of months. This implies that some SNe IIb may be misclassified as Type Ib SNe if they are not caught early enough.

All these observations point toward a continuum between SNe IIb and SNe Ib, which is also supported by theoretical studies. For instance, Yoon et al. (2010) found that many

SN Ib/c progenitors formed in close binary systems are expected to maintain a thin hydrogen layer during their pre-SN stage, producing the high-velocity hydrogen features observed in SNe Ib. In a series of models with various amounts of hydrogen, Hachinger et al. (2012) found that if the hydrogen envelope mass at the time of core collapse is between about 0.025 and 0.033 $M_{\odot}$, the difference between Type Ib and Type IIb could be unclear.

Although observational evidence has suggested that there is likely a continuum in the amount of helium between SNe IIb and SNe Ib (Liu et al., 2016a; Fremling et al., 2018, but see Holmbo et al. 2023), whether SNe IIb and SNe Ib can be clearly differentiated observationally is still an open question. To better characterize the classification of different types of SESNe and thus understand their progenitors, Liu et al. (2016a) performed an analysis of a sample of SESNe. They proposed that the strength of Hα (or the absorption feature around 6200 Å) can be used to differentiate SNe Ib and SNe IIb at all epochs. Prentice & Mazzali (2017) reassessed the classification system of SESNe using the spectra of a sample of SESNe and found that there is a clear distinction between He-poor SNe (SNe Ic) and He-rich SNe (SNe Ib/IIb). They attributed the 6200 Å feature in SNe Ib to Hα and further suggested that the He-rich SNe can be split into subgroups based on the profile of the Hα line. To fully utilize spectra taken of SESNe, Williamson et al. (2019) proposed a new classification technique based on a support vector machine (SVM). This technique can identify transitional SESNe —that is, SNe that present spectral features resembling more than one SESN subtype— and thus reflects the physical properties of their progenitors. These sample studies imply a gradual transition between SNe Ib and SNe IIb depending on the amount of hydrogen remaining in the progenitor envelope.

To better understand the connections between the different SESN types and the evolution of their progenitors, a sample of SESNe that retain a small amount of hydrogen envelope is required. These objects need to be discovered shortly after the explosion since only the very early-time spectra convey signals from the outer layer of the progenitor star. In this paper,

Table 5.1. Basic properties of SN 2022crv

Host galaxy	NGC 3054
RA (J2000)	$09^h54^m25^s91$
DEC (2000)	$-25°42'11\farcs16$
Distance	$31.6^{+6.4}_{-5.3}$ Mpc
Distance modulus	32.5 ± 0.4 mag
Redshift z	0.008091±0.000023
$E(B-V)_{\rm MW}$	$0.0642^{+0.007}_{-0.007}$ mag*
$E(B-V)_{\rm host}$	$0.146^{+0.009}_{-0.009}$ mag
Explosion epoch (JD)	$2,459,627.19 \pm 0.30$ (2022-02-16)
$V_{\rm max}$ (JD)	2,459,645.42 ±0.30 (2022-03-06)

*Schlafly & Finkbeiner (2011a).

we present optical and infrared data for SN 2022crv, a SESN discovered within $\sim$ 12 hr of explosion by the Distance Less Than 40 Mpc (DLT40; Tartaglia et al., 2018) survey and densely monitored for over one year. As we show in this work, a hydrogen feature is detected in SN 2022crv at early phases, which then quickly disappears shortly after maximum brightness. Detailed analyses suggest that there is very little hydrogen in the SN envelope, making the object a transitional object on the continuum between SNe Ib and SNe IIb.

This paper is organized as follows. The observations of SN 2022crv are presented in Section 5.3, while the observational properties, such as the reddening, distance, and explosion epoch are constrained in Section 5.4. We describe the photometric and spectroscopic properties of SN 2022crv in Section 5.5 and 5.6, respectively. The physical implications of the observations are discussed in Section 5.7, and we conclude in Section 5.8.

5.3. Observations

SN 2022crv/DLT22d was discovered at RA(J2000) = $09^h54^m25^s91$, Dec(J2000) = $-25°42'11\farcs16$ in the nearby barred spiral (SBc) galaxy NGC 3054 (see Figure 5.1) on 2022-02-17.20 (UTC

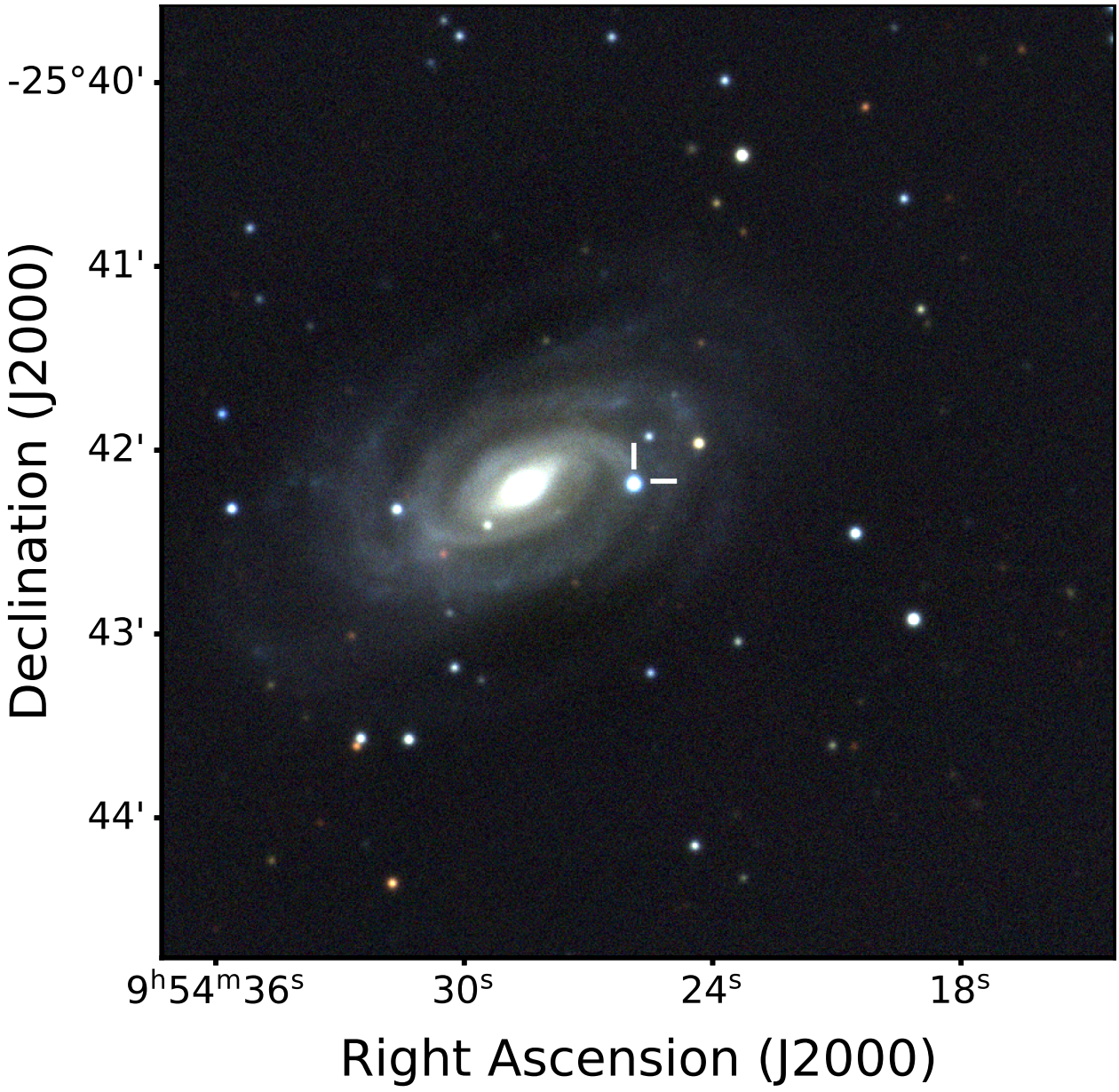

Figure 5.1 Composite *gri* image of SN 2022crv in NGC 3054 obtained with the Las Cumbres Observatory on 2022 March 04. The position of SN 2022crv is indicated by white tick marks.

dates are used throughout this paper; Dong et al. 2022, JD 2,459,627.70, $r = 18.04$ mag), during the course of the DLT40 SN search (Tartaglia et al., 2018), utilizing the 0.4 m PROMPT-MO-1 telescope (Reichart et al., 2005) at the Meckering Observatory. An earlier detection was recovered in the *o*-band imaging taken by the Asteroid Terrestrial-Impact Last Alert

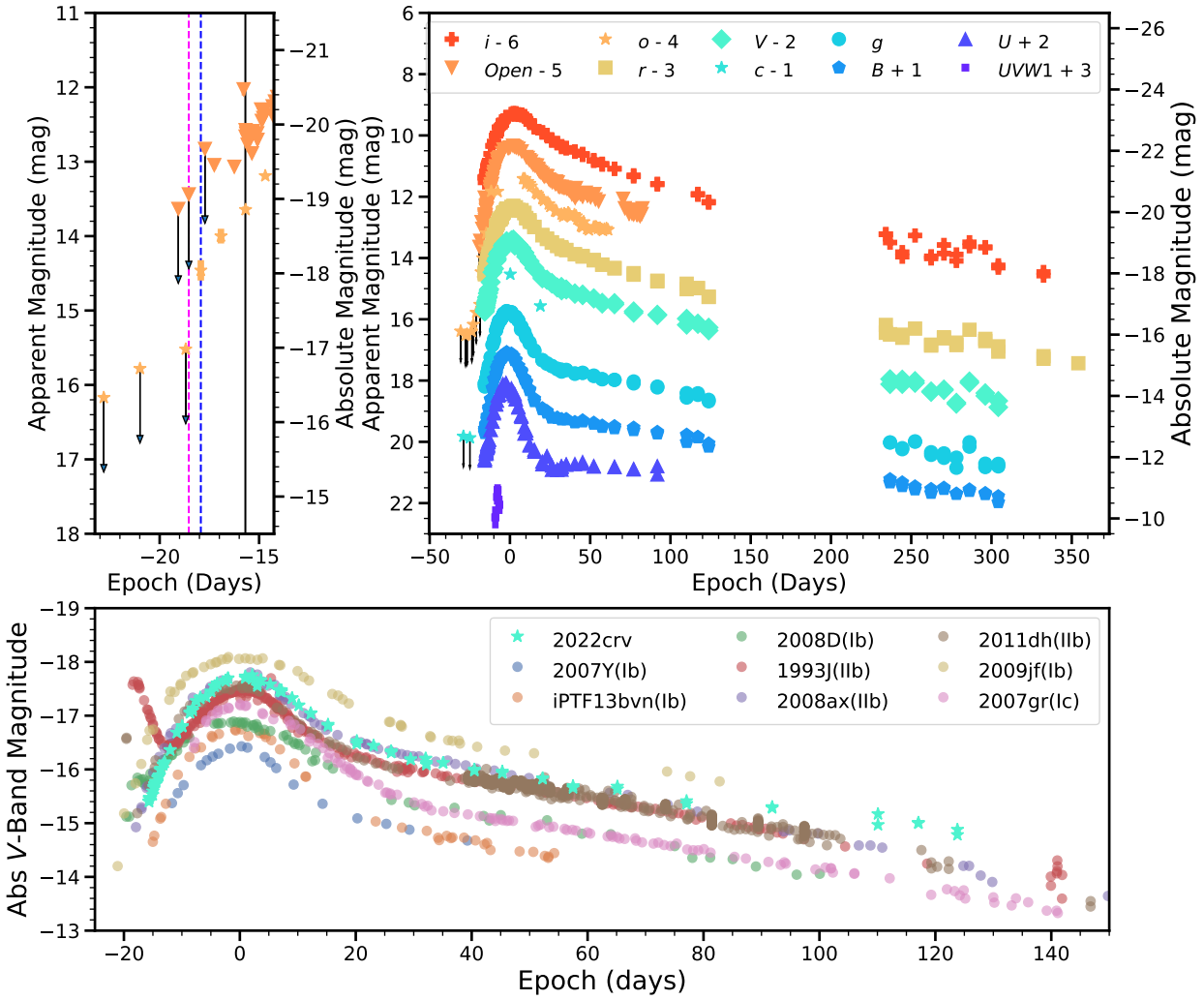

Figure 5.2 *Upper right:* Multiband light curves of SN 2022crv with respect to the time of V-band maximum brightness (JD 2,459,645.42). Marker size is larger than the uncertainties. The DLT40 *Open* filter light curve is calibrated to the r band. *Upper left:* A zoom around a few days before and after the discovery. Only the *Open*- and o-band light curves are plotted here to show the constraint on the explosion epoch. The last nondetection and the earliest detection are marked by the magenta vertical dashed line and blue vertical dashed line, respectively. The black vertical line marks when the multiband follow-up observations began. *Bottom:* The absolute V-band light curve of SN 2022crv compared with that of other SESNe. The data used to create this figure are available.

System (ATLAS; Tonry 2011; Tonry et al. 2018; Smith et al. 2020b) on 2022-02-16.99. The object was initially classified as a Type Ib SN using a spectrum taken with the Gemini Multi-Object Spectrograph (GMOS; Hook et al., 2004; Gimeno et al., 2016) on Gemini North on

Table 5.2. Spectroscopic observations of SN 2022crv.

Phase (days)*	MJD	Telescope	Instrument	Range (Å)
-15.5/2.7	59629.43	Gemini-N	GMOS	3760-7030
-15.5/2.8	59629.46	KeckII	NIRES	9650-24660
-15.3/2.9	59629.61	FTS	FLOYDS	4850-10170
-15.1/3.1	59629.82	SALT	RSS	3930-7790
-13.4/4.8	59631.49	FTN	FLOYDS	3510-9990
-11.5/6.7	59633.39	FTN	FLOYDS	3510-9990
-10.7/7.5	59634.23	SOAR	Goodman	3780-5460
-10.5/7.8	59634.46	FTN	FLOYDS	3500-9990
-7.6/10.6	59637.34	FTN	FLOYDS	3510-10000
-6.6/11.6	59638.32	LBT	MODS	3400-10100
-6.5/11.8	59638.46	FTN	FLOYDS	3510-9990
-3.5/14.7	59641.43	FTS	FLOYDS	3510-9990
-0.6/17.7	59644.35	FTN	FLOYDS	3500-9990
2.3/20.5	59647.22	Bok	B&C	4010-7490
2.7/21.0	59647.65	FTS	FLOYDS	3500-9990
3.4/21.6	59648.29	LBT	MODS	3610-10290
4.4/22.6	59649.28	FTN	FLOYDS	3500-9990
4.4/22.6	59649.32	UH88	SNIFS	3410-9090
6.2/24.4	59651.07	Baade	FIRE	7910-25250
6.4/24.6	59651.34	FTN	FLOYDS	3500-9990

2022-02-19.42 (Andrews et al., 2022). The basic properties of SN 2022crv are summarized in Table 5.1.

Table 5.2 (cont'd)

Phase (days)*	MJD	Telescope	Instrument	Range (Å)
6.6/24.8	59651.50	Baade	IMACS	4230-9410
7.4/25.7	59652.34	KeckII	NIRES	9650-24660
8.3/26.6	59653.27	KeckII	NIRES	9660-24670
10.4/28.6	59655.30	FTN	FLOYDS	3500-10000
12.1/30.3	59657.00	MMT	MMIRS	9500-24290
12.4/30.6	59657.32	UH88	SNIFS	3410-9090
15.6/33.8	59660.50	Baade	IMACS	4230-9410
15.7/33.9	59660.60	FTS	FLOYDS	3510-9500
17.3/35.6	59662.25	Shane	Kast	3620-10750
18.3/36.5	59663.19	LBT	MODS	3400-9990
19.2/37.5	59664.17	MMT	Binospec	5240-6750
19.3/37.6	59664.25	UH88	SNIFS	3410-9090
24.0/42.2	59668.90	NOT	ALFOSC	3410-9660
24.6/42.8	59669.50	Baade	IMACS	4230-9410
25.3/43.5	59670.21	Shane	Kast	3630-10740
28.6/46.9	59673.57	FTS	FLOYDS	3510-9990
35.4/53.6	59680.28	FTN	FLOYDS	3500-9990
35.4/53.6	59680.29	UH88	SNIFS	3410-9090
36.6/54.8	59681.50	Baade	IMACS	4230-9410
44.6/62.9	59689.54	FTS	FLOYDS	3500-10000

Table 5.2 (cont'd)

Phase (days)⋆	MJD	Telescope	Instrument	Range (Å)
48.4/66.6	59693.29	UH88	SNIFS	3410-9090
50.3/68.6	59695.24	KeckI	LRIS	3150-5640
50.3/68.6	59695.24	KeckI	LRIS	5420-10300
50.3/68.6	59695.25	KeckI	LRIS	5490-7140
54.9/73.2	59699.86	SALT	RSS	3930-7790
56.5/74.7	59701.42	FTS	FLOYDS	3500-10000
58.2/76.5	59703.15	LBT	MODS	3720-10000
64.4/82.6	59709.29	KeckII	NIRES	9660-24670
69.3/87.6	59714.25	KeckII	NIRES	9650-24670
70.3/88.6	59715.25	KeckII	NIRES	9660-24670
71.5/89.7	59716.43	FTS	FLOYDS	3500-9990
99.5/117.7	59744.41	FTS	FLOYDS	4010-10000
102.8/121.0	59747.73	SALT	RSS	3930-7790
267.4/285.6	59912.29	SOAR	Goodman	3500-7130
272.3/290.6	59917.27	SOAR	Goodman	5000-9000
321.0/339.2	59965.90	SALT	RSS	5480-8990
353.2/371.4	59998.14	Clay	LDSS3	4000-10000
355.1/373.3	60000.03	GTC	OSIRIS	4000-10000

⋆Phase is measured relative to the dates of $V_{\rm max}$/explosion.

After the discovery, the object was intensely followed by the DLT40 survey using the PROMPT5 and PROMPT-MO telescopes in the *Open* filter and the ATLAS survey in the *o* and *c* filters. In addition, high-cadence multiband photometric observations were collected by the world-wide network of robotic telescopes at Las Cumbres Observatory (Brown et al., 2013a) through the Global Supernova Project. Ultraviolet (UV) and optical imaging was taken with the *Neil Gehrels Swift Observatory* (Gehrels et al., 2004) at early times. The object was also followed by the 0.76 m Katzman Automatic Imaging Telescope (KAIT) as part of the Lick Observatory Supernova Search (LOSS; Filippenko et al., 2001), and the 1 m Nickel telescope at Lick Observatory. *B, V, R,* and *I* images of SN 2022crv were obtained with both telescopes, while additional *Clear*-band (close to the *R* band; see Li et al. 2003)

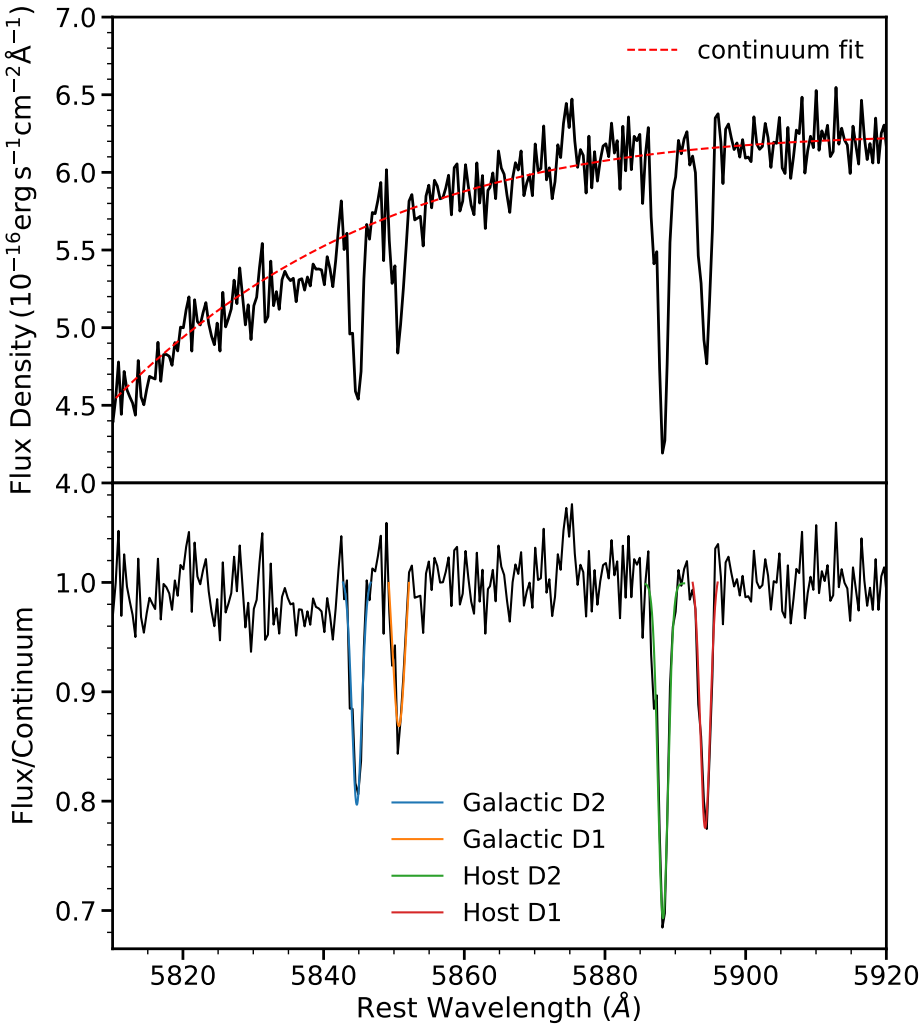

Figure 5.3 *Top:* A high-resolution spectrum taken with LRIS on 2022-04-26 (MJD 59695.25) showing the Na I D lines from the host galaxy and the Milky Way. The continuum is fit with a fourth-order polynomial function. *Bottom:* The continuum-normalized spectrum. The Na I D lines are fitted with Gaussian functions using an MCMC routine.

images were also obtained with KAIT. The multiband light curves are shown in Figure 5.2.

The reduction process of the photometric data is presented in Appendix 5.3.1.

Nineteen low-resolution optical spectra were collected with the FLOYDS spectrographs (Brown et al., 2013a) on the 2 m Faulkes Telescopes South and North (FTS & FTN) through the Global Supernova Project. In addition, many optical spectra were obtained with the Robert Stobie Spectrograph (RSS) on the Southern African Large Telescope (SALT; Smith et al., 2006), the Kast spectrograph on the 3 m Shane telescope (Miller & Stone, 1994) at Lick Observatory, the Boller & Chivens Spectrograph (B&C) on the Bok Telescope (Green et al., 1995), one of the Multi-Object double Spectrographs (MODS1; Pogge et al., 2010) on the Large Binocular Telescope (LBT), the Binospec instrument on the MMT (Fabricant et al., 2019), the Goodman High Throughput Spectrograph on the Southern Astrophysical Research Telescope (SOAR; Clemens et al., 2004), the Low-Resolution Imaging Spectrometer (LRIS; Oke et al., 1995) on the 10 m Keck I telescope, the Gemini Multi-Object Spectrographs (GMOS; Hook et al., 2004; Gimeno et al., 2016) on the Gemini North telescope, the Andalucia Faint Object Spectrograph and Camera (ALFOSC) on the Nordic Optical Telescope (NOT) as part of the NOT Unbiased Transients Survey 2 (NUTS2) collaboration[1], the SuperNova Integral Field Spectrograph (SNIFS; Lantz et al., 2004) mounted at the University of Hawaii 2.2 m telescope (UH88) at Maunakea as part of the Spectroscopic Classification of Astronomical Transients survey (SCAT; Tucker et al., 2022), the Inamori-Magellan Areal Camera & Spectrograph (IMACS; Dressler et al., 2011) on the 6.5 m Magellan Baade telescope as part of the Precision Observations of Infant Supernova Explosions (POISE; Burns et al., 2021), the Optical System for Imaging and low/intermediate-Resolution Integrated Spectroscopy (OSIRIS; Cepa et al., 2000) spectrograph on the 10.4 m Gran Telescopio Canarias (GTC), and the Low-Dispersion Survey Spectrograph 3 (LDSS3, which was updated from LDSS2; Allington-Smith et al., 1994) on the 6.5 m Magellan Clay telescope.

Near-infrared (NIR) spectra were taken with the Near-Infrared Echellette Spectrometer (NIRES; Wilson et al., 2004) on the 10 m Keck II telescope, the Folded-port InfraRed

[1]https://nuts.sn.ie

Echellette (FIRE; Simcoe et al., 2013) on the Magellan Baade telescope, and the MMT and Magellan Infrared Spectrograph (MMIRS) on the MMT (McLeod et al., 2012).

A log of the spectroscopic observations is given in Table 5.3.

5.3.1. Photometric Data Reduction of SN 2022crv. The photometric data from the Las Cumbres Observatory were reduced using the PyRAF-based photometric reduction pipeline LCOGTSNPIPE (Valenti et al., 2016). This pipeline uses a low-order polynomial fit to remove the background and calculates instrumental magnitudes using a standard PSF-fitting technique. Apparent magnitudes were calibrated using the AAVSO Photometric All-Sky Survey (APASS[2]) (g, r, i) and Landolt (U, B, V) catalogs (Landolt, 1992).

Unfiltered (*Open*) DLT40 images were processed with a PyRAF-based pipeline. Background contamination was removed by subtracting a reference image, and the aperture photometry was extracted from the subtracted images. The final photometry is calibrated to the r band using the APASS catalog.

The ATLAS survey is carried out primarily in two filters, *cyan* and *orange*, roughly equivalent to Pan-STARRS filters $g + r$ and $r + i$, respectively. Typically, four sets of 30 s exposures are taken for each field within a 1 hr timeframe. The images are processed and difference imaging is performed in real time to enable rapid discovery of transients in the data stream (Smith et al., 2020b). We obtained the forced photometry at the SN position from the ATLAS forced photometry server (Shingles et al., 2021). We stacked the individual flux measurements for each nightly quad into a single measurement in order to improve the signal-to-noise ratio, and to obtain deeper upper limits for the prediscovery nondetections.

The images obtained with KAIT and Nickel at Lick Observatory were reduced using a custom pipeline[3] detailed by Stahl et al. (2019). PSF photometry was obtained using DAOPHOT (Stetson, 1987) from the IDL Astronomy User's Library[4]. Several nearby stars

[2]https://www.aavso.org/apass
[3]https://github.com/benstahl92/LOSSPhotPypeline
[4]http://idlastro.gsfc.nasa.gov/

were chosen from the Pan-STARRS1[5] catalog for calibration. Their magnitudes were first transformed into Landolt magnitudes using the empirical prescription presented by Tonry et al. (2012), then transformed to the KAIT/Nickel natural system. The final results were transformed to the standard system using local sequence stars and color terms for KAIT4 and Nickel2 (Stahl et al., 2019).

Swift images were reduced using the High-Energy Astrophysics software (HEA-Soft). The background was measured from a region away from any stars. Zero-points were chosen from Breeveld et al. (2011) with time-dependent sensitivity corrections updated in 2020.

5.3.2. Spectroscopic Data Reduction of SN 2022crv. FLOYDS spectra were reduced following standard procedures using the FLOYDS pipeline (Valenti et al., 2014a). The IMACS Baade spectra were reduced using standard methods and IRAF routines[6], as described by Hamuy et al. (2006). The UH88 data were obtained with SNIFS and reduced using the method outlined by Tucker et al. (2022). The SALT spectra were reduced using a custom long-slit pipeline based on the PySALT package (Crawford et al., 2010b). The NOT ALFOSC spectrum was reduced using the PypeIt pipeline (Prochaska et al., 2020; Prochaska et al., 2020; Prochaska et al., 2020)

The spectrum taken with GMOS as part of our program GN-22A-Q-135 used the B600 grating and a 1.″5 slit. Data were reduced with the `DRAGONS` (Data Reduction for Astronomy from Gemini Observatory North and South) package (Labrie et al., 2019), using the recipe for GMOS long-slit reductions. This includes bias correction, flat-fielding, wavelength calibration, and flux calibration.

The spectrum obtained with LDSS3 was reduced using IRAF including bias subtraction, flat-fielding, cosmic-ray rejection, local sky subtraction, and extraction of one-dimensional (1D) spectra. The slit was aligned along the parallactic angle (Filippenko, 1982) to minimize

[5]http://archive.stsci.edu/panstarrs/search.php

[6]IRAF was distributed by the National Optical Astronomy Observatory, which was operated by the Association of Universities for Research in Astronomy (AURA) under cooperative agreement with the National Science Foundation.

differential light losses, and flux calibration was done using a spectrophotometric standard taken that night at similar airmass.

The Keck NIRES data were reduced following standard procedures described in the IDL package `Spextools` version 5.0.2 for NIRES (Cushing et al., 2004). The extracted 1D spectrum was flux calibrated and also corrected for telluric features with `Xtellcorr` (Vacca et al., 2003) version 5.0.2 for NIRES, making use of an A0 V standard star close in time and at similar airmass to the science target.

The two spectra taken with the Kast double spectrograph (Miller & Stone, 1994) mounted on the Shane 3 m telescope at Lick Observatory utilized the 2″ slit, 600/4310 grism, and 300/7500 grating. This instrument configuration has a combined wavelength range of ∼ 3500–10,500 Å, and a spectral resolving power of $R \approx 800$. To minimize slit losses caused by atmospheric dispersion (Filippenko, 1982), the slit was oriented at or near the parallactic angle. The data were reduced following standard techniques for CCD processing and spectrum extraction (Silverman et al., 2012) utilizing IRAF (Tody, 1986) routines and custom Python and IDL codes[7]. Low-order polynomial fits to comparison-lamp spectra were used to calibrate the wavelength scale, and small adjustments derived from night-sky lines in the target frames were applied. The spectra were flux calibrated using observations of appropriate spectrophotometric standard stars observed on the same night, at similar airmasses, and with an identical instrument configuration.

The NIR spectrum obtained using FIRE mounted on the 6.5 m Magellan Baade telescope at Las Campanas Observatory, Chile, was taken in the high-throughput prism mode with a 0.″6 slit. For telluric correction, an A0 V star was observed close in time and at similar airmass to the science target. The spectra were reduced using the IDL pipeline `firehose` (Simcoe et al., 2013). Details of the observation setup and reduction were outlined by Hsiao et al. (2019b).

[7]https://github.com/ishivvers/TheKastShiv

NIR spectra were obtained with the MMT and MMIRS on the 6.5 m MMT Observatory telescope on Mt. Hopkins at the Smithsonian's Fred Lawrence Whipple Observatory using a 1.″0 slit in both the zJ and HK (with the high-throughput $HK3$ filter) spectroscopic modes. The data were reduced using the automated MMIRS pipeline (Chilingarian et al., 2015). Telluric corrections and absolute flux calibrations were performed using observations of the A0 V star HD 72033 close in time and at similar airmass to the science target. We employed the method of Vacca et al. (2003) implemented in the IDL tool XTELLCOR_GENERAL developed by Cushing et al. (2004) as part of the `Spextool` package.

The Keck LRIS optical spectra were reduced in the standard manner with PYPEIT (Prochaska et al., 2020; Prochaska et al., 2020; Prochaska et al., 2020).

The GTC spectrum was reduced following standard procedures with PYRAF routines via the graphical user interface FOSCGUI[8]. The 2D frames were corrected for bias and flat-fielded before the 1D spectral extraction. We wavelength calibrated the spectra via comparison with comparison-lamp spectra and calibrated the flux using spectrophotometric standard stars. These also helped in removing the strongest telluric absorption bands present in the spectrum. Finally, the absolute flux calibration of the spectrum was cross-checked against the broad-band photometry.

5.4. Observational Properties

5.4.1. Explosion Epoch. By combining the early light curves from the DLT40 and ATLAS surveys, we are able to put a strong constraint on the explosion date of SN 2022crv. The SN was not detected during the DLT40 search on JD 2,459,626.89 (with a 3σ limit of 18.44 mag). On JD 2,459,627.49, $\sim$ 14.4 hr after our nondetection, the SN was detected in an o-band ATLAS image. The first detection and the last nondetection of SN 2022crv are highlighted in the left panel of Figure 5.2. By taking the average between the first detection

[8]FOSCGUI is a graphic user interface aimed at extracting SN spectroscopy and photometry obtained with FOSC-like instruments. It was developed by E. Cappellaro. A package description can be found at http://sngroup.oapd.inaf.it/foscgui.html.

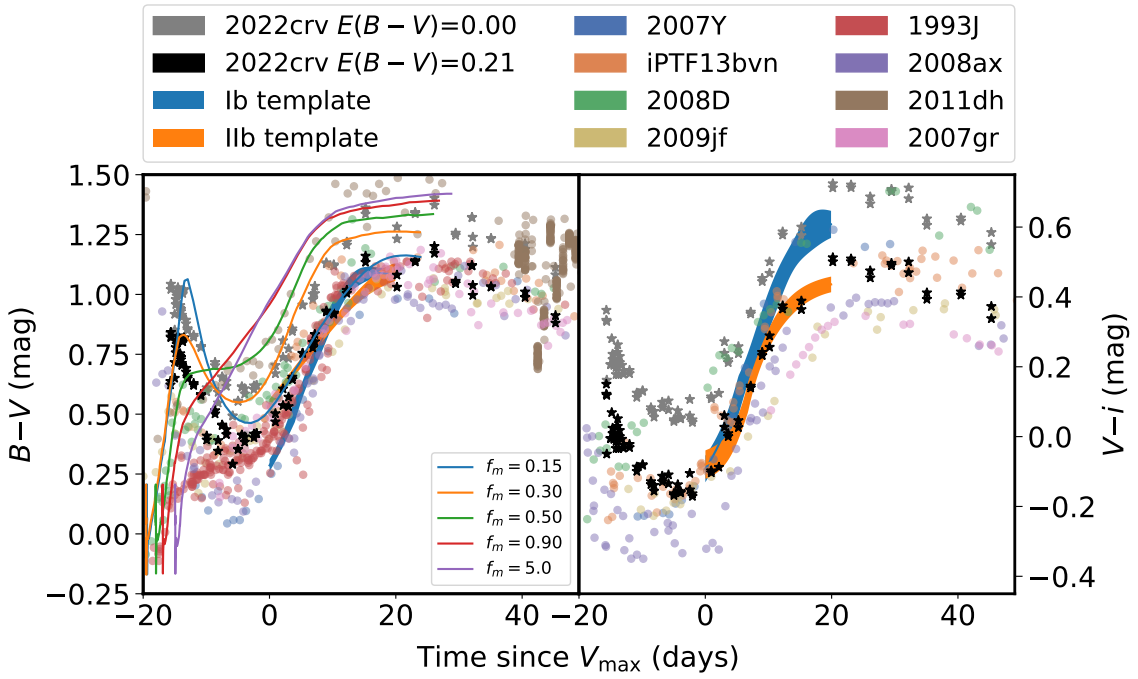

Figure 5.4 Color evolution of SN 2022crv, after correcting for a total color excess of $E(B-V) = 0.21$ mag. The color templates are from Stritzinger et al. (2018). A sample of SNe Ib/IIb after correcting with the published reddening estimates are also plotted. In addition, the $B-V$ color evolution is compared with the SNe Ib color evolution models by Yoon et al. (2019) with various degrees of ^{56}Ni (indicated by f_m). SN 2022crv is more consistent with the $f_m = 0.15/0.3$ model, suggesting relatively weak ^{56}Ni mixing in the ejecta (see Section 5.5).

and the last nondetection, we constrain the explosion epoch to be JD 2,459,627.19 ±0.30, which will be adopted throughout the paper.

5.4.2. Reddening Estimation. The equivalent width (EW) of the Na I D line is often used to estimate the SN reddening with the assumption that it is a good tracer of the amount of gas and dust along the line of sight (e.g., Munari & Zwitter, 1997; Poznanski et al., 2012). In order to measure the line-of-sight reddening toward SN 2022crv, we analyze the medium-resolution spectrum ($R \approx 4000$) taken with LRIS on 2022-04-26 (Figure 5.3). We apply a fourth-order polynomial to fit the continuum, and measure the EW of the Na I D lines on the continuum-normalized spectrum (Figure 5.3 bottom panel). The measured EW of the host galaxy Na I D λ5890 (D_2) and Na I D λ5896 (D_1) are $0.544^{+0.012}_{-0.012}$ Å

and $0.378^{+0.011}_{-0.011}$ Å, respectively. The measured EW of the Galactic Na I D_2 and Na I D_1 are $0.404^{+0.011}_{-0.011}$ Å and $0.247^{+0.011}_{-0.011}$ Å respectively. Using Eq. 9 of Poznanski et al. (2012) and applying the renormalization factor of 0.86 from Schlafly et al. (2010), we found a host extinction of $E(B-V)_{\rm host} = 0.146^{+0.009}_{-0.009}$ mag with 20% systematic uncertainty (Poznanski et al., 2012). The Milky Way extinction is measured to be $E(B-V)_{\rm MW} = 0.070^{+0.004}_{-0.004}$ mag, consistent with the value from Schlafly & Finkbeiner (2011a) of $E(B-V)_{\rm MW} = 0.0642$ (0.0007) mag. The latter will be adopted in this paper.

For SESNe, the intrinsic color shortly after maximum light is found to be tightly distributed, both observationally (Drout et al., 2011; Taddia et al., 2015; Stritzinger et al., 2018) and theoretically (Dessart et al., 2016; Woosley et al., 2021). By studying a sample of SESNe, Drout et al. (2011) and Stritzinger et al. (2018) found that, compared to other phases, the scatter in various color indices for each subtype of SESN is smaller shortly after maximum brightness. Based on the modeling of a range of SESNe, Woosley et al. (2021) confirmed that there are pinches in color indices shortly after the peak. They also found that the model spectra of SESNe are similar to each other ~ 10 days after the peak.

In Figure 5.4, we compare the $B-V$ and $V-i$ evolution of SN 2022crv with those of other well-studied SESNe, including SN 2009jf (Valenti et al., 2011; Sahu et al., 2011), SN 2007Y (Stritzinger et al., 2009), SN 2008D (Modjaz et al., 2009), SN 1993J (Filippenko et al., 1993), SN 2008ax (Pastorello et al., 2008a), SN 2011dh (Ergon et al., 2014), iPTF13bvn (Fremling et al., 2014), and SN 2007gr (Hunter et al., 2009). These objects have been selected because they are SESNe that are among the best, well-sampled light curves and spectral sequences in literature; they cover the very early phases up to the nebular phases, making them suitable as a comparison sample. As we will show in Section 5.5, the peak brightness of each object collectively spans a wide range, representing the diversity of SESNe. The color templates for SNe Ib and IIb from Stritzinger et al. (2018) are also plotted. We found that a total extinction of $E(B-V) = 0.21$ mag gives SN 2022crv a consistent color evolution with our

comparison sample of SNe Ib/IIb and templates shortly after $V_{\rm max}$. In the bottom panel of Figure 5.4, we compare the spectrum of SN 2022crv with the other SNe Ib/IIb at ~ 10 days after $V_{\rm max}$. The original spectrum of SN 2022crv is redder than that of our other objects, while a total extinction of $E(B-V) = 0.21$ mag gives a spectral slope more consistent with the population. Therefore, throughout this paper, we will adopt an $E(B-V)_{\rm tot} = 0.21$ mag, assuming $R_V = 3.1$.

5.4.3. Distance. The distance of NGC 3054 listed in the NASA/IPAC Extragalactic Database (NED) ranges from 12.9 Mpc to 40.0 Mpc. SN 2006T (Type IIb; Monard, 2006) also exploded in NGC 3054, and Lyman et al. (2016) used a distance of 32.9 Mpc for SN 2006T, while Taddia et al. (2018) adopted a distance of 31.6 Mpc. To be consistent with the distance of SN 2006T used by previous works, we assume a distance of $31.6^{+6.4}_{-5.3}$ Mpc (a distance modulus of 32.5 ± 0.4 mag) based on the Tully-Fisher distance (Tully et al., 2009).

5.4.4. Host-Galaxy Properties. SN 2022crv is at a projected offset of $36\farcs4$ ($5.6^{+1.1}_{-0.9}$ kpc) from the host galaxy NGC 3054. To estimate the metallicity at the SN position, we measured the flux of the strong ionized gas emission lines (Hβ, [O III] λ5007, [N II] λ6583, Hα, [S II] $\lambda\lambda$6717, 6731) from the spectrum taken 371.5 days after the SN explosion. The continuum is removed by fitting a linear component around the narrow emission lines. By using the strong-line diagnostics presented by Curti et al. (2020), the weighted average oxygen abundance at the SN site is measured to be $12 + \log({\rm O/H}) = 8.83 \pm 0.08$ and the results for each indicator calibration are shown in Table 5.4.4. We note that the different diagnostics are not fully independent, so the weighted average value provided here is calculated solely for reference. Assuming a solar oxygen abundance of $12 + \log({\rm O/H}) = 8.69$ (Allende Prieto et al., 2001) as well as a solar metallicity ($Z_\odot$) of 0.0134 (Asplund et al., 2009b), $12 + \log({\rm O/H}) = 8.83$ is equivalent to a metallicity of $Z \approx 1.4\,Z_\odot \approx 0.019$. The O_3N_2 calibration indicator of Pettini & Pagel (2004b) gives $12 + \log({\rm O/H}) = 8.88 \pm 0.14$, consistent with our measurements above. Comparing to all the SESNe in the PMAS/PPak Integral-field

Table 5.3. Oxygen abundance from diagnostics of Curti et al. (2020)*.

Indicator	Line Ratio	Value	12 + log[O/H]
R3	[O III] λ5007/Hβ	0.13	8.84±0.07
N2	[N II] λ6583/Hα	0.39	8.75±0.10
S2	[S II] $\lambda\lambda$6717, 6731/Hα	0.18	8.87±0.06
RS_{32}	[O III] λ5007/Hβ + [S II] λ6717, 6731/Hα	0.31	8.85±0.08
O_3S_2	([O III] λ5007/Hβ) / ([S II] $\lambda\lambda$6717, 6731/Hα)	0.72	8.76±0.11
O_3N_2	([O III] λ5007/Hβ) / ([N II] λ6583/Hα)	0.34	8.84±0.09
Weighted Average			8.83±0.08

*Emission-line fluxes at the SN position were measured from the spectrum taken on 2023-03-23 (371 days after the explosion).

Supernova Hosts Compilation (PISCO) sample (Galbany et al., 2018b), SN 2022crv has one of the most metal-rich environments among the SNe Ib/IIb in the sample. Given the high metallicity, the progenitor star of SN 2022crv likely experienced strong wind mass loss (Vink et al., 2001; Crowther, 2007; Mokiem et al., 2007). Just before completing our paper, another paper on SN 2022crv appeared (Gangopadhyay et al., 2023), finding a high progenitor mass-loss rate based on the radio light curve, consistent with what we suggest here. The implication of the high mass-loss rate will be further discussed in Section 5.7.3.2.

5.5. Photometric Evolution

5.5.1. Light-Curve Evolution. The multiband light curves of SN 2022crv are shown in Figure 5.2. SN 2022crv reaches a V-band maximum of $M_V = -17.7 \pm 0.4$ mag on JD 2,459,645.42, $\sim$ 18.2 days after the date of explosion. Around 60 days after $V_{\rm max}$, the light curves show a linear (in mag) decline. The V-band decline rate is about 1.4 mag $(100\ {\rm d})^{-1}$, faster than the expected radioactive decay rate of $^{56}{\rm Co} \rightarrow {}^{56}{\rm Fe}$ [0.98 mag $(100\ {\rm d})^{-1}$] (Nadyozhin, 1994), consistent with other SNe Ib/IIb. In the bottom panel of Figure 5.2, we compare the V-band light curve of SN 2022crv with that of other well-studied SESNe (SNe Ib — SN 2007Y (Stritzinger et al., 2009), iPTF13bvn (Fremling et al., 2014), SN 2008D (Modjaz et al., 2009), SN 2009jf (Valenti et al., 2011); SNe IIb — SN 1993J (Filippenko et al., 1993), SN 2008ax (Pastorello et al., 2008a), SN 2011dh (Ergon et al., 2014); and SN

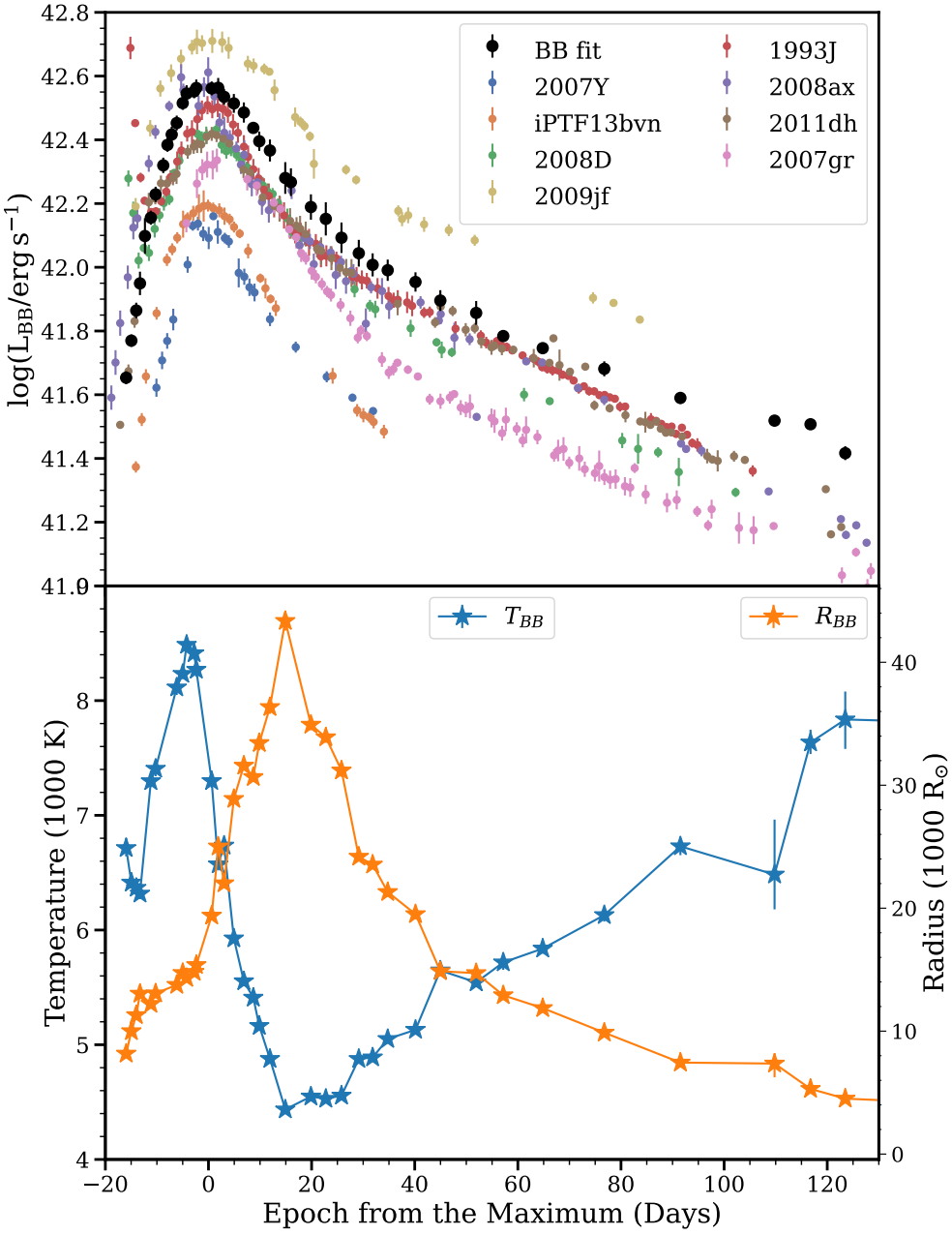

Figure 5.5 *Top:* Bolometric light curve of SN 2022crv compared with other Type Ib/IIb SNe. The unfilled points represent the bolometric light curve from the blackbody fit. *Bottom:* The evolution of temperature and radius of SN 2022crv derived from the blackbody fit.

Ic — SN 2007gr (Hunter et al., 2009)). The reason for choosing these objects for comparison is described in Section 5.4.2. As shown in the bottom panel of Figure 5.2, the objects span a wide range of magnitudes, making them a good representative sample of SESNe.

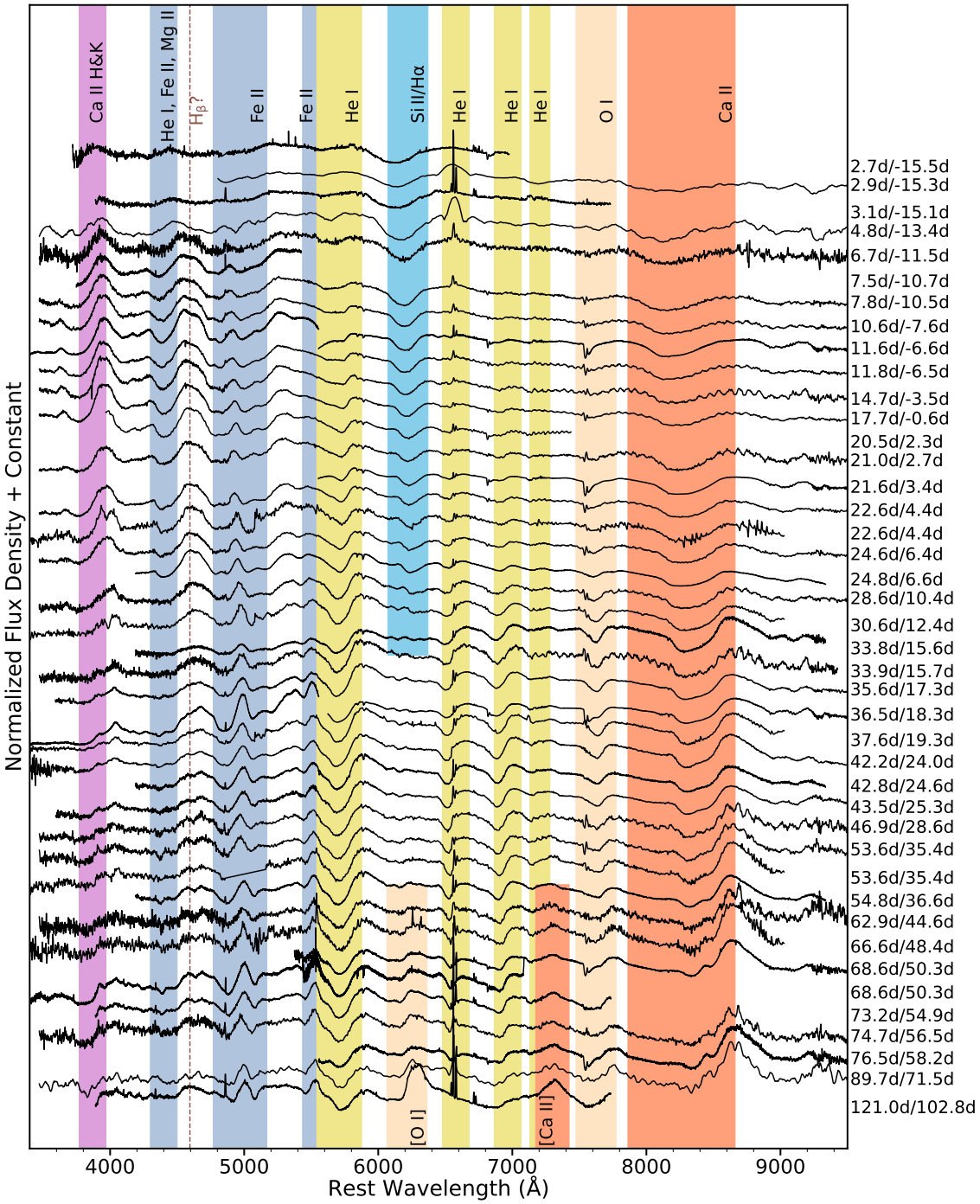

Figure 5.6 The optical spectroscopic evolution of SN 2022crv from the photospheric phase to the early nebular phase. The phase is measured from the dates of explosion and V-band maximum.

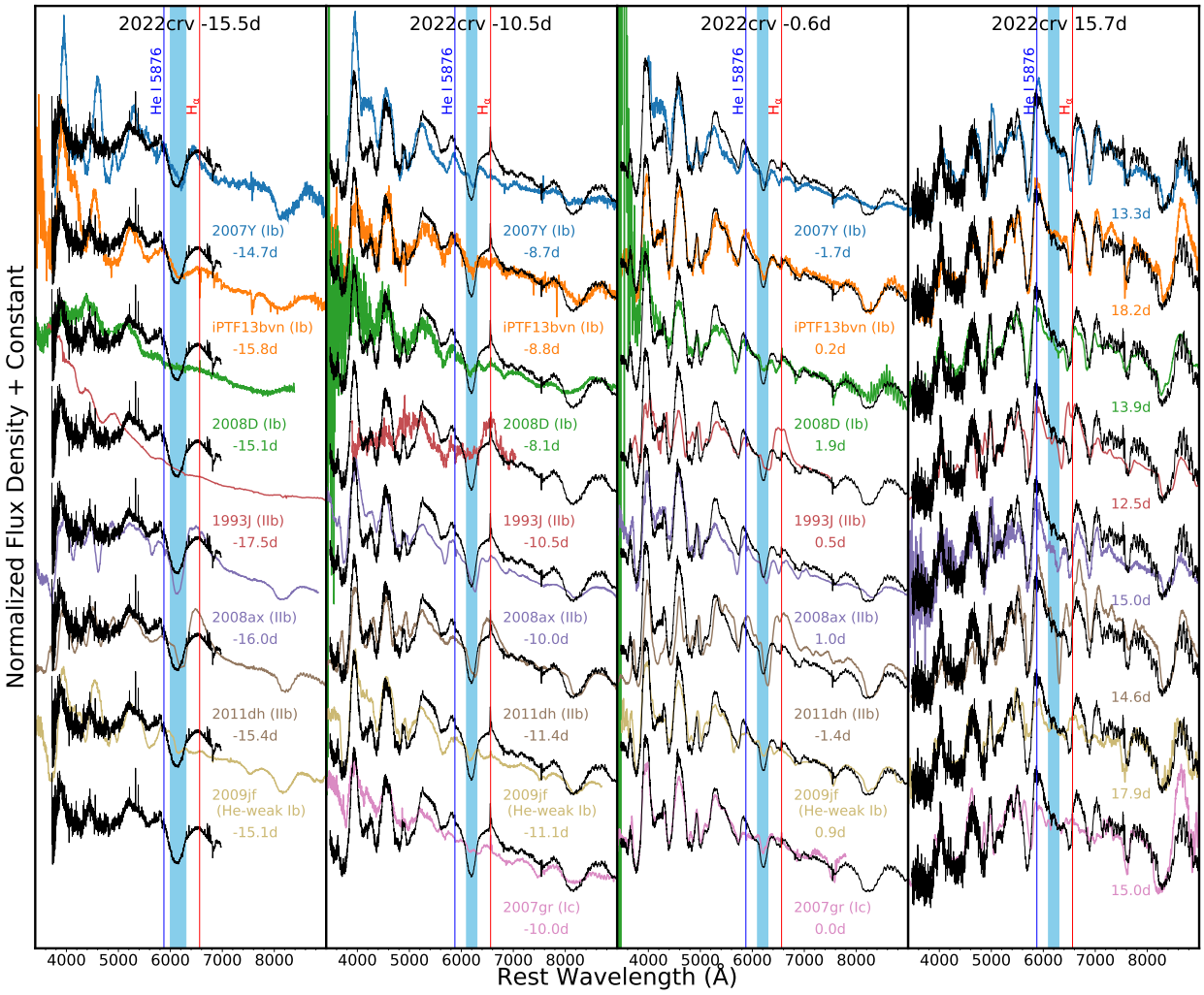

Figure 5.7 Optical spectral comparison of SN 2022crv to other well-studied SESNe, including SNe Ib (SN 2007Y, iPTF13bvn, SN 2008D), SNe IIb (SN 1993J, SN 2008ax, SN 2011dh, SN 2009jf), and SNe Ic (SN 2007gr). The blue shaded areas mark the 6200 Å feature.

We choose the V band for comparison because all of the objects have coverage in V light curves. SN 2022crv does not show an initial peak due to shock cooling like SN 1993J does, and it has a faster rise than SN 2008D. Overall, however, the light-curve shape of SN 2022crv is similar to that of other SESNe.

Chevalier & Soderberg (2010) suggested that SNe IIb can be divided into two categories according to whether the progenitor is compact or extended. If the amount of hydrogen is

sufficiently low, the compact Type IIb would merge into Type Ib. Owing to the absence of cooling-envelope emission, SN 2022crv likely has a compact progenitor, which will be further discussed in Section 5.7.2.

The $B-V$ and $V-i$ color evolution of SN 2022crv are compared to our sample of SNe Ib/IIb in Figure 5.4. The color evolution of SN 2022crv after $V_{\rm max}$ is similar to that of other comparison SESNe. After correcting for reddening, the $B-V$ color of SN 2022crv shows a rapid initial rise and reaches a peak of ~ 0.8 mag. The color then evolves toward the blue down to ~ 0.4 mag. After maximum light, the $B-V$ color increases and reaches a peak of ~ 1.1 mag before entering the nebular phase. The $V-i$ color of SN 2022crv shows a similar trend. Through hydrodynamical simulations, Yoon et al. (2019) found that the early color evolution of SNe Ib/c is strongly affected by the ^{56}Ni mixing level in the SN ejecta. The ^{56}Ni mixing level is characterized by f_m by Yoon et al. (2019), with a larger value of f_m representing more extensive mixing. The $B-V$ evolution of SN 2022crv matches with the $f_m = 0.15$ or the $f_m = 0.3$ model presented by Yoon et al. (2019) (Figure 5.4), implying weak ^{56}Ni mixing in SN 2022crv.

5.5.2. Bolometric Light Curve. In this section, we build the bolometric light curve of SN 2022crv, which will be used to determine the physical parameters of the explosion in Section 5.7.3.4.

We calculate the bolometric light curve by fitting the reddening-corrected spectral energy distribution (SED) of SN 2022crv with a blackbody spectrum at each epoch using a Markov Chain Monte Carlo (MCMC) routine in the Light Curve Fitting package (Hosseinzadeh & Gomez, 2020a). The bolometric light curve of SN 2022crv is shown in Figure 5.5 alongside ones from a sample of Type Ib/IIb SNe. The same method was employed to derive the bolometric light curves for objects in the comparison sample. The peak bolometric luminosity of SN 2022crv is 3.6×10^{42} erg s^{-1}, which places SN 2022crv at the more luminous end among other SNe Ib/IIb (Lyman et al., 2016; Taddia et al., 2018; Prentice et al., 2019).

Table 5.4. Position of the minimum of the absorption component of the P Cygni profile (Å).

Epoch*	MJD	Hα/Si II λ6355	He I λ5876	He I λ6678	Fe II λ4561	Fe II λ5018	Fe II λ5169
2.7	59629.4	6172.5	5623.7	···	···	···	···
2.9	59629.6	6183.5	5590.9	···	···	···	···
3.1	59629.8	6177.0	5638.5	···	···	···	···
4.8	59631.5	6218.0	5678.4	···	···	···	···
6.7	59633.4	6237.1	5709.2		4378.0	4814.7	4997.8
7.5	59634.2	···	···	···	4397.2	4842.4	5014.6
7.8	59634.5	6240.0	5657.1		4400.2	4843.7	5014.8
10.6	59637.3	6246.9	5725.6	6500.2	4418.3	4856.7	5020.4
11.6	59638.3	···	···	···	4419.6	4859.1	5025.3
11.6	59638.3	6252.2	···	6503.2	···	···	···
11.8	59638.5	6247.9	5730.6	6513.6	4417.4	4857.0	5029.8
14.7	59641.4	6253.6	5769.5	6516.0	4428.1	4863.0	5041.3
17.7	59644.3	6261.7	5771.3	6556.0	4436.3	4870.9	5049.0
21.0	59647.6	6271.4	5762.9	6562.6	···	···	···
21.6	59648.3	···	···	···	4438.9	4886.3	5060.6
21.6	59648.3	6279.7	5767.4	6580.3	···	···	···
22.6	59649.3	6280.6	5767.6	6568.9	···	···	···
22.6	59649.3	6290.1	5774.3	6580.0	4440.8	4878.9	5077.2
24.6	59651.3	6288.1	5760.5	6567.7	···	···	···
24.8	59651.5	6289.8	5759.7	6573.8	4438.1	4904.1	5073.3
28.6	59655.3	6303.8	5745.4	6560.9	···	4920.3	5088.0
30.6	59657.3	6320.6	5744.5	6563.6	···	4927.3	5093.5

*Epoch is measured from the explosion (JD 2,459,627.19).

From the blackbody fits, we also derived the radius and temperature evolution of SN 2022crv (bottom panel of Figure 5.5). The temperature initially drops rapidly at early phases, then increases, peaking at $\sim 8500\,\mathrm{K}$ several days before V_{max} and subsequently decreasing rapidly until reaching a minimum of about 4500 K before the object settles into the nebular phase. The behavior of the temperature evolution is consistent with the color evolution shown in Figure 5.4. The radius of SN 2022crv continuously increases until it peaks around 20 days after V_{max}. The radius and temperature evolution of SN 2022crv are similar to those of other SESNe (Taddia et al., 2018).

5.6. Spectroscopic Evolution

5.6.1. Evolution of Optical Spectra. The optical spectra from the photospheric to the early nebular phase are shown in Figure 5.6. The early-time spectra show a prominent

Table 5.5. Absorption flux minimum of P Cygni profile (Å).

Epoch*	MJD	He I λ5876	He I λ6678	Fe II λ5018	Fe II λ5169
33.8	59660.5	5734.7	6549.4	4917.8	5099.7
33.9	59660.6	5738.8	6555.8	4918.7	5105.2
35.6	59662.2	5737.2	6556.6	···	5110.8
37.5	59664.2	5743.4	···	···	···
36.5	59663.2	5745.1	6562.7	···	···
36.5	59663.2	···	···	···	5108.1
37.6	59664.2	5745.6	6566.0	···	5102.7
42.2	59668.9	5737.3	6560.8	···	5111.2
42.8	59669.5	5739.7	6565.4	···	5114.7
43.5	59670.2	5738.8	6565.8	···	5114.1
46.9	59673.6	5738.4	6567.1	···	5089.6
53.6	59680.3	5743.9	6571.8	···	5095.0
53.6	59680.3	5752.6	6582.9	···	···
54.8	59681.5	5744.9	6576.5	···	5116.4
62.9	59689.5	5753.6	6577.4	···	5115.5
66.6	59693.3	5763.9	6590.2	···	5117.6
68.6	59695.2	···	···	···	5119.2
68.6	59695.2	5757.8	6589.7	···	···
68.6	59695.2	5756.4	6594.2	···	···
73.2	59699.9	5756.1	···	···	5118.7
74.7	59701.4	5755.1	6578.9	···	5097.0
76.5	59703.2	···	···	···	5119.2
76.5	59703.2	5755.0	···	···	···
89.7	59716.4	5765.0	6579.4	···	···
121.0	59747.7	5770.3	···	···	5119.7

*Epoch is measured from the explosion date (JD 2,459,627.19).

absorption line at $\sim$ 6200 Å, which could be due to Si II or high-velocity Hα. We also note that a small notch appears at 4595 Å at early phases (marked in Figure 5.6) and could arise from Hβ at a velocity similar to that of Hα. We will discuss the $\sim$ 6200 Å absorption line further in Section 5.7.2. He I λ5876 appears in the first spectrum and its EW gets larger over time. He I λ6678, He I λ7065, and He I λ7281 can be seen after ~ -6 d. The Fe II λ4561, Fe II λ5018, and Fe II λ5169 lines, which are good tracers of photospheric velocity (e.g., Dessart & Hillier, 2005b), can be identified after ~ -11 d. Other typical lines seen in SESNe such as Ca II H&K $\lambda\lambda$3934, 3969, Ca II $\lambda\lambda$8498, 8542, 8662, and O I λ7774 are strong before the object is well into the nebular phase. The [Ca] II $\lambda\lambda$7291, 7323 and [O I] $\lambda\lambda$6300, 6364 doublets start to emerge after day 35 and dominate the late-phase ($\geq$ 100 d) spectra. The evolution of the velocities of He I λ5876, He I λ6678, Fe II λ4561, Fe II λ5018, and

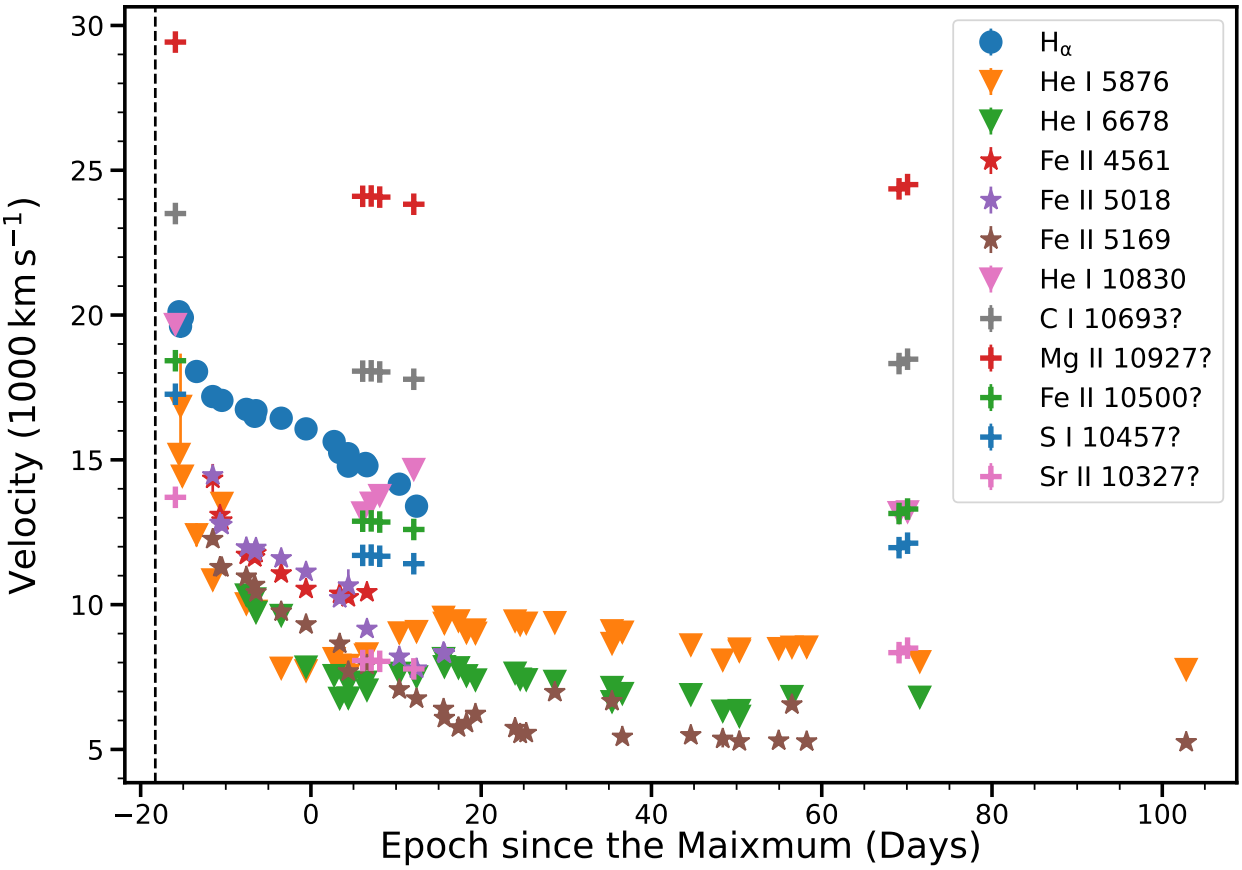

Figure 5.8 Velocity evolution of Hα, He I, Fe II, and feature A (see Section 5.6.3). The epoch of explosion is marked with the vertical dashed line. The velocity of feature A is calculated assuming it is from C I λ1.0693 μm, Mg I λ1.0927 μm, Fe II λ1.05 μm, S I λ1.0457 μm, and Sr I λ1.0327 μm, and is shown with the plus symbol. The velocity of Hα shows a rapid drop after the $V_{\rm max}$. As discussed in Section 5.7.1, the 6200 Å feature is likely dominated by Si II after $V_{\rm max}$, so this drop does not reliably reflect the velocity evolution of the Hα line.

Fe II λ5169 are shown in Figure 5.8. The velocity evolution of the 6200 Å line is also shown in Figure 5.8, assuming it is from Hα. The positions of the flux minima of these lines are listed in Tables 5.4 and 5.5.

In Figure 5.7, we compare the optical spectra of SN 2022crv at day −15.5, day −10.5, day −0.6, and day +15.7 with those of other SESNe at similar epochs, including SNe Ib 2007Y (Stritzinger et al., 2009), iPTF13bvn (Fremling et al., 2014), 2008D (Modjaz et al., 2009; Tanaka et al., 2009), and 2009jf (Valenti et al., 2011; Sahu et al., 2011); SNe IIb 1993J (Filippenko et al., 1993), 2008ax (Pastorello et al., 2008a), and 2011dh (Ergon et al., 2014);

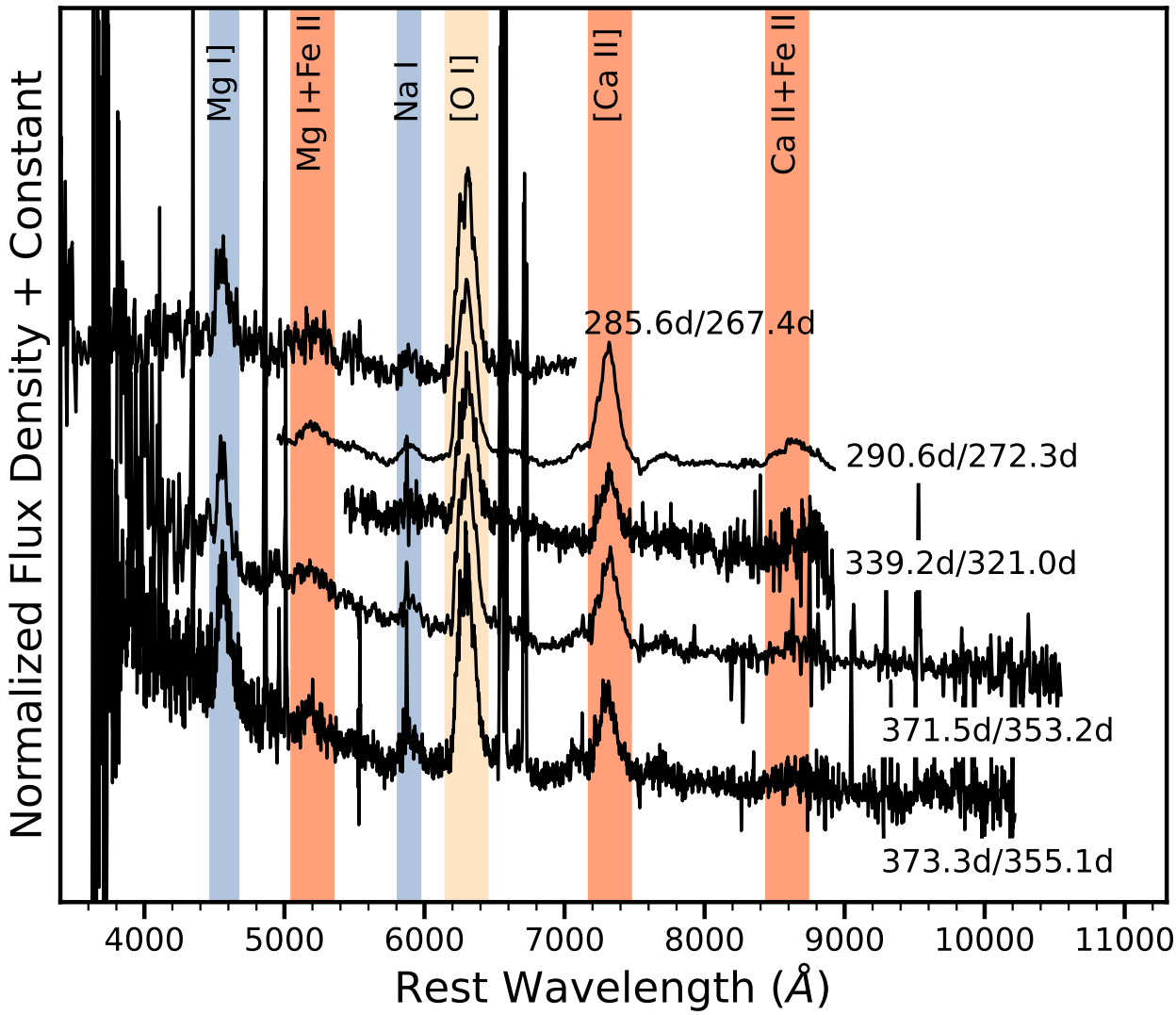

Figure 5.9 The nebular phase spectroscopic evolution of SN 2022crv. Phase is measured from the dates of explosion and V-band maximum brightness. All spectra shown here are rebinned with a second-order Savitzky-Golay filter with a window size of 11 Å.

and SN Ic 2007gr (Hunter et al., 2009). We note that SN 2009jf is a He-weak SN Ib (Valenti et al., 2011), making its spectra more indicative of a transitional object between SNe Ib and Ic. At early phases, SN 2022crv is more similar to the SNe IIb in our comparison sample; however, after maximum light, SN 2022crv closely resembles the SN Ib sample. The 6200 Å feature in SN 2022crv completely disappeared around 15 d after $V_{\rm max}$, while the Hα line in SNe IIb is still strong at similar phases. This will be discussed further in Section 5.7.2.

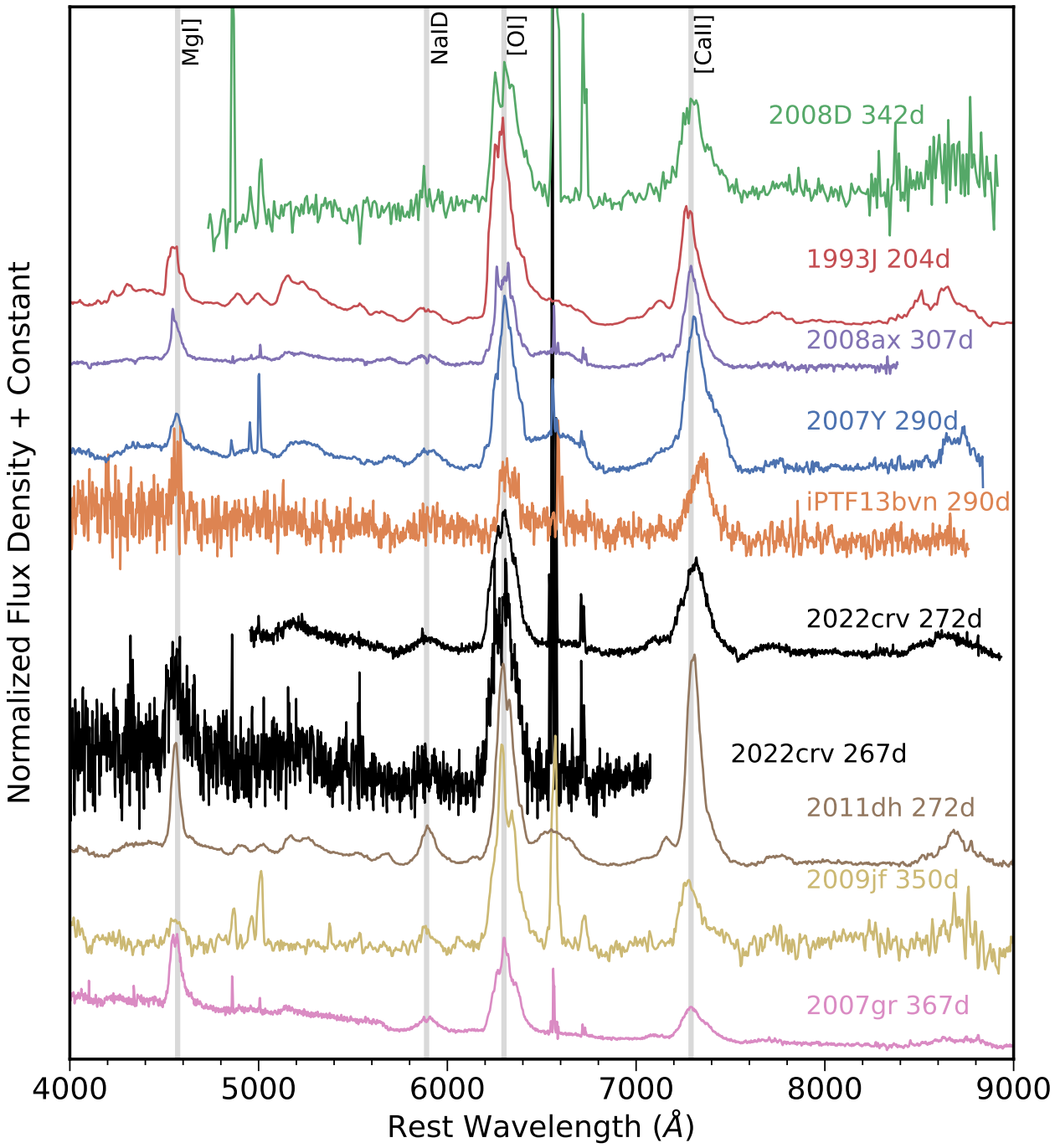

Figure 5.10 Nebular spectra of SN 2022crv compared with those of other SESNe. The phase is measured from the date of V-band maximum brightness.

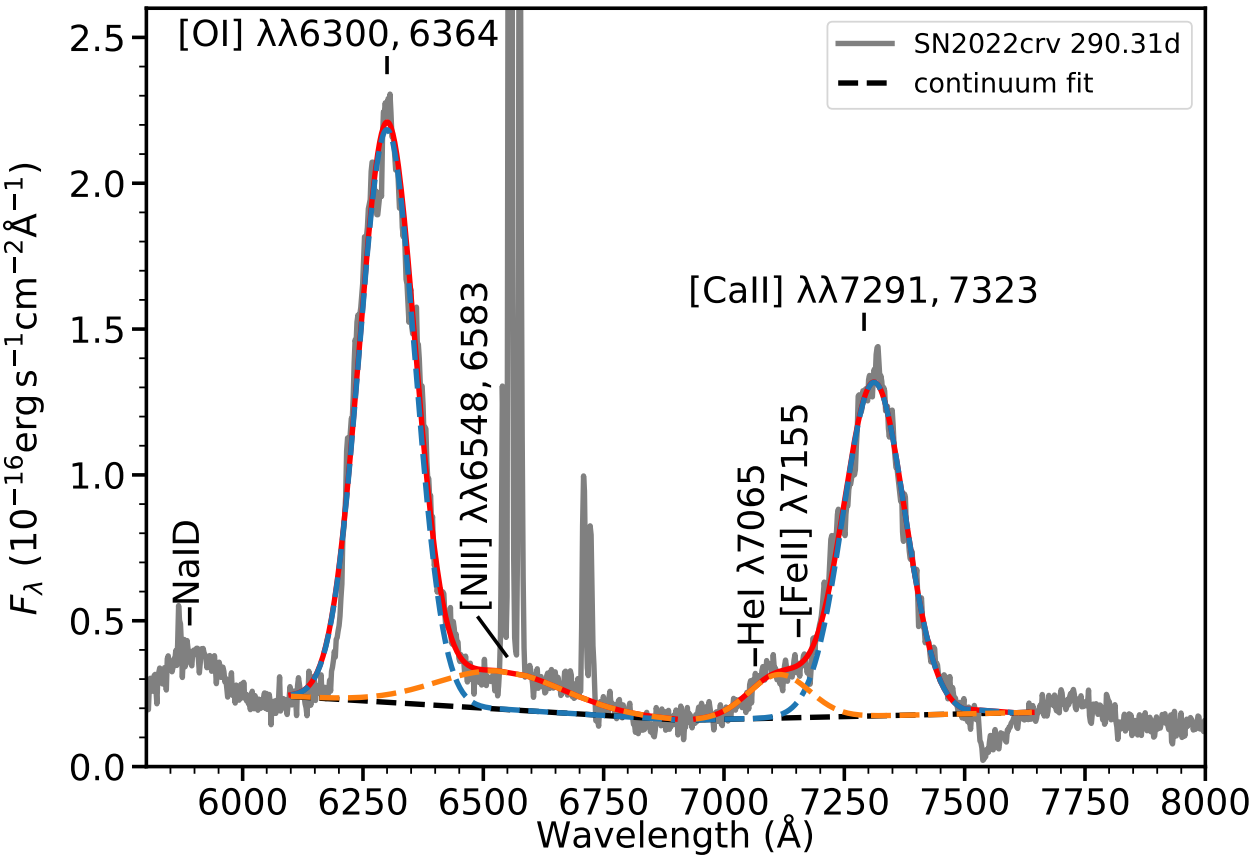

Figure 5.11 Line identification of the nebular spectrum taken on 2022-12-04. A double Gaussian function is fitted around each of 6300 Å and 7300 Å, to respectively deblend [O I] and [Ca II] from other lines. The continuum is defined by a straight segment connecting the two local minima.

5.6.2. Nebular Spectra. The nebular spectra are shown in Figure 5.9. In Figure 5.10, we compare the nebular spectra of SN 2022crv with those of other SNe Ib/IIb at similar epochs, finding that in agreement with the sample, SN 2022crv is dominated by strong [O I] λλ6300, 6364 and [Ca II] λλ7291, 7323. In addition, weak Mg I] λ4571 and the Na I D doublet can be seen in the spectra. The hydrogen emission is nonexistent or very weak, further supporting that SN 2022crv has a compact progenitor (Chevalier & Soderberg, 2010).

The [O I] and [Ca II] lines are often used to constrain the progenitor of SESNe, so a detailed analysis is presented in Figure 5.11. The [O I] doublet is slightly blended with

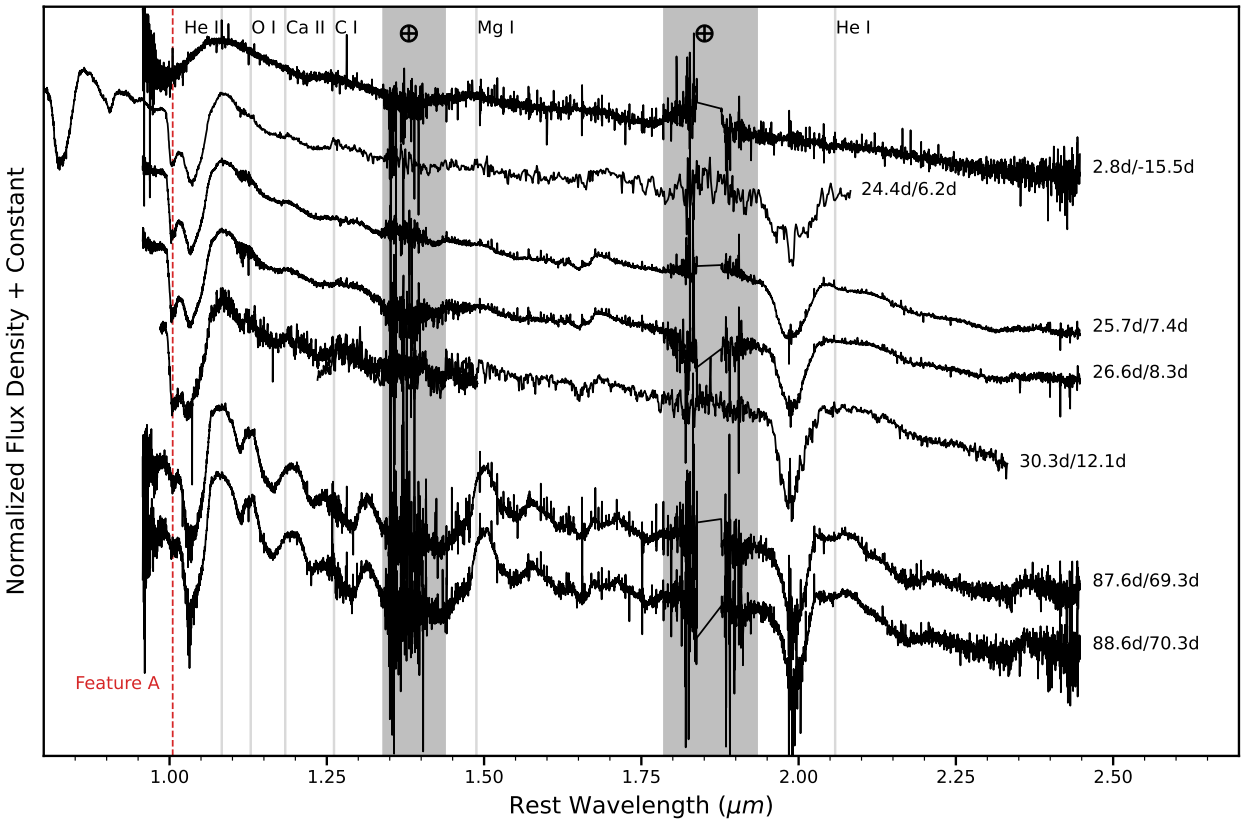

Figure 5.12 NIR spectra of SN 2022crv. The phase is measured from the dates of explosion and V-band maximum brightness. The red dashed line marks the extra absorption feature on the blue side of He I λ1.083 μm. The high telluric absorption regions are marked with gray bands.

[N II] $\lambda\lambda$6548, 6583, and the [Ca II] line is blended with He I λ7065 and [Fe II] λ7155. In order to deblend [O I] and [Ca II] from other lines, we fit two Gaussians around each of [O I] and [Ca II]. The continuum is defined by a line segment connecting the two local minima. The nebular spectrum has been scaled to the r- and i-band photometry, and the fits are shown in Figure 5.11. The flux of [O I] at day 290.3 is measured to be 2.9×10^{-14} erg s^{-1} cm^{-2}, and the [O I]/[Ca II] flux ratio is found to be 1.5. At day 371.3, the [O I]/[Ca II] flux ratio is 1.6, consistent with the value we obtained at 290.3 d. In Section 5.7.3.2, these measurements will be used to constrain the progenitor properties of SN 2022crv.

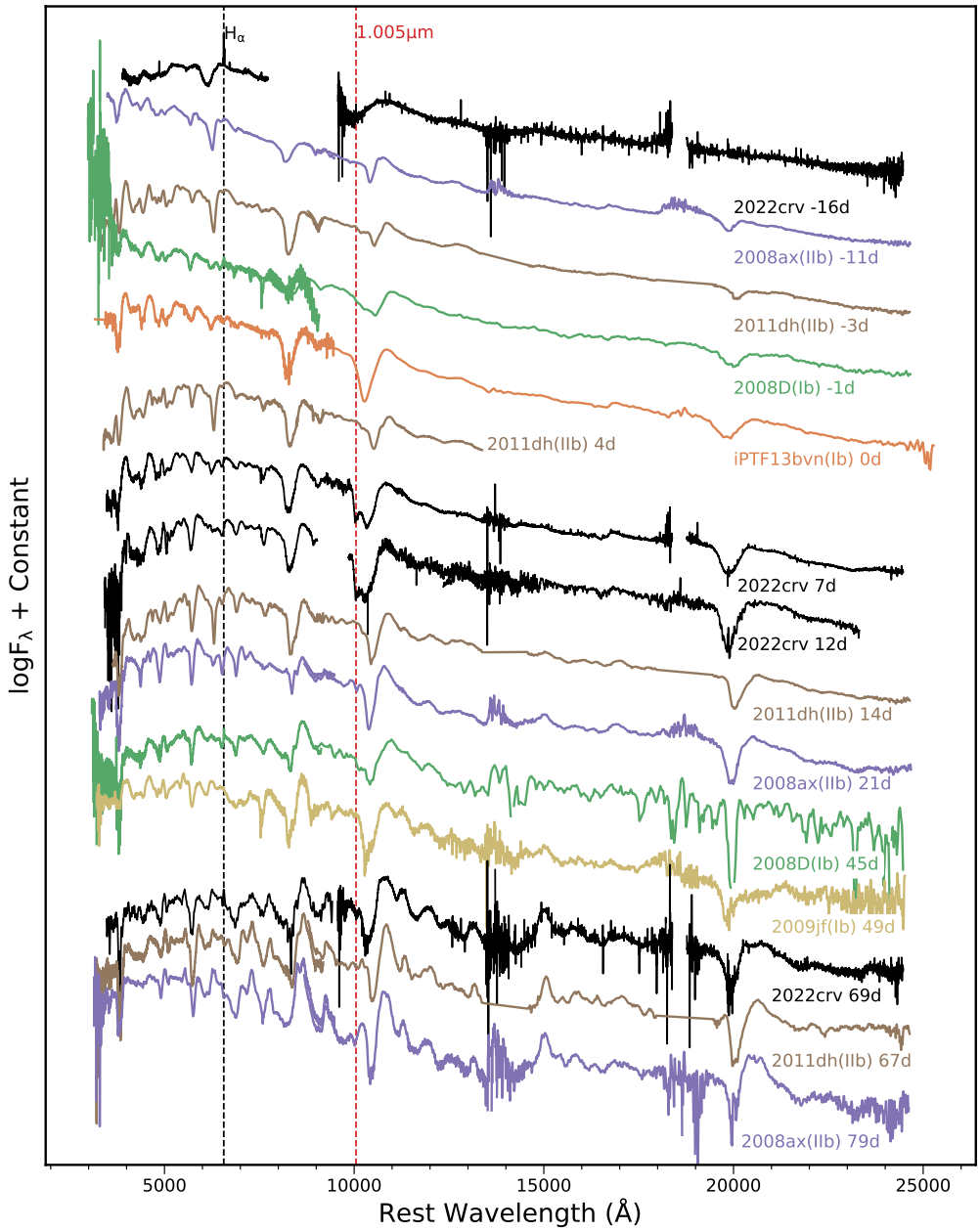

Figure 5.13 Comparison of combined optical and NIR spectra of SN 2022crv with those of other SNe Ib/IIb. The positions of Hα (black dashed line) and 1.005 μm (red dashed line) are marked.

5.6.3. Evolution of NIR Spectra. Figure 5.12 shows the NIR spectroscopic evolution of SN 2022crv. The first spectrum was taken only ∼2.8 days after explosion, and it shows a prominent absorption line on the blue side. If we attribute this line to He I λ1.083 μm,

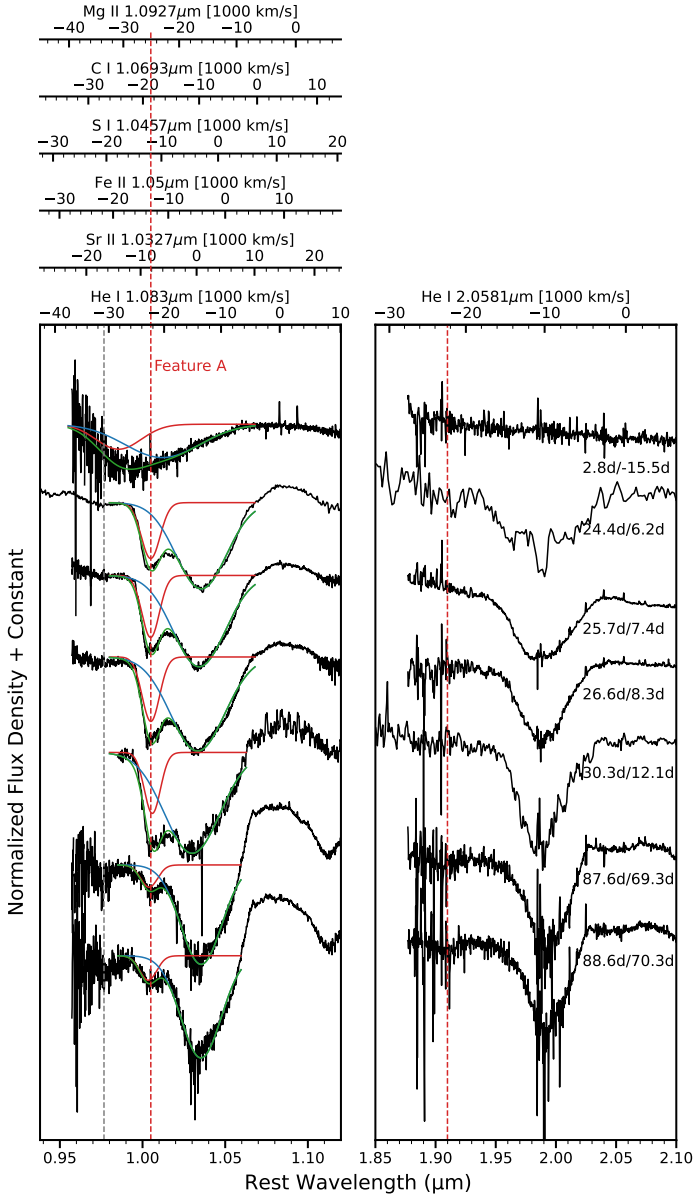

Figure 5.14 Spectral evolution of SN 2022crv in the 1 μm and 2 μm regions. The phase is measured from the dates of explosion and V-band maximum light. Feature A can be fit with a two-Gaussian function. The velocity scales of C I λ1.0693 μm, Mg I λ1.0927 μm, high-velocity (HV) He I λ1.083 μm, Fe II λ1.05 μm, S I λ1.0457 μm, and Sr II λ1.0327 μm are shown in the top abscissa axis. In the left panel, the red dashed line roughly marks the position of feature A at 1.005 μm, corresponding to $\sim 23,280$ km s^{-1} assuming feature A is from He I λ1.083 μm. The red dashed line in the right panel also has a velocity of $\sim 23,280$ km s^{-1} with respect to He I λ20,581. The gray dashed line marks the possible identification of Sr II λ1.0036 μm, at a velocity of ~ 8000 km s^{-1}.

the velocity would be ∼26,000 km s^{-1}, based on the minimum of the absorption. In Figure 5.13, we compare the combined optical and NIR spectrum of SN 2022crv with that of other SESNe at various epochs, including SNe Ib 2008D (Modjaz et al., 2009), 2009jf (Valenti et al., 2011), and iPTF13bvn (Fremling et al., 2014); and SNe IIb 2008ax (Pastorello et al., 2008a) and 2011dh (Ergon et al., 2014). These comparison objects are selected to maintain consistency with the optical comparison. SN 2007Y and SN 1993J are not included in this plot owing to the unavailability of NIR spectra, either because they were not obtained or because they are not publicly available.

In general, the NIR line evolution of SN 2022crv is consistent with that of other SNe Ib/IIb. However, at around 1.005 μm, there is an extra absorption feature on the blue side of He I λ1.083 μm, hereafter referred to as "feature A." A similar feature is likely present in SN 2008D and SN 2008ax, but it is only at late times and not as strong as the feature in SN 2022crv. To our best of our knowledge, this is the first time that such a strong feature is observed in an SESN. In order to isolate feature A from the He I λ1.083 μm line, we fit two Gaussian functions around this region (see the left panel of Figure 5.14). For the origin of feature A, we consider six possibilities: C I λ1.0693 μm, Mg I λ1.0927 μm, high-velocity (HV) He I λ1.083 μm, Fe II λ1.05 μm, S I λ1.0457 μm, and Sr II λ1.0327 μm. The velocity of feature A is indicated in Figure 5.14 as well as in Figure 5.8 assuming this line is from the C I, Mg I, Fe II, S I, and Sr II.

The derived velocities of C I λ1.0693 μm and Mg I λ1.0927 μm are higher than the velocity of Hα, so these two lines can be ruled out unless there is C and Mg present at a higher velocity than the H envelope. In addition, since there is no clear evidence of any blue component around He I λ20,581 (see the right panel of Figure 5.14), it is unlikely this extra absorption line is from HV He I λ1.083 μm.

S I λ1.0457 μm, Fe II λ1.05 μm, and Sr II λ1.0327 μm give reasonable velocities. However, S I λ1.0457 μm is usually seen in He-poor SNe (Teffs et al., 2020; Shahbandeh et al., 2022),

so it is unclear if such strong S I λ1.0457 μm can be present in a He-strong SN. We could not identify other lines from S I in the NIR spectra, probably because other S I lines are rather weak. The Fe II λ1.05 μm line is commonly seen in SNe Ia but not in CCSNe. If feature A is from Fe II λ1.05 μm, the derived velocity is lower than the velocity of Hα but larger than those of He and Fe lines in the optical, indicating that this line is formed in the outer layers of the ejecta. For SESNe, some degree of mixing is required to explain the observed properties (Shigeyama et al., 1990; Woosley & Eastman, 1997; Dessart et al., 2012; Yoon et al., 2019), so it is possible that the Fe II λ1.05 μm line is formed by material mixed into the outer layer. In addition, the ejecta of SESNe can be aspherical (e.g., Taubenberger et al., 2009; Milisavljevic et al., 2010; Fang et al., 2022). In this case, Fe II λ1.05 μm lines could be formed at higher velocities. However, no other Fe II lines are identified in the NIR spectra, making this possibility less realistic. If feature A is from Sr II λ1.0327 μm, its velocity could be similar to the velocity of Fe lines in optical. Sr II λ1.0327 μm is common in SNe II (Davis et al., 2019b), so it is possible this line can be seen in an SESN given that they are all core collapses of massive stars. A possible absorption line from Sr II λ1.0036 μm at the same velocity ($\sim$ 8000 km s^{-1}) is likely present in the NIR spectra, which is marked using a gray dashed line in Figure 5.14. This makes Sr II λ1.0327 μm the most plausible explanation of feature A.

In conclusion, feature A observed in SN 2022crv is likely due to Sr II λ1.0327 μm, but we could not fully exclude Fe II λ1.05 μm and S I λ1.0457 μm. Further detailed hydrodynamic modeling is needed to investigate the origin of feature A.

5.7. Discussion

5.7.1. Classification. Although there are clear definitions for each subtype of SESN, the actual classification for individual objects can be nontrivial. This is because the classification for some objects can be time-dependent (e.g., Milisavljevic et al., 2013; Folatelli et al., 2014; Williamson et al., 2019; Holmbo et al., 2023). In addition, there is likely a continuum

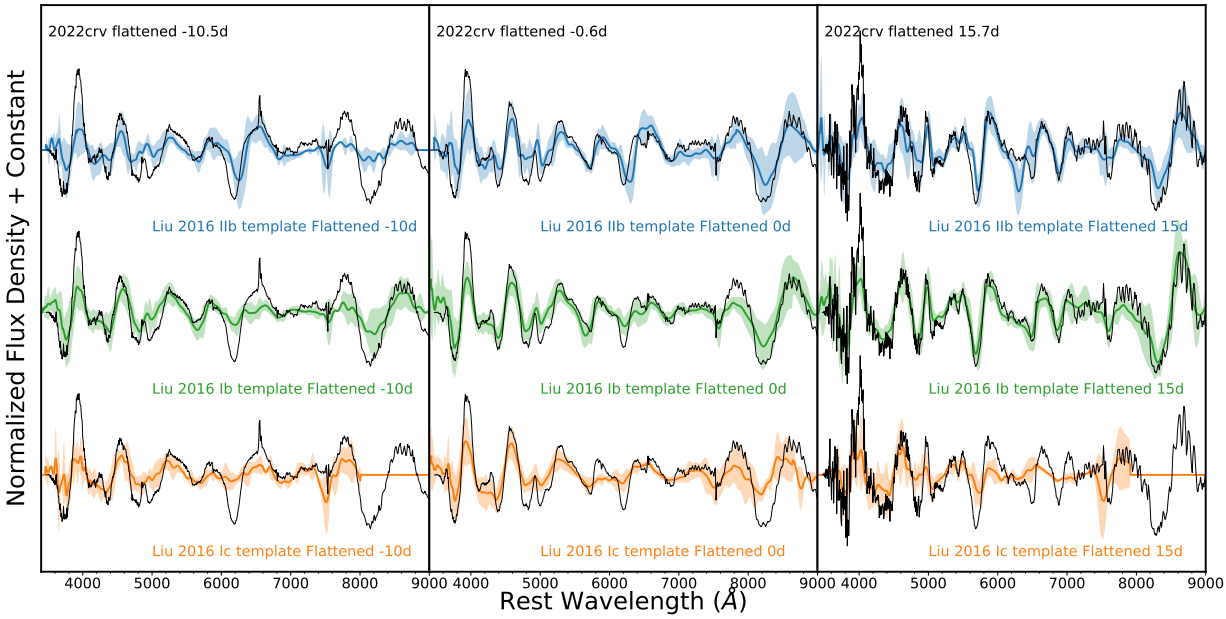

Figure 5.15 Observed spectra of SN 2022crv compared with the mean spectra (the solid lines) and the standard deviations (the shaded regions) of SNe IIb, Ib, and Ic from Liu et al. (2016a). The observed spectra have been flattened using SNID.

between the subtypes (although see Holmbo et al. 2023). For instance, it has been suggested there is likely a gradual transition from Type IIb to Type Ib depending on the amount of residual hydrogen in the envelope (e.g., Prentice & Mazzali, 2017). Furthermore, hydrogen has been suspected to be present in many SNe Ib, suggesting that these objects may still maintain low-mass hydrogen envelopes (e.g., Deng et al., 2000; Branch et al., 2002; Elmhamdi et al., 2006; Parrent et al., 2007; James & Baron, 2010). This makes the distinction between Type Ib and Type IIb more vague.

In recent years, many efforts have been made to improve the classification system of SESNe (Liu et al., 2016a; Prentice & Mazzali, 2017; Williamson et al., 2019; Holmbo et al., 2023). In this section, we will apply the classification methods proposed by Liu et al. (2016a), Prentice & Mazzali (2017), and Williamson et al. (2019) to SN 2022crv. In the studies of Liu et al. (2016a) and Prentice & Mazzali (2017), the absorption line at $\sim$ 6200 Å observed in both Type Ib and Type IIb SNe is attributed to Hα, with the primary differences being the

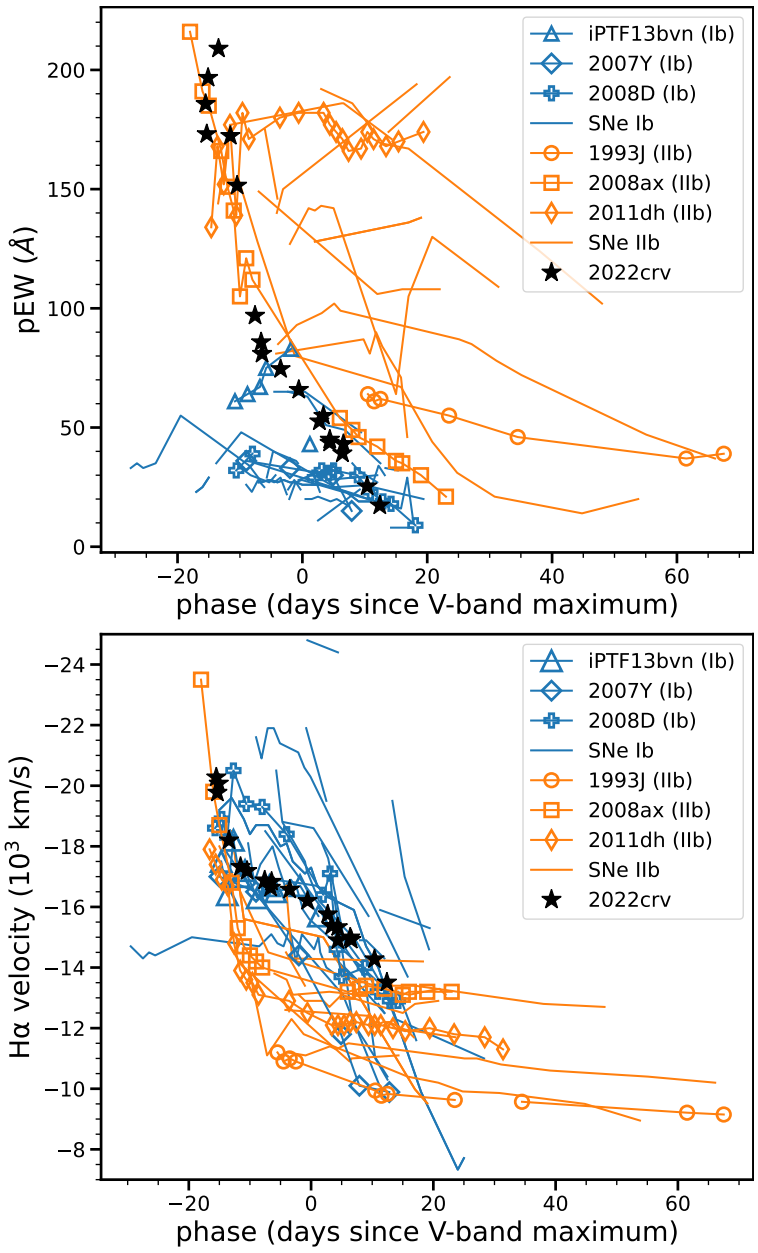

Figure 5.16 *Upper:* The pEW evolution of the 6200 Å feature of SN 2022crv compared with other SESNe. The 6200 Å feature in SN 2022crv shows a large pEW at the beginning, similar to other SNe IIb. Then it quickly decreases until it disappears around 15 days after $V_{\rm max}$. *Bottom:* Velocity evolution of the 6200 Å feature in SN 2022crv assuming it is from Hα. The velocity of the 6200 Å feature in SN 2022crv is generally larger than that in SNe IIb but similar to that in SNe Ib.

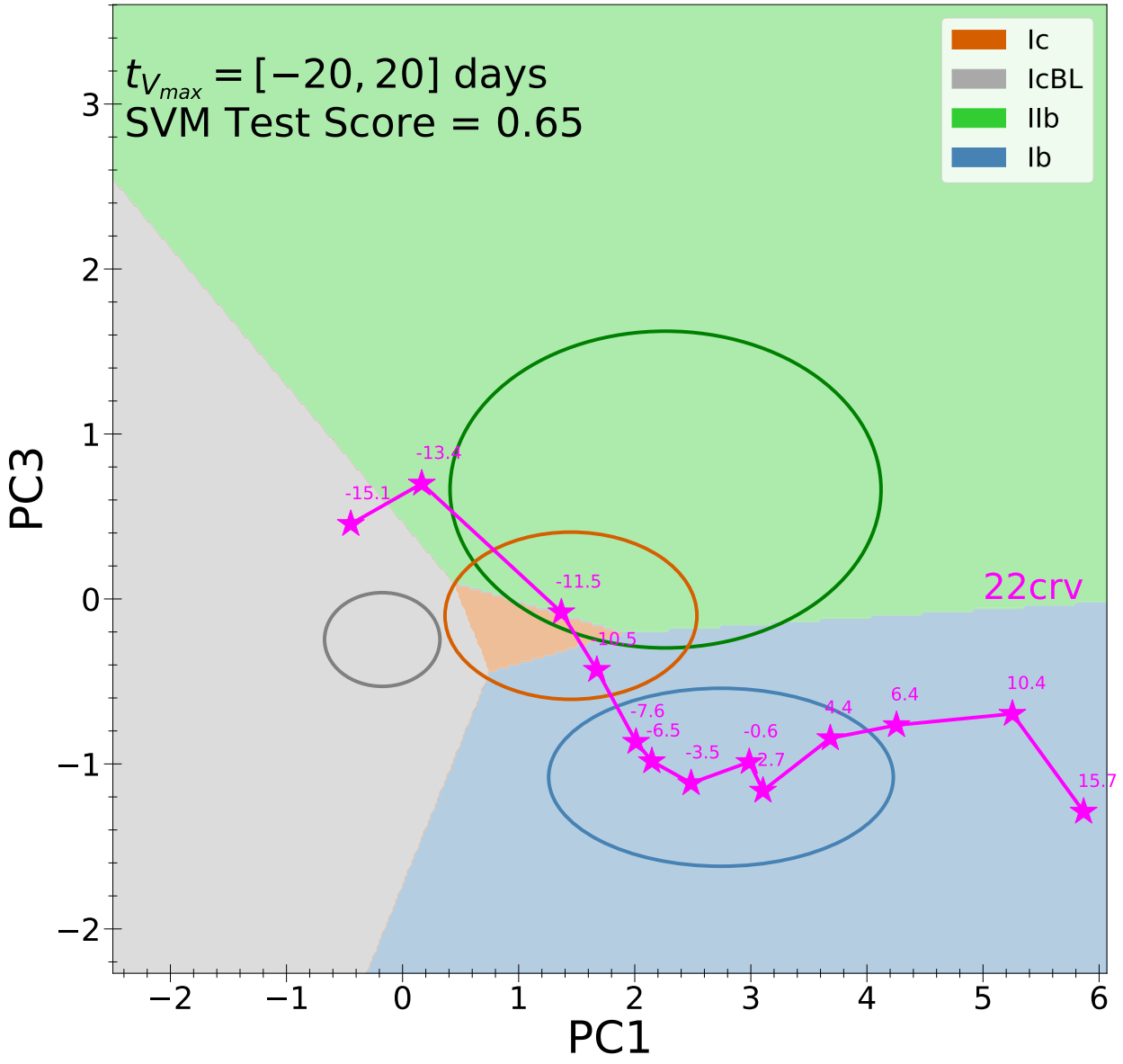

Figure 5.17 An SVM time-dependent spectral classification of SN 2022crv (Williamson & Modjaz 2024, in prep.) based on the methods presented by Williamson et al. (2019). SN 2022crv is classified as a Type IIb SN before around −10 days from V-band maximum brightness. After that, SN 2022crv is more similar to an SN Ib. The trajectory in principal component analysis (PCA) phase space as SN 2022crv evolves (magenta) clearly shows the type transition occurring in the spectra.

evolution and strength of the Hα line. We will discuss the classification of SN 2022crv and demonstrate that this object appears to be an outlier in some of the classification schemes

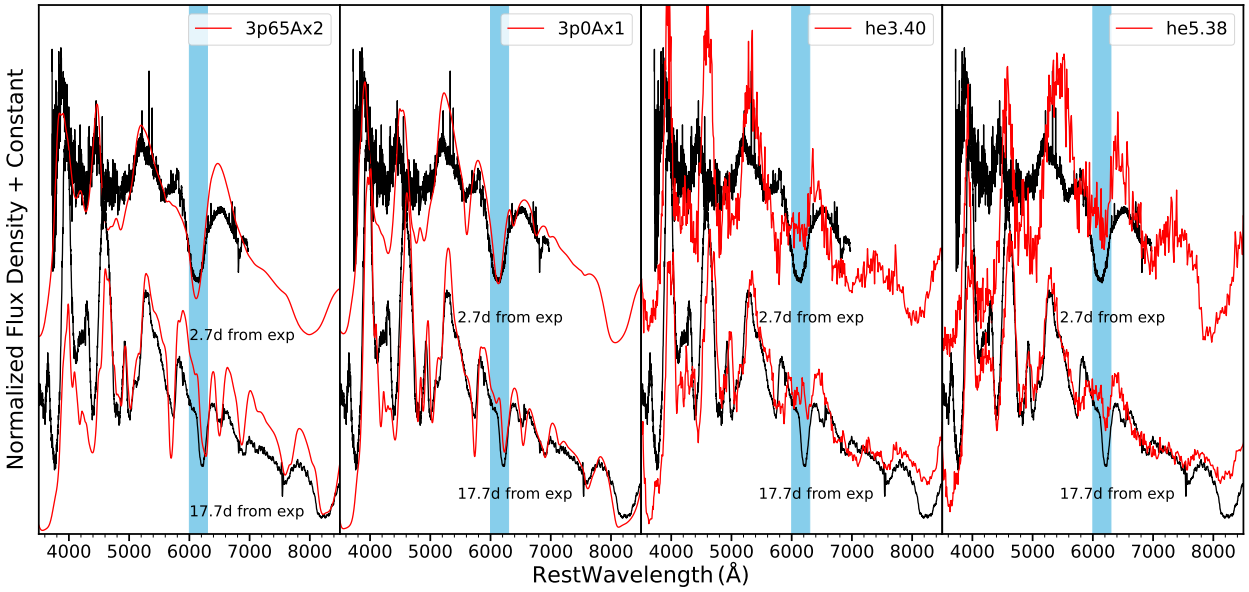

Figure 5.18 Comparison of the optical spectra of SN 2022crv 2.7 and 17.7 days after the explosion with models from Dessart et al. (2016) and Woosley et al. (2021) at similar epochs. The 6200 Å feature is marked by the blue shading. The He3.40 and He5.38 models are hydrogen-free models, while the 3p65Ax2 and 3p0Ax1 models retain a small amount of hydrogen.

mentioned above. It is important to note that the discussion of whether the $\sim$ 6200 Å line in SNe Ib is truly due to Hα is beyond the scope of this paper.

SN 2022crv was initially classified as a Type Ib SN (Andrews et al., 2022). However, as we discussed in Section 5.6, a strong absorption line is visible around 6200 Å during early phases and could be related to Hα. Shortly after maximum brightness, this line disappears and the spectral evolution of SN 2022crv is almost identical to that of other SNe Ib. Such evolution makes SN 2022crv more like a Type IIb SN. A small notch around 4595 Å is observed in the early phases of SN 2022crv (see Figure 5.6) and could be due to Hβ. To get a better sense of where SN 2022crv stands among SESNe, in Figure 5.15 we compare the observed spectra with the mean spectral templates of SNe IIb, Ib, and Ic from Liu et al. (2016a). The observed spectra shown here have been flattened using SNID following the procedure outlined by Blondin & Tonry (2007a). At about days -10 and 0, the 6200 Å absorption line in SN 2022crv is as strong as that in the mean spectra of SNe IIb. The 6200

Å absorption line in SN 2022crv exhibits a higher velocity compared to that in the mean spectra of SNe IIb, and is similar to that in the mean spectra of SNe Ib. At about day 15, the spectrum of SN 2022crv is almost identical to the mean spectra of SNe Ib, while the mean spectra of SNe IIb still display a strong 6200 Å absorption line.

If the 6200 Å line is indeed attributed to Hα, SN 2022crv should be classified as an SN IIb. However, the high velocity and the rapid disappearance of Hα complicates the classification. Liu et al. (2016a) found that the 6200 Å line velocities in SNe Ib are systematically larger than in SNe IIb (assuming the 6200 Å line in SNe Ib is due to Hα), and the pseudoequivalent width (pEW) values of the 6200 Å line in SNe Ib are smaller than in SNe IIb, consistent with the consensus that SNe IIb have more hydrogen in their envelopes. They thus proposed that the pEW can be used to differentiate between SNe Ib and SNe IIb at all epochs. That being said, if an object is classified as a Type Ib/Type IIb using the 6200 Å line pEW, the classification will not change over time since SNe IIb always maintain a larger 6200 Å line pEW. This result has been further supported by Holmbo et al. (2023) based on the spectroscopic analysis of a large sample of SESNe.

In Figure 5.16, we compare the velocity and pEW evolution of the 6200 Å absorption line in SN 2022crv assuming it is from Hα with those of objects presented by Liu et al. (2016a). SN 2022crv shows a high pEW at early phases similar to other SNe IIb, followed by a rapid decline, and has a similar pEW value to other SNe Ib about 10 days after V-band maximum brightness. The velocity of the 6200 Å line in SN 2022crv is generally higher than in SNe IIb and is more similar to that in SNe Ib. This pEW transition from SNe IIb to SNe Ib seems to be an outlier in the classification scheme using the pEW of the 6200 Å line proposed by Liu et al. (2016a).

To quantitatively illustrate the complications involved in this classification, we applied the principal component and SVM classification method described by Williamson et al. (2019). The code has been updated to allow a time-dependent classification of SESNe (Williamson &

Modjaz 2024, in prep.). The result is shown in Figure 5.17. Initially, SN 2022crv is located in the SN Ic-BL (broad line) region. This is likely due to the spectrum at day −15.1 dominated by the strong high-velocity Hα, which can be misidentified as the broad Si II λ6355 line in SNe Ic-BL. At roughly day −13 to day −10, SN 2022crv is more similar to SNe IIb. After day −10, it is more consistent with SNe Ib.

Prentice & Mazzali (2017) proposed to use the strength and ratio between absorption and emission of Hα to classify He-rich SNe. They suggested that He-rich SESNe can be split into four groups [IIb, IIb(I), Ib(II), and Ib] from hydrogen rich to hydrogen poor. Following the method described by Prentice & Mazzali (2017), the ratio between absorption and emission of Hα in SN 2022crv before peak brightness is measured to be ~ 0.3, and the average EW before maximum brightness is about 73 Å. These values make SN 2022crv marginally fall into the IIb(I) category. The ratio between absorption and emission of Hα is a good probe of the extent of the hydrogen envelope, and a larger ratio indicates a more extended hydrogen envelope (Prentice & Mazzali, 2017). A classification of IIb(I) implies that the amount of hydrogen in SN 2022crv is larger than in normal SNe Ib but smaller than in SNe IIb, suggesting that SN 2022crv is an intermediate object between these two classes.

In summary, SN 2022crv shares similarities with both SNe IIb and SNe Ib. The 6200 Å line velocity evolution of SN 2022crv is consistent with that of SNe Ib. The 6200 Å line pEW evolution of SN 2022crv gradually transitions from SNe IIb to SNe Ib, a behavior not observed in the sample studied by Liu et al. (2016a). The amount of hydrogen in SN 2022crv is likely between that in SNe Ib and SNe IIb, suggesting SN 2022crv is a representative transitional object on the proposed continuum between SNe IIb and SNe Ib.

5.7.2. Hydrogen Envelope. Quantifying how much hydrogen is still present in the progenitor right before the explosion is important for understanding the mass-loss history and thus the progenitor system. In this section, we will use both a semianalytic method and

hydrodynamic modeling to constrain the mass of hydrogen retained in the progenitor right before the explosion.

The velocity of Hα in SN 2022crv is generally higher than that of SNe IIb. The higher velocity of Hα could be a result of larger explosion energy or smaller hydrogen mass. Assuming that the He I line appears when the surrounding hydrogen envelope becomes optically thin and the SN expansion is homologous, Marion et al. (2014) proposed a method to roughly estimate the mass of the hydrogen envelope: $M_{\rm H} \propto (v_{\rm H}\, t_{\rm He})^2$, where $v_{\rm H}$ is the velocity of the outer edge of the hydrogen envelope and $t_{\rm He}$ is the time when the He line is first observed, and the constant of proportionality is empirically calculated by scaling to a reference SN. For SN 2022crv, $v_{\rm H}$ is about 30,000 $\rm km\,s^{-1}$. The He line in SN 2022crv can be clearly seen in the first spectrum, so we can limit $t_{\rm He} < 2.7$ d. Using SN 1993J and SN 2011dh as references, we find $\rm M_H(2022crv) < 0.14\,M_H(2011dh)$ and $\rm M_H(2022crv) < 0.05\,M_H(1993J)$. For SN 2011dh and SN 1993J, a recent study by Gilkis & Arcavi (2022) estimated hydrogen masses of $\sim$0.035 $\rm M_\odot$ and $\sim$0.1 $\rm M_\odot$, respectively. Therefore, the hydrogen envelope mass in SN 2022crv can be constrained to be $\rm M_H(2022crv) < 5 \times 10^{-3}\ M_\odot$. This small hydrogen mass is consistent with the higher velocity and the quick disappearance of the Hα in SN 2022crv. However, this seems to contradict the large pEW at early phases.

In order to investigate if a small hydrogen envelope can produce the evolution of the Hα line in SN 2022crv, we compare the observed spectra of SN 2022crv with the SESN models of Dessart et al. (2015, 2016) (3p65Ax2 and 3p0Ax1) and Woosley et al. (2021) (He3.40 and He5.38); see Figure 5.18. The He3.40 and the He5.38 spectra are produced based on models presented by Woosley (2019a) and Ertl et al. (2020a), and they do not include any hydrogen. The 3p65Ax2 and the 3p0Ax1 spectra are based on models presented by Yoon et al. (2010), with hydrogen masses of 4.72×10^{-3} $\rm M_\odot$ and 7.92×10^{-4} $\rm M_\odot$, respectively.

Both the 3p65Ax2 and 3p0Ax1 models nicely reproduce the early-time broad absorption line at 6200 Å and other main features in the observed spectra (Figure 5.18), while the

3p0Ax1 model gives a better fit. The 6200 Å feature in these two models has been attributed to Hα at early phases and Si II before maximum light (Dessart et al., 2015). This is also likely what happened in SN 2022crv. At early times, the broad absorption line at 6200 Å is mainly from hydrogen, but as the object evolves, the 6200 Å feature becomes narrower and more dominated by Si II. The 6200 Å feature is missing in the hydrogen-free He3.40 and He5.38 models at 2.7 d. At 17.7 d after the explosion, these models show weak absorption lines around 6200 Å which are identified as Si II by Woosley et al. (2021). We note that the models we use here are not specifically made for SN 2022crv, so the hydrogen mass we derive can be treated only as an order of magnitude estimate. For example, the models from Dessart et al. (2016) have peak luminosities fainter than that of SN 2022crv, possibly due to a lower explosion energy or lower nickel mass synthesized in the model. Detailed modeling would be required in future studies to better constrain the mass of hydrogen left in the progenitor envelope of SN 2022crv.

The early light curve of SN 2022crv does not show signs of cooling envelope emission, and the nebular spectra also lack hydrogen emission, consistent with the compact progenitor scenario proposed by Chevalier & Soderberg (2010). Therefore, SN 2022crv likely has a compact progenitor with an extremely small amount of hydrogen.

In conclusion, the hydrogen envelope in SN 2022crv is likely on the order of 10^{-3} $M_{\odot}$. From the model comparison, we found that the 6200 Å line is likely a mixture of Hα and Si II. At early phases (within 15 days after the explosion), the 6200 Å line is likely dominated by hydrogen; thereafter, it is likely mainly due to Si II.

5.7.3. Explosion Properties.

5.7.3.1. *Explosion Geometry.* At late times, when the SN ejecta become optically thin, spectra can provide useful information about the inner structure of the SN. For SESNe, the line profile of [O I] $\lambda\lambda$6300, 6364 is often used to study the geometry of the explosion (Mazzali et al., 2005; Maeda et al., 2008; Modjaz et al., 2008; Taubenberger et al., 2009; Milisavljevic

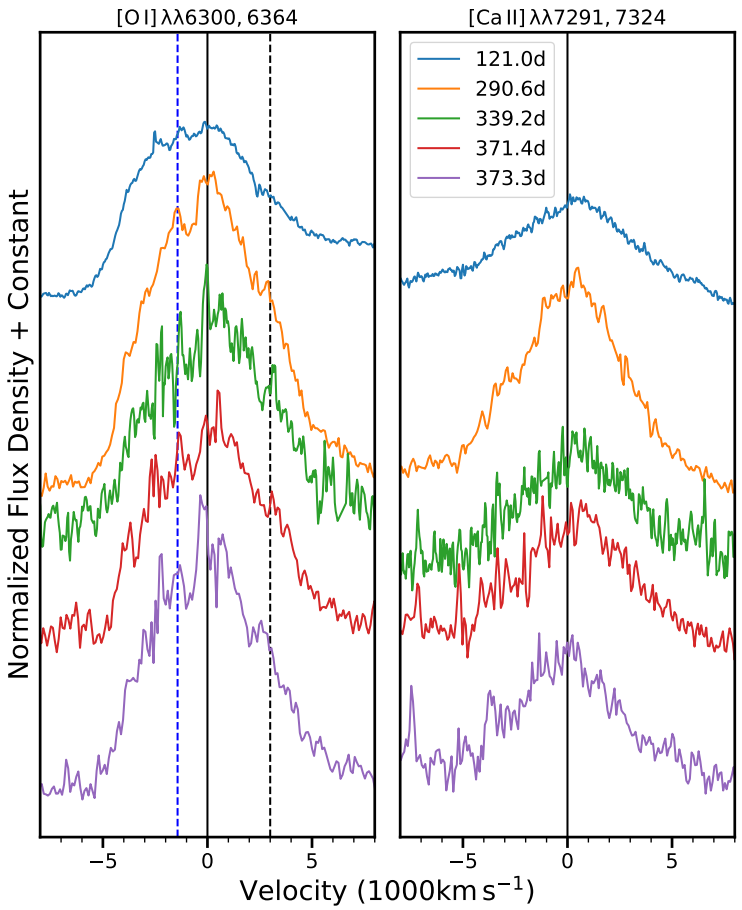

Figure 5.19 Late-time profile of [O I] $\lambda\lambda$6300, 6364 and [Ca II] $\lambda\lambda$7291, 7323. The phase is measured from the explosion. The zero points for [O I] and [Ca II] are 6300 Å and 7307.5 Å respectively, and are marked by the solid vertical lines in each panel. The black vertical dashed line in the left panel indicates 6364 Å. The blue vertical dashed line corresponds to the blueshifted peak around 6270 Å.

et al., 2010; Fang et al., 2022). The [O I] line in SN 2022crv shows an asymmetric profile (see Figure 5.19), with a prominent peak at around 6300 Å and a blueshifted peak around 6270 Å (-1430 km s^{-1}). The separation of the two peaks is 30 Å smaller than the separation of the [O I] $\lambda\lambda$6300, 6364 doublet. An asymmetric profile could originate from the oxygen-rich material with a torus-like structure (Mazzali et al., 2005; Maeda et al., 2008; Valenti et al., 2008). However, in this model, the [O I] line would display either a double-peaked profile if viewed from a direction close to the plane of the torus or a single-peaked profile if viewed

Table 5.6. Nebular spectral models for SN 2022crv.

Model	$M_{\rm ZAMS}$ ($M_\odot$)	$M_{\rm preSN}$ ($M_\odot$)	$M_{\rm He}$ ($M_\odot$)	$M_{\rm O}$ ($M_\odot$)	Reference*
Dessart He5.0	20.8	3.81	5.0	0.592	a
Dessart He6.0	23.3	4.44	6.0	0.974	a
Dessart He8.0	27.9	5.63	8.0	1.71	a
Jerkstrand m12C	12	3.12		0.3	b
Jerkstrand m13G	13	3.52		0.52	b
Jerkstrand m17A	17	5.02		1.3	b

*(a) Woosley (2019a), Ertl et al. (2020a), Dessart et al. (2021); (b) Woosley & Heger (2007), Jerkstrand et al. (2015).

from a direction perpendicular to the torus. Such a scenario is hard to explain in the case of SN 2022crv owing to the lack of a redshifted emission line. If this asymmetric profile is indeed from a torus-like structure, then the emission from the rear side is likely scattered by the ejecta or absorbed by dust (Milisavljevic et al., 2010). For SN 2022crv, a clear sign of CO formation is detected about 100 days after the explosion (Rho et al., in prep.), implying that dust could form at sufficiently late phases.

Maurer et al. (2010) suggested that the double-peaked profile observed in the [O I] line can be caused by the high-velocity Hα absorption. Given that a high-velocity feature is detected at early phases in SN 2022crv, this scenario cannot be ruled out. If the trough around 6285 Å is due to Hα absorption, the corresponding velocity would be $\sim 12,700$ km s^{-1}. There is no clear evidence of Hβ found in the nebular spectra of SN 2022crv, likely owing to the low signal-to-noise ratio of the blue portion of the spectra. If Hα is responsible for the asymmetric profile of the [O I] line, the ejecta of SN 2022crv would be almost spherically symmetric.

5.7.3.2. *Oxygen Mass and Progenitor Mass.* Theoretical studies have shown that the initial progenitor mass of an SN strongly correlates with the oxygen mass in the SN ejecta (Woosley & Weaver, 1995; Jerkstrand et al., 2015; Dessart et al., 2021, 2023). The flux of

the [O I] $\lambda\lambda$6300, 6364 emission line during the nebular phase has been demonstrated to be a powerful diagnostic tool to constrain the oxygen mass (Uomoto, 1986; Jerkstrand et al., 2012; Dessart et al., 2021). In addition, the line ratio of [O I] $\lambda\lambda$6300, 6364/[Ca II] $\lambda\lambda$7291, 7323 can be an indicator of the progenitor mass of an SESN, since synthesized Ca is not sensitive to the main-sequence mass of the progenitor (Nomoto et al., 2006).

Uomoto (1986) showed that the minimal oxygen mass in the SN ejecta can be calculated as

$$\frac{M_{\rm oxygen}}{\rm M_\odot} = 10^8\,(D/{\rm Mpc})^2\,F([{\rm O\ I}])\,\exp(2280\ {\rm K}/T), \tag{5.1}$$

where D is the distance of the SN in Mpc, F([O I]) is the flux of the [O I] line in erg s^{-1} cm^{-2}, and T is the temperature of the oxygen-emitting gas in K. T can be estimated by using the [O I] λ5577/[O I] $\lambda\lambda$6300, 6364 flux ratio (Houck & Fransson, 1996; Elmhamdi et al., 2004). This method is only valid when the gas density is low and the [O I] lines are formed mainly by collisional excitation. However, the [O I] λ5577 line in SN 2022crv is not clearly detected, indicating a low temperature. [O I] λ5577 was also not detected in SN 1990I, and Elmhamdi et al. (2004) put a lower limit on the [O I] λ5577/[O I] $\lambda\lambda$6300, 6364 flux ratio by using a temperature of 3200–3500 K for the line-emitting region of SN 1990I. Sahu et al. (2011) used a temperature of 4000 K for SN 2009jf since the [O I] λ5577 line was not visible in its nebular spectra. For SN 2022crv, we assume the temperature of the line-emitting region is $\sim$ 3200–4000 K, which results in an oxygen mass of $\sim$ 0.9–3.5 M$_\odot$.

In Section 5.6.2, the [O I]/[Ca II] ratio in SN 2022crv is measured to be $\sim$ 1.5. Kuncarayakti et al. (2015) measured the [O I]/[Ca II] ratio in a group of CCSNe, and they found that there is a natural spread among SNe Ib/c. This observed spread is likely an indication of two progenitor populations of SESNe: a single massive Wolf-Rayet star and a low-mass star in a binary system (Kuncarayakti et al., 2015). An [O I]/[Ca II] ratio of 1.5 indicates that the progenitor of SN 2022crv is more likely a less massive star. At solar metallicity, the

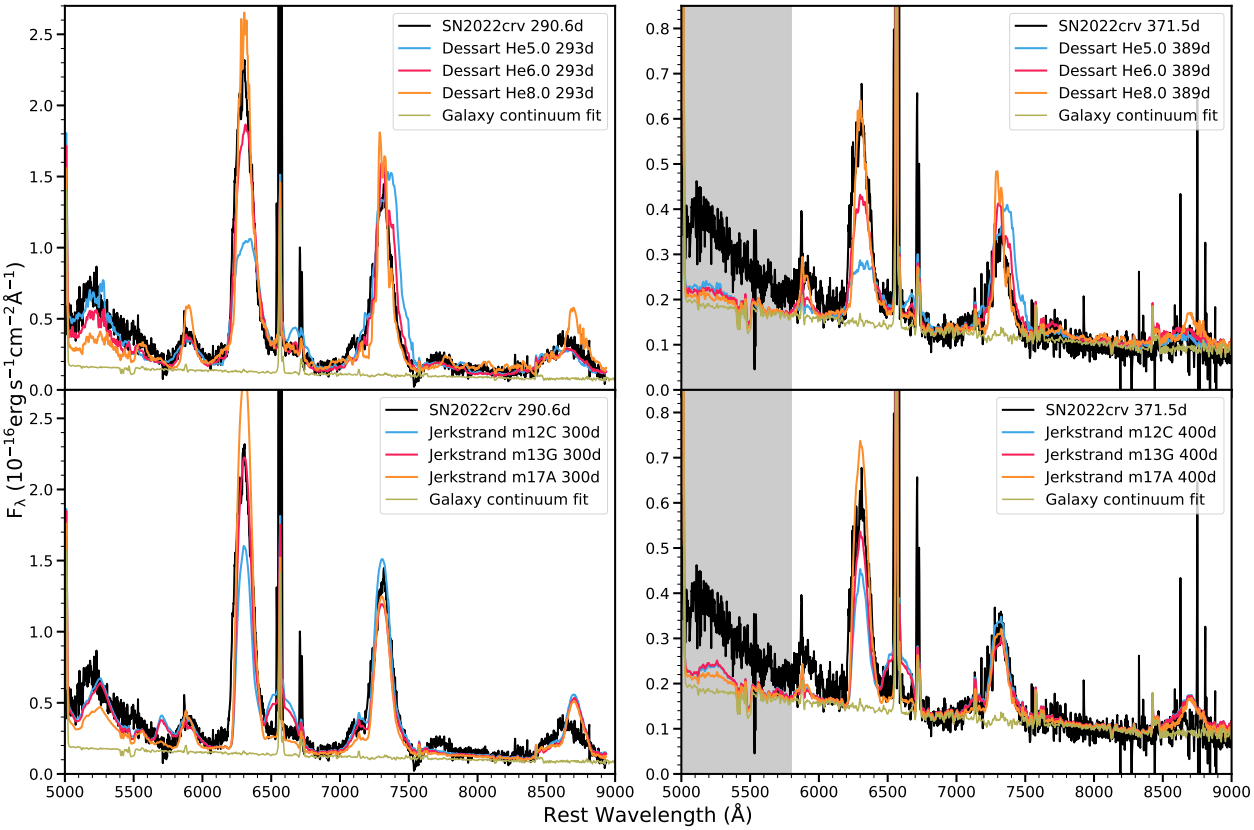

Figure 5.20 Comparison of the nebular spectra of SN 2022crv at 290.6 d and 371.5 d post-explosion with models from Jerkstrand et al. (2015) and Dessart et al. (2021). The spectra are contaminated by the host galaxy, so we fit them with a combination of a star-forming galaxy spectrum and the model SN spectra. For the spectrum at day 371.5, there is strong background contamination below $\sim$ 5800 Å (marked with gray shading), which makes the observed spectrum clearly depart from the assumed star-forming galaxy spectrum.

minimum zero-age main-sequence (ZAMS) mass ($M_{\rm ZAMS}$) for a single star to lose its hydrogen envelope via stellar winds and become a Wolf-Rayet star is about 25–35 $M_\odot$ (Crowther, 2007; Sukhbold et al., 2016b; Ertl et al., 2020a). As we discussed in Section 5.4.4, the metallicity at the location of SN 2022crv is only slightly larger than solar metallicity. This implies that the progenitor was likely in a binary system with $M_{\rm ZAMS}$ less than about 25–35 $M_\odot$, and at least a part of the hydrogen envelope was stripped during the binary interaction.

5.7.3.3. *Progenitor Mass from Nebular Spectral Modeling.* To further constrain the progenitor properties of SN 2022crv, we compare the observed spectrum with theoretical models

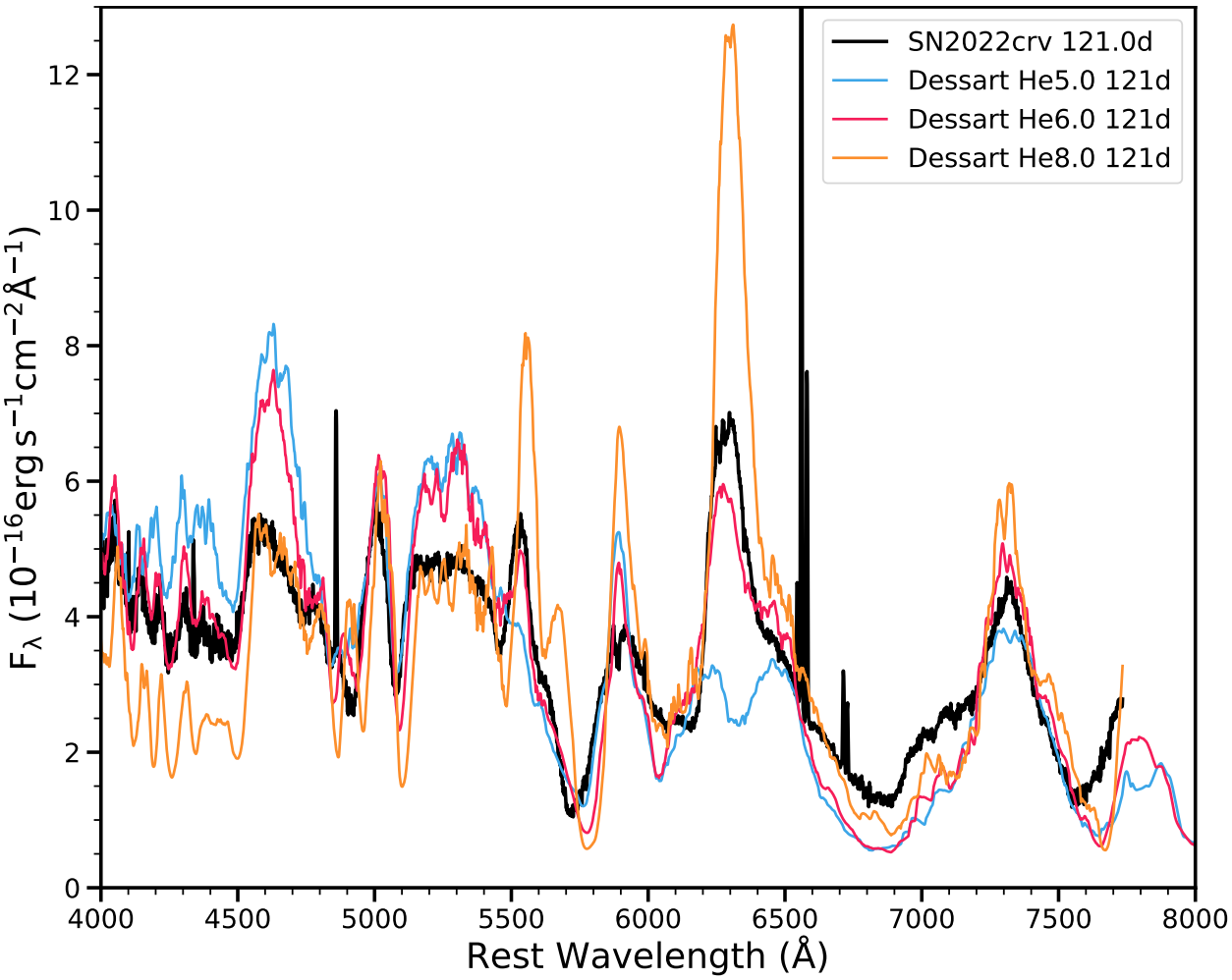

Figure 5.21 Comparison of the spectrum of SN 2022crv at 121 d after the explosion with models from Dessart et al. (2023).

from Jerkstrand et al. (2015), Dessart et al. (2021), and Dessart et al. (2023). Jerkstrand et al. (2015) took the single-star SN II models from Woosley & Heger (2007) and artificially removed most of the hydrogen envelope, and then produced spectra for SNe IIb. Dessart et al. (2021, 2023) modelled nebular spectra of SNe Ib/c based on models from Woosley (2019a) and Ertl et al. (2020a), which also include the effects of wind loss from the He star after the H envelope is fully stripped via the binary interaction. Dessart et al. (2023) found that the spectral features of SESNe are mainly dependent on their presupernova masses

($M_{\rm preSN}$) and the oxygen yields, so these models can provide constraints on the oxygen mass and $M_{\rm preSN}$ of SN 2022crv.

The nebular spectra of SN 2022crv at days 290.6 and 371.5 are likely contaminated by the host-galaxy background. Therefore, we fit the observed spectrum with a linear combination of the SN spectrum and a star-forming galaxy template spectrum from Kinney et al. (1996) as the first-order approximation of the host background. As the SN fades, this contamination becomes more dominant and harder to remove from the SN spectrum. At day 371.5, the object is highly contaminated by the host background below $\sim$ 5800 Å. However, we note that this contamination does not affect our estimation of the progenitor properties since we are only interested in the region redward of $\sim$ 6000 Å. The comparisons are shown in Figure 5.20 and 5.21, while the physical properties of these models are summarized in Table 5.6.

For the models from Dessart et al. (2021, 2023), we found that the [O I] intensity of SN 2022crv is between those of the He6.0 and He8.0 models. Other features of the observed spectrum, such as Na I $\lambda\lambda$5896, 5890, [N II] $\lambda\lambda$ 6548,6583, and [Ca II] $\lambda\lambda$7291, 7323, can also be reproduced by these two models. This indicates that the mass of oxygen in SN 2022crv is 1.0–1.7 $M_\odot$, and $M_{\rm preSN}$ is 4.5–5.6 $M_\odot$. For the models from Jerkstrand et al. (2015), we found that the best-fit models are m13G and m17A, while [N II] $\lambda\lambda$6548, 6583 is stronger in model m13G than in the observed spectrum. This suggests that the oxygen mass produced in SN 2022crv is 0.5–1.3 $M_\odot$, and $M_{\rm preSN}$ is 3.5–5 $M_\odot$.

The oxygen mass and $M_{\rm preSN}$ derived from the models of Dessart et al. (2021, 2023) are consistent with those derived from the models of Jerkstrand et al. (2015), and they are also consistent with the oxygen mass we estimated using the flux of [O I] emission. Since the models in Woosley (2019a) used by Dessart et al. (2021, 2023) employed a more updated progenitor evolution treatment than the models of Woosley & Heger (2007) used by Jerkstrand et al. (2015), we will adopt an oxygen mass of 1.0–1.7 $M_\odot$ and an $M_{\rm preSN}$ of 4.5–5.6 $M_\odot$ derived from models of Dessart et al. (2021, 2023).

The value of $M_{\rm ZAMS}$ of the progenitor depends on the mass-loss history of the progenitor star. Since the progenitor of SN 2022crv only retained a tiny amount of hydrogen before explosion, $M_{\rm preSN}$ is roughly equivalent to its He-core mass. We can put constraints on $M_{\rm ZAMS}$ by considering two extreme mass-loss histories: (1) the whole hydrogen envelope of the progenitor is removed only right before the explosion, similar to the treatment by Jerkstrand et al. (2015); (2) the whole hydrogen envelope of the progenitor is lost close to the time of He ignition, and there is no more mass loss after that, similar to the treatment of the models without mass loss by (Dessart et al., 2023).

In the first case, the He-core mass would continue to grow until the explosion. To achieve the same He-core mass, the progenitor in this scenario would require a smaller $M_{\rm ZAMS}$ than the progenitor of SN 2022crv. From Sukhbold et al. (2016b), we find that a massive star that finally has a He-core mass of 4.5–5.6 $M_\odot$ would have a $M_{\rm ZAMS}$ of $\sim$ 16–19 $M_\odot$. In the second case, the He-core mass stops growing close to the time of He-core ignition. To produce the same He-core mass, $M_{\rm ZAMS}$ in this scenario would be larger than that of SN 2022crv's progenitor. Based on Eq. 4 of Woosley (2019a), we find that a massive star that has a He-core mass of 4.5–5.6 $M_\odot$ at He ignition would have a $M_{\rm ZAMS}$ of $\sim$ 20–22 $M_\odot$. Therefore, $M_{\rm ZAMS}$ of the progenitor of SN 2022crv can be roughly constrained to be $\sim$ 16–22 $M_\odot$. However, we note that it is possible that the mass loss rate prescriptions in stellar evolution models of Sukhbold et al. (2016b) could be too high compared to those observed in red supergiants (Beasor et al., 2020). How this affects the $M_{\rm ZAMS}$ we derive here is beyond the scope of this paper.

In Section 5.4.4, we found that the metallicity at the site of SN 2022crv is slightly larger than solar metallicity, implying that the progenitor experienced strong stellar wind mass loss. However, the progenitor of SN 2022crv ($M_{\rm ZAMS} \approx$ 16–22 $M_\odot$) is still not massive enough to strip most of its hydrogen envelope by itself (Crowther, 2007; Sukhbold et al., 2016b), so the progenitor has to be in a binary system.

Binary interaction usually cannot fully strip the hydrogen envelope from the progenitor star (Yoon et al., 2017; Götberg et al., 2017). Whether the progenitor can shed the rest of the hydrogen depends on its wind mass-loss rate (Yoon et al., 2017; Gotberg et al., 2023). Since the progenitor of SN 2022crv likely had a high mass-loss rate ($\sim 2 \times 10^{-5}$ $M_\odot\,yr^{-1}$; Gangopadhyay et al., 2023), the orbital separation of the binary system needs to be large to prevent the hydrogen envelope from being fully stripped by wind and binary interaction (Yoon et al., 2017; Götberg et al., 2017; Gotberg et al., 2023). Yoon et al. (2017) studied a grid of SN Ib/IIb models in binary systems, and they found that at metallicity $Z = 0.02$, assuming a mass ratio of $q = 0.9$, an orbital period above 2000 days (or an initial orbital separation larger than ~ 2200 $R_\odot$) is required for a progenitor with $M_{\rm ZAMS} = 18$ $M_\odot$ in a binary system in order to have some remaining hydrogen envelope left. For a progenitor with $M_{\rm ZAMS} = 16$ $M_\odot$, the orbital period would be larger than ~ 1700 days, which is equivalent to an initial orbital separation of ~ 1900 $R_\odot$. If the initial orbital separation is on the order of 100 $R_\odot$, the progenitor would lose all its hydrogen envelope with $Z \approx 0.02$. Therefore, the progenitor of SN 2022crv was likely in a binary system with an initial orbital separation larger than ~ 1000 $R_\odot$.

In conclusion, by comparing with hydrodynamic models, we found that the oxygen synthesized in the progenitor is about 1.0–1.7 $M_\odot$, and the progenitor is likely a He star with a final mass of $\sim$ 4.5–5.6 $M_\odot$ that has evolved from a 16–22 $M_\odot$ ZAMS star. Given the high mass-loss rate at the SN site and the very low-mass hydrogen envelope, the progenitor of SN 2022crv is likely in a binary system with a large initial orbital separation.

5.7.3.4. ^{56}Ni *Model Fit.* In order to estimate the physical parameters of the object, we applied a simple analytical model to the bolometric light curve of SN 2022crv obtained in Section 5.5.2. This "Arnett model" was proposed for Type Ia SNe (Arnett, 1982; Sutherland & Wheeler, 1984; Cappellaro et al., 1997), and can also be used for SESNe (Clocchiatti &

Wheeler, 1997; Valenti et al., 2008, 2011; Chatzopoulos et al., 2009, 2012; Lyman et al., 2016).

Following Valenti et al. (2008), we divided the light curve into photospheric and nebular phases. We assumed an optical opacity $\kappa_{\rm opt} = 0.07$ cm^2 g^{-1} and a γ-ray opacity $\kappa_\gamma = 0.027$ cm^2 g^{-1}. The exact ^{56}Ni and ^{56}Co decay data presented by Nadyozhin (1994) were used for calculations. For the photospheric phase, we note that the gamma-ray leakage term we adopted is slightly different from what some studies have used in the literature (e.g., Chatzopoulos et al. 2012).

Specifically, the bolometric light-curve evolution during the photospheric phase is written as

$$\begin{aligned} L_{\rm bol,phot}(t) = M_{\rm Ni,0}\ e^{-x^2} \\ \times [(\epsilon_{\rm Ni} - \epsilon_{\rm Co}) \int_0^x A(z)\Gamma(z)dz \\ + \epsilon_{\rm Co} \int_0^x B(z)\Gamma(z)dz], \end{aligned} \tag{5.2}$$

where x is a function of time, $\Gamma(z)$ is the gamma-ray leakage term, and $\tau_{\rm Co}$ and $\tau_{\rm Ni}$ represent the rates of energy production for ^{56}Co and ^{56}Ni (respectively). For detailed expressions of $A(z)$ and $B(z)$, we refer the reader to (Valenti et al., 2008). The γ-ray leakage term here is a function of time, so it should be included within the integral. Although not explicitly mentioned by Valenti et al. (2008), in that study the γ-ray leakage term was actually within the integral when calculating the model light curves, as we do here.

The fit was conducted with an MCMC method. The free parameters are t_0, $M_{\rm ej}$, and $M_{\rm Ni,0}$ with uniform priors, where t_0 is the explosion epoch. The upper and lower bounds of t_0 are set to be the first detection and the last nondetection, respectively. The fitting range was chosen to be from -10 to 15 days from mamximum light and 60 days post-maximum following Valenti et al. (2008) and Lyman et al. (2016). The best-fitting parameters are

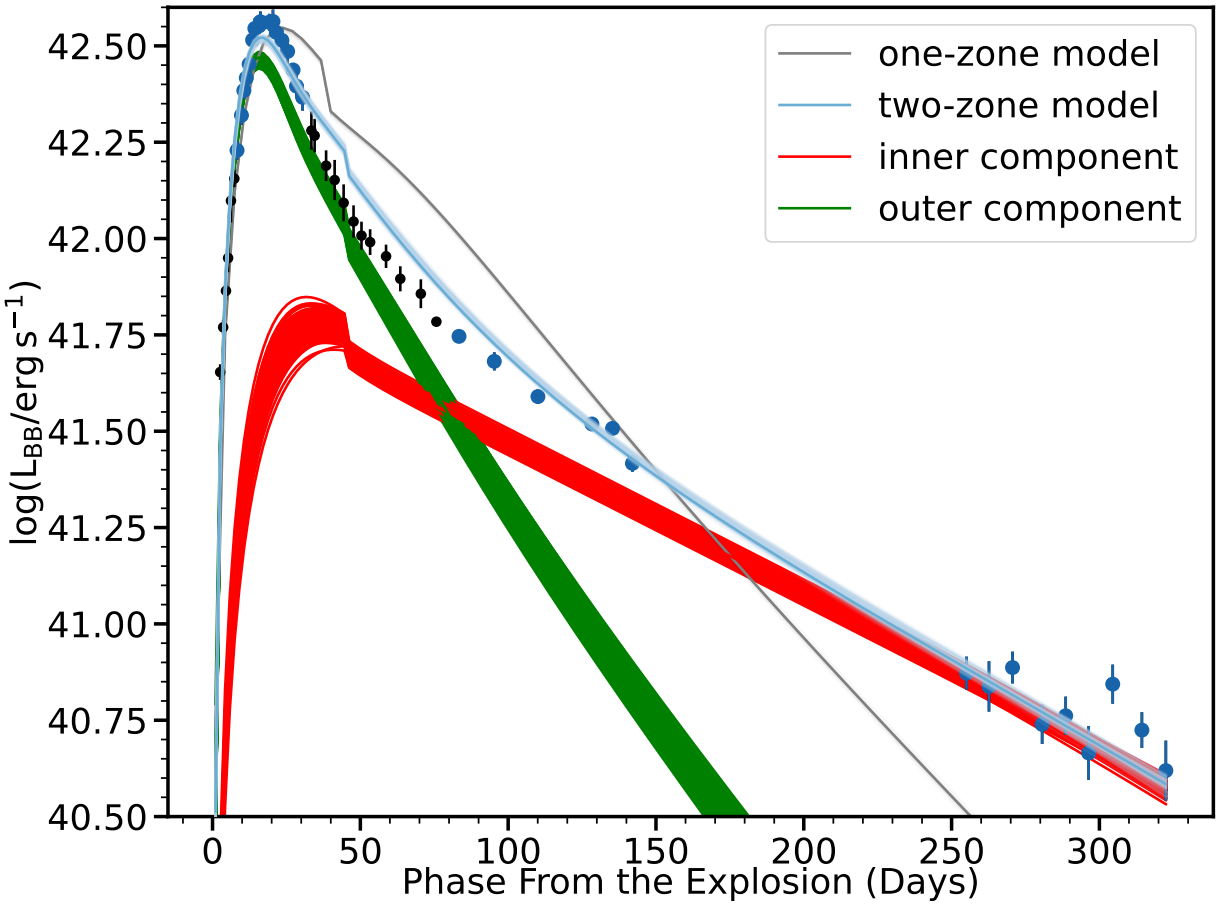

Figure 5.22 Arnett model fit of the bolometric light curve. The fit is done with an MCMC routine. The best-fitting results are represented by the 100 randomly chosen models drawn from the MCMC chain. The blue lines are the two-component fit and the gray lines are the one-component fit. The red lines and the green lines are the contributions from the inner region and the outer region, respectively. Only the blue points are used for the fit. The phase is shown with respect to the explosion epoch.

constrained to be $M_{\rm Ni,0} = 0.21^{+0.01}_{-0.01}\,{\rm M}_\odot$, $M_{\rm ej} = 4.61^{+0.07}_{-0.05}\,{\rm M}_\odot$, and $E_{\rm kin} = 2.22^{+0.02}_{-0.03} \times 10^{51}$ erg. The best-fitting model is shown in Figure 5.22 (black line).

The model we use here cannot simultaneously reproduce the photospheric and nebular phases of the light curve of SN 2022crv. If we fit these two phases separately, the nickel mass derived from the photospheric phase will be larger than that derived from the nebular phase. The ejecta mass derived from the photospheric phase is too small, resulting in a low γ-ray trapping rate at late phases, leading to a too steep tail. This contradiction can be

easily solved if a two-zone model is considered, one of which dominates the photospheric phase and the other contributes to the nebular phase (Valenti et al., 2008). In the model we adopted above, the nickel is assumed to be concentrated in the center of the progenitor. To explain the observational properties of SESNe, nickel needs to be mixed in the ejecta to some extent (Woosley & Eastman, 1997; Dessart et al., 2012; Bersten et al., 2013; Dessart et al., 2015, 2016; Yoon et al., 2019). Therefore, we adopted the two-zone model initially proposed by Maeda et al. (2003) that has been used for some SESNe (Valenti et al., 2008, 2011; Cano et al., 2014). However, we note that since dust likely started to form at late phases in SN 2022crv (Rho et al., in prep.), dust attenuation could also contribute to this contradiction. If this is true, the late-time light curve would be brighter than what we have calculated. Therefore, the nickel mass obtained by only fitting the nebular phase would actually be larger, which would ease the contradiction.

In this model, the SN ejecta are divided into two separate zones: a high-density inner region and a low-density outer region. The nickel is assumed to be homogeneously distributed in the two regions. In this two-zone model, the free parameters are the time of explosion t_0, the total nickel mass $M_{\rm Ni,total}$, the total ejecta mass $M_{\rm ej,total}$, the kinetic energy of the inner region $E_{\rm kin,inner}$, and the mass fraction of the inner region to the whole ejecta $F_{\rm inner}$. The final best-fitting parameters are constrained to be $M_{\rm Ni,total} = 0.18^{+0.01}_{-0.01}\,{\rm M}_\odot$, $M_{\rm ej,total} = 2.59^{+0.07}_{-0.08}\,{\rm M}_\odot$, $E_{\rm kin,total} = 0.88^{+0.02}_{-0.02} \times 10^{51}$ erg, and $F_{\rm inner} = 0.30^{+0.01}_{-0.01}$. The two-component model does give a better fit and the best-fitting model is shown in Figure 5.22.

Lyman et al. (2016) analyzed a group of bolometric light curves of SESNe by fitting the Arnett model. They found that the average explosion parameters for SNe IIb are $M_{\rm Ni} = 0.11(0.04)\,{\rm M}_\odot$, $M_{\rm ej} = 2.2(0.8)\,{\rm M}_\odot$, and $E_{\rm kin} = 1.0(0.6) \times 10^{51}$ erg. For SNe Ib, these values are $M_{\rm Ni} = 0.17(0.16)\,{\rm M}_\odot$, $M_{\rm ej} = 2.6(1.1)\,{\rm M}_\odot$, and $E_{\rm kin} = 1.6(0.9) \times 10^{51}$ erg. Similar values have also been found for SESNe in more recent studies (e.g., Taddia et al., 2018). The

parameters we derived for SN 2022crv are more similar to those of SNe Ib, but considering the uncertainties, they are consistent with those of both SNe IIb and Ib.

5.7.3.5. ^{56}Ni + *Magnetar Fit.* Magnetars are thought to be a possible energy source for SESNe (Maeda et al., 2007; Kasen & Bildsten, 2010). We use a hybrid model in which the object is powered by both ^{56}Ni decay and magnetar spin down. The luminosity of an SN powered by a central magnetar can be written as (Wang et al., 2015)

$$L_{\rm bol,mag} = e^{-x^2} \times \frac{E_{\rm NS}}{\tau_{\rm NS}} \times \int_0^x C(z)dz\,, \tag{5.3}$$

where $C(z) = 2ze^{z^2}/(1+z\frac{\tau_m}{\tau_{\rm NS}})^2(1-e^{-A(z\tau_m)^{-2}})$, with $A = \frac{3\kappa_\gamma M_{\rm ej}}{4\pi v^2}$. Also,

$$E_{\rm NS} = 2\times10^{52}\frac{M_{\rm NS}}{1.4\,M_\odot}\left(\frac{P_0}{1\text{ ms}}\right)^{-2}\left(\frac{R_{\rm NS}}{10\text{ km}}\right)^2 \text{ erg} \tag{5.4}$$

and

$$\tau_{\rm NS} = 1.3\left(\frac{B}{10^{14}\text{ G}}\right)^{-2}\left(\frac{P_0}{10\text{ ms}}\right)^2 \tag{5.5}$$

are the rotational energy and the spin-down timescale of the magnetar, respectively.

We found that the best-fitting model is dominated by the magnetar, and only a small amount of nickel is present in the ejecta. However, for SESNe, a certain amount of nickel should be in the ejecta and power the early part of the light curve (e.g., Woosley, 2019a; Woosley et al., 2021). Therefore, a magnetar-dominated model is likely not suitable in the case of SN 2022crv.

5.7.3.6. *Search for a Progenitor Candidate.* We identified a pre-explosion image at the site of SN 2022crv in the Mikulski Archive for Space Telescopes (MAST). This image was taken with the *Hubble Space Telescope* (*HST*) Wide Field Planetary Camera (WFPC2) in the F606W filter (PI Stiavelli, SNAP-6359) on 1997 March 27.

We employed a 60 s r-band MODS acquisition image of the SN obtained with the LBT on 2022 March 10 to isolate the SN position in the *HST* image mosaic. 17 stars were

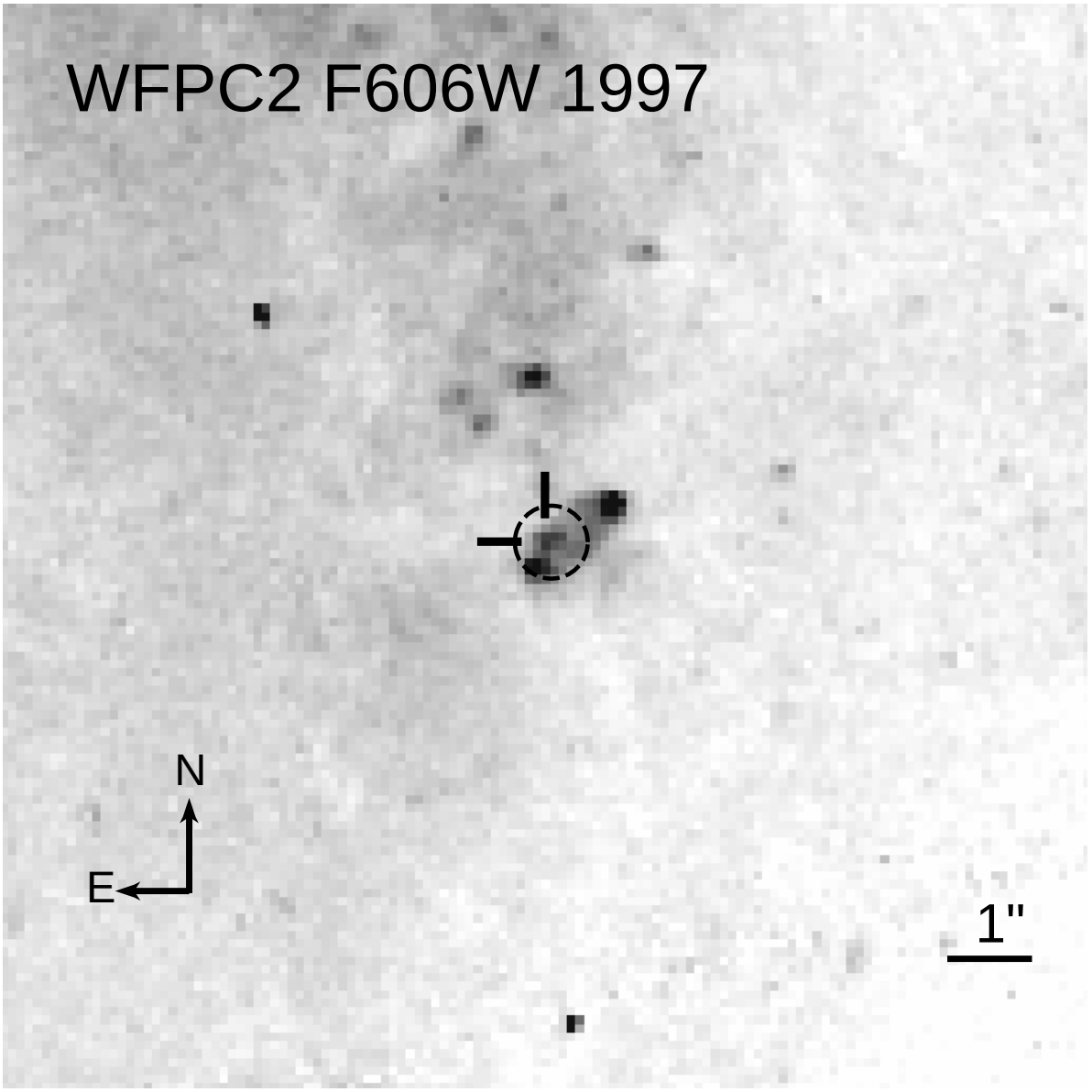

Figure 5.23 A portion of the *HST* WFPC2 F606W image mosaic from March 1997, with the location of the SN site indicated by a dashed circle (with radius corresponding to the 3σ uncertainty in the astrometric registration using an LBT r-band image of the SN from March 2022). A stellar-like object with $M_{\rm F606W} \approx -8.2$ mag is indicated by the black tick marks. We tentatively identify this object as the progenitor candidate. North is up, and east is to the left.

identified in common between the two image datasets. Using Photutils centroiding and the PyRAF tasks `geomap` and `geotran`, we were able to locate the position with a 1σ astrometric uncertainty of 1.4 WFPC2 pixels ($0\farcs14$; see Figure 5.23). The SN site appears to be in a luminous complex of stars or star clusters. We subsequently ran Dolphot (Dolphin, 2016) with point-spread-function (PSF) fitting photometry on the individual WFPC2 frames and found an object, indicated to be stellar by the routine, with brightness $m_{\rm F606W} = 24.07 \pm 0.05$ mag. Corrected by our assumed distance and extinction to SN 2022crv, this corresponds to an absolute brightness of $M_{\rm F606W} \approx -8.2$ mag.

We tentatively identify this object as the progenitor candidate, although some caution should be applied, given the comparatively low *HST* resolution with WFPC2. Additionally, with only the single *HST* band, we have no knowledge of the object's color. Nevertheless, a comparison of its inferred luminosity with that of SN 2011dh's progenitor reveals interesting insights. Maund et al. (2011) found $M_{\rm F555W} \approx -7.5$ mag at the assumed distance of 7.1 Mpc. This number is adjusted to ~ -7.6 mag based on the recent Cepheid distance from Csörnyei et al. 2023. Similarly, Van Dyk et al. (2011) estimated $M_V^0 \approx -7.7$ mag at an assumed distance of 7.6 Mpc. Therefore, the progenitor candidate for SN 2022crv appears to be plausible, albeit somewhat more luminous than the SN 2011dh progenitor. We note, however, that Eldridge et al. (2015) found that the absolute brightness of the iPTF13bvn progenitor was at most $M_{\rm F555W} \approx -6.5$ mag, so the progenitor candidate for SN 2022crv is significantly more luminous. Whether this object is truly the SN progenitor will require confirmation, with follow-up *HST* observations when the SN has faded significantly (well below mag 24 in F606W).

5.8. Summary

We present optical and NIR observations of SN 2022crv. In general, the optical photometric and spectroscopic evolution of SN 2022crv resembles those of both SNe IIb and Ib. The object showed conspicuous high-velocity H lines at early phases around 6200 Å, which

rapidly disappeared shortly after maximum brightness. The 6200 Å line in SN 2022crv is likely due to Hα at early phases and is dominated by Si II λ6355 after maximum light. The evolution of the Hα line pEW in SN 2022crv is similar to those of SNe IIb at early phases, but falls into the SN Ib category shortly after maximum light. In addition, we applied an SVM classification method to the spectra ranging from -15 days to 15 days relative to peak brightness, classifying SN 2022crv as an SN IIb before -10 days and an SN Ib afterward. This makes SN 2022crv a transitional object on the continuum between SNe Ib and IIb, suggesting that there is a continuum between these two SN subtypes.

We found that a hydrogen envelope mass of $\sim 10^{-3}$ $M_\odot$ in the progenitor can reproduce the behaviors of the H lines in SN 2022crv, and the progenitor is constrained to be a He star with a final mass of $\sim$ 4.5–5.6 $M_\odot$ evolving from a $\sim$ 16–22 $M_\odot$ ZAMS star in a binary system. Since the progenitor of SN 2022crv likely experienced relatively strong mass loss, an initial orbital separation of the binary system larger than ~ 1000 $R_\odot$ is needed in order to retain a small amount of the hydrogen envelope. We found that the bolometric light curve of SN 2022crv can be best fitted by a model with a nickel mass of $0.18^{+0.01}_{-0.01}\,M_\odot$, $M_{\rm ej}$ of $2.59^{+0.07}_{-0.08}\,M_\odot$, and $E_{\rm kin}$ of $0.88^{+0.02}_{-0.02} \times 10^{51}$ erg.

The NIR spectroscopic evolution of SN 2022crv is generally similar to that of other SNe IIb/Ib. However, an extra absorption feature is observed in the NIR spectra, near the blue side of the He I λ1.083 μm line, referred to as feature A in this paper. To the best of our knowledge, feature A has never been observed in other SNe IIb/Ib. We found that this line is most likely from Sr II λ1.0327 μm, but we could not safely exclude Fe I λ1.05 μm and S I λ1.0457 μm. Future detailed modeling is required to further investigate the origin of feature A.

The peculiar features observed in the optical and NIR spectra of SN 2022crv illustrate that SESNe still have many unsolved mysteries. This emphasizes the importance of obtaining NIR spectra and the early discovery of SESNe. As the number of SESNe characterized with

detailed datasets increases, the gap between SNe IIb and SNe Ib could be filled, giving us a comprehensive picture of the evolutionary channel and history of the SESN progenitors.

Acknowledgements

We thank Luc Dessart for providing the model spectra and beneficial discussions, as well as J. Craig Wheeler, Emmanouil Chatzopoulos, and Jozsef Vinkó for useful discussions. We acknowledge Stanford Woosley for generating and providing the model spectra, and Sung-Chul Yoon for providing the model light curves. We are grateful to the staffs at the various observatories where data were obtained. Y.D. would like to thank the hospitality and support of L.Z. in Philadelphia during completion of this paper.

Research by Y.D., S.V., N.M.R, E.H., and D.M. is supported by National Science Foundation (NSF) grant AST-2008108. Time-domain research by the University of Arizona team and D.J.S. is supported by NSF grants AST-1821987, 1813466, 1908972, 2108032, and 2308181, and by the Heising-Simons Foundation under grant #2020-1864. M.M. acknowledges support in part from ADAP grant 80NSSC22K0486, from NSF grant AST-2206657, and from *HST* grant GO-16656. This work makes use of data from the Las Cumbres Observatory global telescope network. The Las Cumbres Observatory group is supported by NSF grants AST-1911151 and AST-1911225. N.E.R. acknowledges support from the PRIN-INAF 2022, "Shedding light on the nature of gap transients: from the observations to the models." K.A.B. is supported by an LSSTC Catalyst Fellowship; this publication was thus made possible through the support of Grant 62192 from the John Templeton Foundation to LSSTC. The opinions expressed in this publication are those of the authors and do not necessarily reflect the views of LSSTC or the John Templeton Foundation. L.A.K. acknowledges support by NASA FINESST fellowship 80NSSC22K1599. S.M. acknowledges support from the Magnus Ehrnrooth Foundation and the Vilho, Yrjö, and Kalle Väisälä Foundation. L.G. acknowledges financial support from the Spanish Ministerio de Ciencia e Innovación

(MCIN), the Agencia Estatal de Investigación (AEI) 10.13039/501100011033, and the European Social Fund (ESF) "Investing in your future" under the 2019 Ramón y Cajal program RYC2019-027683-I and the PID2020-115253GA-I00 HOSTFLOWS project, from Centro Superior de Investigaciones Científicas (CSIC) under the PIE project 20215AT016, and the program Unidad de Excelencia María de Maeztu CEX2020-001058-M. M.D.S. is funded by the Independent Research Fund Denmark (IRFD) via Project 2 grant 10.46540/2032-00022B. The SALT data presented here were obtained through Rutgers University programs 2021-1-MLT-007 and 2022-1-MLT-004 (PI S.W.J.). A.V.F.'s research group at UC Berkeley acknowledges financial assistance from NASA/HST grant AR-14259 from STScI, the Christopher R. Redlich Fund, Gary and Cynthia Bengier, Clark and Sharon Winslow, Alan Eustace (W.Z. is a Bengier-Winslow-Eustace Specialist in Astronomy), William Draper, Timothy and Melissa Draper, Briggs and Kathleen Wood, Sanford Robertson (T.G.B. is a Draper-Wood-Robertson Specialist in Astronomy), and numerous other donors.

Based in part on observations obtained at the international Gemini Observatory, a program of NSF's NOIRLab, which is managed by the Association of Universities for Research in Astronomy (AURA) under a cooperative agreement with the NSF. On behalf of the Gemini Observatory partnership: the National Science Foundation (United States), National Research Council (Canada), Agencia Nacional de Investigación y Desarrollo (Chile), Ministerio de Ciencia, Tecnología e Innovación (Argentina), Ministério da Ciência, Tecnologia, Inovações e Comunicações (Brazil), and Korea Astronomy and Space Science Institute (Republic of Korea). This work was enabled by observations made from the Gemini North telescope, located within the Maunakea Science Reserve and adjacent to the summit of Maunakea. We are grateful for the privilege of observing the Universe from a place that is unique in both its astronomical quality and its cultural significance.

Some of the data reported here were obtained at the MMT Observatory, a joint facility of the University of Arizona and the Smithsonian Institution. This paper uses data gathered

with the 6.5 m Magellan telescopes at Las Campanas Observatory, Chile. The LBT is an international collaboration among institutions in the United States, Italy, and Germany. LBT Corporation Members are The University of Arizona on behalf of the Arizona Board of Regents; Istituto Nazionale di Astrofisica, Italy; LBT Beteiligungsgesellschaft, Germany, representing the Max-Planck Society, The Leibniz Institute for Astrophysics Potsdam, and Heidelberg University; The Ohio State University, and The Research Corporation, on behalf of The University of Notre Dame, University of Minnesota and University of Virginia.

This research is based in part on observations made with the NASA/ESA *Hubble Space Telescope* obtained from the Space Telescope Science Institute, which is operated by the Association of Universities for Research in Astronomy, Inc., under NASA contract NAS 5-26555. The data were obtained from the Mikulski Archive for Space Telescopes (MAST) at the Space Telescope Science Institute.

Based in part on observations made with the Gran Telescopio Canarias (GTC), installed at the Spanish Observatorio del Roque de los Muchachos of the Instituto de Astrofísica de Canarias, on the island of La Palma. This work is partly based on data obtained with the instrument OSIRIS, built by a Consortium led by the Instituto de Astrofísica de Canarias in collaboration with the Instituto de Astronomía of the Universidad Autónoma de México. OSIRIS was funded by GRANTECAN and the National Plan of Astronomy and Astrophysics of the Spanish Government.

KAIT and its ongoing operation at Lick Observatory were made possible by donations from Sun Microsystems, Inc., the Hewlett-Packard Company, AutoScope Corporation, Lick Observatory, the U.S. NSF, the University of California, the Sylvia & Jim Katzman Foundation, and the TABASGO Foundation. A major upgrade of the Kast spectrograph on the Shane 3 m telescope at Lick Observatory, led by Brad Holden, was made possible through generous gifts from the Heising-Simons Foundation, William and Marina Kast, and the University of California Observatories. We thank U.C. Berkeley undergraduate students Ivan

Altunin, Kate Bostow, Kingsley Ehrich, Nachiket Girish, Neil Pichay, and James Sunseri for their effort in taking Lick/Nickel data. Research at Lick Observatory is partially supported by a generous gift from Google.

Some of the data presented herein were obtained at the W. M. Keck Observatory, which is operated as a scientific partnership among the California Institute of Technology, the University of California, and NASA; the observatory was made possible by the generous financial support of the W. M. Keck Foundation.

This research has made use of the NASA/IPAC Extragalactic Database (NED), which is funded by the National Aeronautics and Space Administration and operated by the California Institute of Technology.

This research made use of Photutils, an Astropy package for detection and photometry of astronomical sources (Bradley et al., 2022).

CHAPTER 6

SN 2023fyq: A Type Ibn Supernova With Long-standing Precursor Activity Due to Binary Interaction

Dong et al. 2024 (under review), submitted to ApJ. arXiv, arXiv:2405.04583.

6.1. Abstract

We present photometric and spectroscopic observations of SN 2023fyq, a type Ibn supernova in the nearby galaxy NGC 4388 (D$\simeq$18 Mpc). In addition, we trace the three-year-long precursor emission at the position of SN 2023fyq using data from DLT40, ATLAS, ZTF, ASAS-SN, Swift, and amateur astronomer Koichi Itagaki. The double-peaked post-explosion light curve reaches a luminosity of $\sim 10^{43}$ erg s^{-1}. The strong intermediate-width He lines observed in the nebular spectrum imply the interaction is still active at late phases. We found that the precursor activity in SN 2023fyq is best explained by the mass transfer in a binary system involving a low-mass He star and a compact companion. An equatorial disk is likely formed in this process ($\sim$0.6M$_\odot$), and the interaction of SN ejecta with this disk powers the main peak of the supernova. The early SN light curve reveals the presence of dense extended material ($\sim$0.3M$_\odot$) at $\sim$3000R$_\odot$ ejected weeks before the SN explosion, likely due to final-stage core silicon burning or runaway mass transfer resulting from binary orbital shrinking, leading to rapid rising precursor emission within $\sim$30 days prior to explosion. The final explosion could be triggered either by the core-collapse of the He star or by the merger of the He star with a compact object. SN 2023fyq, along with SN 2018gjx and SN 2015G, forms a unique class of Type Ibn SNe which originate in binary systems and are likely to

exhibit detectable long-lasting pre-explosion outbursts with absollute magnitudes ranging from -10 to -13.

6.2. Introduction

Type Ibn supernovae (SNe) are a subclass of interaction-powered SNe that show narrow helium (He) lines but not hydrogen (H) lines in their spectra (e.g., Smith, 2017; Modjaz et al., 2019). Although it has been more than two decades since the discovery of the first Type Ibn SN (SN 1999cp, Matheson et al. 2000), our understanding of Type Ibn progenitors remains limited. The light curves of Type Ibn SNe tend to be short-lived and some of them even resemble the evolution of fast-evolving transients (Ho et al., 2023; Fox & Smith, 2019). A general interpretation is that SNe Ibn are Wolf-Rayet/He stars that experience enhanced mass loss right before the SN explosion. The interaction of SN ejecta with the surrounding dense He-rich circumstellar material (CSM) powers some of the SN light curve and ionizes the outer CSM, producing the narrow lines we observe (Pastorello et al., 2007; Hosseinzadeh et al., 2017).

Light curve modeling of Type Ibn SNe has supported the presence of dense CSM close to the progenitors (Gangopadhyay et al., 2020; Pellegrino et al., 2022; Ben-Ami et al., 2023). Both SNe Ibn and their H-rich counterparts, SNe IIn, have CSM interaction signatures that point to pre-SN mass loss that is much stronger than normal massive-star winds (Smith, 2014b, 2017). However, the mechanisms driving the enhanced mass loss near the time of explosion remain a subject of active debate. This enhanced mass loss could be attributed to the final-stage stellar activities of massive stars, where the dense CSM could be produced by eruptive outbursts through pulsational pair instability (Yoshida et al., 2016; Woosley, 2017) or wave-driven outbursts excited by late-stage nuclear burning (Quataert & Shiode, 2012; Shiode & Quataert, 2014; Fuller, 2017; Fuller & Ro, 2018; Morozova et al., 2020). Alternatively, the dense CSM might be generated through binary interactions (Smith, 2014b; Smith & Arnett, 2014b; Metzger, 2022; Wu & Fuller, 2022; Dessart et al., 2022; Tsuna et al.,

2024). In this scenario the progenitor does not necessarily have to be a very massive star, as the mass loss would be significantly enhanced by the presence of a binary companion.

One way to constrain the progenitor of Type Ibn SNe is by searching for evidence of a massive star or a binary companion in deep images once the SN fades. The absence of evidence for massive star progenitors and the possible detection of binary companions have been reported for some Type Ibn SNe (Maund et al., 2016; Shivvers et al., 2017; Hosseinzadeh et al., 2019).

Alternatively, a direct way to constrain the mass loss history of SN progenitors is by searching for signs of pre-explosion activity or precursor emission prior to the SN explosion. Precursor emission is commonly observed in Type IIn SNe (e.g., Mauerhan et al., 2013; Smith et al., 2010; Ofek et al., 2013; Tartaglia et al., 2016; Pastorello et al., 2013, 2018; Hiramatsu et al., 2024). The bright precursor outbursts in Type IIn SNe may be due to eruptive mass loss from LBV-like progenitors (e.g., Smith, 2017) or pulsational pair instability outbursts (Smith & McCray, 2007; Woosley et al., 2007; Smith, 2014b). Alternatively, these outbursts could be caused by red supergiants with a compact object companion (Fryer & Woosley, 1998; Schrøder et al., 2020; Smith et al., 2024; Tsuna et al., 2024), or other late-stage binary interaction (Smith & Arnett, 2014b). To date, precursor emission has been identified in two Type Ibn SNe, SN 2006jc (Pastorello et al., 2007) and SN 2019uo (Strotjohann et al., 2021a). The precursor outbursts in these events are shorter and fainter compared to those observed in Type IIn SNe, and have been interpreted as resulting from single massive star activities or binary interactions (Pastorello et al., 2007; Foley et al., 2007; Smith et al., 2008; Tsuna et al., 2024).

In this paper we present the optical observations of SN 2023fyq, one of the closest SNe Ibn. The light curves and spectra of this object closely resemble those of Type Ibn SNe. Notably, relatively steady precursor activity is observed up to approximately three years prior to the SN explosion. The detection of precursor emission in SN 2023fyq allows us

to investigate the final-stage stellar activity and the nature of its progenitor system. The pre-explosion observations of SN 2023fyq are also presented in Brennan et al. (2024), where they identify an asymmetric CSM structure, likely related to unstable stellar activities of the progenitor.

The paper is organized as follows: the photometric and spectroscopic observations are described in Section 6.3. We constrain the reddening and distance of SN 2023fyq in Section 6.4. We describe the photometric and spectroscopic evolution of SN 2023fyq in Sections 6.5 and 6.6. The progenitor scenario and the physical mechanism of precursor activities are discussed in Section 6.7. We summarize the main results in Section 6.8.

6.3. Observations

SN 2023fyq was discovered on 2023 April 17 by the Zwicky Transient Facility (ZTF) survey at RA(2000) = $12^h25^m45^s.847$, Dec(2000) = $+12°39'48''.87$ in NGC 4388 (De, 2023) (see Figure 6.1). On 2023 June 14 a rapid rebrightening of SN 2023fyq was observed and reported by amateur astronomer Koichi Itagaki. On 2023 June 25 SN 2023fyq was classified as a peculiar Type Ib due the presence of helium lines and the lack of hydrogen lines in the optical spectrum (Valerin et al., 2023).

In this section we present the photometric data of SN 2023fyq taken by Las Cumbres Observatory (Brown et al., 2013c) via the Global Supernova Project, the Distance Less Than 40 Mpc (DLT40, Tartaglia et al., 2018) survey, ZTF (Bellm et al., 2019; Graham et al., 2019), the Asteroid Terrestrial-Impact Last Alert System (ATLAS, Tonry 2011; Tonry et al. 2018; Smith et al. 2020b), the All-Sky Automated Survey for Supernovae (ASAS-SN, Shappee et al. 2014c; Kochanek et al. 2017b), the Neil Gehrels *Swift* Observatory (Gehrels et al., 2004), and amateur astronomer Itagaki. We also report the spectroscopic followup of SN 2023fyq taken after the SN explosion. All spectroscopic observations from this paper

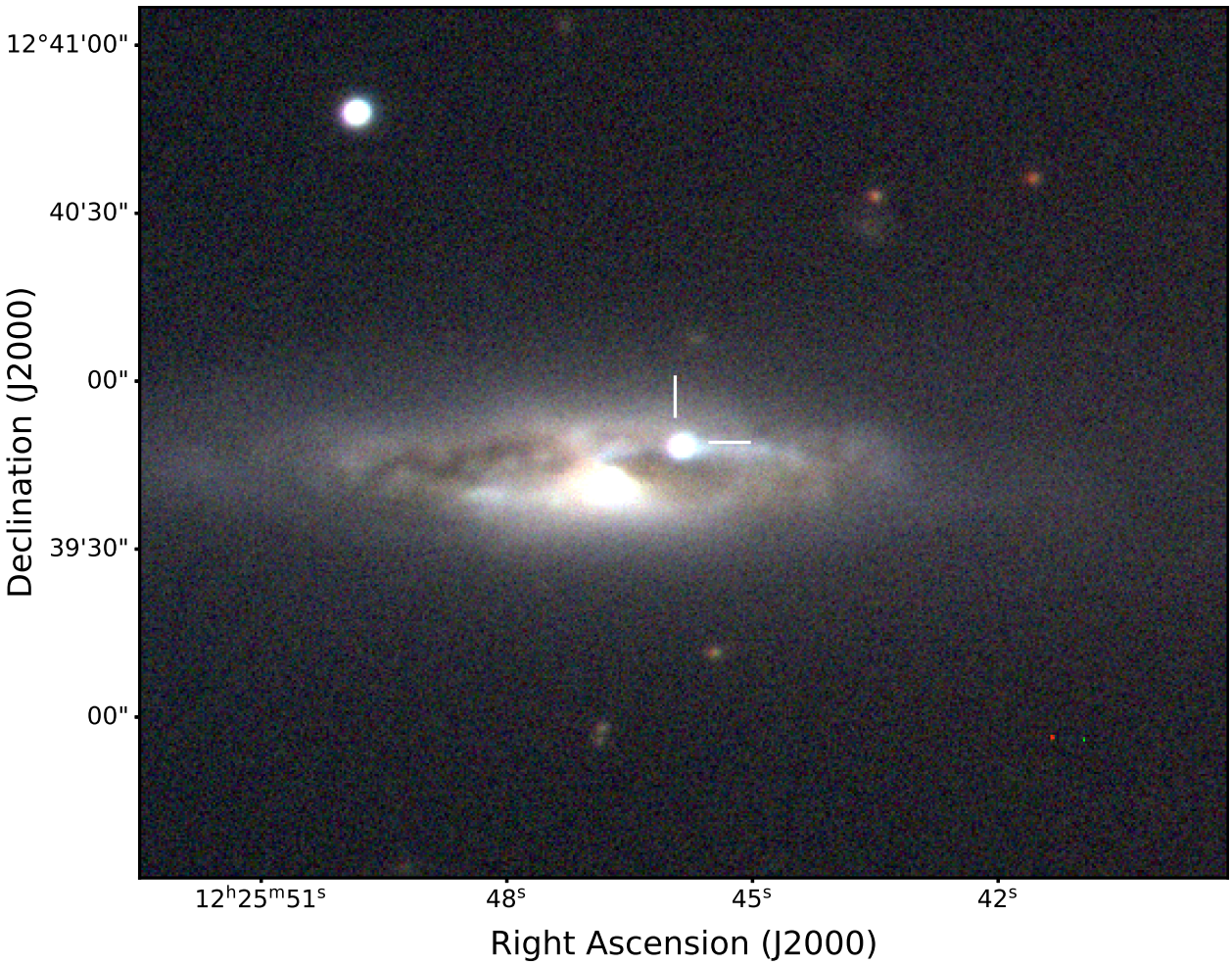

Figure 6.1 Composite *gri* image of SN 2023fyq in NGC 4388 obtained with the Las Cumbres Observatory on 2023 August 11. The position of SN 2023fyq is indicated by white tick markers.

can be found at https://github.com/yizedong/SN2023fyq_data and will be available on WISeREP (Yaron & Gal-Yam, 2012)[1].

6.3.1. Photometric Observations. For the photometry we adopt a signal-to-noise threshold of 3 for source detections and a signal-to-noise threshold of 5 for computing the upper limit, following the suggestions of Masci (2011). The light curves are shown in Figure 6.2 and 6.3.

[1] https://www.wiserep.org/

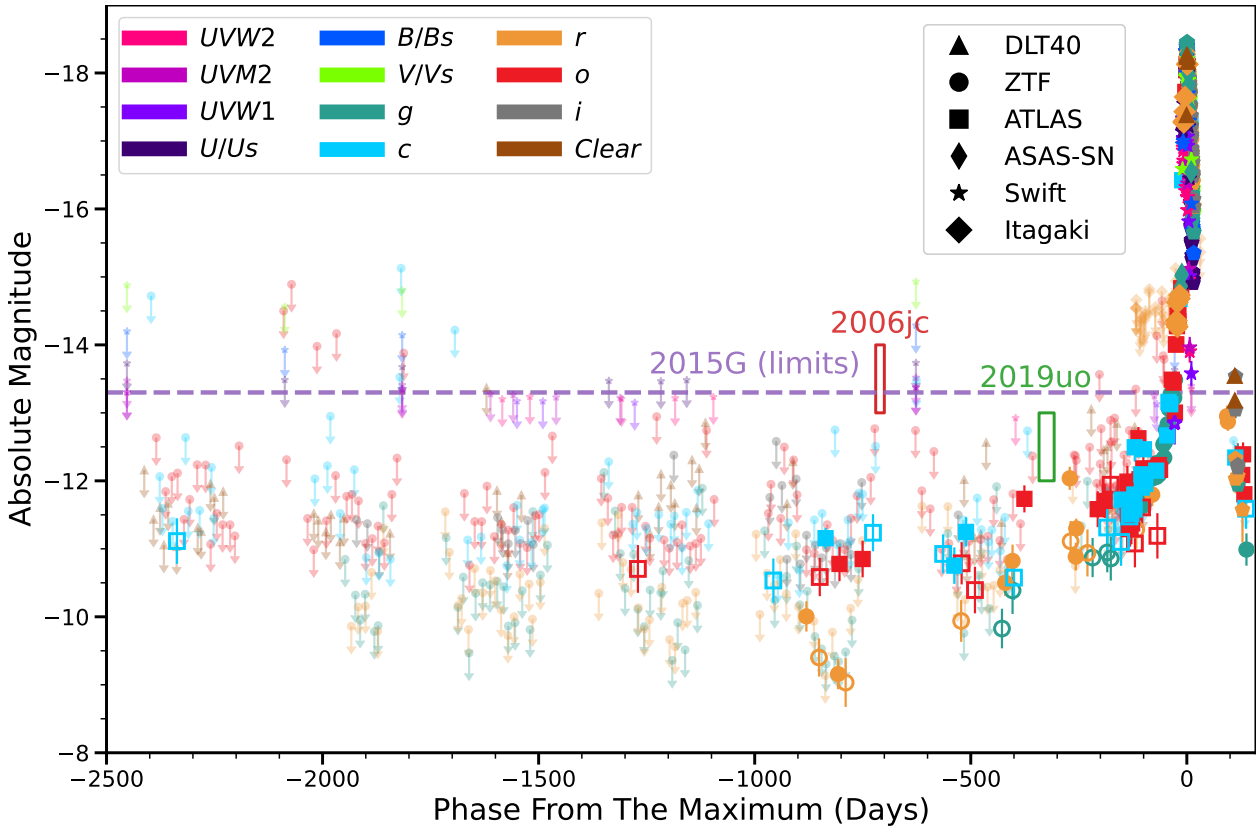

Figure 6.2 Photometric limits and detections of SN 2023fyq prior to and after explosion. Detections with S/N>4 are indicated by large solid symbols, while detections with 3<S/N≤4 are indicated by hollow symbols. The smaller symbols are nondetection limits with S/N≤3. The precursor activities detected in Type Ibn SN 2006jc (R band) and SN 2019uo (r band) are indicated in the red and green rectangles, respectively. The limits on the precursor activities on Type Ibn SN 2015G are shown with the purple dashed line. All of the bands are in the AB magnitude system.

6.3.1.1. *Las Cumbres Observatory Observations.* Our multiband photometric followup campaign with Las Cumbres Observatory was initiated on 2023 July 26. The images were reduced using the PyRAF-based photometric reduction pipeline LCOGTSNPIPE (Valenti et al., 2016). Apparent magnitudes were calibrated using the APASS (g, r, i) and Landolt (U, B, V) catalogs.

6.3.1.2. *DLT40 Observations.* The DLT40 survey is a targeted one-day cadence SN search for very young transients within 40 Mpc (Tartaglia et al., 2018; Yang et al., 2019c).

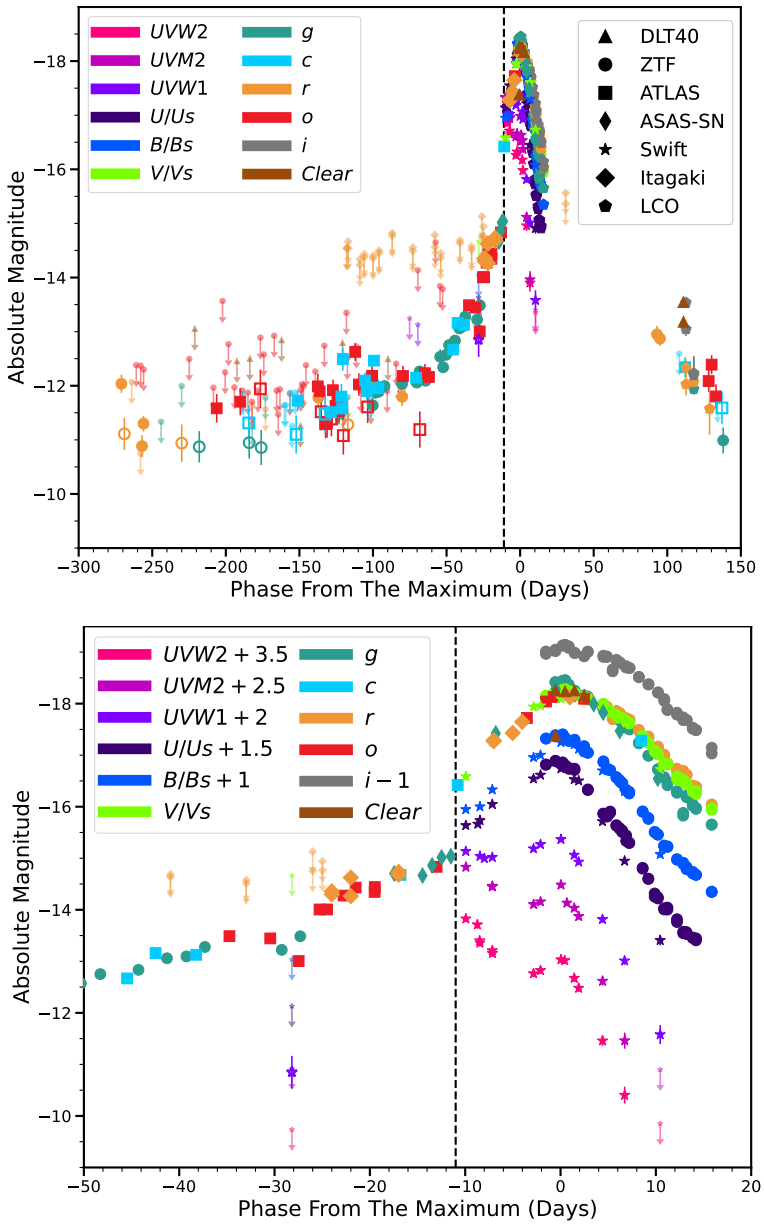

Figure 6.3 The light curve evolution of SN 2023fyq. The *Clear* filter is calibrated to the r band. The hollow symbol indicates the data with $3<S/N\leq4$, while the solid symbol indicates the data with $S/N>4$. Light curves in the bottom panel have been shifted by the indicated amounts to enhance clarity. All of the bands are in the AB magnitude system. The black dashed line marks the epoch of the first light of the SN (−11 d), as adopted in the paper.

DLT40 has been monitoring the field of SN 2023fyq since 2014 in the *Clear* filter. All of the images have been visually inspected to remove those with bad qualities, including

images taken at full moon, images with pointing issues, and images with irregular point spread functions. A deep template was made with the images taken between 2014 June 20 and 2015 February 01 using Swarp (Bertin et al., 2002). The rest of the images were stacked in windows of 15 days and were then subtracted against the template using HOTPANTS (Becker, 2015). We used aperture photometry at the position of SN 2023fyq through a pipeline based on Photutils (Bradley et al., 2022). The photometry was calibrated to the r band.

6.3.1.3. *ZTF Observations.* ZTF is a time-domain survey using a wide-field camera mounted on the Palomar 48-inch Schmidt telescope (Bellm et al., 2019; Graham et al., 2019). The ZTF public survey searches for transients and variables in the northern sky with a three-day cadence in g and r filters.

The position of SN 2023fyq has been monitored by ZTF since 2018. We obtained the reference image subtracted forced photometry from the ZTF Forced Photometry Service (Masci et al., 2023b). We removed bad-quality data following the instructions in Masci et al. (2023b). For images taken after -300d, the transient was bright enough to be detected in single images, and so the observations were stacked in 1-day time bins. For images taken prior to -300d, the observations were stacked in 15-day time bins to improve the signal to noise ratio (S/N).

6.3.1.4. *ATLAS Observations.* The ATLAS survey is an all-sky daily cadence survey (Smith et al., 2020b) carried out in two filters, cyan (c) and orange (o), roughly equivalent to Pan-STARRS filters $g + r$ and $r + i$, respectively.

The position of SN 2023fyq has been monitored by ATLAS since 2015. Forced photometry at the supernova position was obtained from the ATLAS forced photometry server (Shingles et al., 2021). Using the method presented in Young (2022), we stacked the measurements to improve the signal-to-noise ratio and obtain deeper upper limits. For images taken after

−300d, the observations were stacked in 1-day time bins. For images taken before −300d, the observations were stacked in 15-day time bins.

6.3.1.5. *ASAS-SN Observations.* ASAS-SN is an untargeted all-sky survey to a depth of g∼18.5 mag. (Shappee et al., 2014c; Kochanek et al., 2017b). We obtained the ASAS-SN reference image subtracted forced photometry from the ASAS-SN sky portal[2].

6.3.1.6. *Swift Observations.* The position of SN 2023fyq has been observed by the UVOT instrument on the Neil Gehrels *Swift* Observatory (Gehrels et al., 2004) since 2015. We performed aperture photometry at the position of SN 2023fyq on *Swift* UVOT images using the High-Energy Astrophysics software (HEA-Soft). Background variations in individual images were removed using an aperture placed on a blank section of the sky. To remove the underlying galaxy background contamination, we subtracted the flux extracted from *Swift* UVOT images taken on 2016 November 08. Zero-points were chosen from Breeveld et al. (2011) with time-dependent sensitivity corrections updated in 2020.

6.3.1.7. *Koichi Itagaki's Observations.* We also incorporated observations taken with Koichi Itagaki's Bitran BN-83MCCD imager mounted on a 0.5m telescope in Okayama Prefecture, Japan. We solved the astrometry of the images using Astrometry.net (Lang et al., 2010). The aperture photometry was performed using a pipeline based on Photutils (Bradley et al., 2022) and was calibrated to r-band magnitudes in the Sloan system (Fukugita et al., 1996).

6.3.2. Spectroscopic Observations. We collected four optical spectra from the FLOYDS spectrograph (Brown et al., 2013c) on the 2m Faulkes Telescope South in Australia at the Las Cumbres Observatory via the Global Supernova Project. The FLOYDS spectra were reduced following standard procedures using the FLOYDS pipeline (Valenti et al., 2014a). We triggered Gemini-North Target of Opportunity (ToO) observations with the Gemini Multi-Object Spectrograph (GMOS; Hook et al., 2004) and the B600 grating on 2023 July 27 and

[2]https://asas-sn.osu.edu/

2023 August 01 through proposal GN-2023A-Q-136. The Gemini spectra were reduced by using the IRAF Gemini package. We triggered further ToO observations with the Andalucia Faint Object Spectrograph and Camera (ALFOSC) on the Nordic Optical Telescope (NOT) at the Spanish "Roque de los Muchachos" Observatory (ORM) on 2023 August 04 through proposal 67-112. The NOT ALFOSC spectrum was observed using Grism #4 and a 1.″0 slit and was reduced using the PypeIt pipeline (Prochaska et al., 2020; Prochaska et al., 2020). We obtained spectra on 2023 December 12 and 2024 May 1 from the Low-Resolution Imaging Spectrometer (LRIS; Oke et al., 1995) on the Keck I telescope. The LRIS spectra were reduced in a standard way using the LPipe pipeline (Perley, 2019). A low-resolution spectrum was taken on 2024 January 23 with the Goodman High Throughput Spectrograph (GHTS) on the Southern Astrophysical Research Telescope (SOAR; Clemens et al., 2004), and was reduced with the Goodman pipeline (Torres et al., 2017). One spectrum was obtained with the Multi-Object Double Spectrographs (MODS, Pogge et al., 2010) on the twin 8.4 m Large Binocular Telescope (LBT) at Mount Graham International Observatory. The spectrum was reduced using standard techniques, including bias subtraction and flat-fielding using the MODSCCDred package (Pogge, 2019) and further reduced with IRAF including cosmic ray rejection, local sky subtraction, and extraction of one-dimensional spectra. A log of the spectroscopic observations is presented in Table 4.1. We also present an unpublished nebular spectrum of Type Ibn SN 2019kbj taken at 80 d after the peak. The spectrum was taken on 2019 September 23 with the DEep Imaging Multi-Object Spectrograph (DEIMOS, Faber et al., 2003) on the Keck II telescope. The DEIMOS spectrum was reduced using the PypeIt pipeline (Prochaska et al., 2020; Prochaska et al., 2020). A detailed analysis of SN 2019kbj has been presented in Ben-Ami et al. (2023).

6.4. Observational Properties

6.4.1. Reddening. The empirical correlation between the equivalent width (EW) of the Na I D line and the amount of gas and dust along the line of sight has often been

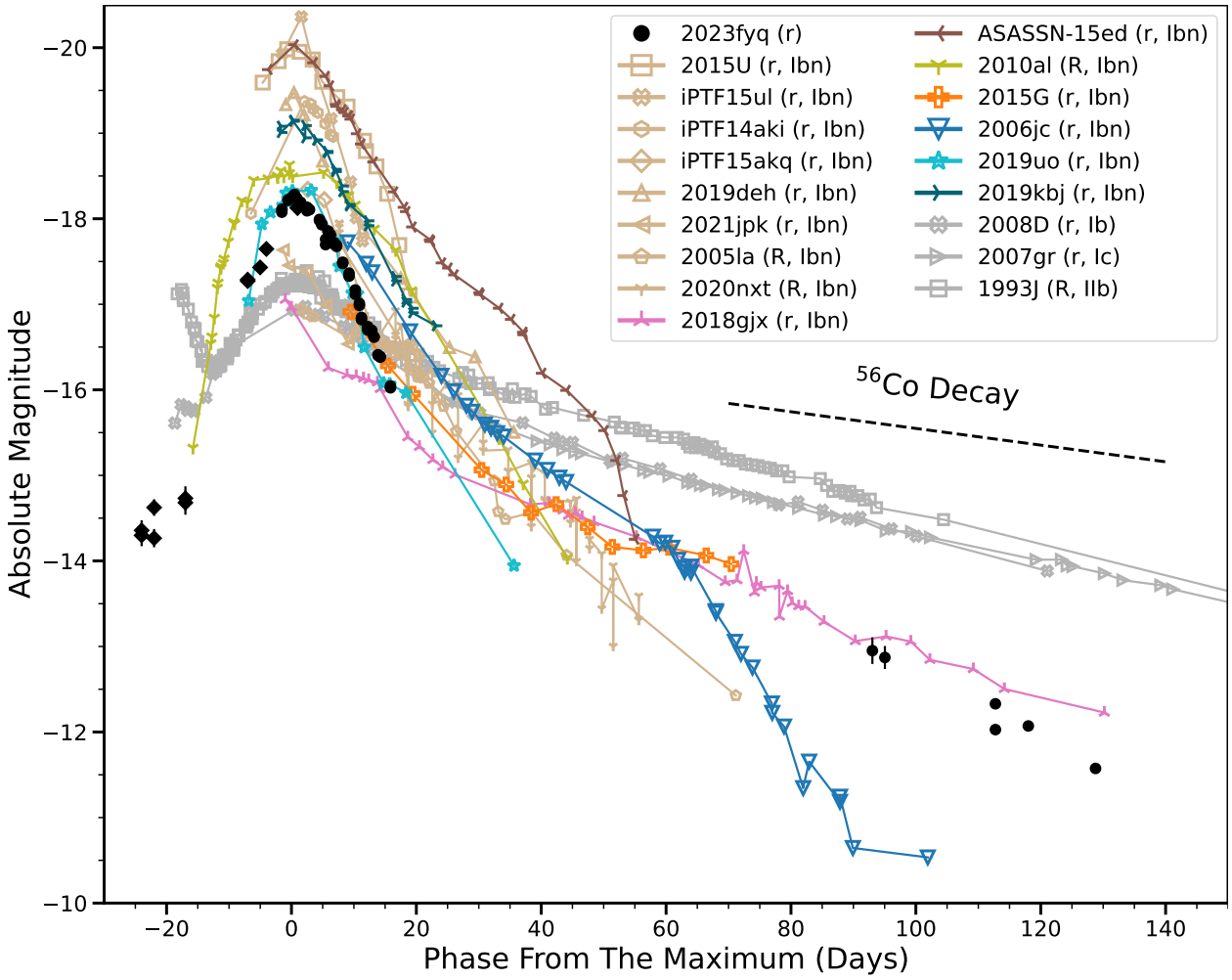

Figure 6.4 r/R Light curve comparison between SN 2023fyq, a sample of Type Ibn SNe, and well-studied normal SESNe. The Vega magnitudes have been converted to the AB magnitude system. The evolution of SN 2023fyq is similar to those of Type Ibn SNe. The SNe used in this plot includes Type IIb SN 1993J (Filippenko et al., 1993), Type Ib SN 2008D (Modjaz et al., 2009), Type Ic SN 2007gr (Hunter et al., 2009)), and Type Ibn SNe: SN 2015U (Tsvetkov et al., 2015; Pastorello et al., 2015a; Hosseinzadeh et al., 2017), iPTF15ul (Hosseinzadeh et al., 2017), iPTF14aki (Hosseinzadeh et al., 2017), iPTF15akq (Hosseinzadeh et al., 2017), SN 2019deh (Pellegrino et al., 2022), SN 2021jpk (Pellegrino et al., 2022), SN 2005la (Pastorello et al., 2008b), SN 2020nxt (Wangq et al., 2024), SN 2018gjx (Prentice et al., 2020), ASASSN-15ed (Pastorello et al., 2015b), SN 2010al (Pastorello et al., 2015c), SN 2015G (Shivvers et al., 2017; Hosseinzadeh et al., 2017), SN 2006jc (Pastorello et al., 2007), SN 2019uo (Gangopadhyay et al., 2020), and SN 2019kbj (Ben-Ami et al., 2023). SN 2018gjx, ASASSN-15ed, SN 2010al, SN 2015G, SN 2006jc, SN 2019uo, and SN 2019kbj will be used for further comparison in the paper, while a broader sample of SNe Ibn are shown in tan. SESNe are shown in grey.

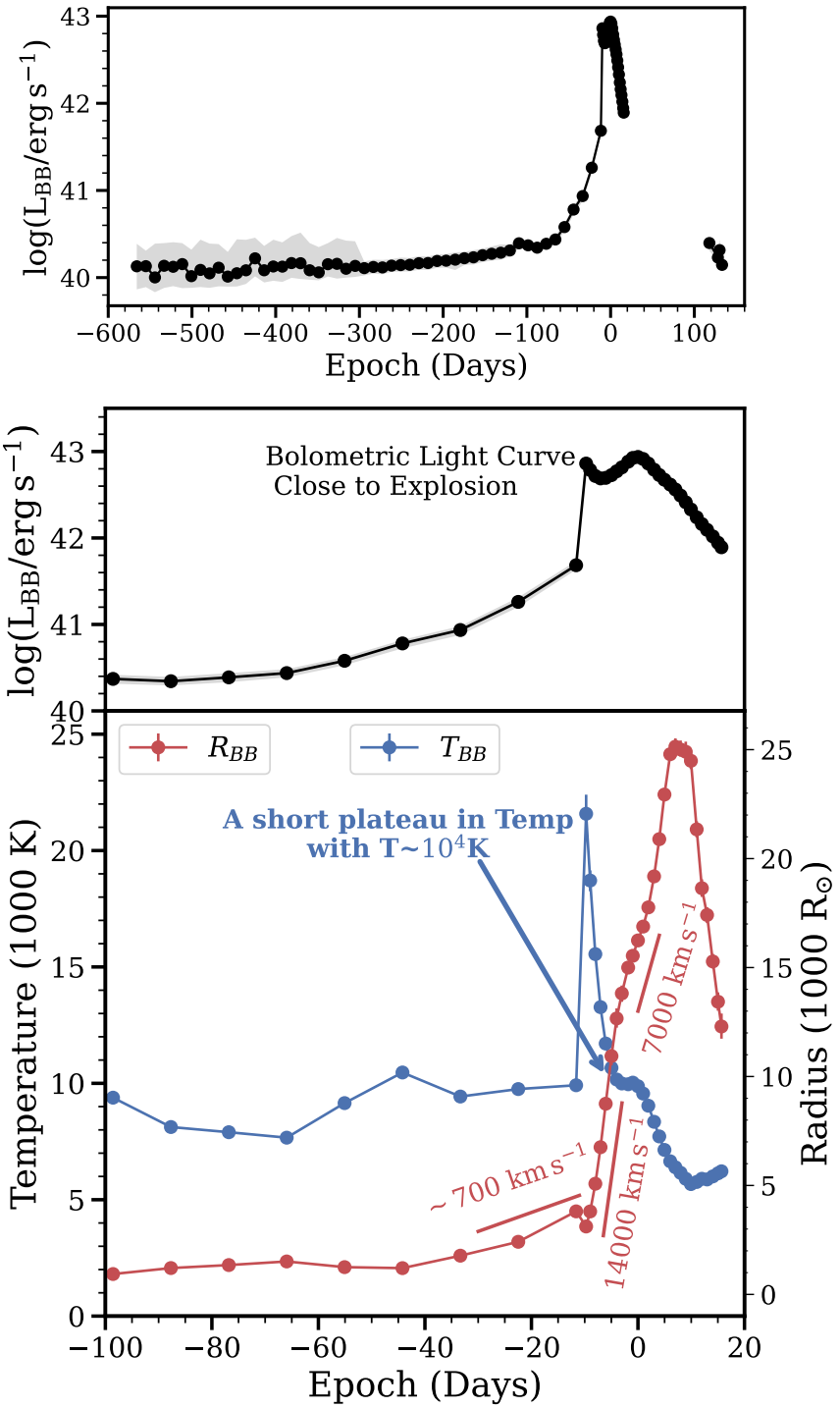

Figure 6.5 The pre- and post-explosion bolometric light curve (upper two panels) and the blackbody temperature and radius evolution (bottom panel) of SN 2023fyq at the precursor phases and the early SN phases. The uncertainties are indicated by the shaded area.

used in extinction estimations (Munari & Zwitter, 1997). In order to measure the line-of-sight reddening towards SN 2023fyq, we analyzed the medium-resolution spectrum (R∼1800) taken with Gemini North on 2023 August 1. The measured EW of the host galaxy Na I D λ5890 (D_2) and Na I D λ5896 (D_1) are 0.27 ± 0.04 Å and 0.15 ± 0.04 Å, respectively. The measured EW of the Galactic Na I D_2 and Na I D_1 are 0.23 ± 0.02 Å and 0.16 ± 0.01 Å respectively. Using Eq.9 in Poznanski et al. (2012) and applying the renormalization factor of 0.86 from Schlafly et al. (2010), we found a host extinction of $E(B-V)_{\rm host} = 0.037 \pm 0.01$ mag. The Milky Way extinction is measured to be $E(B-V)_{\rm MW} = 0.035 \pm 0.01$ mag, which is consistent with the Milky Way extinction of $E(B-V)_{\rm MW} = 0.0286$ mag from the extinction map by Schlafly & Finkbeiner (2011b). We adopt the latter for the Milky Way extinction. Throughout the paper, we will adopt a total extinction of $E(B-V) = 0.066 \pm 0.01$ mag.

We note that Brennan et al. (2024) found a larger host extinction value ($E(B-V)_{\rm host} = 0.4 \pm 0.1$ mag) using the Balmer ratio measured from the host emission lines. The disagreement is probably because this method measures the full column of gas including the background. In this case, there is likely some dust between the SN and the underlying HII region, which is responsible for this greater implied extinction value.

6.4.2. Distance. The distance of NGC 4388 listed on the NASA/IPAC Extragalactic Database (NED) ranges from 13.6 Mpc to 25.7 Mpc (μ = 30.67 – 32.05 mag). We adopt the most recent Tully-Fisher distance (based on photometry at 3.6μm with Spitzer Space Telescope), 18.0±3.7 Mpc (μ = 31.28±0.45 mag; Tully et al. 2016).

6.5. Photometric Evolution

In Figure 6.2 we present the photometric evolution of SN 2023fyq dating back to 2015, illustrating our search for precursor activities. In Figure 6.3 we take a closer look at the evolution from one year before the SN explosion. All phases mentioned in the paper are with respect to the maximum light in the r band, which is measured to be at JD = 2460154

after fitting the light curve with a spline function. At ~ -11 d, a sudden rise of $\sim$1.5 mag within $\sim$17 hrs is clearly observed (see lower panel of Figure 6.3). As we will discuss below, we attribute this rapid rise to the SN first light. Consequently, we divide the photometric evolution of SN 2023fyq into two phases: the precursor phase (< -11 d) and the SN phase (> -11 d).

6.5.1. Precursor Detections. The precursor is detected from ~ -1000 d to ~ -11 d. There are also single detections at around -2300 d and -1300 d. These detections have $3<S/N\leq 4$, and are bracketed by nondetections of similar depth. Therefore, they are likely not true detections of precursor emission. As illustrated in Figure 6.2, the precursor activities remain relatively stable at -10 to -12 mag between ~ -1300 d and ~ -100 d. Then, starting from -100 d, the object slowly brightens to ~ -15 mag. Between ~ -2500 and ~ -100 d, the UV observations from Swift only give nondetection limits (See Figure 6.2). As the precursor gets brighter, at ~ -28 d, a source is detected in the $UVW1$ filter at ~ -13 mag, with similar magnitudes observed in g and o bands. From -300 to -11 d, the precursor light curves seem to exhibit multiple bumps, indicative of pre-explosion activities, such as small eruptions, from the progenitor star. As shown in Figure 6.2, the precursor emission detected in SN 2023fyq appears fainter and longer compared to that observed in Type Ibn SN 2006jc (Pastorello et al., 2007) and SN 2019uo (Strotjohann et al., 2021a), even when accounting for uncertainties in the distance measurement of SN 2023fyq. Pre-explosion activities were not detected for Type Ibn SN 2015G down to -13.3 ± 0.5 mag (Shivvers et al., 2017). It should be noted that the precursor searches for SN 2006jc and SN 2019uo only go down to around -13 mag. Therefore, fainter precursor activities like those observed in SN 2023fyq can not be excluded for these events.

6.5.2. SN Light Curve. The bluer-band ($UVW2$, $UVM2$, $UVW1$) light curves of SN 2023fyq exhibit a notable bump from -11 d to -4 d, before reaching the second peak and then falling off rapidly. This initial bump in the blue bands is likely attributable to the

cooling following shock breakout. For the rest of the bands, the SN light curves show a fast rise and also a fast decline. The peak r-band magnitude is measured to be $M_r = -18.5$ mag. In Figure 6.4, we compare the r-band light curve of SN 2023fyq with the r/R-band light curves of a sample of Type Ibn SNe and well-studied normal stripped-envelope SNe (SESNe). At early times SN 2023fyq appears more luminous than the typical SESNe, and the evolution of SN 2023fyq is overall similar to those of Type Ibn SNe. At late times SN 2023fyq declines similarly to SN 2018gjx and SN 2015G, but slower than SN 2006jc. The steep decline of SN 2006jc in the optical is likely due to dust formation in the SN ejecta or in the surrounding CSM (e.g., Smith et al., 2008). The slower decline of SN 2023fyq, SN 2018gjx, and SN 2015G at late times could be an indication of less efficient dust formation than in SN 2006jc. However, due to the lack of late-phase observations of Type Ibn SNe, it is not clear if SN 2006jc is really an outlier. SN 2023fyq declines faster than normal SESNe at nebular phases. This may be due to an inefficient trapping of γ-rays in SN 2023fyq if the light curve tail is powered by ^{56}Ni decay, a power source other than ^{56}Ni decay, or dust formation in SN 2023fyq.

6.5.3. Bolometric Light Curve. We constructed the bolometric light curve of SN 2023fyq using data from ZTF, ATLAS, ASAS-SN, Swift, and Itagaki. To build the spectral energy distribution (SED) in the regions without complete multiband coverage, we reconstruct the multiband light curves using a neural network based light curve fitting method presented in Demianenko et al. (2023). This method is able to capture correlations across different observations over time and among various passbands, and compute an approximate light curve within the specified time and wavelength ranges. The final bolometric light curve is calculated by fitting the SED with a blackbody function using a Markov Chain Monte Carlo (MCMC) routine in the Light Curve Fitting package (Hosseinzadeh & Gomez, 2020b). The blackbody temperatures measured from the pre-explosion spectra of SN 2023fyq in Brennan et al. (2024) are used as priors for the SED fitting. We present the bolometric light curve

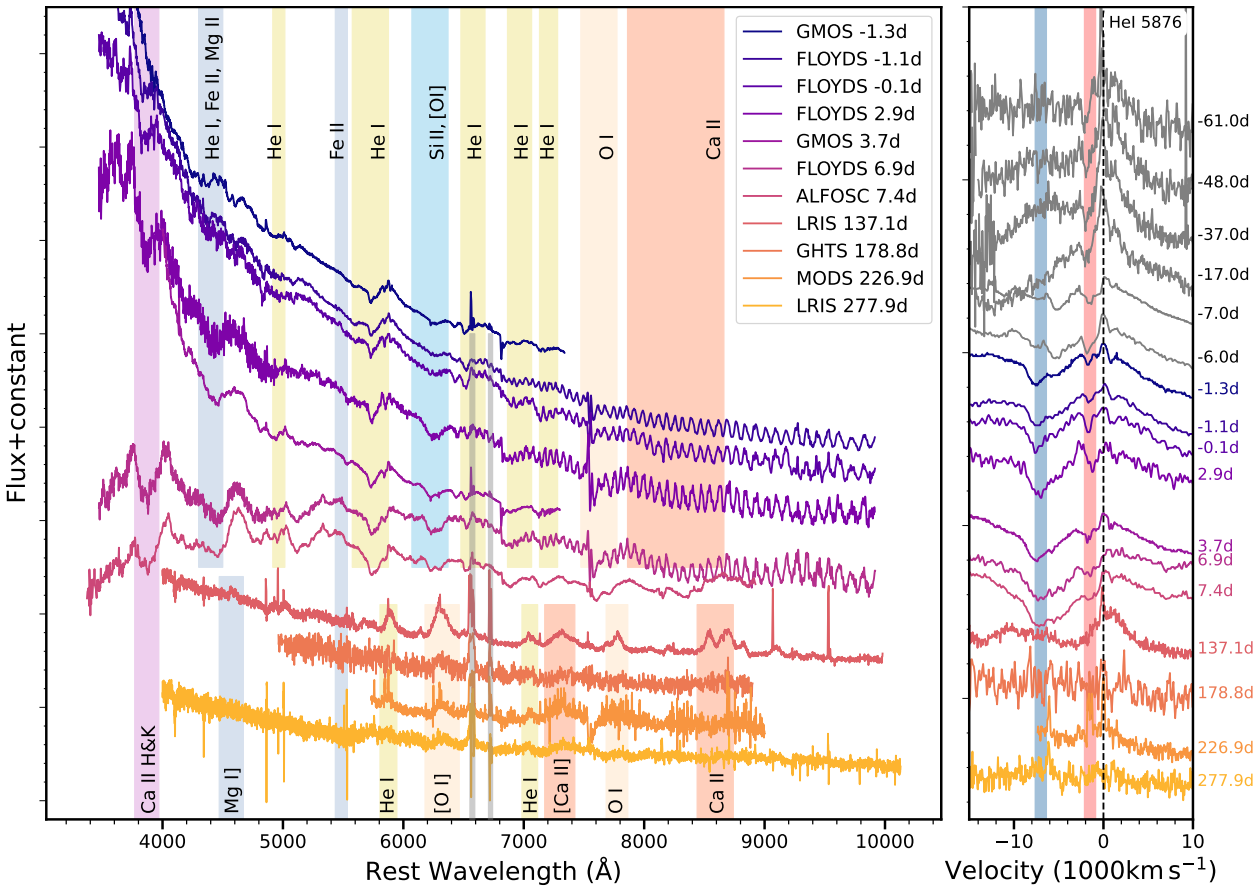

Figure 6.6 Left: The optical spectroscopic evolution of SN 2023fyq. The phase is measured from the r-band maximum. The grey bands mark the emission lines from the galaxy. Right: The evolution of the He I λ5876 line. The pre-maximum spectra marked in grey are from Brennan et al. (2024). The He I λ5876 line shows a high-velocity component (marked with the blue band) and a low-velocity component (marked with the red band), which may come from the SN ejecta and He-rich CSM, respectively.

of SN 2023fyq, and the corresponding blackbody temperature (T_{BB}) and radius (R_{BB}), in the precursor phase and the SN phase, in Figure 6.5. We note that we only focus on the long-term evolution of the bolometric light curve, and small variations in the light curves are not reflected in the final bolometric light curve.

Before $\sim$−100 d, the precursor of SN 2023fyq is in a relatively stable state with a luminosity of $\sim 1 \times 10^{40}$ erg s^{-1}. During that time, T_{BB} and R_{BB} are around 10,000 K and 600 R$_\odot$, respectively. After −100 d, SN 2023fyq shows a faster rise and, at $\sim$−11 d, the

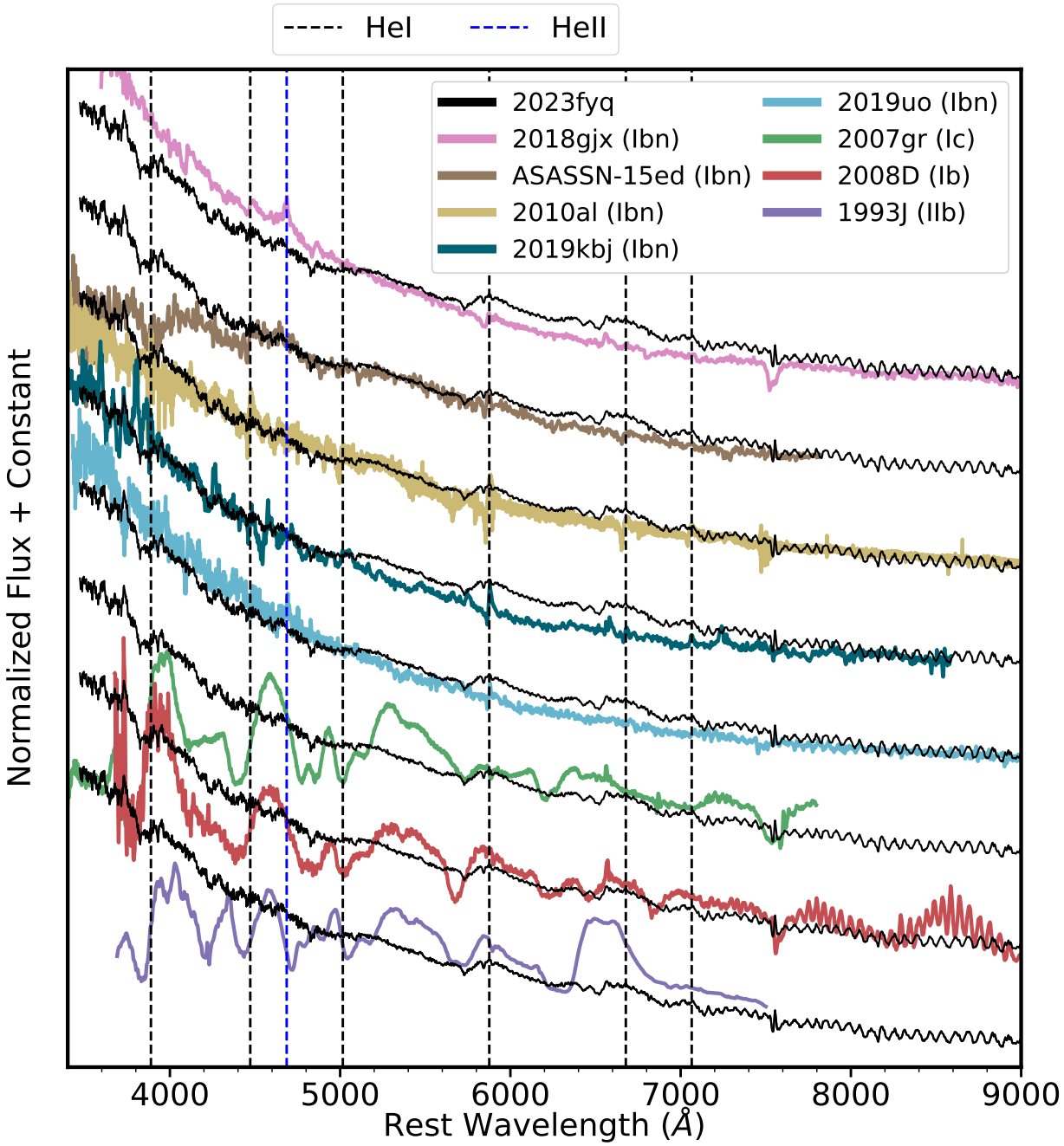

Figure 6.7 Optical spectral comparison of SN 2023fyq at ∼0 d to other Type Ibn SNe and normal SESNe.

luminosity suddenly increases over an order of magnitude (i.e., from $\sim 4 \times 10^{41}$ erg s^{-1} to $\sim 7 \times 10^{42}$ erg s^{-1}). Later, after a brief decline, the SN reaches its main peak and declines

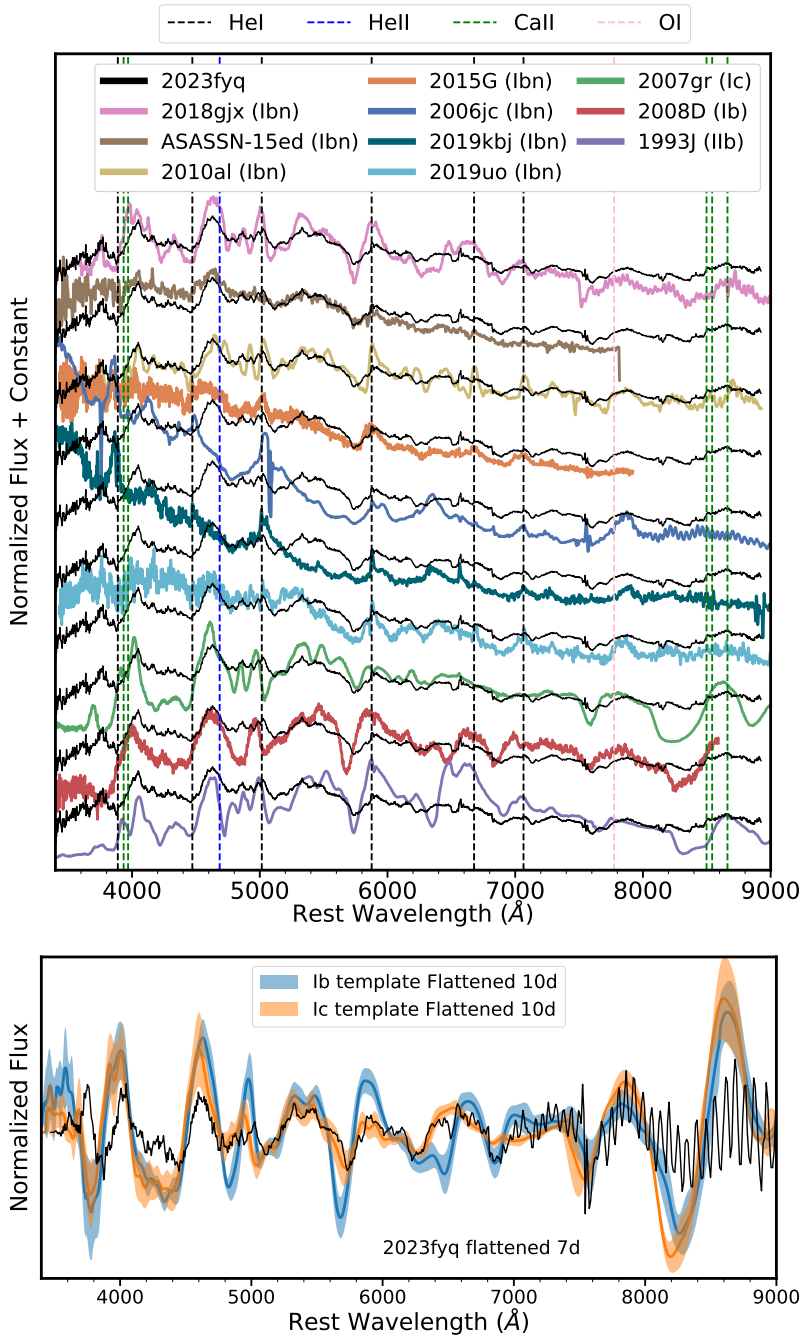

Figure 6.8 Upper: Optical spectral comparison of SN 2023fyq at ∼7 d to other Type Ibn SNe and normal SESNe. Bottom: The optical spectrum taken at ∼7 d compared to the mean spectra (the solid lines) and the standard deviations (the shaded regions) of SN Ib and Ic at ∼10 d from Liu et al. (2016b). SN 2023fyq has several features in common with these normal SESNe, suggesting SN 2023fyq is likely from an explosion of a stripped star.

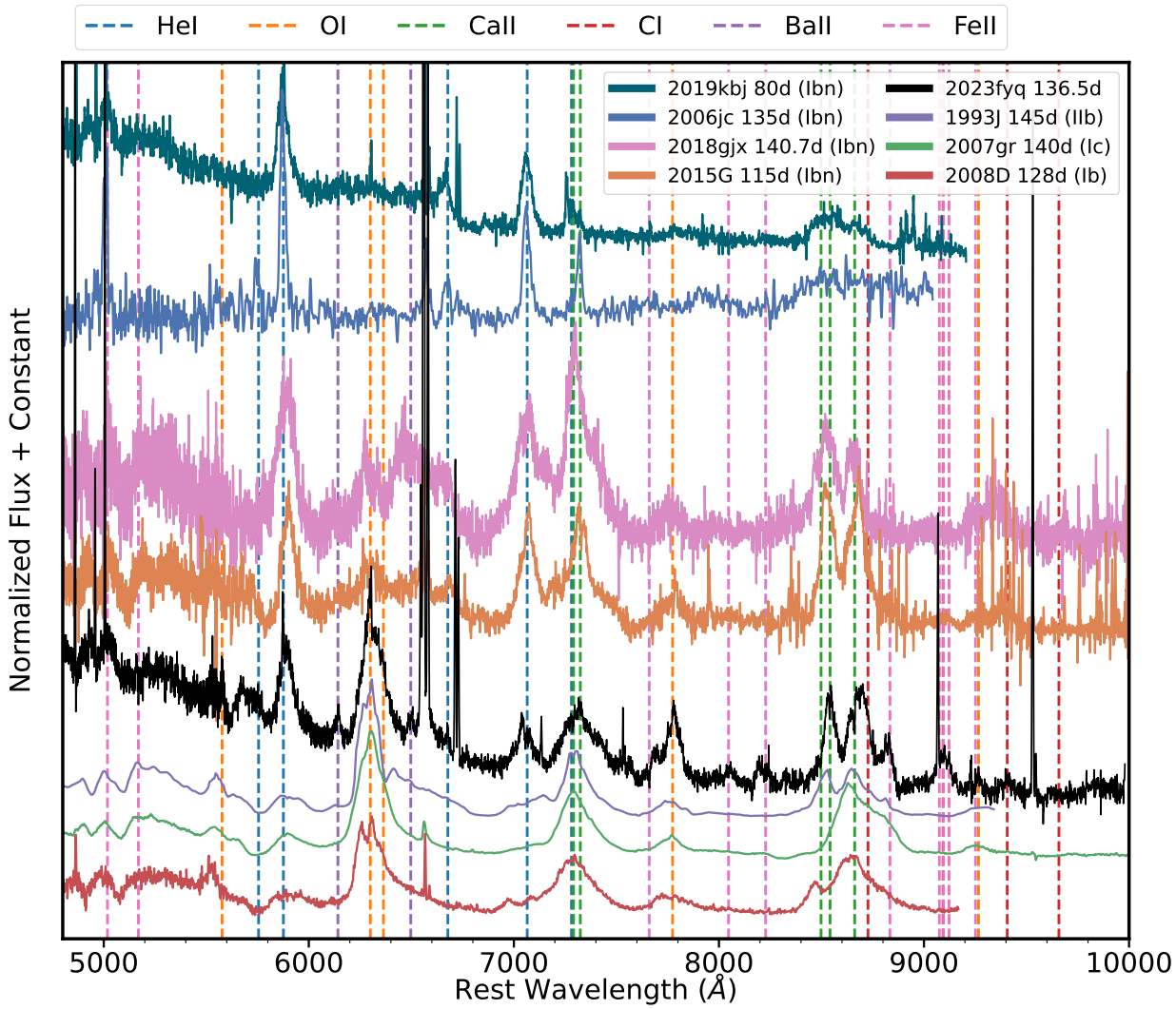

Figure 6.9 Nebular spectral comparison of SN 2023fyq to other Type Ibn SNe with nebular spectra and normal SESNe. The phases are relative to the time of maximum light. A continuum spectrum of the background galaxy is subtracted from the spectrum of SN 2023fyq. At nebular phases, SNe Ibn appear to fall into two distinct classes: one exhibiting only narrow He lines (SN 2019kbj and SN 2006jc), and another displaying intermediate-width He lines and oxygen lines (SN 2023fyq, SN 2015G, and SN 2018gjx).

afterwards. The decline of luminosity shortly after $\sim$−11 d is likely due to the shock cooling after the shock breakout. For T_{BB}, after jumping to $\sim$22,000 K at $\sim$−11 d, it rapidly declines until entering a brief plateau phase between $\sim$−5 and 0 d with $T_{BB}\simeq$10,000K. The initial rapid decrease of T_{BB} is likely associated with the shock cooling process, while the plateau

phase is likely due to the recombination of He I and will be further discussed in Section 6.7.1. After around −40 d, R_{BB} shows a gradual expansion with a velocity of ∼700 km s^{-1}. After −11 d, R_{BB} continuously increases, reflecting an increase of the photospheric radius with the expansion of SN ejecta. The expansion rate of R_{BB} is ∼14,000 km s^{-1} initially, which slows down to ∼7000 km s^{-1} after around -2 d. After around 5 d, as will be discussed in the next section, the spectra of SN 2023fyq are dominated by absorption lines from the SN ejecta, so R_{BB} may not accurately reflect the position of the photosphere.

6.6. Spectroscopic Evolution

The spectroscopic evolution of SN 2023fyq is presented in Figure 6.6. At -1.3 d, the spectrum shows a blue continuum with a prominent He I λ5876 line. Other He lines, such as He I λ5015, He I λ6678, He I λ7065, and He I λ7281, are also observed. The He I λ5876 line shows a rather asymmetric profile (right panel of Figure 6.6). In the blue wing, the He I λ5876 line shows a two-component profile, with a narrow absorption feature at ∼−1000 km s^{-1} and a broad absorption feature at ∼−7000 km s^{-1}. The detection of a two-component He I line profile in SN 2023fyq is consistent with those observed in other Type Ibn SNe (Pastorello et al., 2016), and is likely from different emitting regions. The broad component is from the fast moving ejecta, while the narrow component is likely from the surrounding unshocked He-rich CSM. In the red wing, there is an additional emission component at around 1500 km s^{-1}. This component is also observed during the pre-explosion phase of SN 2023fyq (Brennan et al., 2024), and could be due to an asymmetric CSM structure formed before the SN explosion. A few days later the object quickly becomes redder, and the Ca II H&K $\lambda\lambda$3934, 3969 and Ca II $\lambda\lambda$8498, 8542, 8662 lines appear more prominent. No broad hydrogen features are observed in the spectra of SN 2023fyq. However, we can not exclude the presence of narrow hydrogen lines since the spectra are heavily contaminated by the host-galaxy emission. At ∼137 d, the spectrum is dominated by strong [O I] $\lambda\lambda$6300, 6364 and [Ca II] $\lambda\lambda$7291, 7323. He lines, such as He I λ5876 and He I λ7065 are also strong at

this phase. Other lines, including Mg I] λ4571 and Ca II $\lambda\lambda$8498, 8542, 8662, can be seen in the spectrum. After that, the spectra we have are mainly dominated by the host, while weak [O I] $\lambda\lambda$6300, 6364 lines are still present.

We compare the spectra of SN 2023fyq around 0 d and 7 d with other SNe Ibn and normal SESNe at similar phases in Figure 6.7 and Figure 6.8. At around 0 d, other SNe Ibn show blue continua plus narrow He I λ5876 lines in their spectra. The velocities of those narrow He I λ5876 lines are consistent with that of the narrow component of the He I λ5876 line in SN 2023fyq. At around 0 d, normal SESNe are redder than SN 2023fyq and other SNe Ibn. This is probably due to the ongoing CSM interaction in the SNe Ibn, which is not significant in SESNe. SESNe start to show lines from iron-group elements at this phase, whereas these features are not strong in SN 2023fyq or other SNe Ibn at a similar phase. The He lines in Type Ib/IIb SNe are also much broader than those shown in SN 2023fyq.

At around 7 d, SN 2023fyq is very similar to SNe Ibn SN 2018gjx, ASASSN-15ed, SN 2010al, and SN 2015G, which start to show signatures from deeper layers of the ejecta. The He I λ5876 lines of SN 2018gjx, ASASSN-15ed, SN 2010al, and SN 2015G grow broader, with velocities similar to that of the broad component of He I λ5876 in SN 2023fyq. Interestingly, some similarities between SN 2023fyq and normal SESNe are also observed at around 7 d. To better illustrate this, we flatten the spectrum of SN 2023fyq at $\sim$7 d using SNID following the procedure outlined in Blondin & Tonry (2007b) and compare the flattened spectrum with Type Ib and Ic templates at 10 d from Liu et al. (2016b) in the bottom panel of Figure 6.8. This comparison clearly indicates that SN 2023fyq exhibits spectral features similar to those of Type Ic SNe, suggesting that its progenitor is likely a stripped/He star.

When the object enters the nebular phase, the ejecta become optically thin, providing an unique opportunity to study the core of the progenitor star. However, it is challenging to follow up SNe Ibn at nebular phases since they rapidly get fainter. In Figure 6.9, we

compare the nebular spectrum of SN 2023fyq at ∼136.5d with a few SNe Ibn with late-time observations and normal SESNe at similar phases. The underlying continuum of the background galaxy, obtained from a pre-explosion spectrum taken at -504 d as presented in Brennan et al. (2024) when the signal from the host is dominant, is subtracted from the spectrum presented here. SN 2023fyq shows strong intermediate-width He emission lines, similar to Type Ibn SN 2018gjx and SN 2015G, but the [O I] $\lambda\lambda$6300, 6364 line in SN 2023fyq is significantly stronger than those in other objects. Type Ibn SN 2006jc and SN 2019kbj only show narrow He lines and have no signatures of oxygen. SNe Ibn at nebular phases seem to fall into two distinct classes, with one still showing only narrow lines and another showing intermediate-width He lines and oxygen lines. This topic will be further discussed in Section 6.7.4. Compared to normal SESNe SN 1993J, SN 2008D, and SN 2007gr, SN 2023fyq shows prominent He emission lines, but otherwise SN 2023fyq is similar to those normal SESNe at the nebular phase.

Overall, the spectroscopic evolution SN 2023fyq is similar to those of some SNe Ibn. However, the difference between SESNe and SN 2023fyq shortly after the light curve maximum is less evident. A transition between Type Ibn and Type Ic is clearly observed. Similar behaviors have been reported in several previous studies of other Type Ibn SNe (e.g., Pastorello et al., 2015b; Prentice et al., 2020). If SN 2023fyq is indeed dominated by CSM interaction at peak light, the transition to Type Ic could be due to the CSM-interaction region becoming transparent over time, allowing us to see more signatures from the SN ejecta. It is also possible that the SN ejecta has moved beyond the dense CSM. This suggests that SN 2023fyq is likely exploded from a stripped/He star within He-rich CSM. The He lines observed at the nebular phase indicate that the interaction with the He-rich CSM is still ongoing. It is natural to link the pre-existing He-rich CSM with the pre-explosion activities of the progenitor system, which likely also produces the precursor emission observed in SN 2023fyq. This topic will be further discussed in Section 6.7.3.

6.7. Discussions

The detection of sustained precursor emission in SN 2023fyq provides an invaluable opportunity to study the progenitor system of Type Ibn SNe. Below is a summary of the primary observed characteristics of SN 2023fyq:

(1) A long-standing and continuously rising precursor emission starting from years before the SN explosion;

(2) The light curve following the explosion exhibits an evolution similar to Type Ibn SNe; the bolometric light curve exhibits two peaks.

(3) The early- and late-phase spectra both show narrow/intermediate-width He lines. The nebular spectra show prominent [O I] $\lambda\lambda$6300, 6364 emission, suggesting that SN 2023fyq is likely a stripped/He star exploded within He-rich CSM.

Any progenitor scenario for SN 2023fyq needs to explain the above behaviors. In this section we will discuss the progenitor system and possible powering mechanisms of the precursor and the SN light curve.

6.7.1. What Powers The First Peak of The SN Bolometric Light Curve? The light curve of SN 2023fyq reaches its initial peak at around -11 d. The later decrease of luminosity is associated with a prompt decline of T_{BB} and a rapid expansion of R_{BB}. This process is likely the shock cooling phase after the shock breakout. During this phase, the expansion of the ejecta is nearly adiabatic, converting the thermal energy into kinetic energy. The rapid decline of the photospheric temperature can produce a decrease in brightness in bluer bands and an increase in brightness in redder bands as the temperature moves through the optical bands, which is consistent with what is observed in SN 2023fyq (Figure 6.3 and Brennan et al. 2024). It is noteworthy that, around the shock breakout, R_{BB} is about $2\sim3\times1000$ $R_\odot$ ($\sim1\text{-}2\times10^{14}$ cm), so the shock breakout likely originates from an extended envelope/CSM wind instead of from the stellar surface. A similar conclusion is also drawn by

Brennan et al. (2024) based on the pre-explosion spectroscopic and photometric observations of SN 2023fyq.

When T_{BB} drops down to $\simeq$10,000 K, it enters a brief plateau phase (Figure 6.5). Interestingly this temperature is consistent with the recombination temperature of He I ($\sim$10,000 K) (Kleiser & Kasen, 2014). In the meantime, the expansion of R_{BB} slows down. Given that the early SN spectra are dominated by He lines, the outer envelope is likely He-rich. We argue that this T_{BB} plateau phase is due to the recombination of He I, and the decrease of R_{BB} expansion rate is due to the recession of the photosphere into the extended envelope. After this process, the outer envelope becomes almost transparent due to the drop of electron scattering opacity. This is consistent with the fact that we start to see more signals, such as Ca lines, from the deeper SN ejecta after 0 d.

In conclusion, the first peak of the SN bolometric light curve of SN 2023fyq is likely due to shock breakout in an extended envelope/CSM wind located at $\sim 2000 - 3000$ $R_\odot$.

6.7.2. What Powers The Second Peak of The SN Bolometric Light Curve?

At 0 d, SN 2023fyq reaches its second peak. It should be noted that all bands (from UV to optical) show peaks at this phase, so this second peak is not an effect of temperature evolution and is instead powered by energy processes.

6.7.2.1. *Radioactive decay (RAD).* We first consider the possibility that the SN light curve around the second peak is powered by the ^{56}Ni decay. The early light curve evolution of SNe is regulated by the photon diffusion time, which depends on the SN ejecta mass, the ejecta velocity, and the opacity (Arnett, 1982). Assuming that the rise time of the light curve is equal to the photon diffusion time and Arnett's law holds for this object, i.e., the peak luminosity is close to the instantaneous decay power at the peak, we can estimate the ^{56}Ni mass (M_{Ni}) and the ejecta mass (M_{ej}). We fix the optical opacity κ_{opt} to be 0.1 $\mathrm{cm^2\,g^{-1}}$. Given a peak luminosity of 9.5×10^{42} $\mathrm{erg\,s^{-1}}$, we get $M_{Ni} \simeq 0.28$ $M_\odot$ and $M_{ej} \simeq 0.54 M_\odot (v_{ph}/7000 \mathrm{km\,s^{-1}})(t/10\mathrm{d})^2$.

Therefore, to power the light curve with only ^{56}Ni decay, around half of the ejecta is composed of ^{56}Ni. This ratio is much higher than those in typical CCSNe (e.g., Lyman et al., 2016) and similar to those found in Type Ia SNe (e.g., Könyves-Tóth et al., 2020; Graham et al., 2022). If the ejecta is ^{56}Ni-rich, when the ejecta become optically thin, the optical spectra would be dominated by forbidden lines from Fe and Co. However, as we discussed in Section 6.6, the nebular spectrum of SN 2023fyq is mainly dominated by He, O and Ca. Therefore, we disfavor the ^{56}Ni decay as the dominant power source of the early light curve of SN 2023fyq.

6.7.2.2. *CSM interaction?* Since the evolution of SN 2023fyq is similar to those of Type Ibn SNe, it is likely that the light curve around the second peak is powered by CSM interaction. We use the model presented in Jiang et al. (2020), which generalizes the self-similar solution to the interaction of stellar ejecta with surrounding CSM originally presented in (Chevalier, 1982). In this model, the density of CSM is described by a power law, $\rho \propto qr^{-s}$, while the ejecta are divided by an inner region ($\rho_{ej} \propto r^{-\delta}$) and an outer region ($\rho_{ej} \propto r^{-n}$). We fix the optical opacity (κ) to be 0.1 cm^2 g^{-1}, $n = 10$, $s = 0$, and $\delta = 1$ following Pellegrino et al. (2022). The value of $\kappa \approx 0.1$ cm^2 g^{-1} is motivated by the opacity of singly-ionized He at $\sim 10^4$ K (e.g., Kleiser & Kasen, 2014). We also attempted to fit the data with $s = 2$ (wind-like CSM), but did not achieve a reasonable fit. This result is consistent with the findings reported by Karamehmetoglu et al. (2017), Gangopadhyay et al. (2020), and Ben-Ami et al. (2023). The ejecta velocity (7,000 km s^{-1}) is obtained from the velocity of the P Cygni minimum of the He I lines near peak. The free parameters in our fit are the explosion epoch (t_{exp}), the ejecta mass (M_{ej}), the inner radius of the CSM (R_0), the CSM mass (M_{csm}), the density of the CSM at R_0 ($\rho_{csm,0}$), and the conversion efficiency of the shock kinetic energy to radiation (ϵ).

To account for the initial shock cooling phase we have incorporated the shock breakout (SBO) model presented by (Margalit, 2022). This model provides an analytic solution for

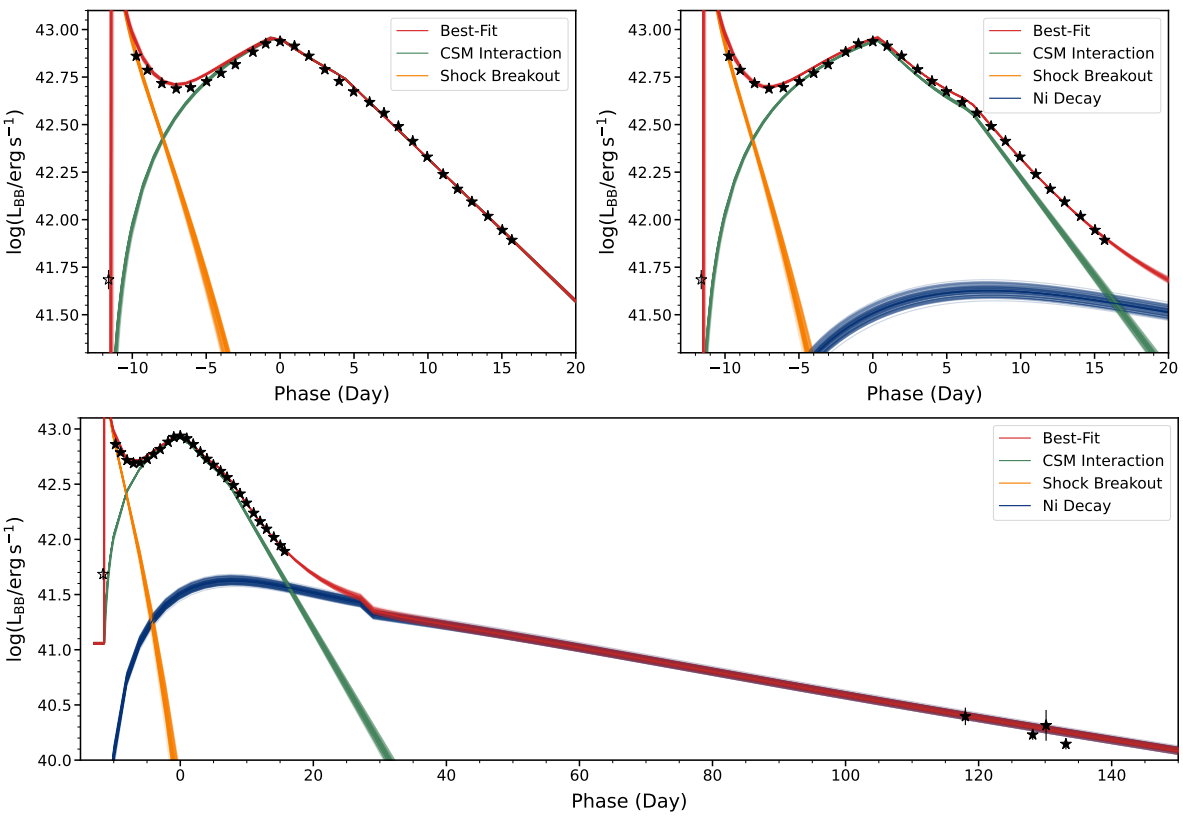

Figure 6.10 Upper-Left: Fits to the bolometric light curve of SN 2023fyq using a combination of shock breakout and CSM interaction models. Bottom: Fits to the bolometric light curve of SN 2023fyq using a combination of shock breakout, CSM interaction, and ^{56}Ni decay models. The dip observed around 30 days in the ^{56}Ni decay model is due to the transition from the photospheric phase to the nebular phase (see Valenti et al. (2008) for more details). The upper-right panel is a zoom-in of the bottom panel to better illustrate the fit close to the SN peak. The initial bump is qualitatively fitted by the shock breakout model. The hollow point is at the precursor phase, so it is not included in the fit.

the shock cooling phase following shock breakout from extended optically thick material, which is suitable for the case of SN 2023fyq. We fix the velocity of the inner envelope at 7,000 km s^{-1}. Additionally, we introduce two free parameters into our fit: the radius of the extended material (R_e) and the mass of the extended material (M_e).

The model fit to the observed light curve is performed using an MCMC routine. As illustrated in the upper-left panel of Figure 6.10, both the initial bump and the subsequent evolution of the light curve are qualitatively fitted by the model. The best-fitting parameters

are detailed in Table 6.1 (CSM+SBO model). It is important to note that the models presented here are likely simplified, so the parameters derived can only be considered as estimations of the order of magnitude.

The M_{ej} and M_{csm} derived for SN 2023fyq are roughly consistent with those found in other studies (e.g., Pellegrino et al., 2022; Ben-Ami et al., 2023). The low ejecta mass implies that the progenitor is likely a low-mass He star. However, this model can only fit the light curve around the peak and cannot explain the light curve flattening at late times (see Figure 6.5). At later times, the light curve is likely powered by another source of energy.

6.7.2.3. *RAD+CSM interaction?* Since SN 2023fyq is similar to normal SESNe shortly after peak and during nebular phases, it is plausible that a certain amount of ^{56}Ni is produced during the explosion. Therefore, it is natural to consider ^{56}Ni decay as an additional energy source. A ^{56}Ni decay model has been employed to interpret the late-time light curves of many other Type Ibn SNe, often revealing low ^{56}Ni masses across previous studies (Gangopadhyay et al., 2020; Pellegrino et al., 2022; Ben-Ami et al., 2023).

We use the ^{56}Ni decay model presented in (Arnett, 1982; Valenti et al., 2008). The full SN light curve is fitted by a combination of CSM interaction, shock breakout, and ^{56}Ni decay models. We fix the optical opacity to be κ =0.1 $\mathrm{cm^2\,g^{-1}}$ and the γ-ray opacity to be 0.03 $\mathrm{cm^2\,g^{-1}}$. The ejecta velocity is fixed to be 7,000 $\mathrm{km\,s^{-1}}$. The best-fit model is shown in the upper-right panel and the bottom panel of Figure 6.10, and the best-fit parameters are presented in Table 6.1 (the CSM+SBO+RAD model). Both the amount of ^{56}Ni ($\sim$0.02 $\mathrm{M_\odot}$) and the ejecta mass ($\sim$1.2$\mathrm{M_\odot}$) are lower than those of SESNe (Lyman et al., 2016). The low ejecta mass implies that the progenitor of SN 2023fyq is less massive than those of normal SESNe right before the SN explosion. One caveat of the model is that we did not consider the CSM interaction at late phase, so the ^{56}Ni mass we derive here can only be treated as an upper limit.

The radius of the extended material (R_e) is around 21×10^{13}cm ($\sim$3000 $R_\odot$). This large radius is consistent with the blackbody radius of SN 2023fyq around the shock breakout (Figure 6.5). This indicates that, at the explosion, the progenitor is surrounded by an extended envelope with a mass of 0.3 $M_\odot$ at a radius of $R_e \sim 3000 R_\odot$, consistent with what we discussed in Section 6.7.1. Considering the width of the narrow line component in the SN spectra (Figure 6.6) and the narrow lines observed pre-explosion (Brennan et al., 2024), the extended material likely expands with a velocity of $\sim$1000 km s^{-1}. Such a velocity suggests that the material at around $\sim$3000 $R_\odot$ was formed within around 20 days before the explosion.

In such a scenario, the pre-explosion photophere would be located within the extended material where the optical depth is sufficiently high. For a wind profile $\rho \propto r^{-2}$, R_{BB} is roughly proportional to $\dot{M}/V_{wind}$, where $\dot{M}$ is the mass-loss rate and V_{wind} is the expansion velocity of the extended material. Consequently the expansion of R_{BB}, starting from around -100 d (Figure 6.5), is likely due to an increase of mass loss. The more pronounced rise between ~ -40 d and -11 d can be attributed to a more eruptive mass loss immediately preceding the explosion. If the majority of the material characterized by M_e is formed during this eruptive phase, the mass loss rate can be estimated to be

$$\dot{M} \approx \frac{M_e V_{wind}}{R_e} \approx 4.5\ \mathrm{M_\odot\,yr^{-1}} \frac{\mathrm{M_e}}{0.3\mathrm{M_\odot}} \frac{3000\mathrm{R_\odot}}{\mathrm{R_e}} \frac{\mathrm{V_{wind}}}{1000\mathrm{km\,s^{-1}}}. \tag{6.1}$$

Interestingly, eruptive mass ejections on the order $\sim$0.1–1 $M_\odot$ are anticipated for low-mass He stars with masses of 2.5–3.2 $M_\odot$ due to core silicon deflagration or detonation weeks prior to core collapse (Woosley, 2019b; Ertl et al., 2020b). The mass and velocity of the ejected material depends on the amount of silicon that burns (Ertl et al., 2020b). An ejection mass of $\sim$0.3 $M_\odot$ with a velocity of $\sim$1000 km s^{-1} is consistent with the typical values of such events (see figure 14 and table 4 of Woosley 2019b).

The CSM characterized by M_{CSM} is likely more extended and formed during the earlier phase of the precursor activities. Detailed discussion on this topic are provided in Section 6.7.3.2.

Shortly after the peak, the spectra of SN 2023fyq exhibit broad absorption lines from the SN ejecta, indicating an optically thin CSM interaction region between the observer and the SN ejecta. However, the model fit indicates that the light curve is still predominantly influenced by the CSM interaction. One possible explanation for this discrepancy is that our analytical model is oversimplified, leading to an overestimation of the contribution from the CSM interaction. Alternatively, the CSM may not be spherically symmetric. For instance, if the SN were surrounded by a disk/torus-like CSM, strong CSM interaction would mainly occur in the equatorial region. Consequently, an observer looking along the polar direction would observe less obscured signals from the SN ejecta while the majority of the luminosity arises from the CSM interaction. The physical picture of this disk-like CSM scenario has been extensively discussed in Smith (2017).

In summary, neither radioactive decay nor CSM interaction alone can be the power source of SN 2023fyq. Approximately a few weeks before the explosion, about 0.3 $M_{\odot}$ of material is ejected with a velocity of $\sim$1000 $\mathrm{km\,s^{-1}}$ due to an increase in mass loss from the progenitor. This material expands to a radius of $\sim$3000 $\mathrm{R_{\odot}}$ at the time of the explosion. After the explosion, the energy deposited by the shock breakout from the extended material produces the initial light curve bump. Around 0 d the light curve is at least partially powered by the interaction between the SN ejecta and the surrounding CSM, with the kinetic energy of the ejecta converted into thermal energy, resulting in a bright peak. After that, as the strength of the CSM interaction decreases over time, the light curve becomes more influenced by radioactive decay, leading to a relatively flat light curve.

6.7.3. What Powers The Precursor of SN 2023fyq?

Table 6.1. Best-fit parameters of the CSM+Shock Breakout model and the CSM+Shock Breakout+RAD model.

Model	t_{exp} (Day)	M_{ej} ($M_\odot$)	R_0 (10^{13} cm)	M_{csm} ($M_\odot$)	$\rho_{csm,0}$ (log10(g cm^{-3}))	ϵ	R_e (10^{13} cm)	M_e ($M_\odot$)	M_{Ni} ($M_\odot$)
CSM+SBO	$-11.5^{+0.1}_{-0.1}$	$1.3^{+0.1}_{-0.1}$	$16.0^{+14.2}_{-9.7}$	$0.7^{+0.1}_{-0.1}$	$-11.9^{+0.1}_{-0.1}$	$5^{+0.1}_{-0.1} \times 10^{-2}$	$24.2^{+0.6}_{-1.1}$	$0.4^{+0.1}_{-0.1}$	...
CSM+SBO+RAD	$-11.4^{+0.1}_{-0.1}$	$1.2^{+0.1}_{-0.1}$	$15.0^{+12.5}_{-10.0}$	$0.6^{+0.1}_{-0.1}$	$-12.2^{+0.1}_{-0.1}$	$5^{+0.1}_{-0.1} \times 10^{-2}$	$21.4^{+0.7}_{-0.6}$	$0.3^{+0.1}_{-0.1}$	$0.02^{+0.01}_{-0.01}$

6.7.3.1. *Single massive star activities?* SN Precursors have been commonly observed in Type IIn SNe (e.g., Mauerhan et al., 2013; Smith et al., 2010; Ofek et al., 2013, 2014; Tartaglia et al., 2016; Pastorello et al., 2013, 2018; Strotjohann et al., 2021a; Hiramatsu et al., 2024), but are rarely found in Type Ibn SNe and Type II SNe. To date, the pre-explosion activities for Type Ibn SNe have only been detected in SN 2006jc (Pastorello et al., 2007) and SN 2019uo (Strotjohann et al., 2021a). Searches for precursors in other SNe Ibn yielded only upper limits, ranging from around −15 to −13 mag (e.g., Pastorello et al., 2008b; Shivvers et al., 2017; Wangq et al., 2024). This may be because those SNe Ibn had no precursors or only fainter and shorter ones, and also because most of these events occur at greater distances than SN 2023fyq. Compared to SN 2006jc and SN 2019uo, one unique characteristic of SN 2023fyq is the long-standing precursor emission. Precursor emission observed in SN 2006jc and SN 2019uo is around hundreds of days before the SN explosions with duration of ∼10 days. The precursor observed in these events are much shorter and brighter than that in SN 2023fyq (see Figure 6.2).

We first consider the possibility that the precursor of SN 2023fyq is produced by the final-stage stellar activities of a single massive star. In this case, the precursor can be powered by mass ejection driven by wave transport during the late-stage nuclear burning in the core (Quataert & Shiode, 2012; Shiode & Quataert, 2014; Fuller, 2017; Fuller & Ro, 2018; Morozova et al., 2020) or pulsational pair instability (Yoshida et al., 2016; Woosley, 2017).

Massive stars with He core masses of 30 – 64 $M_\odot$ experience pulsational pair instability after carbon burning, producing violent mass ejections before their cores collapse (Woosley,

2017). Pulsational pair instability in massive stars have been suggested to be a promising channel of Type Ibn SNe (Yoshida et al., 2016; Woosley, 2017; Leung et al., 2019; Renzo et al., 2020). The pulsing activities can last for hours to 10,000 years, depending on the He core mass, before the SN explosion (Yoshida et al., 2016; Woosley, 2017). In SN 2023fyq, precursor emission is detected for ∼3 years before the SN explosion. Therefore, if pulsational pair instability powers the precursor emission of SN 2023fyq, the progenitor would be a He star with a ZAMS mass larger than ∼52 $M_\odot$ (Woosley, 2017). However, the outbursts caused by the pulses of these more massive stars are usually energetic and can result in sharply rising light curves, which is inconsistent with the relatively steady precursor emission of SN 2023fyq. Additionally, the low ejecta mass we derived in Section 6.7.2 does not align with a very massive He star progenitor. Therefore, we disfavor pulsational pair instability as the powering mechanism of precursor emission in SN 2023fyq.

Strong temperature gradients can form during late-stage nuclear burning in massive stars, which generates convection, exciting internal gravity waves. The gravity waves may carry their energy to the envelope of the star and deposit it there (Quataert & Shiode, 2012; Shiode & Quataert, 2014; Fuller, 2017; Fuller & Ro, 2018), which may trigger eruptive mass ejections (Leung & Fuller, 2020; Matzner & Ro, 2021). The mass ejection itself and the collision between the ejecta generated from multiple outbursts can potentially produce SN precursor emission (Leung & Fuller, 2020; Strotjohann et al., 2021a; Tsuna et al., 2023). However, it would be difficult to reproduce the time scale of the observed precursor with a single event of dynamical envelope ejection from a stripped star (Tsuna et al., 2024). This is because the timescale is regulated by radiative diffusion from the precursor ejecta, which is only weeks to months for stripped stars, thus it would work for the precursors of SN 2006jc or SN 2019uo (Tsuna et al., 2024), but not for SN 2023fyq. In order to produce the precursor emission seen in SN 2023fyq, multiple fine-tuned mass ejections would be needed. Therefore,

a more plausible scenario is a continuous mass loss over the timescale of years, with some continuous powering mechanism for the precursor.

6.7.3.2. *Binary interaction?* A low-mass He star in a binary system has been proposed to be a possible progenitor scenario for Type Ibn SNe (Maund et al., 2016; Dessart et al., 2022; Tsuna et al., 2024), which is supported by the lack of star formation at the site of some members of the class (Sanders et al., 2013; Hosseinzadeh et al., 2019). In this section we explore the possibility that the progenitor of SN 2023fyq is an exploded stripped star, such as a He star, in a binary system and that the binary mass transfer generated the precursor activities.

The stripped SN progenitor in a binary system expands at some point in its evolution near core-collapse, filling its Roche lobe and initiating mass transfer onto the companion. Such a scenario is expected for stripped stars with He core masses in the range of 2.5–3 $M_\odot$, which can inflate their envelopes to up to $\sim 100\ R_\odot$ at the oxygen/neon burning phase in the final years to decades of their lives (e.g., Wu & Fuller, 2022, and references therein). Thus for orbital separations of $\sim$(1–few) $\times 100\ R_\odot$ (orbital period of order 100 days for a companion of order $\sim 1 M_\odot$), we expect intense mass transfer to initiate during this time period.

If the accretor is a compact object, the mass transfer rate is typically orders of magnitude higher than its Eddington rate, $\dot{M}_{\rm Edd} \sim 2 \times 10^{-8}\ {\rm M}_\odot\ {\rm yr}^{-1} (M_{\rm comp}/1 M_\odot)(\kappa_{opt}/0.1\ {\rm cm}^2\ {\rm g}^{-1})^{-1}$ (where a radiation efficiency of 10% was assumed), and thus most of the transferred mass actually escapes from the binary system without being accreted onto the compact object. Even if the companion is not a compact object, for large mass transfer rates of $\gtrsim 10^{-4}$–$10^{-3}\ M_\odot\ {\rm yr}^{-1}$, most of the mass is expected to still escape through the binary's outer Lagrange point (Lu et al., 2023). In either case, this escaped material becomes the CSM that later powers the bright SN.

In Section 6.7.2 we found that the CSM required to power the main SN light curve is around $0.6^{+0.1}_{-0.1}$ $M_\odot$, which requires a time-averaged mass loss rate of around a few $0.1 M_\odot$ yr^{-1} given that the mass loss is linked to the observed 1000-day precursor.

For binary systems exhibiting such high mass loss rates suggested by Wu & Fuller (2022), those with orbital periods ranging from 10 to 100 days are favored. These systems have orbital velocities of $\sim$100 – a few 100 $\mathrm{km\,s^{-1}}$. Assuming the velocity of the CSM that escapes the binary system is $\sim$200 $\mathrm{km\,s^{-1}}$, the mass loss rate via mass transfer should be at least larger than $\sim 2\times10^{-2}$ $M_\odot$ yr^{-1} to power the light curve peak (the detailed derivation is shown in Appendix A.1), which is consistent with what we found in Section 6.7.2.

Given the required $\dot{M}$, we can consider two mechanisms to power the precursor emission. The first is a collision of the mass-transfer outflow with external material, which may exist due to a previous mass-transfer episode (e.g., Pejcha et al., 2016; Metzger & Pejcha, 2017). While we remain agnostic to the origin of the pre-existing matter, the maximum available power is given by the kinetic luminosity of the outflow as

$$L_{\rm out} \approx \frac{1}{2}\dot{M} v_{\rm CSM}^2 \sim 1.3\times10^{39}\ \mathrm{erg\ s^{-1}} \times \left(\frac{\dot{M}}{0.1 M_\odot\ \mathrm{yr}^{-1}}\right)\left(\frac{v_{\rm CSM}}{200\ \mathrm{km\ s^{-1}}}\right)^2. \tag{6.2}$$

Thus the precursor may be explained, but only for favorably high CSM velocity as well as high efficiencies for dissipation and radiation conversion close to unity.

In the case for a compact object companion, an accretion disk forming around the compact object can be a promising energy source. While most of the transferred mass is removed from the outer L2 point, a small fraction can still accrete onto the companion and form a disk. The disk, if its accretion rate is super-Eddington, can launch a fast radiation-driven wind that can collide with the rest of the mass and dissipate its kinetic energy.

The hydrodynamics of the transferred mass has been considered recently in Lu et al. (2023). For a neutron star companion with an orbital separation of $a \approx$ (1–few)$\times 100$ $R_\odot$

and mass transfer rate $\gg 10^{-3}\ M_\odot\ \mathrm{yr}^{-1}$, most of the mass is indeed lost from the L2 point (their $f_{\rm L2} \sim 1$). However the accretion rate can still reach $\dot{M}_{\rm acc} \sim (3\text{–}7) \times 10^{-4}\ M_\odot\ \mathrm{yr}^{-1}$ (Figure A2 of Lu et al. 2023), which is orders of magnitude larger than the Eddington rate.

For a binary mass ratio of $q = M_{\rm NS}/M_* \approx 0.5$, the (Keplerian) circularization radius of the disk is found from the fitting formula in Lu et al. (2023) as

$$R_c \approx 0.10a \sim 7 \times 10^{11}\ \mathrm{cm} \left(\frac{a}{100 R_\odot}\right). \tag{6.3}$$

We expect a disk wind to be launched roughly where the local luminosity exceeds the Eddington luminosity of the NS, within a disk radius (equation 31 of Lu et al. 2023)

$$\begin{aligned} R_{\rm sph} &\approx \frac{\dot{M}_{\rm acc}\kappa}{4\pi c} \\ &\sim 2 \times 10^{10}\ \mathrm{cm} \left(\frac{\dot{M}_{\rm acc}}{5 \times 10^{-4} M_\odot\ \mathrm{yr}^{-1}}\right) \left(\frac{\kappa}{0.2\ \mathrm{cm}^2\ \mathrm{g}^{-1}}\right), \end{aligned} \tag{6.4}$$

which is typically less than $R_{\rm c}$ for an orbital separation of $a \sim 100\ R_\odot$. We have taken the opacity here to be $\kappa \approx 0.2\ \mathrm{cm}^2\ \mathrm{g}^{-1}$ as helium is expected to be fully ionized in the interior of the disk. In line with many theoretical works that model super-Eddington disk winds, we assume a power-law accretion rate $\dot{M}$ of $\dot{M} \propto r^p$ ($R_{\rm NS} < r < R_{\rm sph}$), where we adopt $R_{\rm NS} = 10$ km. This means that a fraction of the accreted mass is expelled at each radius, and we assume that the wind velocity is equivalent to the local disk escape velocity. Consequently, the wind kinetic luminosity, integrated over the range of r, is estimated as

$$\begin{aligned} L_{\rm wind} &\approx \frac{p}{2(1-p)} \dot{M}_{\rm acc} \frac{G M_{\rm NS}}{R_{\rm NS}} \left(\frac{R_{\rm NS}}{R_{\rm sph}}\right)^p \\ &\sim 2 \times 10^{40}\ \mathrm{erg\ s}^{-1} \left(\frac{\dot{M}_{\rm acc}}{5 \times 10^{-4} M_\odot\ \mathrm{yr}^{-1}}\right)^{1/2} \\ &\times \left(\frac{M_{\rm NS}}{1.4 M_\odot}\right) \left(\frac{\kappa}{0.2\ \mathrm{cm}^2\ \mathrm{g}^{-1}}\right)^{-1/2} \end{aligned} \tag{6.5}$$

where we have adopted $p = 0.5$ in the last equation while a possible range of $0.3 \leq p \leq 0.8$ is suggested (Yuan & Narayan, 2014). We thus find that the disk wind carries the appropriate kinetic luminosity to explain the precursor in the steady-state phase.

As the disk wind carries much smaller mass than the rest of the material around the system, its kinetic energy will be efficiently dissipated by their collision. We check that the dissipated energy would be successfully radiated as the precursor. For a wind profile the diffusion timescale in the CSM is

$$\begin{aligned} t_{\rm diff} &\approx \frac{\kappa \dot{M}}{4\pi v_{\rm CSM} c} \\ &\sim 8 \times 10^4 \ {\rm sec} \left(\frac{\dot{M}}{0.1 M_\odot \ {\rm yr}^{-1}} \right) \left(\frac{\kappa}{0.1 \ {\rm cm}^2 \ {\rm g}^{-1}} \right) \left(\frac{v_{\rm CSM}}{200 \ {\rm km \ s}^{-1}} \right)^{-1} \end{aligned} \tag{6.6}$$

and the adiabatic expansion timescale from the dissipation region, whose size is roughly comparable to the orbital separation, is

$$t_{\rm exp} \approx \frac{a}{v_{\rm CSM}} \sim 3 \times 10^5 \ {\rm sec} \left(\frac{a}{100 \ R_\odot} \right) \left(\frac{v_{\rm CSM}}{200 \ {\rm km \ s}^{-1}} \right)^{-1} \tag{6.7}$$

Thus we expect that the dissipated energy can be successfully radiated away without adiabatic losses. The radiation will be reprocessed in the CSM, and finally be emitted as optical radiation at $r \approx R_{\rm BB}$. The mass loss via the L2 point can form an equatorial disk (e.g., Lu et al., 2023). The interaction of the equatorial disk with the SN ejecta may contribute to the main peak of the SN light curve. In this case, the parameter M_{CSM} mentioned in Section 6.7.2 roughly characterizes the mass of the equatorial disk. The interaction of SN ejecta with this dense CSM may still continue in the nebular phase, producing the intermediate-width He lines we observe.

6.7.3.3. *The rise after −100 d in the pre-explosion light curve?* As we mentioned in Section 6.5.3, the pre-explosion light curve shows a rapid rise after −100 d, with a more pronounced rise occurring between −40 d and −11 d. This may be associated with eruptive

mass loss right before the SN explosion. For the more pronounced rise between −40 d and −11 d, we consider two possibilities: 1) the rise is due to orbital shrinking of the binary, leading to a runaway of mass transfer and resulting in a rapid-rising pre-explosion light curve (i.e., MacLeod et al., 2018). 2) The rise is influenced by the core silicon burning of the He star, which ejects a large amount of material and powers the fast-rising light curve just before the core collapses.

For the first case we initially consider the orbital evolution of this binary system over the few-year timescale during which we observe the precursor. The mass loss from the Lagrange point carries away angular momentum as well, which can affect the orbital separation of the binary. This generally leads to shrinking of the orbit, which may have been witnessed as the sharp rise of the light curve as we approach the explosion epoch. From Figure 5 of Lu et al. (2023) we find the orbital shrinking rate for mass ratio $q = 0.5$ and $f_{\rm L2} = 1$ as

$$\frac{\dot{a}}{a} \approx (-5)\frac{\dot{M}}{M_*} \sim -(6\ {\rm yr})^{-1} \left(\frac{\dot{M}}{0.1 M_\odot\ {\rm yr}^{-1}}\right) \left(\frac{M_*}{3 M_\odot}\right)^{-1} \tag{6.8}$$

which means that for a mass loss rate of $\sim 0.1 M_\odot\ {\rm yr}^{-1}$, the orbital separation can significantly shrink in the several years that we observe the precursor. The orbital shrinking of the binary may cause an unstable mass transfer and accretion onto the compact object, resulting in a runaway mass loss. This may explain the rapid rise after around −40 d in the precursor light curve. Given the anticipated significant orbital shrinking within several years for the system under consideration, the shallower rise in the light curve between −100 d and ∼ −40 d is likely also influenced by the orbital shrinking. This may only lead to a gently increase in the accretion rate onto the compact companion, resulting in the rise of the light curve.

In this scenario the final SN explosion can be due to the merger of the He star with a compact object (e.g., Chevalier, 2012b; Soker, 2019; Metzger, 2022). Such merger-driven explosions have been proposed to explain some long gamma-ray bursts (Fryer & Woosley, 1998; Zhang & Fryer, 2001; Thöne et al., 2011; Fryer et al., 2013), which are usually associated

with a subtype of Type Ic SNe that exhibit broad spectral lines. This He-merger scenario can connect the observed rapid increase in the light curve's brightness at the end of the precursor phase with the following SN-like explosion. However, the characteristics of the final explosion post-merger remain poorly understood. For example, the predicted explosion energies are uncertain by many orders of magnitude (Fryer & Woosley, 1998; Zhang & Fryer, 2001; Schrøder et al., 2020). While the merger-driven explosion might explain the spectral features observed, detailed spectral modeling of these events is still lacking.

For the second case, a core-collapse SN explosion is anticipated after significant mass transfer over years from low-mass stripped stars ranging from 2.5 to $3M_{\odot}$ (Wu & Fuller, 2022). Additionally an explosive mass ejection weeks before the explosion due to silicon burning is indeed expected in recent studies for low mass He stars with masses of 2.5 – 3.2 $M_{\odot}$ (Woosley, 2019b). The mass ejected can range from 10^{-2} to 1 $M_{\odot}$ with velocities from $\sim$100 km s^{-1} to a few 1000 km s^{-1}. In Section 6.7.2 we found that there is likely an eruptive mass loss of $\sim$0.3 $M_{\odot}$ a few weeks before the SN explosion with a velocity of $\sim$1000 km s^{-1}, which is consistent with the silicon burning phase for low-mass He stars. The eruptive mass loss may explain the more pronounced rise of the precursor light curve between ~ -40 d and -11 d, and the ejected material in turn produces the first SN peak. However, we note that detailed light curve modeling is necessary to confirm this hypothesis. In this case, the shallower rise in the light curve between -100 d and ~ -40 d is likely still attributed to the orbital shirking of the binary system, like discussed above.

In this scenario the final SN explosion results from the core collapse of the He star. This explanation accounts for the observed spectral similarities between SN 2023fyq and SESNe both post-peak and during the nebular phases.

Both the merger-driven and core-collapse scenarios can account for certain observed features of SN 2023fyq. In either case, the progenitor system would likely be asymmetric, which aligns with observations of SN 2023fyq. The ^{56}Ni yields from a merger-driven explosion

are likely low (Fryer et al., 2013; Metzger, 2022) and, similarly, low ^{56}Ni production is expected from core-collapse explosions in low-mass helium stars (Woosley, 2019b). These predictions are consistent with the low ^{56}Ni mass derived from the late-time light curves of SN 2023fyq.

An important difference between these two scenarios is that a merger-driven explosion typically results in a single compact object in the remnant, whereas a core-collapse explosion generally leaves behind a compact binary. In the latter case fallback accretion post-explosion could produce observable X-ray emissions approximately 100 to 1000 days after the explosion, which may show time variations tied to the orbital motion of the binary (Kashiyama et al., 2022). For SN 2023fyq, conducting X-ray follow-up years after the explosion could be helpful in distinguishing between these two scenarios in future studies (see Appendix A.2 for details).

In conclusion the timescale and brightness of the precursor observed in SN 2023fyq before -100 d can be attributed to mass transfer in a binary system. The companion star is likely a compact object, as the energetics of the disk wind launched from super-Eddington accretion onto the compact object can naturally explain the luminosity of the precursor. An equatorial circumbinary disk, formed during the mass transfer, later interacts with the SN ejecta, powering the main SN peak. During the nebular phases the ongoing interaction between the equatorial disk and the SN ejecta produces the intermediate-width He lines observed. The rise of the light curve between -100 d and ~ -40 d is likely due to orbital shrinking. The more pronounced rise of the light curve starting around -40 d may be linked to 1) an eruptive mass ejection due to final-stage silicon burning, or 2) runaway mass transfer caused by orbital shrinking of the binary system. In the first scenario, the subsequent explosion would result from the core-collapse of the He star. In the second scenario, it would result from the merger of the He star with the compact object. Both scenarios can launch materials into the polar region. The shock breakout from this extended material and the following cooling emission power the first bright SN peak.

6.7.4. Connections to Other Transient Phenomena and Implications for The CSM Structure. It is noteworthy that the light curve morphology (both the pre- and post-explosion phase) of SN 2023fyq is quite similar to those of luminous red novae (Soker & Tylenda, 2003; Tylenda et al., 2011; Mauerhan et al., 2015; Smith et al., 2016; Blagorodnova et al., 2017), which are generally understood to be the product of binary mergers (e.g., Metzger & Pejcha, 2017). The pre-explosion activities in luminous red novae are often associated with binary mass transfer (e.g., Pejcha, 2014), and the pre-explosion brightening is due to the increase in the mass-loss rate caused by orbital shrinking. The post-explosion light curves of luminous red novae are double-peaked, in which the first peak is likely from the shock cooling and the second peak is from the interaction between the ejecta and a pre-existing equatorial disc formed during binary mass transfer (Metzger & Pejcha, 2017).

The scenario for luminous red novae is analogous to what we proposed for SN 2023fyq, and the primary difference is just the explosion energy source. Such an asymmetric CSM structure is consistent with the multi-component profile of the He I λ5876 line as we discussed in Section 6.6 and also the asymmetric line profiles observed during the pre-explosion phase of SN 2023fyq (Brennan et al., 2024). Similarities between luminous red novae and interaction-powered SNe have also been reported in previous studies (e.g., Hiramatsu et al., 2024).

The SN light curve evolution of SN 2023fyq is similar to those of ultra-stripped SNe (De et al., 2018; Yao et al., 2020). The first bright SN light curve peak in these ultra-stripped SNe is generally understood as a result of shock breakout from the dense CSM ejected weeks before the SN explosion. The second peak of these objects is usually around $10^{42}\mathrm{erg\,s^{-1}}$, much fainter than that of SN 2023fyq, and is thought to be powered by ^{56}Ni decay (De et al., 2018; Yao et al., 2020). It may be that in these objects the CSM is more confined and a more extended ($\sim 10^{15}$ cm) dense equatorial disk is lacking, resulting in insufficient CSM at these radii to power the second peak through interaction like that observed in SN 2023fyq.

SNe Ibn can show a wide variety of spectral features at early phases (Hosseinzadeh et al., 2017), which is not surprising if all SNe Ibn experience strong interaction with asymmetric CSM (e.g., Smith et al., 2015b; Smith, 2017). Only a few SNe Ibn are observed until late phases since they can decline fast. Interestingly, as we show in Figure 6.9, at late times, these SNe Ibn seem to fall into two distinct classes: Class I that shows broad lines and share many similarities with normal SESNe (SN 2023fyq, SN 2015G, SN 2018gjx) and Class II that is still dominated by narrow emission lines (SN 2006jc, SN 2019kbj). Assuming the progenitors of all these SNe Ibn are He stars, the objects in Class II may be surrounded by more massive CSM and/or have lower explosion energy (Dessart et al., 2022).

For the objects in Class I, the intensity of the [O I] $\lambda\lambda$6300, 6364 line can vary significantly among different objects while the other spectral features are quite similar. If the progenitors of all these objects are surrounded by an equatorial disk, the difference in the intensity of the [O I] $\lambda\lambda$6300, 6364 line can be naturally explained by different viewing angles (See Figure 6.11). If the system is observed from the equatorial direction, the central [O I] $\lambda\lambda$6300, 6364 line forming region can be obscured by the disk. Instead, a polar observer would be able to see the whole nebular emission from the inner ejecta. For both observers, intermediate-width He emission lines from the ongoing interaction of the SN ejecta with the equatorial disk can be seen.

A disk/torus-like CSM is also invoked in previous studies to explain the spectroscopic evolution of SNe Ibn (Prentice et al., 2020) and SNe IIn (e.g., Smith & Arnett, 2014b; Smith et al., 2015b; Andrews & Smith, 2018; Smith & Andrews, 2020). Such a disk/torus-like CSM scenario could potentially explain the diversity we see in SNe Ibn in Class I, and is consistent with the precursor model we discussed in Section 6.7.3.2. This suggests that Class I SNe Ibn may originate from a similar progenitor channel but with variations in viewing angles.

Long-lasting and relatively stable precursor activities due to binary interaction are commonly seen in luminous red novae (e.g., Tylenda et al., 2011; Mauerhan et al., 2015; Blagorodnova et al., 2017). Given the similarity of the progenitor scenario of luminous red novae and SN 2023fyq, it is possible that precursor activities are not rare in SNe Ibn in Class I. If this is true, the long-lasting and slowly rising pre-explosion emission may serve as a unique early warning for this subclass of Type Ibn SNe. The evolution of the precursor light curves may vary depending on the viewing angle, as the emission could be obscured by the equatorial disk for observers near the equatorial plane. Given that the viewing angle also influences the intensity of the [OI] lines in the nebular spectra, combining the precursor emission with late-time spectroscopy could serve as a unique probe for the progenitor scenario we propose.

6.8. Summary

The evolution of SN 2023fyq closely resemble that of Type Ibn SNe. The optical spectra post-peak and the nebular spectrum of SN 2023fyq share similarities with those of normal SESNe, implying that the progenitor is a stripped/He star. The SN light curve can be reproduced by a CSM interaction + shock breakout + ^{56}Ni decay model, implying the presence of dense CSM around the progenitor, a low progenitor mass and a low ^{56}Ni production. The precursor emission of SN 2023fyq is observed up to around three years before the SN explosion, which is best explained by the mass transfer in a binary system involving a low-mass He star.

Putting all these together, we summarize a possible timeline for SN 2023fyq:

(1) ~-1000 d to ~-100 d (upper panel of Figure 6.11): A low-mass He star (2.5 – 3 $M_\odot$) expands substantially at the oxygen/neon burning phase, triggering mass transfer to its companion compact object, which produces the precursor emission we observe. The outflow via L2 point produces the He-rich CSM around the progenitor system and forms an equatorial disk ($\sim$0.6$M_\odot$).

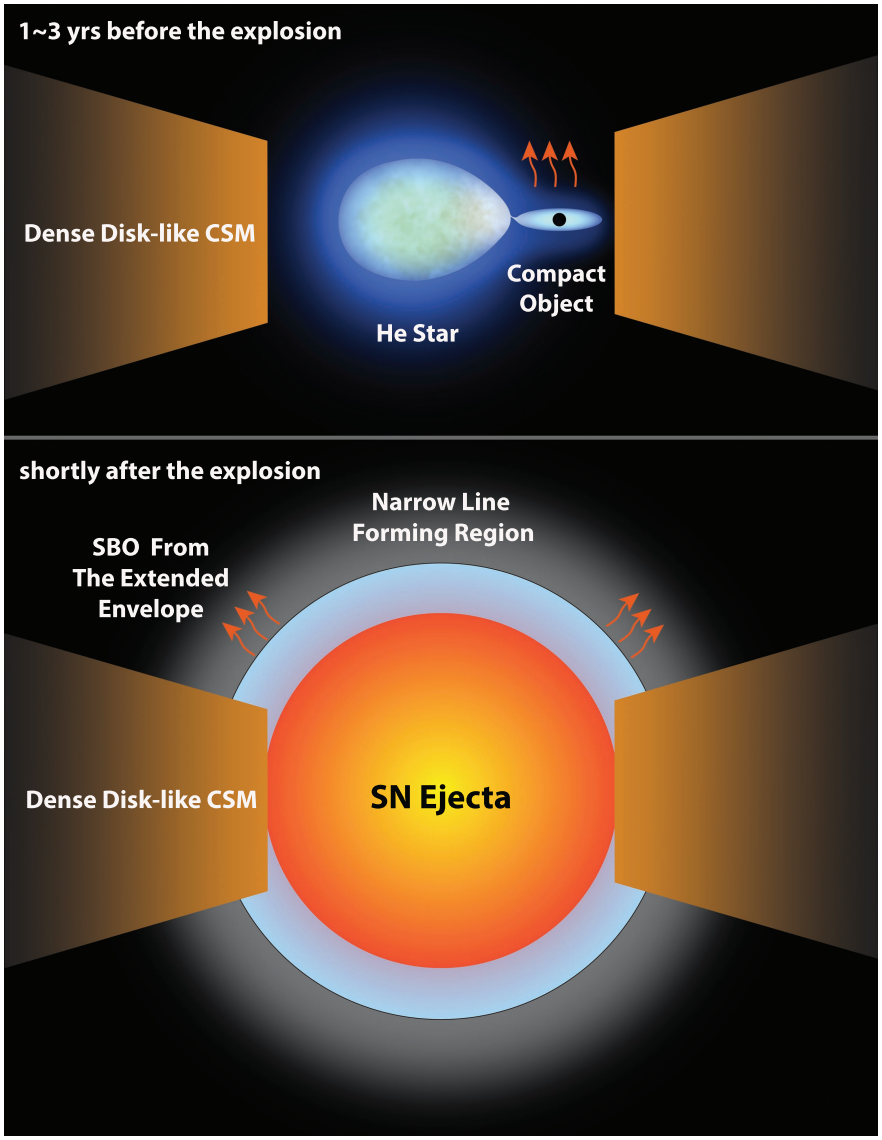

Figure 6.11 A sketch of the possible progenitor system of SN 2023fyq. Upper: around a few years before the explosion, the progenitor (a He star with a mass of $\sim 2.5 - 3\ M_{\odot}$) expands at the oxygen/neon burning phase, filling its Roche lobe. This triggers mass transfer onto its companion compact object, resulting in the precursor emission we observe. Around weeks before the explosion, an eruptive mass ejection is triggered through core silicon burning in the low-mass He star or runaway mass transfer due to orbital shrinking, launching dense material to the polar region. The subsequent explosion is likely due to either core-collapse of the He star or by the merger of the He star with its compact object companion. Bottom: Immediately after the explosion, the shock breaks out from the dense polar material formed weeks before the explosion, producing the first light curve peak. The interaction of SN ejecta with the equatorial disk formed by the pre-explosion binary interaction contributes to the second peak.

(2) ~ -100 d to ~ -11 d: The shrinkage of the orbit leads to an increase in the accretion rate onto the companion compact object, resulting in a rise in the light curve. The more pronounced light curve rise after ~ -40 d is likely due to either the core silicon burning or the runaway mass transfer caused by orbital shrinking, which triggers an eruptive mass ejection ($\sim 0.3 M_\odot$) with a velocity of $\sim 1000 \mathrm{km\,s^{-1}}$. This launches dense material to the polar region.

(3) ~ -11 d (bottom panel of Figure 6.11): A SN explosion is triggered either by the core-collapse of the He star or by the merger of the He star with a compact object, which sends a shock through the polar material ($\sim 3000\ R_\odot$). The energy deposited during the shock breakout produces the initial bump of the light curve.

(4) ~ -11 d to ~ 20 d: The SN ejecta collide with the equatorial He-rich CSM ($\sim 0.6 M_\odot$), converting the kinetic energy of the SN ejecta into thermal energy, contributing to the SN light curve and generating a very blue spectrum with only prominent He lines. With the expansion of the ejecta, the optical depth decreases so that more signals from the SN ejecta are observed.

(5) after ~ 20 d: The strength of the CSM interaction decreases and the SN fades, and radioactive decay likely starts to contribute more to the light curve. Later, the ejecta become more optically thin and the object transitions into the nebular phase. Given our proximity to the polar direction of the system, signals from the inner part of the ejecta are revealed, which closely resemble those of normal SESNe at nebular phases. Additionally, the continuing interaction between the ejecta and the He-rich equatorial CSM produces strong intermediate-width He emission lines.

Given the similarities between SN 2023fyq and other Type Ibn SNe, precursor activities may be common for a certain subclass of Type Ibn SNe. If an equatorial disk is indeed formed during the precursor phase, the precursor emission and the intensity of the [OI] lines at the nebular phases for this class of objects would be dependent on the viewing

angle. It is worth noting that this mechanism does not apply to the very brief, singular pre-explosion outburst observed in SN 2006jc and SN 2019uo. For the upcoming LSST survey, a single 30-second visit will achieve a 5σ depth of approximately 24 mag (Bianco et al., 2022). By stacking images, even deeper limits can be achieved. This enables LSST to effectively constrain the precursors of Type Ibn SNe, such as SN 2023fyq, within 150 Mpc, assuming a typical precursor brightness of -12 mag. A sample of Type Ibn SNe with well-constrained precursor activities, combined with the late-time spectroscopy, will test the progenitor scenario we propose. We also encourage detailed spectral and light curve modeling of merger-driven explosions, as well as the silicon burning phase in low-mass He stars just prior to core collapse. By comparing these models with a large sample of observations, we can deepen our understanding of the final stages of stellar evolution.

Acknowledgements

We would like to thank Jim Fuller for the assistance with the manuscript in its early stages. We would like to thank Kyle Davis for sharing the SOAR spectrum from his program. Y.D. would like to thank L.Z. for redesigning and redrawing Figure 11 in the paper.

Research by Y.D., S.V., N.M.R, E.H., and D.M. is supported by NSF grant AST-2008108. D.T. is supported by the Sherman Fairchild Postdoctoral Fellowship at the California Institute of Technology.

Time-domain research by the University of Arizona team and D.J.S. is supported by NSF grants AST-1821987, 1813466, 1908972, 2108032, and 2308181, and by the Heising-Simons Foundation under grant #2020-1864.

This work makes use of data from the Las Cumbres Observatory global telescope network. The LCO group is supported by NSF grants AST-1911225 and AST-1911151.

A.Z.B. acknowledges support from the European Research Council (ERC) under the European Union's Horizon 2020 research and innovation program (grant agreement No. 772086).

This publication was made possible through the support of an LSST-DA Catalyst Fellowship to K.A.B, funded through Grant 62192 from the John Templeton Foundation to LSST Discovery Alliance. The opinions expressed in this publication are those of the authors and do not necessarily reflect the views of LSST-DA or the John Templeton Foundation.

Based on observations obtained at the international Gemini Observatory, a program of NSF's NOIRLab, which is managed by the Association of Universities for Research in Astronomy (AURA) under a cooperative agreement with the National Science Foundation. On behalf of the Gemini Observatory partnership: the National Science Foundation (United States), National Research Council (Canada), Agencia Nacional de Investigación y Desarrollo (Chile), Ministerio de Ciencia, Tecnología e Innovación (Argentina), Ministério da Ciência, Tecnologia, Inovações e Comunicações (Brazil), and Korea Astronomy and Space Science Institute (Republic of Korea).

This work was enabled by observations made from the Gemini North telescope, located within the Maunakea Science Reserve and adjacent to the summit of Maunakea. We are grateful for the privilege of observing the Universe from a place that is unique in both its astronomical quality and its cultural significance.

This work includes observations obtained at the Southern Astrophysical Research (SOAR) telescope, which is a joint project of the Ministério da Ciência, Tecnologia e Inovações (MCTI/LNA) do Brasil, the US National Science Foundation's NOIRLab, the University of North Carolina at Chapel Hill (UNC), and Michigan State University (MSU).

Some of the data presented herein were obtained at Keck Observatory, which is a private 501(c)3 non-profit organization operated as a scientific partnership among the California Institute of Technology, the University of California, and the National Aeronautics and Space Administration. The Observatory was made possible by the generous financial support of the W. M. Keck Foundation. The authors wish to recognize and acknowledge the very significant cultural role and reverence that the summit of Maunakea has always had within

the indigenous Hawaiian community. We are most fortunate to have the opportunity to conduct observations from this mountain.

The LBT is an international collaboration among institutions in the United States, Italy and Germany. LBT Corporation Members are: The University of Arizona on behalf of the Arizona Board of Regents; Istituto Nazionale di Astrofisica, Italy; LBT Beteiligungsgesellschaft, Germany, representing the Max-Planck Society, The Leibniz Institute for Astrophysics Potsdam, and Heidelberg University; The Ohio State University, and The Research Corporation, on behalf of The University of Notre Dame, University of Minnesota and University of Virginia.

This research has made use of the NASA/IPAC Extragalactic Database (NED), which is funded by the National Aeronautics and Space Administration and operated by the California Institute of Technology.

This research made use of Photutils, an Astropy package for detection and photometry of astronomical sources (Bradley et al., 2022).

CHAPTER 7

Conclusion

In this thesis, I have presented my work on SN 2018cuf (Type II), SN 2023ixf (Type II), SN 2016dsg (Type I), SN 2022crv (Type IIb), and SN 2023fyq (Type Ibn). Utilizing both observational data and theoretical models, I was able to constrain the progenitors of these SNe.

- ⋆ I confirmed that normal Type II SNe can be surrounded by dense and confined CSM. Observational constraints on the nearby Type II SN 2023ixf imply that there are likely multiple mechanisms contributing to the dense CSM.
- ⋆ I found that SN 2016dsg is consistent with the theoretical predictions of a thick helium shell detonation. Remarkably, the signature of unburnt helium after the explosion strongly supports a helium shell detonation scenario. This suggests that helium shell detonation can be a promising channel for thermonuclear SNe, potentially contributing to normal Type Ia SNe in some cases.
- ⋆ By comparing the observed data of SN 2022crv with those of a sample of SESNe, I found that SN 2022crv is likely a transitional object on the continuum between Type Ib SNe and Type IIb SNe, supporting the idea of a continuum between these two SN types. Further analyses showed that SN 2022crv was likely formed in a binary system.
- ⋆ I was able to identify the long-standing precursor emission in the closest Type Ibn SN 2023fyq, marking the first Type Ibn to show such pre-explosion activities. The precursor emission is best explained by the mass transfer in a binary system comprising a low-mass helium star and a compact object. An equatorial disk likely

formed during this mass transfer, and the interaction of SN ejecta with this disk powered the main peak of the light curve. By analyzing a group of Type Ibn SNe, I conclude that precursor activities may be common in Type Ibn SNe, and there are likely two distinct progenitor channels for Type Ibn SNe.

Although significant progress has been made, many questions remain for future studies. For example, what exactly is the mechanism behind the dense CSM around Type II SNe? What proportion of Type Ia supernovae are produced by helium-shell detonation, and could this introduce systematic errors when measuring distances for cosmology studies? What accounts for the mysterious absorption feature at approximately 1.005μm in the NIR spectra? How does SN 2023fyq ultimately explode—through binary merger or core collapse?

To address these questions, it is crucial to collect a well-sampled dataset spanning from the very early to the very late phases of these events. With the operation of LSST in 2025 and the upcoming Nancy Grace Roman Space Telescope, the discovery of numerous transients will open a new window on the dynamic universe and the largely unknown parameter space of transients will be explored. These surveys will have the capability to detect final-stage stellar activities, such as strong stellar winds or short-scale outbursts, immediately preceding the explosions of many nearby supernovae. Comprehensive photometric and spectroscopic data can be collected by other space- or ground-based telescopes. With this complete dataset, we will gain new insights into the mass loss history of massive stars, and better understand final-stage stellar evolution.

APPENDIX A

A.1. The Mass Loss Rate in binary interaction scenario

This appendix calculates the mass loss rate needed for a binary system to explain the observations, as discussed in Section 6.7.3.2. We begin with estimating the required mass loss rate $\dot{M}$ of the CSM, which in our scenario is equivalent to the mass transfer rate if the rate is much larger than the Eddington rate and the companion cannot accrete most of the transferred material. The CSM must be optically thick within the observed blackbody radius $R_{\rm BB} \approx 600\ R_\odot$ at the precursor phase. For a mass loss rate of $\dot{M}$, the optical depth at $R_{\rm BB}$ is

$$\begin{aligned} \tau_{\rm CSM}(r = R_{\rm BB}) &\approx \frac{\kappa \dot{M}}{4\pi R_{\rm BB} v_{\rm CSM}} \\ &\sim 60 \left(\frac{\dot{M}}{0.1\ M_\odot\ {\rm yr}^{-1}}\right) \left(\frac{\kappa}{0.1\ {\rm cm}^2\ {\rm g}^{-1}}\right) \left(\frac{v_{\rm CSM}}{200\ {\rm km\ s}^{-1}}\right)^{-1} \end{aligned} \tag{A.1}$$

where $v_{\rm CSM}$ is the velocity of the CSM that escapes the binary system. This is typically the orbital velocity for outflows from mass transfer, which is ~ 200 km s^{-1} for the orbital separation of interest (see Section 6.7.3.2), but the arguments below would not depend much on the adopted value. The value of $\kappa \approx 0.1$ cm^2 g^{-1} is motivated from that of singly-ionized helium at around 10^4 K (e.g., Kleiser & Kasen, 2014). The optical depth then poses a lower limit in $\dot{M}$ of

$$\dot{M} \geq \dot{M}_{\rm min} \approx 2 \times 10^{-3} M_\odot\ {\rm yr}^{-1} \left(\frac{\kappa}{0.1\ {\rm cm}^2\ {\rm g}^{-1}}\right)^{-1} \left(\frac{v_{\rm CSM}}{200\ {\rm km\ s}^{-1}}\right) \tag{A.2}$$

which confirms the super-Eddington mass transfer rate[1]. As a cross check, we can also roughly infer $\dot{M}$ from the observed SN. The collision of the SN with the CSM generates a shock that powers the SN light curve. The kinetic energy dissipation rate is

$$L_{\rm kin} = 2\pi r^2 \left(\frac{\dot{M}}{4\pi r^2 v_{\rm CSM}}\right) v_{\rm sh}^3$$
$$\sim 5.5\times10^{43}\ {\rm erg\ s^{-1}} \left(\frac{\dot{M}}{0.1 M_\odot\ {\rm yr^{-1}}}\right) \left(\frac{v_{\rm CSM}}{200\ {\rm km\ s^{-1}}}\right)^{-1} \left(\frac{v_{\rm sh}}{7000\ {\rm km\ s^{-1}}}\right)^{3} \quad \text{(A.3)}$$

where $v_{\rm sh}$ is the forward shock velocity. Assuming that the luminosity at the second peak is generated by the interaction with CSM generated in the precursor phase, we infer a mass loss rate of

$$\dot{M} \sim 2\times10^{-2}\ M_\odot\ {\rm yr^{-1}} \epsilon^{-1} \left(\frac{L_{\rm rad}}{10^{43}\ {\rm erg\ s^{-1}}}\right) \left(\frac{v_{\rm CSM}}{200\ {\rm km\ s^{-1}}}\right) \left(\frac{v_{\rm sh}}{7000\ {\rm km\ s^{-1}}}\right)^{-3}, \quad \text{(A.4)}$$

where $\epsilon = L_{\rm rad}/L_{\rm kin} \leq 1$ is the radiation conversion efficiency. While this estimate is quite sensitive to the assumed $v_{\rm sh}$, it implies that a similarly high $\dot{M}$ is also required to explain the SN. The required mass transfer rate of ~ 0.02–$0.2 M_\odot\ {\rm yr^{-1}}$ for $\epsilon \approx 0.1$–1 roughly overlaps with the range obtained from simulations of binaries composed of a low-mass (2.5–3 $M_\odot$) He star and a neutron star, years to decades before the SN (Wu & Fuller, 2022, Figure 2).

A.2. Late-time X-ray detectability of SN 2023fyq

In this appendix, we roughly estimate the X-ray detectability of SN 2023fyq for future followup. We expect X-ray emission when it is transparent to photoionization by oxygen and carbon in the ejecta. Our modeling favors low-mass (a few $M_\odot$) helium stars for the progenitor, with carbon-oxygen cores of mass ≈ 1.5–$2\ M_\odot$. For an explosion ejecta from such

[1]As the blackbody temperature is $\sim 10^4$ K during the precursor phase, even for $\dot{M} \gg \dot{M}_{\rm min}$, we expect that the blackbody radius would not be too much larger than the observed value. This is because the temperature drops as a function of radius, and the opacity at $r > R_{\rm BB}$ will rapidly drop with radius due to helium recombination (analogous to the recombination front of SN II-P).

progenitors, we infer the mass of carbon/oxygen-rich material to be roughly $M_{\rm ej,C/O} \sim 0.1$–$1\ M_\odot$. The lower limit applies if a neutron star is left behind in the explosion (as in ultra-stripped SNe considered in Kashiyama et al. 2022), and the upper limit is if the bulk of the CO-core is disrupted (e.g. by a merger) and becomes part of the SN ejecta. Adopting the ejecta velocity of $v_{\rm ej} = 7000$ km s^{-1} and the X-ray photoionization cross section of $\sigma_{\rm X} \sim 10^{-19}\ {\rm cm}^2 (h\nu/{\rm keV})^{-3}$, we expect X-rays with energy $h\nu$ to be transparent at

$$t_{\rm trans} \sim \sqrt{\frac{\sigma_{\rm X} M_{\rm ej,C/O}/14 m_p}{4\pi v_{\rm ej}^2}} \sim 1\ {\rm yr} \left(\frac{M_{\rm ej,C/O}}{0.1\ M_\odot}\right)^{1/2} \left(\frac{h\nu}{5\ {\rm keV}}\right)^{-3/2}. \tag{A.5}$$

Thus follow-up in hard X-rays at years after the explosion is encouraged, although the X-ray luminosity would depend on the uncertain degree of fallback. If the fallback is similar to the ultra-stripped SN models in Kashiyama et al. (2022), we expect the source to be detectable by current X-ray facilities thanks to the proximity of this event.

Bibliography

Aldering, G., Humphreys, R. M., & Richmond, M. 1994, AJ, 107, 662, doi: 10.1086/116886

Allende Prieto, C., Lambert, D. L., & Asplund, M. 2001, ApJ, 556, L63, doi: 10.1086/322874

Allington-Smith, J., Breare, M., Ellis, R., et al. 1994, PASP, 106, 983, doi: 10.1086/133471

Anderson, J. P. 2019, A&A, 628, A7, doi: 10.1051/0004-6361/201935027

Anderson, J. P., González-Gaitán, S., Hamuy, M., et al. 2014, ApJ, 786, 67, doi: 10.1088/0004-637X/786/1/67

Anderson, J. P., Dessart, L., Gutiérrez, C. P., et al. 2018, Nature Astronomy, 2, 574, doi: 10.1038/s41550-018-0458-4

Andrews, J. E., & Smith, N. 2018, MNRAS, 477, 74, doi: 10.1093/mnras/sty584

Andrews, J. E., Lundquist, M., Sand, D. J., et al. 2022, Transient Name Server Classification Report, 2022-454, 1

Appenzeller, I., Fricke, K., Fürtig, W., et al. 1998, The Messenger, 94, 1

Arcavi, I., Hosseinzadeh, G., Brown, P. J., et al. 2017, ApJ, 837, L2, doi: 10.3847/2041-8213/aa5be1

Arnett, W. D. 1982, ApJ, 253, 785, doi: 10.1086/159681

Asplund, M., Grevesse, N., Sauval, A. J., & Scott, P. 2009a, ARA&A, 47, 481, doi: 10.1146/annurev.astro.46.060407.145222

—. 2009b, ARA&A, 47, 481, doi: 10.1146/annurev.astro.46.060407.145222

Baade, W. 1926, Astronomische Nachrichten, 228, 359, doi: 10.1002/asna.19262282003

Bacon, R., Accardo, M., Adjali, L., et al. 2010, in Society of Photo-Optical Instrumentation Engineers (SPIE) Conference Series, Vol. 7735, Ground-based and Airborne Instrumentation for Astronomy III, 773508, doi: 10.1117/12.856027

Beasor, E. R., Davies, B., Smith, N., et al. 2020, MNRAS, 492, 5994, doi: 10.1093/mnras/staa255

Becker, A. 2015, HOTPANTS: High Order Transform of PSF ANd Template Subtraction. http://ascl.net/1504.004

Bellm, E. C., Kulkarni, S. R., Graham, M. J., et al. 2019, PASP, 131, 018002, doi: 10.1088/1538-3873/aaecbe

Ben-Ami, T., Arcavi, I., Newsome, M., et al. 2023, ApJ, 946, 30, doi: 10.3847/1538-4357/acb432

Bernstein, R., Shectman, S. A., Gunnels, S. M., Mochnacki, S., & Athey, A. E. 2003, in Society of Photo-Optical Instrumentation Engineers (SPIE) Conference Series, Vol. 4841, Proc. SPIE, ed. M. Iye & A. F. M. Moorwood, 1694–1704, doi: 10.1117/12.461502

Bersten, M. C., Benvenuto, O., & Hamuy, M. 2011, ApJ, 729, 61, doi: 10.1088/0004-637X/729/1/61

Bersten, M. C., & Mazzali, P. A. 2017, in Handbook of Supernovae, ed. A. W. Alsabti & P. Murdin, 723, doi: 10.1007/978-3-319-21846-5_25

Bersten, M. C., Tanaka, M., Tominaga, N., Benvenuto, O. G., & Nomoto, K. 2013, ApJ, 767, 143, doi: 10.1088/0004-637X/767/2/143

Bersten, M. C., Folatelli, G., García, F., et al. 2018, Nature, 554, 497, doi: 10.1038/nature25151

Bertin, E., Mellier, Y., Radovich, M., et al. 2002, in Astronomical Society of the Pacific Conference Series, Vol. 281, Astronomical Data Analysis Software and Systems XI, ed. D. A. Bohlender, D. Durand, & T. H. Handley, 228

Bianco, F. B., Ivezić, Ž., Jones, R. L., et al. 2022, ApJS, 258, 1, doi: 10.3847/1538-4365/ac3e72

Bildsten, L., Shen, K. J., Weinberg, N. N., & Nelemans, G. 2007, ApJ, 662, L95, doi: 10.1086/519489

Blagorodnova, N., Kotak, R., Polshaw, J., et al. 2017, ApJ, 834, 107, doi: 10.3847/1538-4357/834/2/107

Blondin, S., Dessart, L., Hillier, D. J., & Khokhlov, A. M. 2017, MNRAS, 470, 157, doi: 10.1093/mnras/stw2492

Blondin, S., & Tonry, J. L. 2007a, ApJ, 666, 1024, doi: 10.1086/520494

—. 2007b, ApJ, 666, 1024, doi: 10.1086/520494

Boos, S. J., Townsley, D. M., Shen, K. J., Caldwell, S., & Miles, B. J. 2021, ApJ, 919, 126, doi: 10.3847/1538-4357/ac07a2

Bose, S., Dong, S., Kochanek, C. S., et al. 2020, arXiv e-prints, arXiv:2007.00008. https://arxiv.org/abs/2007.00008

Bostroem, K. A., Valenti, S., Horesh, A., et al. 2019, MNRAS, 485, 5120, doi: 10.1093/mnras/stz570

Bostroem, K. A., Valenti, S., Sand, D. J., et al. 2020, ApJ, 895, 31, doi: 10.3847/1538-4357/ab8945

Bostroem, K. A., Pearson, J., Shrestha, M., et al. 2023, Early Spectroscopy and Dense Circumstellar Medium Interaction in SN 2023ixf. https://arxiv.org/abs/2306.10119

Boyle, A., Sim, S. A., Hachinger, S., & Kerzendorf, W. 2017, A&A, 599, A46, doi: 10.1051/0004-6361/201629712

Bradley, L., Sipőcz, B., Robitaille, T., et al. 2022, astropy/photutils: 1.5.0, 1.5.0, Zenodo, doi: 10.5281/zenodo.6825092

Branch, D., Livio, M., Yungelson, L. R., Boffi, F. R., & Baron, E. 1995, PASP, 107, 1019, doi: 10.1086/133657

Branch, D., & Wheeler, J. C. 2017, Supernova Explosions, doi: 10.1007/978-3-662-55054-0

Branch, D., Benetti, S., Kasen, D., et al. 2002, ApJ, 566, 1005, doi: 10.1086/338127

Breeveld, A. A., Landsman, W., Holland, S. T., et al. 2011, in American Institute of Physics Conference Series, Vol. 1358, Gamma Ray Bursts 2010, ed. J. E. McEnery, J. L. Racusin, & N. Gehrels, 373–376, doi: 10.1063/1.3621807

Brennan, S. J., Sollerman, J., Irani, I., et al. 2024, arXiv e-prints, arXiv:2401.15148, doi: 10.48550/arXiv.2401.15148

Brethauer, D., Margutti, R., Milisavljevic, D., et al. 2022, ApJ, 939, 105, doi: 10.3847/1538-4357/ac8b14

Brown, P. J., Breeveld, A. A., Holland, S., Kuin, P., & Pritchard, T. 2014, Ap&SS, 354, 89, doi: 10.1007/s10509-014-2059-8

Brown, P. J., Holland, S. T., Immler, S., et al. 2009, AJ, 137, 4517, doi: 10.1088/0004-6256/137/5/4517

Brown, T. M., Baliber, N., Bianco, F. B., et al. 2013a, PASP, 125, 1031, doi: 10.1086/673168

—. 2013b, PASP, 125, 1031, doi: 10.1086/673168

—. 2013c, PASP, 125, 1031, doi: 10.1086/673168

Bruch, R. J., Gal-Yam, A., Schulze, S., et al. 2021, ApJ, 912, 46, doi: 10.3847/1538-4357/abef05

Bruch, R. J., Gal-Yam, A., Yaron, O., et al. 2023, ApJ, 952, 119, doi: 10.3847/1538-4357/acd8be

Burke, J., Howell, D. A., Sarbadhicary, S. K., et al. 2021, ApJ, 919, 142, doi: 10.3847/1538-4357/ac126b

Burns, C., Hsiao, E., Suntzeff, N., et al. 2021, The Astronomer's Telegram, 14441, 1

Buzzoni, B., Delabre, B., Dekker, H., et al. 1984, The Messenger, 38, 9

Cano, Z., Maeda, K., & Schulze, S. 2014, MNRAS, 438, 2924, doi: 10.1093/mnras/stt2400

Cappellaro, E., Mazzali, P. A., Benetti, S., et al. 1997, A&A, 328, 203, doi: 10.48550/arXiv.astro-ph/9707016

Cardelli, J. A., Clayton, G. C., & Mathis, J. S. 1989, ApJ, 345, 245, doi: 10.1086/167900

Cepa, J., Aguiar-Gonzalez, M., Gonzalez-Escalera, V., et al. 2000, in Optical and IR Telescope Instrumentation and Detectors, ed. M. Iye & A. F. M. Moorwood, Vol. 4008, International Society for Optics and Photonics (SPIE), 623 – 631, doi: 10.1117/12.395520

Chatzopoulos, E., Wheeler, J. C., & Vinko, J. 2009, ApJ, 704, 1251, doi: 10.1088/0004-637X/704/2/1251

—. 2012, ApJ, 746, 121, doi: 10.1088/0004-637X/746/2/121

Chevalier, R. A. 1982, ApJ, 258, 790, doi: 10.1086/160126

—. 2012a, ApJ, 752, L2, doi: 10.1088/2041-8205/752/1/L2

—. 2012b, ApJ, 752, L2, doi: 10.1088/2041-8205/752/1/L2

Chevalier, R. A., & Fransson, C. 1994, ApJ, 420, 268, doi: 10.1086/173557

Chevalier, R. A., & Soderberg, A. M. 2010, ApJ, 711, L40, doi: 10.1088/2041-8205/711/1/L40

Chilingarian, I., Beletsky, Y., Moran, S., et al. 2015, PASP, 127, 406, doi: 10.1086/680598

Chugai, N. N., Chevalier, R. A., & Utrobin, V. P. 2007, ApJ, 662, 1136, doi: 10.1086/518160

Clemens, J. C., Crain, J. A., & Anderson, R. 2004, in Society of Photo-Optical Instrumentation Engineers (SPIE) Conference Series, Vol. 5492, Ground-based Instrumentation for Astronomy, ed. A. F. M. Moorwood & M. Iye, 331–340, doi: 10.1117/12.550069

Clocchiatti, A., & Wheeler, J. C. 1997, ApJ, 491, 375, doi: 10.1086/304961

Crawford, S. M., Still, M., Schellart, P., et al. 2010a, in Society of Photo-Optical Instrumentation Engineers (SPIE) Conference Series, Vol. 7737, Observatory Operations: Strategies, Processes, and Systems III, ed. D. R. Silva, A. B. Peck, & B. T. Soifer, 773725, doi: 10.1117/12.857000

Crawford, S. M., Still, M., Schellart, P., et al. 2010b, in Society of Photo-Optical Instrumentation Engineers (SPIE) Conference Series, Society of Photo-Optical Instrumentation Engineers (SPIE) Conference Series, 25, doi: 10.1117/12.857000

Crowther, P. A. 2007, ARA&A, 45, 177, doi: 10.1146/annurev.astro.45.051806.110615

Csörnyei, G., Anderson, R. I., Vogl, C., et al. 2023, arXiv e-prints, arXiv:2305.13943, doi: 10.48550/arXiv.2305.13943

Curti, M., Mannucci, F., Cresci, G., & Maiolino, R. 2020, MNRAS, 491, 944, doi: 10.1093/mnras/stz2910

Cushing, M. C., Vacca, W. D., & Rayner, J. T. 2004, PASP, 116, 362, doi: 10.1086/382907

Czerny, B., Beaton, R., Bejger, M., et al. 2018, Space Sci. Rev., 214, 32, doi: 10.1007/s11214-018-0466-9

Davies, B., & Beasor, E. R. 2018, MNRAS, 474, 2116, doi: 10.1093/mnras/stx2734

—. 2020, MNRAS, 496, L142, doi: 10.1093/mnrasl/slaa102

Davies, B., Plez, B., & Petrault, M. 2022, MNRAS, 517, 1483, doi: 10.1093/mnras/stac2427

Davis, S., Hsiao, E. Y., Ashall, C., et al. 2019a, ApJ, 887, 4, doi: 10.3847/1538-4357/ab4c40

—. 2019b, ApJ, 887, 4, doi: 10.3847/1538-4357/ab4c40

De, K. 2023, Transient Name Server Discovery Report, 2023-825, 1

De, K., Kasliwal, M. M., Ofek, E. O., et al. 2018, Science, 362, 201, doi: 10.1126/science.aas8693

De, K., Kasliwal, M. M., Polin, A., et al. 2019, ApJ, 873, L18, doi: 10.3847/2041-8213/ab0aec

De, K., Kasliwal, M. M., Tzanidakis, A., et al. 2020, ApJ, 905, 58, doi: 10.3847/1538-4357/abb45c

de Jaeger, T., Anderson, J. P., Galbany, L., et al. 2018, MNRAS, 476, 4592, doi: 10.1093/mnras/sty508

Delgado, A., Harrison, D., Hodgkin, S., et al. 2016, Transient Name Server Discovery Report, 2016-481, 1

Demianenko, M., Malanchev, K., Samorodova, E., et al. 2023, A&A, 677, A16, doi: 10.1051/0004-6361/202245189

Deng, J. S., Qiu, Y. L., Hu, J. Y., Hatano, K., & Branch, D. 2000, ApJ, 540, 452, doi: 10.1086/309335

Dessart, L., & Hillier, D. J. 2005a, A&A, 439, 671, doi: 10.1051/0004-6361:20053217

—. 2005b, A&A, 439, 671, doi: 10.1051/0004-6361:20053217

—. 2015, MNRAS, 447, 1370, doi: 10.1093/mnras/stu2520

Dessart, L., Hillier, D. J., & Kuncarayakti, H. 2022, A&A, 658, A130, doi: 10.1051/0004-6361/202142436

Dessart, L., Hillier, D. J., Li, C., & Woosley, S. 2012, MNRAS, 424, 2139, doi: 10.1111/j.1365-2966.2012.21374.x

Dessart, L., Hillier, D. J., Livne, E., et al. 2011, MNRAS, 414, 2985, doi: 10.1111/j.1365-2966.2011.18598.x

Dessart, L., Hillier, D. J., Sukhbold, T., Woosley, S. E., & Janka, H. T. 2021, A&A, 656, A61, doi: 10.1051/0004-6361/202141927

Dessart, L., Hillier, D. J., Woosley, S., et al. 2015, MNRAS, 453, 2189, doi: 10.1093/mnras/stv1747

—. 2016, MNRAS, 458, 1618, doi: 10.1093/mnras/stw418

Dessart, L., Hillier, D. J., Woosley, S. E., & Kuncarayakti, H. 2023, arXiv e-prints, arXiv:2306.12092, doi: 10.48550/arXiv.2306.12092

Dolphin, A. 2016, DOLPHOT: Stellar photometry, Astrophysics Source Code Library, record ascl:1608.013. http://ascl.net/1608.013

Dong, Y., Valenti, S., Sand, D. J., et al. 2022, Transient Name Server Discovery Report, 2022-448, 1

Dressler, A., Bigelow, B., Hare, T., et al. 2011, PASP, 123, 288, doi: 10.1086/658908

Drout, M. R., Soderberg, A. M., Gal-Yam, A., et al. 2011, ApJ, 741, 97, doi: 10.1088/0004-637X/741/2/97

Drout, M. R., Milisavljevic, D., Parrent, J., et al. 2016, ApJ, 821, 57, doi: 10.3847/0004-637X/821/1/57

Eikenberry, S., Elston, R., Raines, S. N., et al. 2006, Society of Photo-Optical Instrumentation Engineers (SPIE) Conference Series, Vol. 6269, FLAMINGOS-2: the facility near-infrared wide-field imager and multi-object spectrograph for Gemini, 626917, doi: 10.1117/12.672095

Ekström, S., Georgy, C., Eggenberger, P., et al. 2012, A&A, 537, A146, doi: 10.1051/0004-6361/201117751

Eldridge, J. J., Fraser, M., Maund, J. R., & Smartt, S. J. 2015, MNRAS, 446, 2689, doi: 10.1093/mnras/stu2197

Eldridge, J. J., Fraser, M., Smartt, S. J., Maund, J. R., & Crockett, R. M. 2013, MNRAS, 436, 774, doi: 10.1093/mnras/stt1612

Eldridge, J. J., & Tout, C. A. 2004, MNRAS, 353, 87, doi: 10.1111/j.1365-2966.2004.08041.x

Elmhamdi, A., Danziger, I. J., Branch, D., et al. 2006, A&A, 450, 305, doi: 10.1051/0004-6361:20054366

Elmhamdi, A., Danziger, I. J., Cappellaro, E., et al. 2004, A&A, 426, 963, doi: 10.1051/0004-6361:20041318

Ergon, M., Sollerman, J., Fraser, M., et al. 2014, A&A, 562, A17, doi: 10.1051/0004-6361/201321850

Ertl, T., Woosley, S. E., Sukhbold, T., & Janka, H. T. 2020a, ApJ, 890, 51, doi: 10.3847/1538-4357/ab6458

—. 2020b, ApJ, 890, 51, doi: 10.3847/1538-4357/ab6458

Faber, S. M., Phillips, A. C., Kibrick, R. I., et al. 2003, in Society of Photo-Optical Instrumentation Engineers (SPIE) Conference Series, Vol. 4841, Instrument Design and Performance for Optical/Infrared Ground-based Telescopes, ed. M. Iye & A. F. M. Moorwood, 1657–1669, doi: 10.1117/12.460346

Fabricant, D., Fata, R., Epps, H., et al. 2019, PASP, 131, 075004, doi: 10.1088/1538-3873/ab1d78

Fang, Q., Maeda, K., Kuncarayakti, H., et al. 2022, ApJ, 928, 151, doi: 10.3847/1538-4357/ac4f60

Faran, T., Poznanski, D., Filippenko, A. V., et al. 2014, MNRAS, 442, 844, doi: 10.1093/mnras/stu955

Filippenko, A. V. 1982, PASP, 94, 715, doi: 10.1086/131052

—. 1988, AJ, 96, 1941, doi: 10.1086/114940

—. 1997, ARA&A, 35, 309, doi: 10.1146/annurev.astro.35.1.309

Filippenko, A. V., Li, W. D., Treffers, R. R., & Modjaz, M. 2001, in Astronomical Society of the Pacific Conference Series, Vol. 246, IAU Colloq. 183: Small Telescope Astronomy on Global Scales, ed. B. Paczynski, W.-P. Chen, & C. Lemme, 121

Filippenko, A. V., Matheson, T., & Ho, L. C. 1993, ApJ, 415, L103, doi: 10.1086/187043

Filippenko, A. V., Richmond, M. W., Branch, D., et al. 1992, AJ, 104, 1543, doi: 10.1086/116339

Fink, M., Röpke, F. K., Hillebrandt, W., et al. 2010, A&A, 514, A53, doi: 10.1051/0004-6361/200913892

Folatelli, G., Bersten, M. C., Kuncarayakti, H., et al. 2014, ApJ, 792, 7, doi: 10.1088/0004-637X/792/1/7

Folatelli, G., Van Dyk, S. D., Kuncarayakti, H., et al. 2016, ApJ, 825, L22, doi: 10.3847/2041-8205/825/2/L22

Foley, R. J. 2015, MNRAS, 452, 2463, doi: 10.1093/mnras/stv789

Foley, R. J., Smith, N., Ganeshalingam, M., et al. 2007, ApJ, 657, L105, doi: 10.1086/513145

Foreman-Mackey, D., Hogg, D. W., Lang, D., & Goodman, J. 2013, PASP, 125, 306, doi: 10.1086/670067

Förster, F., Moriya, T. J., Maureira, J. C., et al. 2018, Nature Astronomy, 2, 808, doi: 10.1038/s41550-018-0563-4

Fox, O. D., & Smith, N. 2019, MNRAS, 488, 3772, doi: 10.1093/mnras/stz1925

Fremling, C., Sollerman, J., Taddia, F., et al. 2014, A&A, 565, A114, doi: 10.1051/0004-6361/201423884

Fremling, C., Sollerman, J., Kasliwal, M. M., et al. 2018, A&A, 618, A37, doi: 10.1051/0004-6361/201731701

Freudling, W., Romaniello, M., Bramich, D. M., et al. 2013, A&A, 559, A96, doi: 10.1051/0004-6361/201322494

Fryer, C. L., Belczynski, K., Berger, E., et al. 2013, ApJ, 764, 181, doi: 10.1088/0004-637X/764/2/181

Fryer, C. L., & Woosley, S. E. 1998, ApJ, 502, L9, doi: 10.1086/311493

Fryer, C. L., Mazzali, P. A., Prochaska, J., et al. 2007, PASP, 119, 1211, doi: 10.1086/523768

Fukugita, M., Ichikawa, T., Gunn, J. E., et al. 1996, AJ, 111, 1748, doi: 10.1086/117915

Fuller, J. 2017, MNRAS, 470, 1642, doi: 10.1093/mnras/stx1314

Fuller, J., & Ro, S. 2018, MNRAS, 476, 1853, doi: 10.1093/mnras/sty369

Gal-Yam, A. 2017, in Handbook of Supernovae (Springer International Publishing), 195–237, doi: 10.1007/978-3-319-21846-5_35

Galbany, L., Hamuy, M., Phillips, M. M., et al. 2016a, AJ, 151, 33, doi: 10.3847/0004-6256/151/2/33

Galbany, L., Anderson, J. P., Rosales-Ortega, F. F., et al. 2016b, MNRAS, 455, 4087, doi: 10.1093/mnras/stv2620

Galbany, L., Anderson, J. P., Sánchez, S. F., et al. 2018a, ApJ, 855, 107, doi: 10.3847/1538-4357/aaaf20

—. 2018b, ApJ, 855, 107, doi: 10.3847/1538-4357/aaaf20

Galbany, L., Ashall, C., Höflich, P., et al. 2019, A&A, 630, A76, doi: 10.1051/0004-6361/201935537

Gall, C., Hjorth, J., Watson, D., et al. 2014, Nature, 511, 326, doi: 10.1038/nature13558

Gangopadhyay, A., Misra, K., Hiramatsu, D., et al. 2020, ApJ, 889, 170, doi: 10.3847/1538-4357/ab6328

Gangopadhyay, A., Maeda, K., Singh, A., et al. 2023, ApJ, 957, 100, doi: 10.3847/1538-4357/acfa94

Gehrels, N., Chincarini, G., Giommi, P., et al. 2004, ApJ, 611, 1005, doi: 10.1086/422091

Geier, S., Marsh, T. R., Wang, B., et al. 2013, A&A, 554, A54, doi: 10.1051/0004-6361/201321395

Gilkis, A., & Arcavi, I. 2022, MNRAS, 511, 691, doi: 10.1093/mnras/stac088

Gimeno, G., Roth, K., Chiboucas, K., et al. 2016, in Ground-based and Airborne Instrumentation for Astronomy VI, ed. C. J. Evans, L. Simard, & H. Takami, Vol. 9908, International Society for Optics and Photonics (SPIE), 872 – 885, doi: 10.1117/12.2233883

Gimeno, G., Roth, K., Chiboucas, K., et al. 2016, in Society of Photo-Optical Instrumentation Engineers (SPIE) Conference Series, Vol. 9908, Proc. SPIE, 99082S, doi: 10.1117/12.2233883

Goldberg, J. A., & Bildsten, L. 2020, ApJ, 895, L45, doi: 10.3847/2041-8213/ab9300

Goldberg, J. A., Bildsten, L., & Paxton, B. 2019, ApJ, 879, 3, doi: 10.3847/1538-4357/ab22b6

Götberg, Y., de Mink, S. E., & Groh, J. H. 2017, A&A, 608, A11, doi: 10.1051/0004-6361/201730472

Götberg, Y., de Mink, S. E., Groh, J. H., et al. 2018, A&A, 615, A78, doi: 10.1051/0004-6361/201732274

Gotberg, Y., Drout, M. R., Ji, A. P., et al. 2023, arXiv e-prints, arXiv:2307.00074, doi: 10.48550/arXiv.2307.00074

Graham, M. J., Kulkarni, S. R., Bellm, E. C., et al. 2019, PASP, 131, 078001, doi: 10.1088/1538-3873/ab006c

Graham, M. L., Kennedy, T. D., Kumar, S., et al. 2022, MNRAS, 511, 3682, doi: 10.1093/mnras/stac192

Green, R., Schmidt, G., Oey, S., Wittman, D., & Hall, P. 1995, Steward Observatory 2.3-m Boller and Chivens Spectrograph Manual. http://james.as.arizona.edu/~psmith/90inch/bcman/html/bcman.html

Grefenstette, B. W., Brightman, M., Earnshaw, H. P., Harrison, F. A., & Margutti, R. 2023, arXiv e-prints, arXiv:2306.04827, doi: 10.48550/arXiv.2306.04827

Gronow, S., Collins, C., Ohlmann, S. T., et al. 2020, A&A, 635, A169, doi: 10.1051/0004-6361/201936494

Gutiérrez, C. P., Anderson, J. P., Hamuy, M., et al. 2017, ApJ, 850, 89, doi: 10.3847/1538-4357/aa8f52

Hachinger, S., Mazzali, P. A., Taubenberger, S., et al. 2012, MNRAS, 422, 70, doi: 10.1111/j.1365-2966.2012.20464.x

Hamuy, M., Pinto, P. A., Maza, J., et al. 2001, ApJ, 558, 615, doi: 10.1086/322450

Hamuy, M., Maza, J., Pinto, P. A., et al. 2002, AJ, 124, 417, doi: 10.1086/340968

Hamuy, M., Folatelli, G., Morrell, N. I., et al. 2006, PASP, 118, 2, doi: 10.1086/500228

Harkness, R. P., Wheeler, J. C., Margon, B., et al. 1987, ApJ, 317, 355, doi: 10.1086/165283

Heger, A., Fryer, C. L., Woosley, S. E., Langer, N., & Hartmann, D. H. 2003, ApJ, 591, 288, doi: 10.1086/375341

Henden, A. A., Levine, S. E., Terrell, D., Smith, T. C., & Welch, D. 2012, **??**jnlJAAVSO, 40, 430

Hiramatsu, D., Howell, D. A., Moriya, T. J., et al. 2021, ApJ, 913, 55, doi: 10.3847/1538-4357/abf6d6

Hiramatsu, D., Matsumoto, T., Berger, E., et al. 2024, ApJ, 964, 181, doi: 10.3847/1538-4357/ad2854

Ho, A. Y. Q., Perley, D. A., Gal-Yam, A., et al. 2023, ApJ, 949, 120, doi: 10.3847/1538-4357/acc533

Hodgkin, S. T., Harrison, D. L., Breedt, E., et al. 2021, A&A, 652, A76, doi: 10.1051/0004-6361/202140735

Hoeflich, P. 2017, Explosion Physics of Thermonuclear Supernovae and Their Signatures, ed. A. W. Alsabti & P. Murdin, 1151, doi: 10.1007/978-3-319-21846-5_56

Hoeflich, P., & Khokhlov, A. 1996, ApJ, 457, 500, doi: 10.1086/176748

Holmbo, S., Stritzinger, M. D., Karamehmetoglu, E., et al. 2023, A&A, 675, A83, doi: 10.1051/0004-6361/202245334

Hook, I. M., Jørgensen, I., Allington-Smith, J. R., et al. 2004, PASP, 116, 425, doi: 10.1086/383624

Horiuchi, S., Nakamura, K., Takiwaki, T., Kotake, K., & Tanaka, M. 2014, MNRAS, 445, L99, doi: 10.1093/mnrasl/slu146

Hosseinzadeh, G. 2020, griffin-h/lightcurve_fitting v0.1.0, v0.1.0, Zenodo, doi: 10.5281/zenodo.3908580

Hosseinzadeh, G., & Gomez, S. 2020a, Light Curve Fitting, Zenodo, doi: 10.5281/zenodo.4312178

—. 2020b, Light Curve Fitting, v0.2.0, Zenodo, doi: 10.5281/zenodo.4312178

Hosseinzadeh, G., McCully, C., Zabludoff, A. I., et al. 2019, ApJ, 871, L9, doi: 10.3847/2041-8213/aafc61

Hosseinzadeh, G., Arcavi, I., Valenti, S., et al. 2017, ApJ, 836, 158, doi: 10.3847/1538-4357/836/2/158

Hosseinzadeh, G., Valenti, S., McCully, C., et al. 2018, ApJ, 861, 63, doi: 10.3847/1538-4357/aac5f6

Hosseinzadeh, G., Farah, J., Shrestha, M., et al. 2023, arXiv e-prints, arXiv:2306.06097, doi: 10.48550/arXiv.2306.06097

Houck, J. C., & Fransson, C. 1996, ApJ, 456, 811, doi: 10.1086/176699

Howell, D. A. 2011, Nature Communications, 2, doi: 10.1038/ncomms1344

Hsiao, E. Y., Phillips, M. M., Marion, G. H., et al. 2019a, PASP, 131, 014002, doi: 10.1088/1538-3873/aae961

—. 2019b, PASP, 131, 014002, doi: 10.1088/1538-3873/aae961

Hunter, D. J., Valenti, S., Kotak, R., et al. 2009, A&A, 508, 371, doi: 10.1051/0004-6361/200912896

Iben, I., J., & Tutukov, A. V. 1984, ApJS, 54, 335, doi: 10.1086/190932

Inserra, C., Turatto, M., Pastorello, A., et al. 2012, MNRAS, 422, 1122, doi: 10.1111/j.1365-2966.2012.20685.x

Inserra, C., Sim, S. A., Wyrzykowski, L., et al. 2015, ApJ, 799, L2, doi: 10.1088/2041-8205/799/1/L2

IRSA. 2022, Zwicky Transient Facility Image Service, IPAC, doi: 10.26131/IRSA539

Itagaki, K. 2023, TNSTR, 1158, 1. https://www.wis-tns.org/object/2023ixf/discovery-cert

Jacobson-Galán, W. V., Polin, A., Foley, R. J., et al. 2020, ApJ, 896, 165, doi: 10.3847/1538-4357/ab94b8

Jacobson-Galán, W. V., Dessart, L., Jones, D. O., et al. 2022, ApJ, 924, 15, doi: 10.3847/1538-4357/ac3f3a

Jacobson-Galan, W. V., Dessart, L., Margutti, R., et al. 2023, arXiv e-prints, arXiv:2306.04721, doi: 10.48550/arXiv.2306.04721

James, S., & Baron, E. 2010, ApJ, 718, 957, doi: 10.1088/0004-637X/718/2/957

Jencson, J. E., Pearson, J., Beasor, E. R., et al. 2023, A Luminous Red Supergiant and Dusty Long-period Variable Progenitor for SN 2023ixf. https://arxiv.org/abs/2306.08678

Jerkstrand, A., Ergon, M., Smartt, S. J., et al. 2015, A&A, 573, A12, doi: 10.1051/0004-6361/201423983

Jerkstrand, A., Ertl, T., Janka, H. T., et al. 2018, MNRAS, 475, 277, doi: 10.1093/mnras/stx2877

Jerkstrand, A., Fransson, C., & Kozma, C. 2011, A&A, 530, A45, doi: 10.1051/0004-6361/201015937

Jerkstrand, A., Fransson, C., Maguire, K., et al. 2012, A&A, 546, A28, doi: 10.1051/0004-6361/201219528

Jerkstrand, A., Smartt, S. J., Fraser, M., et al. 2014, MNRAS, 439, 3694, doi: 10.1093/mnras/stu221

Jha, S. 2018, Transient Name Server Classification Report, 2018-884, 1

Jiang, B., Jiang, S., & Ashley Villar, V. 2020, Research Notes of the American Astronomical Society, 4, 16, doi: 10.3847/2515-5172/ab7128

Jiang, J.-A., Doi, M., Maeda, K., et al. 2017, Nature, 550, 80, doi: 10.1038/nature23908

Johnson, S. A., Kochanek, C. S., & Adams, S. M. 2018, MNRAS, 480, 1696, doi: 10.1093/mnras/sty1966

Jones, D. H., Saunders, W., Colless, M., et al. 2004, MNRAS, 355, 747, doi: 10.1111/j.1365-2966.2004.08353.x

Jones, M. I., Hamuy, M., Lira, P., et al. 2009, ApJ, 696, 1176, doi: 10.1088/0004-637X/696/2/1176

Jordi, C., Gebran, M., Carrasco, J. M., et al. 2010, A&A, 523, A48, doi: 10.1051/0004-6361/201015441

Karamehmetoglu, E., Taddia, F., Sollerman, J., et al. 2017, A&A, 602, A93, doi: 10.1051/0004-6361/201629619

Kasen, D., & Bildsten, L. 2010, ApJ, 717, 245, doi: 10.1088/0004-637X/717/1/245

Kasen, D., & Woosley, S. E. 2009, ApJ, 703, 2205, doi: 10.1088/0004-637X/703/2/2205

Kashiyama, K., Sawada, R., & Suwa, Y. 2022, ApJ, 935, 86, doi: 10.3847/1538-4357/ac7ff7

Kasliwal, M. M., Kulkarni, S. R., Gal-Yam, A., et al. 2010, ApJ, 723, L98, doi: 10.1088/2041-8205/723/1/L98

—. 2012, ApJ, 755, 161, doi: 10.1088/0004-637X/755/2/161

Kennicutt, Robert C., J. 1998, ApJ, 498, 541, doi: 10.1086/305588

Kerzendorf, W., Sim, S., Vogl, C., et al. 2022, tardis-sn/tardis: TARDIS v2022.2.6, release-2022.2.6, Zenodo, doi: 10.5281/zenodo.5979739

Kerzendorf, W. E., & Sim, S. A. 2014, MNRAS, 440, 387, doi: 10.1093/mnras/stu055

Khazov, D., Yaron, O., Gal-Yam, A., et al. 2016, ApJ, 818, 3, doi: 10.3847/0004-637X/818/1/3

Kilpatrick, C. D., Foley, R. J., Abramson, L. E., et al. 2017, MNRAS, 465, 4650, doi: 10.1093/mnras/stw3082

Kilpatrick, C. D., Drout, M. R., Auchettl, K., et al. 2021, MNRAS, 504, 2073, doi: 10.1093/mnras/stab838

Kilpatrick, C. D., Foley, R. J., Jacobson-Galán, W. V., et al. 2023, arXiv e-prints, arXiv:2306.04722. https://arxiv.org/abs/2306.04722

Kinney, A. L., Calzetti, D., Bohlin, R. C., et al. 1996, ApJ, 467, 38, doi: 10.1086/177583

Kirshner, R. P., & Kwan, J. 1974, ApJ, 193, 27, doi: 10.1086/153123

Kleiser, I. K. W., & Kasen, D. 2014, MNRAS, 438, 318, doi: 10.1093/mnras/stt2191

Kochanek, C. S. 2019, MNRAS, 483, 3762, doi: 10.1093/mnras/sty3363

Kochanek, C. S., Khan, R., & Dai, X. 2012, ApJ, 759, 20, doi: 10.1088/0004-637X/759/1/20

Kochanek, C. S., Shappee, B. J., Stanek, K. Z., et al. 2017a, PASP, 129, 104502, doi: 10.1088/1538-3873/aa80d9

—. 2017b, PASP, 129, 104502, doi: 10.1088/1538-3873/aa80d9

Könyves-Tóth, R., Vinkó, J., Ordasi, A., et al. 2020, ApJ, 892, 121, doi: 10.3847/1538-4357/ab76bb

Kromer, M., Sim, S. A., Fink, M., et al. 2010, ApJ, 719, 1067, doi: 10.1088/0004-637X/719/2/1067

Kuncarayakti, H., Maeda, K., Bersten, M. C., et al. 2015, A&A, 579, A95, doi: 10.1051/0004-6361/201425604

Kupfer, T., Bauer, E. B., van Roestel, J., et al. 2022, ApJ, 925, L12, doi: 10.3847/2041-8213/ac48f1

Labrie, K., Anderson, K., Cárdenes, R., Simpson, C., & Turner, J. E. H. 2019, in Astronomical Society of the Pacific Conference Series, Vol. 523, Astronomical Data Analysis Software and Systems XXVII, ed. P. J. Teuben, M. W. Pound, B. A. Thomas, & E. M. Warner, 321

Landolt, A. U. 1992, AJ, 104, 340, doi: 10.1086/116242

Lang, D., Hogg, D. W., Mierle, K., Blanton, M., & Roweis, S. 2010, AJ, 139, 1782, doi: 10.1088/0004-6256/139/5/1782

Lantz, B., Aldering, G., Antilogus, P., et al. 2004, in Society of Photo-Optical Instrumentation Engineers (SPIE) Conference Series, Vol. 5249, Optical Design and Engineering, ed. L. Mazuray, P. J. Rogers, & R. Wartmann, 146–155, doi: 10.1117/12.512493

Leonard, D. C., Filippenko, A. V., Barth, A. J., & Matheson, T. 2000, ApJ, 536, 239, doi: 10.1086/308910

Leonard, D. C., Filippenko, A. V., Li, W., et al. 2002a, AJ, 124, 2490, doi: 10.1086/343771

Leonard, D. C., Filippenko, A. V., Gates, E. L., et al. 2002b, PASP, 114, 35, doi: 10.1086/324785

Leung, S.-C., & Fuller, J. 2020, ApJ, 900, 99, doi: 10.3847/1538-4357/abac5d

Leung, S.-C., Nomoto, K., & Blinnikov, S. 2019, ApJ, 887, 72, doi: 10.3847/1538-4357/ab4fe5

Li, W., Filippenko, A. V., Chornock, R., & Jha, S. 2003, PASP, 115, 844, doi: 10.1086/376432

Li, W., Leaman, J., Chornock, R., et al. 2011, MNRAS, 412, 1441, doi: 10.1111/j.1365-2966.2011.18160.x

Liu, Y.-Q., Modjaz, M., Bianco, F. B., & Graur, O. 2016a, ApJ, 827, 90, doi: 10.3847/0004-637X/827/2/90

—. 2016b, ApJ, 827, 90, doi: 10.3847/0004-637X/827/2/90

Livne, E. 1990, ApJ, 354, L53, doi: 10.1086/185721

Livne, E., & Arnett, D. 1995, ApJ, 452, 62, doi: 10.1086/176279

Livne, E., & Glasner, A. S. 1991, ApJ, 370, 272, doi: 10.1086/169813

Lu, W., Fuller, J., Quataert, E., & Bonnerot, C. 2023, MNRAS, 519, 1409, doi: 10.1093/mnras/stac3621

Lupton, R. H., Jurić, M., Ivezić, Z., et al. 2005, in American Astronomical Society Meeting Abstracts, Vol. 207, 133.08

Lyman, J. D., Levan, A. J., Church, R. P., Davies, M. B., & Tanvir, N. R. 2014, MNRAS, 444, 2157, doi: 10.1093/mnras/stu1574

Lyman, J. D., Levan, A. J., James, P. A., et al. 2016, MNRAS, 458, 1768, doi: 10.1093/mnras/stw477

MacLeod, M., Ostriker, E. C., & Stone, J. M. 2018, ApJ, 863, 5, doi: 10.3847/1538-4357/aacf08

Maeda, K., Jiang, J.-a., Shigeyama, T., & Doi, M. 2018, ApJ, 861, 78, doi: 10.3847/1538-4357/aac8d8

Maeda, K., Mazzali, P. A., Deng, J., et al. 2003, ApJ, 593, 931, doi: 10.1086/376591

Maeda, K., Tanaka, M., Nomoto, K., et al. 2007, ApJ, 666, 1069, doi: 10.1086/520054

Maeda, K., Kawabata, K., Mazzali, P. A., et al. 2008, Science, 319, 1220, doi: 10.1126/science.1149437

Magee, M. R., Maguire, K., Kotak, R., & Sim, S. A. 2021, MNRAS, 502, 3533, doi: 10.1093/mnras/stab201

Margalit, B. 2022, ApJ, 933, 238, doi: 10.3847/1538-4357/ac771a

Marion, G. H., Vinko, J., Kirshner, R. P., et al. 2014, ApJ, 781, 69, doi: 10.1088/0004-637X/781/2/69

Martinez, L., & Bersten, M. C. 2019, A&A, 629, A124, doi: 10.1051/0004-6361/201834818

Masci, F. 2011, Computing flux upper-limits for non-detections. https://web.ipac.caltech.edu/staff/fmasci/home/mystats/UpperLimits_FM2011.pdf

Masci, F. J., Laher, R. R., Rusholme, B., et al. 2023a, arXiv e-prints, arXiv:2305.16279, doi: 10.48550/arXiv.2305.16279

—. 2019, PASP, 131, 018003, doi: 10.1088/1538-3873/aae8ac

—. 2023b, arXiv e-prints, arXiv:2305.16279, doi: 10.48550/arXiv.2305.16279

Matheson, T., Filippenko, A. V., Chornock, R., Leonard, D. C., & Li, W. 2000, AJ, 119, 2303, doi: 10.1086/301352

Mathewson, D. S., Ford, V. L., & Buchhorn, M. 1992, ApJS, 81, 413, doi: 10.1086/191700

Matsuoka, T., & Sawada, R. 2023, Binary Interaction Can Yield a Diversity of Circumstellar Media around Type II Supernova Progenitors. https://arxiv.org/abs/2307.00727

Matzner, C. D., & Ro, S. 2021, ApJ, 908, 23, doi: 10.3847/1538-4357/abd03b

Mauerhan, J., & Smith, N. 2012, MNRAS, 424, 2659, doi: 10.1111/j.1365-2966.2012.21325.x

Mauerhan, J. C., Smith, N., Filippenko, A. V., et al. 2013, MNRAS, 430, 1801, doi: 10.1093/mnras/stt009

Mauerhan, J. C., Van Dyk, S. D., Graham, M. L., et al. 2015, MNRAS, 447, 1922, doi: 10.1093/mnras/stu2541

Maund, J. R., Pastorello, A., Mattila, S., Itagaki, K., & Boles, T. 2016, ApJ, 833, 128, doi: 10.3847/1538-4357/833/2/128

Maund, J. R., Smartt, S. J., Kudritzki, R. P., Podsiadlowski, P., & Gilmore, G. F. 2004, Nature, 427, 129, doi: 10.1038/nature02161

Maund, J. R., Fraser, M., Ergon, M., et al. 2011, ApJ, 739, L37, doi: 10.1088/2041-8205/739/2/L37

Maurer, I., Mazzali, P. A., Taubenberger, S., & Hachinger, S. 2010, MNRAS, 409, 1441, doi: 10.1111/j.1365-2966.2010.17186.x

Mazzali, P. A., Kawabata, K. S., Maeda, K., et al. 2005, Science, 308, 1284, doi: 10.1126/science.1111384

McLeod, B., Fabricant, D., Nystrom, G., et al. 2012, PASP, 124, 1318, doi: 10.1086/669044

Metzger, B. D. 2022, ApJ, 932, 84, doi: 10.3847/1538-4357/ac6d59

Metzger, B. D., & Pejcha, O. 2017, MNRAS, 471, 3200, doi: 10.1093/mnras/stx1768

Meynet, G., & Maeder, A. 2005, A&A, 429, 581, doi: 10.1051/0004-6361:20047106

Milisavljevic, D., Fesen, R. A., Gerardy, C. L., Kirshner, R. P., & Challis, P. 2010, ApJ, 709, 1343, doi: 10.1088/0004-637X/709/2/1343

Milisavljevic, D., Margutti, R., Soderberg, A. M., et al. 2013, ApJ, 767, 71, doi: 10.1088/0004-637X/767/1/71

Miller, A. A., Magee, M. R., Polin, A., et al. 2020, ApJ, 898, 56, doi: 10.3847/1538-4357/ab9e05

Miller, J. S., & Stone, R. P. S. 1994, The Kast Double Spectograph, Lick Observatory Tech. Rep. No. 66 (Santa Cruz: Lick Observatory)

Minkowski, R. 1941, PASP, 53, 224, doi: 10.1086/125315

Modjaz, M., Gutiérrez, C. P., & Arcavi, I. 2019, Nature Astronomy, 3, 717, doi: 10.1038/s41550-019-0856-2

Modjaz, M., Kirshner, R. P., Blondin, S., Challis, P., & Matheson, T. 2008, ApJ, 687, L9, doi: 10.1086/593135

Modjaz, M., Li, W., Butler, N., et al. 2009, ApJ, 702, 226, doi: 10.1088/0004-637X/702/1/226

Mokiem, M. R., de Koter, A., Vink, J. S., et al. 2007, A&A, 473, 603, doi: 10.1051/0004-6361:20077545

Monard, L. A. G. 2006, IAU Circ., 8666, 2

Moorwood, A., Cuby, J. G., & Lidman, C. 1998, The Messenger, 91, 9

Morozova, V., Piro, A. L., Fuller, J., & Van Dyk, S. D. 2020, ApJ, 891, L32, doi: 10.3847/2041-8213/ab77c8

Morozova, V., Piro, A. L., Renzo, M., et al. 2015, ApJ, 814, 63, doi: 10.1088/0004-637X/814/1/63

Morozova, V., Piro, A. L., & Valenti, S. 2017, ApJ, 838, 28, doi: 10.3847/1538-4357/aa6251

—. 2018, ApJ, 858, 15, doi: 10.3847/1538-4357/aab9a6

Müller, T., Prieto, J. L., Pejcha, O., & Clocchiatti, A. 2017, ApJ, 841, 127, doi: 10.3847/1538-4357/aa72f1

Munari, U., & Zwitter, T. 1997, A&A, 318, 269

Nadyozhin, D. K. 1994, ApJS, 92, 527, doi: 10.1086/192008

Nakaoka, T., Kawabata, K. S., Maeda, K., et al. 2018, ApJ, 859, 78, doi: 10.3847/1538-4357/aabee7

Neustadt, J. M. M., Kochanek, C. S., & Rizzo Smith, M. 2023, arXiv e-prints, arXiv:2306.06162. https://arxiv.org/abs/2306.06162

Noebauer, U. M., Kromer, M., Taubenberger, S., et al. 2017, MNRAS, 472, 2787, doi: 10.1093/mnras/stx2093

Nomoto, K. 1982a, ApJ, 253, 798, doi: 10.1086/159682

—. 1982b, ApJ, 257, 780, doi: 10.1086/160031

Nomoto, K., Thielemann, F. K., & Yokoi, K. 1984, ApJ, 286, 644, doi: 10.1086/162639

Nomoto, K., Tominaga, N., Umeda, H., Kobayashi, C., & Maeda, K. 2006, Nucl. Phys. A, 777, 424, doi: 10.1016/j.nuclphysa.2006.05.008

Nugent, P., Baron, E., Branch, D., Fisher, A., & Hauschildt, P. H. 1997, ApJ, 485, 812, doi: 10.1086/304459

Nugent, P. E., Sullivan, M., Cenko, S. B., et al. 2011, Nature, 480, 344, doi: 10.1038/nature10644

Ofek, E. O., Sullivan, M., Cenko, S. B., et al. 2013, Nature, 494, 65, doi: 10.1038/nature11877

Ofek, E. O., Sullivan, M., Shaviv, N. J., et al. 2014, ApJ, 789, 104, doi: 10.1088/0004-637X/789/2/104

Oke, J. B., Cohen, J. G., Carr, M., et al. 1995, PASP, 107, 375, doi: 10.1086/133562

Olivares E., F., Hamuy, M., Pignata, G., et al. 2010, ApJ, 715, 833, doi: 10.1088/0004-637X/715/2/833

Osterbrock, D. E., & Ferland, G. J. 2006, Astrophysics of gaseous nebulae and active galactic nuclei

Parrent, J., Branch, D., Troxel, M. A., et al. 2007, PASP, 119, 135, doi: 10.1086/512494

Pastorello, A., Sauer, D., Taubenberger, S., et al. 2006, MNRAS, 370, 1752, doi: 10.1111/j.1365-2966.2006.10587.x

Pastorello, A., Smartt, S. J., Mattila, S., et al. 2007, Nature, 447, 829, doi: 10.1038/nature05825

Pastorello, A., Kasliwal, M. M., Crockett, R. M., et al. 2008a, MNRAS, 389, 955, doi: 10.1111/j.1365-2966.2008.13618.x

Pastorello, A., Quimby, R. M., Smartt, S. J., et al. 2008b, MNRAS, 389, 131, doi: 10.1111/j.1365-2966.2008.13603.x

Pastorello, A., Cappellaro, E., Inserra, C., et al. 2013, ApJ, 767, 1, doi: 10.1088/0004-637X/767/1/1

Pastorello, A., Tartaglia, L., Elias-Rosa, N., et al. 2015a, MNRAS, 454, 4293, doi: 10.1093/mnras/stv2256

Pastorello, A., Prieto, J. L., Elias-Rosa, N., et al. 2015b, MNRAS, 453, 3649, doi: 10.1093/mnras/stv1812

Pastorello, A., Benetti, S., Brown, P. J., et al. 2015c, MNRAS, 449, 1921, doi: 10.1093/mnras/stu2745

Pastorello, A., Wang, X. F., Ciabattari, F., et al. 2016, MNRAS, 456, 853, doi: 10.1093/mnras/stv2634

Pastorello, A., Kochanek, C. S., Fraser, M., et al. 2018, MNRAS, 474, 197, doi: 10.1093/mnras/stx2668

Paxton, B., Schwab, J., Bauer, E. B., et al. 2018, ApJS, 234, 34, doi: 10.3847/1538-4365/aaa5a8

Pejcha, O. 2014, ApJ, 788, 22, doi: 10.1088/0004-637X/788/1/22

Pejcha, O., Metzger, B. D., & Tomida, K. 2016, MNRAS, 455, 4351, doi: 10.1093/mnras/stv2592

Pellegrino, C., Howell, D. A., Vinkó, J., et al. 2022, ApJ, 926, 125, doi: 10.3847/1538-4357/ac3e63

Pereira, R., Thomas, R. C., Aldering, G., et al. 2013, A&A, 554, A27, doi: 10.1051/0004-6361/201221008

Perets, H. B., Gal-Yam, A., Mazzali, P. A., et al. 2010, Nature, 465, 322, doi: 10.1038/nature09056

Perley, D., & Gal-Yam, A. 2023, TNSCR, 1164, 1. https://www.wis-tns.org/object/2023ixf/classification-cert

Perley, D. A. 2019, PASP, 131, 084503, doi: 10.1088/1538-3873/ab215d

Pettini, M., & Pagel, B. E. J. 2004a, MNRAS, 348, L59, doi: 10.1111/j.1365-2966.2004.07591.x

—. 2004b, MNRAS, 348, L59, doi: 10.1111/j.1365-2966.2004.07591.x

Phillips, M. M., Simon, J. D., Morrell, N., et al. 2013, ApJ, 779, 38, doi: 10.1088/0004-637X/779/1/38

Piro, A. L. 2015, ApJ, 801, 137, doi: 10.1088/0004-637X/801/2/137

Piro, A. L., Muhleisen, M., Arcavi, I., et al. 2017, ApJ, 846, 94, doi: 10.3847/1538-4357/aa8595

Podsiadlowski, P., Joss, P. C., & Hsu, J. J. L. 1992, ApJ, 391, 246, doi: 10.1086/171341

Pogge, R. 2019, rwpogge/modsCCDRed 2.0, 2.0, Zenodo, doi: 10.5281/zenodo.2550741

Pogge, R. W., Atwood, B., Brewer, D. F., et al. 2010, in Society of Photo-Optical Instrumentation Engineers (SPIE) Conference Series, Vol. 7735, Ground-based and Airborne Instrumentation for Astronomy III, ed. I. S. McLean, S. K. Ramsay, & H. Takami, 77350A, doi: 10.1117/12.857215

Polin, A., Nugent, P., & Kasen, D. 2019, ApJ, 873, 84, doi: 10.3847/1538-4357/aafb6a

—. 2021, ApJ, 906, 65, doi: 10.3847/1538-4357/abcccc

Poznanski, D., Nugent, P. E., & Filippenko, A. V. 2010, ApJ, 721, 956, doi: 10.1088/0004-637X/721/2/956

Poznanski, D., Prochaska, J. X., & Bloom, J. S. 2012, MNRAS, 426, 1465, doi: 10.1111/j.1365-2966.2012.21796.x

Prentice, S. J., & Mazzali, P. A. 2017, MNRAS, 469, 2672, doi: 10.1093/mnras/stx980

Prentice, S. J., Ashall, C., James, P. A., et al. 2019, MNRAS, 485, 1559, doi: 10.1093/mnras/sty3399

Prentice, S. J., Maguire, K., Boian, I., et al. 2020, MNRAS, 499, 1450, doi: 10.1093/mnras/staa2947

Prochaska, J. X., Hennawi, J. F., Westfall, K. B., et al. 2020, arXiv e-prints, arXiv:2005.06505. https://arxiv.org/abs/2005.06505

Prochaska, J. X., Hennawi, J. F., Westfall, K. B., et al. 2020, Journal of Open Source Software, 5, 2308, doi: 10.21105/joss.02308

Prochaska, J. X., Hennawi, J., Cooke, R., et al. 2020, pypeit/PypeIt: Release 1.0.0, v1.0.0, Zenodo, doi: 10.5281/zenodo.3743493

Quataert, E., & Shiode, J. 2012, MNRAS, 423, L92, doi: 10.1111/j.1745-3933.2012.01264.x

Rabinak, I., & Waxman, E. 2011, ApJ, 728, 63, doi: 10.1088/0004-637X/728/1/63

Reichart, D., Nysewander, M., Moran, J., et al. 2005, Nuovo Cimento C Geophysics Space Physics C, 28, 767, doi: 10.1393/ncc/i2005-10149-6

Renzo, M., Farmer, R., Justham, S., et al. 2020, A&A, 640, A56, doi: 10.1051/0004-6361/202037710

Riess, A. G., Yuan, W., Macri, L. M., et al. 2022, ApJ, 934, L7, doi: 10.3847/2041-8213/ac5c5b

Rui, L., Wang, X., Mo, J., et al. 2019, MNRAS, 485, 1990, doi: 10.1093/mnras/stz503

Sahu, D. K., Gurugubelli, U. K., Anupama, G. C., & Nomoto, K. 2011, MNRAS, 413, 2583, doi: 10.1111/j.1365-2966.2011.18326.x

Salpeter, E. E. 1955, ApJ, 121, 161, doi: 10.1086/145971

Sanders, N. E., Soderberg, A. M., Foley, R. J., et al. 2013, ApJ, 769, 39, doi: 10.1088/0004-637X/769/1/39

Sapir, N., & Waxman, E. 2017, ApJ, 838, 130, doi: 10.3847/1538-4357/aa64df

Savitzky, A., & Golay, M. J. E. 1964, Analytical Chemistry, 36, 1627

Schlafly, E. F., & Finkbeiner, D. P. 2011a, ApJ, 737, 103, doi: 10.1088/0004-637X/737/2/103

—. 2011b, ApJ, 737, 103, doi: 10.1088/0004-637X/737/2/103

Schlafly, E. F., Finkbeiner, D. P., Schlegel, D. J., et al. 2010, ApJ, 725, 1175, doi: 10.1088/0004-637X/725/1/1175

Schmelling, M. 1995, Phys. Scr, 51, 676, doi: 10.1088/0031-8949/51/6/002

Schrøder, S. L., MacLeod, M., Loeb, A., Vigna-Gómez, A., & Mandel, I. 2020, ApJ, 892, 13, doi: 10.3847/1538-4357/ab7014

Shahbandeh, M., Hsiao, E. Y., Ashall, C., et al. 2022, ApJ, 925, 175, doi: 10.3847/1538-4357/ac4030

Shappee, B. J., Prieto, J. L., Grupe, D., et al. 2014a, ApJ, 788, 48, doi: 10.1088/0004-637X/788/1/48

—. 2014b, ApJ, 788, 48, doi: 10.1088/0004-637X/788/1/48

—. 2014c, ApJ, 788, 48, doi: 10.1088/0004-637X/788/1/48

Shen, K. J., & Bildsten, L. 2014, ApJ, 785, 61, doi: 10.1088/0004-637X/785/1/61

Shen, K. J., Boos, S. J., Townsley, D. M., & Kasen, D. 2021, ApJ, 922, 68, doi: 10.3847/1538-4357/ac2304

Shen, K. J., Kasen, D., Miles, B. J., & Townsley, D. M. 2018, ApJ, 854, 52, doi: 10.3847/1538-4357/aaa8de

Shen, K. J., Kasen, D., Weinberg, N. N., Bildsten, L., & Scannapieco, E. 2010, ApJ, 715, 767, doi: 10.1088/0004-637X/715/2/767

Shen, K. J., & Moore, K. 2014, ApJ, 797, 46, doi: 10.1088/0004-637X/797/1/46

Shen, K. J., Quataert, E., & Pakmor, R. 2019, ApJ, 887, 180, doi: 10.3847/1538-4357/ab5370

Shigeyama, T., Nomoto, K., Tsujimoto, T., & Hashimoto, M.-A. 1990, ApJ, 361, L23, doi: 10.1086/185818

Shingles, L., Smith, K. W., Young, D. R., et al. 2021, Transient Name Server AstroNote, 7, 1

Shiode, J. H., & Quataert, E. 2014, ApJ, 780, 96, doi: 10.1088/0004-637X/780/1/96

Shivvers, I., Zheng, W., Van Dyk, S. D., et al. 2017, MNRAS, 471, 4381, doi: 10.1093/mnras/stx1885

Shivvers, I., Filippenko, A. V., Silverman, J. M., et al. 2019, MNRAS, 482, 1545, doi: 10.1093/mnras/sty2719

Siebert, M. R., Dimitriadis, G., Polin, A., & Foley, R. J. 2020, ApJ, 900, L27, doi: 10.3847/2041-8213/abae6e

Silverman, J. M., Foley, R. J., Filippenko, A. V., et al. 2012, MNRAS, 425, 1789, doi: 10.1111/j.1365-2966.2012.21270.x

Sim, S. A., Fink, M., Kromer, M., et al. 2012, MNRAS, 420, 3003, doi: 10.1111/j.1365-2966.2011.20162.x

Sim, S. A., Röpke, F. K., Hillebrandt, W., et al. 2010, ApJ, 714, L52, doi: 10.1088/2041-8205/714/1/L52

Simcoe, R. A., Burgasser, A. J., Schechter, P. L., et al. 2013, PASP, 125, 270, doi: 10.1086/670241

Singh Teja, R., Singh, A., Dutta, A., et al. 2023, arXiv e-prints, arXiv:2306.10284, doi: 10.48550/arXiv.2306.10284

Smartt, S. J. 2009, ARA&A, 47, 63, doi: 10.1146/annurev-astro-082708-101737

—. 2015, PASA, 32, e016, doi: 10.1017/pasa.2015.17

Smartt, S. J., Eldridge, J. J., Crockett, R. M., & Maund, J. R. 2009, MNRAS, 395, 1409, doi: 10.1111/j.1365-2966.2009.14506.x

Smartt, S. J., Valenti, S., Fraser, M., et al. 2015, A&A, 579, A40, doi: 10.1051/0004-6361/201425237

Smith, K. W., Smartt, S. J., Young, D. R., et al. 2020a, arXiv e-prints, arXiv:2003.09052. https://arxiv.org/abs/2003.09052

—. 2020b, PASP, 132, 085002, doi: 10.1088/1538-3873/ab936e

Smith, M. P., Nordsieck, K. H., Burgh, E. B., et al. 2006, in Society of Photo-Optical Instrumentation Engineers (SPIE) Conference Series, Vol. 6269, Society of Photo-Optical Instrumentation Engineers (SPIE) Conference Series, ed. I. S. McLean & M. Iye, 62692A, doi: 10.1117/12.672415

Smith, N. 2014a, ARA&A, 52, 487, doi: 10.1146/annurev-astro-081913-040025

—. 2014b, ARA&A, 52, 487, doi: 10.1146/annurev-astro-081913-040025

—. 2017, in Handbook of Supernovae, ed. A. W. Alsabti & P. Murdin, 403, doi: 10.1007/978-3-319-21846-5_38

Smith, N., & Andrews, J. E. 2020, MNRAS, 499, 3544, doi: 10.1093/mnras/staa3047

Smith, N., Andrews, J. E., Milne, P., et al. 2024, MNRAS, 530, 405, doi: 10.1093/mnras/stae726

Smith, N., & Arnett, W. D. 2014a, ApJ, 785, 82, doi: 10.1088/0004-637X/785/2/82

—. 2014b, ApJ, 785, 82, doi: 10.1088/0004-637X/785/2/82

Smith, N., Foley, R. J., & Filippenko, A. V. 2008, ApJ, 680, 568, doi: 10.1086/587860

Smith, N., Li, W., Filippenko, A. V., & Chornock, R. 2011, MNRAS, 412, 1522, doi: 10.1111/j.1365-2966.2011.17229.x

Smith, N., & McCray, R. 2007, ApJ, 671, L17, doi: 10.1086/524681

Smith, N., Pearson, J., Sand, D. J., et al. 2023, arXiv e-prints, arXiv:2306.07964, doi: 10.48550/arXiv.2306.07964

Smith, N., Miller, A., Li, W., et al. 2010, AJ, 139, 1451, doi: 10.1088/0004-6256/139/4/1451

Smith, N., Mauerhan, J. C., Cenko, S. B., et al. 2015a, MNRAS, 449, 1876, doi: 10.1093/mnras/stv354

—. 2015b, MNRAS, 449, 1876, doi: 10.1093/mnras/stv354

Smith, N., Andrews, J. E., Van Dyk, S. D., et al. 2016, MNRAS, 458, 950, doi: 10.1093/mnras/stw219

Soker, N. 2013, arXiv e-prints, arXiv:1302.5037, doi: 10.48550/arXiv.1302.5037

—. 2019, Science China Physics, Mechanics, and Astronomy, 62, 119501, doi: 10.1007/s11433-019-9402-x

—. 2021, ApJ, 906, 1, doi: 10.3847/1538-4357/abca8f

—. 2023, arXiv e-prints, arXiv:2306.15270, doi: 10.48550/arXiv.2306.15270

Soker, N., & Tylenda, R. 2003, ApJ, 582, L105, doi: 10.1086/367759

Soraisam, M. D., Szalai, T., Van Dyk, S. D., et al. 2023, arXiv e-prints, arXiv:2306.10783, doi: 10.48550/arXiv.2306.10783

Spergel, D. N., Bean, R., Doré, O., et al. 2007, ApJS, 170, 377, doi: 10.1086/513700

Spiro, S., Pastorello, A., Pumo, M. L., et al. 2014, MNRAS, 439, 2873, doi: 10.1093/mnras/stu156

Stahl, B. E., Zheng, W., de Jaeger, T., et al. 2019, MNRAS, 490, 3882, doi: 10.1093/mnras/stz2742

Stephenson, F. R. 2017, in Handbook of Supernovae, ed. A. W. Alsabti & P. Murdin, 49, doi: 10.1007/978-3-319-21846-5_44

Stetson, P. B. 1987, PASP, 99, 191, doi: 10.1086/131977

Stritzinger, M., Mazzali, P., Phillips, M. M., et al. 2009, ApJ, 696, 713, doi: 10.1088/0004-637X/696/1/713

Stritzinger, M. D., Taddia, F., Burns, C. R., et al. 2018, A&A, 609, A135, doi: 10.1051/0004-6361/201730843

Strotjohann, N. L., Ofek, E. O., Gal-Yam, A., et al. 2021a, ApJ, 907, 99, doi: 10.3847/1538-4357/abd032

—. 2021b, ApJ, 907, 99, doi: 10.3847/1538-4357/abd032

Sukhbold, T., Ertl, T., Woosley, S. E., Brown, J. M., & Janka, H. T. 2016a, ApJ, 821, 38, doi: 10.3847/0004-637X/821/1/38

—. 2016b, ApJ, 821, 38, doi: 10.3847/0004-637X/821/1/38

Sutherland, P. G., & Wheeler, J. C. 1984, ApJ, 280, 282, doi: 10.1086/161995

Taddia, F., Sollerman, J., Leloudas, G., et al. 2015, A&A, 574, A60, doi: 10.1051/0004-6361/201423915

Taddia, F., Stritzinger, M. D., Bersten, M., et al. 2018, A&A, 609, A136, doi: 10.1051/0004-6361/201730844

Takáts, K., Pignata, G., Pumo, M. L., et al. 2015, MNRAS, 450, 3137, doi: 10.1093/mnras/stv857

Tanaka, M., Tominaga, N., Nomoto, K., et al. 2009, ApJ, 692, 1131, doi: 10.1088/0004-637X/692/2/1131

Tartaglia, L., Pastorello, A., Sullivan, M., et al. 2016, MNRAS, 459, 1039, doi: 10.1093/mnras/stw675

Tartaglia, L., Fraser, M., Sand, D. J., et al. 2017, ApJ, 836, L12, doi: 10.3847/2041-8213/aa5c7f

Tartaglia, L., Sand, D. J., Valenti, S., et al. 2018, ApJ, 853, 62, doi: 10.3847/1538-4357/aaa014

Taubenberger, S., Valenti, S., Benetti, S., et al. 2009, MNRAS, 397, 677, doi: 10.1111/j.1365-2966.2009.15003.x

Teffs, J., Ertl, T., Mazzali, P., Hachinger, S., & Janka, T. 2020, MNRAS, 492, 4369, doi: 10.1093/mnras/staa123

Terreran, G., Jacobson-Galán, W. V., Groh, J. H., et al. 2022, ApJ, 926, 20, doi: 10.3847/1538-4357/ac3820

Thöne, C. C., de Ugarte Postigo, A., Fryer, C. L., et al. 2011, Nature, 480, 72, doi: 10.1038/nature10611

Tody, D. 1986, in Society of Photo-Optical Instrumentation Engineers (SPIE) Conference Series, Vol. 627, Instrumentation in astronomy VI, ed. D. L. Crawford, 733, doi: 10.1117/12.968154

Tomasella, L., Cappellaro, E., Fraser, M., et al. 2013, MNRAS, 434, 1636, doi: 10.1093/mnras/stt1130

Tonry, J. L. 2011, PASP, 123, 58, doi: 10.1086/657997

Tonry, J. L., Stubbs, C. W., Lykke, K. R., et al. 2012, ApJ, 750, 99, doi: 10.1088/0004-637X/750/2/99

Tonry, J. L., Denneau, L., Heinze, A. N., et al. 2018, PASP, 130, 064505, doi: 10.1088/1538-3873/aabadf

Torres, S., Briceño, C., & Quint, B. 2017, Goodman HTS Pipeline Documentation 1.3.6. https://soardocs.readthedocs.io/projects/goodman-pipeline/

Townsley, D. M., Miles, B. J., Shen, K. J., & Kasen, D. 2019, ApJ, 878, L38, doi: 10.3847/2041-8213/ab27cd

Tsuna, D., Matsumoto, T., Wu, S. C., & Fuller, J. 2024, arXiv e-prints, arXiv:2401.02389, doi: 10.48550/arXiv.2401.02389

Tsuna, D., Takei, Y., & Shigeyama, T. 2023, ApJ, 945, 104, doi: 10.3847/1538-4357/acbbc6

Tsvetkov, D. Y., Volkov, I. M., & Pavlyuk, N. N. 2015, Information Bulletin on Variable Stars, 6140, 1, doi: 10.48550/arXiv.1504.01864

Tucker, M. A., Shappee, B. J., Huber, M. E., et al. 2022, PASP, 134, 124502, doi: 10.1088/1538-3873/aca719

Tully, R. B., Courtois, H. M., & Sorce, J. G. 2016, AJ, 152, 50, doi: 10.3847/0004-6256/152/2/50

Tully, R. B., Rizzi, L., Shaya, E. J., et al. 2009, AJ, 138, 323, doi: 10.1088/0004-6256/138/2/323

Tylenda, R., Hajduk, M., Kamiński, T., et al. 2011, A&A, 528, A114, doi: 10.1051/0004-6361/201016221

Uomoto, A. 1986, ApJ, 310, L35, doi: 10.1086/184777

Utrobin, V. P., & Chugai, N. N. 2015, A&A, 575, A100, doi: 10.1051/0004-6361/201424822

—. 2017, MNRAS, 472, 5004, doi: 10.1093/mnras/stx2415

Vacca, W. D., Cushing, M. C., & Rayner, J. T. 2003, PASP, 115, 389, doi: 10.1086/346193

Valenti, S., Sand, D. J., & Wyatt, S. 2018, Transient Name Server Discovery Report, 2018-876, 1

Valenti, S., Benetti, S., Cappellaro, E., et al. 2008, MNRAS, 383, 1485, doi: 10.1111/j.1365-2966.2007.12647.x

Valenti, S., Fraser, M., Benetti, S., et al. 2011, MNRAS, 416, 3138, doi: 10.1111/j.1365-2966.2011.19262.x

Valenti, S., Sand, D., Pastorello, A., et al. 2014a, MNRAS, 438, L101, doi: 10.1093/mnrasl/slt171

—. 2014b, MNRAS, 438, L101, doi: 10.1093/mnrasl/slt171

Valenti, S., Yuan, F., Taubenberger, S., et al. 2014c, MNRAS, 437, 1519, doi: 10.1093/mnras/stt1983

Valenti, S., Howell, D. A., Stritzinger, M. D., et al. 2016, MNRAS, 459, 3939, doi: 10.1093/mnras/stw870

Valerin, G., Benetti, S., Elias–Rosa, N., et al. 2023, Transient Name Server Classification Report, 2023-1777, 1

Van Dyk, S. D. 2017, Philosophical Transactions of the Royal Society of London Series A, 375, 20160277, doi: 10.1098/rsta.2016.0277

Van Dyk, S. D., Li, W., & Filippenko, A. V. 2003a, PASP, 115, 1289, doi: 10.1086/378308

—. 2003b, PASP, 115, 1, doi: 10.1086/345748

Van Dyk, S. D., Li, W., Cenko, S. B., et al. 2011, ApJ, 741, L28, doi: 10.1088/2041-8205/741/2/L28

Van Dyk, S. D., Zheng, W., Fox, O. D., et al. 2014, AJ, 147, 37, doi: 10.1088/0004-6256/147/2/37

Van Dyk, S. D., Bostroem, K. A., Andrews, J. E., et al. 2023, arXiv e-prints, arXiv:2302.00274, doi: 10.48550/arXiv.2302.00274

Vink, J. S., de Koter, A., & Lamers, H. J. G. L. M. 2001, A&A, 369, 574, doi: 10.1051/0004-6361:20010127

Waldman, R., Sauer, D., Livne, E., et al. 2011, ApJ, 738, 21, doi: 10.1088/0004-637X/738/1/21

Walmswell, J. J., & Eldridge, J. J. 2012, MNRAS, 419, 2054, doi: 10.1111/j.1365-2966.2011.19860.x

Wang, S. Q., Wang, L. J., Dai, Z. G., & Wu, X. F. 2015, ApJ, 807, 147, doi: 10.1088/0004-637X/807/2/147

Wangq, Q., Goel, A., Dessart, L., et al. 2024, MNRAS, doi: 10.1093/mnras/stae1038

Waxman, E., & Katz, B. 2017, in Handbook of Supernovae, ed. A. W. Alsabti & P. Murdin, 967, doi: 10.1007/978-3-319-21846-5_33

Webbink, R. F. 1984, ApJ, 277, 355, doi: 10.1086/161701

Wellons, S., Soderberg, A. M., & Chevalier, R. A. 2012, ApJ, 752, 17, doi: 10.1088/0004-637X/752/1/17

Wellstein, S., & Langer, N. 1999, A&A, 350, 148, doi: 10.48550/arXiv.astro-ph/9904256

Wheeler, J. C., & Harkness, R. P. 1990, Reports on Progress in Physics, 53, 1467, doi: 10.1088/0034-4885/53/12/001

Whelan, J., & Iben, Icko, J. 1973, ApJ, 186, 1007, doi: 10.1086/152565

Williamson, M., Modjaz, M., & Bianco, F. B. 2019, ApJ, 880, L22, doi: 10.3847/2041-8213/ab2edb

Willick, J. A., Courteau, S., Faber, S. M., et al. 1997, ApJS, 109, 333, doi: 10.1086/312983

Wilson, J. C., Henderson, C. P., Herter, T. L., et al. 2004, in Society of Photo-Optical Instrumentation Engineers (SPIE) Conference Series, Vol. 5492, Ground-based Instrumentation for Astronomy, ed. A. F. M. Moorwood & M. Iye, 1295–1305, doi: 10.1117/12.550925

Woosley, S. E. 2017, ApJ, 836, 244, doi: 10.3847/1538-4357/836/2/244

—. 2019a, ApJ, 878, 49, doi: 10.3847/1538-4357/ab1b41

—. 2019b, ApJ, 878, 49, doi: 10.3847/1538-4357/ab1b41

Woosley, S. E., Blinnikov, S., & Heger, A. 2007, Nature, 450, 390, doi: 10.1038/nature06333

Woosley, S. E., & Eastman, R. G. 1997, in NATO Advanced Study Institute (ASI) Series C, Vol. 486, Thermonuclear Supernovae, ed. P. Ruiz-Lapuente, R. Canal, & J. Isern, 821, doi: 10.1007/978-94-011-5710-0_51

Woosley, S. E., & Heger, A. 2007, Phys. Rep., 442, 269, doi: 10.1016/j.physrep.2007.02.009

Woosley, S. E., Heger, A., & Weaver, T. A. 2002, Reviews of Modern Physics, 74, 1015, doi: 10.1103/RevModPhys.74.1015

Woosley, S. E., & Kasen, D. 2011, ApJ, 734, 38, doi: 10.1088/0004-637X/734/1/38

Woosley, S. E., Langer, N., & Weaver, T. A. 1993, ApJ, 411, 823, doi: 10.1086/172886

—. 1995, ApJ, 448, 315, doi: 10.1086/175963

Woosley, S. E., Sukhbold, T., & Kasen, D. N. 2021, ApJ, 913, 145, doi: 10.3847/1538-4357/abf3be

Woosley, S. E., & Weaver, T. A. 1986, ARA&A, 24, 205, doi: 10.1146/annurev.aa.24.090186.001225

—. 1994, ApJ, 423, 371, doi: 10.1086/173813

—. 1995, ApJS, 101, 181, doi: 10.1086/192237

Wu, S. C., & Fuller, J. 2022, ApJ, 940, L27, doi: 10.3847/2041-8213/ac9b3d

Yamanaka, M., Fujii, M., & Nagayama, T. 2023, arXiv e-prints, arXiv:2306.00263, doi: 10.48550/arXiv.2306.00263

Yang, S., Valenti, S., Cappellaro, E., et al. 2017, ApJ, 851, L48, doi: 10.3847/2041-8213/aaa07d

Yang, S., Sand, D. J., Valenti, S., et al. 2019a, ApJ, 875, 59, doi: 10.3847/1538-4357/ab0e06

—. 2019b, ApJ, 875, 59, doi: 10.3847/1538-4357/ab0e06

—. 2019c, ApJ, 875, 59, doi: 10.3847/1538-4357/ab0e06

Yao, Y., De, K., Kasliwal, M. M., et al. 2020, ApJ, 900, 46, doi: 10.3847/1538-4357/abaa3d

Yaron, O., & Gal-Yam, A. 2012, PASP, 124, 668, doi: 10.1086/666656

Yaron, O., Perley, D. A., Gal-Yam, A., et al. 2017, Nature Physics, 13, 510, doi: 10.1038/nphys4025

Yoon, S.-C. 2015, PASA, 32, e015, doi: 10.1017/pasa.2015.16

—. 2017, MNRAS, 470, 3970, doi: 10.1093/mnras/stx1496

Yoon, S.-C., Chun, W., Tolstov, A., Blinnikov, S., & Dessart, L. 2019, ApJ, 872, 174, doi: 10.3847/1538-4357/ab0020

Yoon, S.-C., Dessart, L., & Clocchiatti, A. 2017, ApJ, 840, 10, doi: 10.3847/1538-4357/aa6afe

Yoon, S. C., Woosley, S. E., & Langer, N. 2010, ApJ, 725, 940, doi: 10.1088/0004-637X/725/1/940

Yoshida, T., Umeda, H., Maeda, K., & Ishii, T. 2016, MNRAS, 457, 351, doi: 10.1093/mnras/stv3002

Young, D. 2022, Plot Results from ATLAS Force Photometry Service. https://gist.github.com/thespacedoctor/86777fa5a9567b7939e8d84fd8cf6a76

Yuan, F., & Narayan, R. 2014, ARA&A, 52, 529, doi: 10.1146/annurev-astro-082812-141003

Zampieri, L. 2017, in Handbook of Supernovae, ed. A. W. Alsabti & P. Murdin, 737, doi: 10.1007/978-3-319-21846-5_26

Zhang, W., & Fryer, C. L. 2001, ApJ, 550, 357, doi: 10.1086/319734